

ABSTRACT

Title of Document: MODELING AND SIMULATION OF MIXING LAYER FLOWS FOR ROCKET ENGINE FILM COOLING

Kiran Hamilton Jeffrey Dellimore,
Doctor of Philosophy, 2010

Directed By: Associate Professor, Christopher P. Cadou,
Department of Aerospace Engineering

Film cooling has been selected for the thermal protection of the composite nozzle extension of the J-2X engine which is currently being developed for the second stage of NASA's next generation launch vehicle, the Ares I rocket. However, several challenges remain in order to achieve effective film cooling of the nozzle extension and to ensure its safe operation. The extreme complexity of the flow (three-dimensional wakes, lateral flows, vorticity, and flow separation) makes predicting film cooling performance difficult. There is also a dearth of useful supersonic film cooling data available for engineers to use in engine design and a lack of maturity of CFD tools to quantitatively match supersonic film cooling data. This dissertation advances the state of the art in film cooling by presenting semi-empirical analytical models which improve the basic physical understanding and prediction of the effects of pressure gradients, compressibility and density gradients on film cooling effectiveness. These models are shown to correlate most experimental data well and to resolve several conflicts in the open literature. The core-to-coolant stream velocity ratio, R , and the Kays acceleration parameter, K_P , are identified as the critical

parameters needed to understand how pressure gradients influence film cooling performance. The convective Mach number, M_c , the total temperature ratio, θ_0 , and the Mach number of the high speed stream, M_{HS} , are shown to be important when explaining the effects of compressibility and density gradient on film cooling effectiveness. An advance in the simulation of film cooling flows is also presented through the development of a computationally inexpensive RANS methodology capable of correctly predicting film cooling performance under turbulent, subsonic conditions. The subsonic simulation results suggest that in order to obtain accurate predictions using RANS it is essential to thoroughly characterize the turbulent states at the inlet of the coolant and core streams of the film cooling flow. The limitations of this approach are established using a Grid Convergence Index (GCI) Test and a demonstration of the extension of this RANS methodology to supersonic conditions is presented.

Modeling and Simulation of Mixing Layer Flows For Rocket Engine Film Cooling

By

Kiran Hamilton Jeffrey Dellimore

Dissertation submitted to the Faculty of the Graduate School of the
University of Maryland, College Park, in partial fulfillment
of the requirements for the degree of
Doctor of Philosophy
2010

Advisory Committee:

Associate Professor Christopher P. Cadou, Chair

Associate Professor Arnaud Trouvé, Co-Chair

Associate Professor Kenneth H. Yu

Associate Professor James Baeder

Professor J. Gordon Leishman

Professor Peter W. Wolfe

© Copyright by
Kiran Hamilton Jeffrey Dellimore
2010

Dedication

This dissertation is dedicated to all of the people who helped and supported me after my near fatal accident on the night of March 10th 2007. My parents Jeffrey and Jeanette; my best friend Alon and his wife Sylvie; my coworkers and friends Anand and Shyam; my brothers Chike and Imari; my aunts Jaqueline, Madeleine and Odette; my uncles Simon, Bruce and Ewart; my surgeon Dr. Stephen Gunther; the nursing staff at the Washington Hospital Center; my ex-girlfriend Ying; my occupational therapists Susan and Barbara; my advisor Dr. Christopher Cadou; my research group members Dr. André Marshall, Dr. Arnaud Trouvé, Andrew, Fernando, Daanish and Carlos; the staff at the Graduate Legal Aid Office; my mentor Dr. Darryl Pines; my friends Rahwa, Chi, Marc, Ayodeji, Jamie and Rudy; my squash teammates and friends Mike S., Anand B., Mike H., Jane, Neil, Taimur, Prasanth, Dave, Mike L. and Moses; my wonderful girlfriend Preyasha and many others. Without your help I would have never made a full recovery from my injuries and I wouldn't have had the opportunity to finish my Ph.D. Thank you all!

Acknowledgements

This work has been sponsored by the Space Vehicles Technology Institute, grant NCC3-989, one of the NASA University Institutes, with joint sponsorship from the Department of Defense. Appreciation is expressed to Claudia Meyer of the NASA Glenn Research Center, program manager of the University Institute activity, and to Dr. John Schmisser and Dr. Walter Jones of the Air Force Office of Scientific Research. Special thanks also to Joseph Ruf, Douglas Westra and Kevin Tucker at NASA Marshall Space Flight Center for their assistance and guidance during many of the critical phases of this work.

Table of Contents

Dedication	ii
Acknowledgements	iii
Table of Contents	iv
List of Tables.....	vii
Chapter 1: Introduction	1
1.1 Motivation: What is film cooling and why are we interested in it?	1
1.2 The Key Challenges in Rocket Engine Film Cooling	5
1.3 Review of Previous Work	9
1.3.1 Introduction	9
1.3.2 Free mixing layer flows.....	10
1.3.3 Film cooling flows (confined mixing layer flows with thermal gradients).....	20
1.3.4 Overall Summary:	44
1.4 Main Objectives	45
1.5 Organization of This Thesis	46
Chapter 2: The Influence of Pressure Gradients on Film Cooling Performance	48
2.1 Introduction	48
2.2 Background	48
2.2.1 Types of Pressure Gradients.....	48
2.2.2 Quantification of Pressure Gradients	49
2.3 Analysis.....	50
2.3.1 Film Cooling Model Development	52
2.3.2 Isobaric Case (Simon’s Model).....	56
2.3.3 Non-isobaric case	58
2.4 Selection of Model Parameters	61
2.4.1 Introduction	61
2.4.2 Sensitivity Analysis.....	62
2.4.3 Least Squares Analysis Details	64
2.4.4 Experimental Data.....	68
2.5 Results	72
2.5.1 Introduction	72
2.5.2 Constant Pressure Gradient Results	72
2.5.3 Physical Explanation	74
2.5.5 Reconciling Anomalies in the Literature	77
2.6 Conclusions	80
Chapter 3: The Influence of Density Gradients on Film Cooling Performance.....	82
3.1 Introduction	82
3.2 Background	82
3.2.1 Quantifying Density Gradient Effects.....	82
3.2.2 Quantifying the Magnitude of Density Gradient Effects	84
3.3 Effect of Density Gradients and Compressibility on Mixing Layer Growth Rate	85
3.3.1 Introduction	85

3.3.2	Development of a Compressible Shear Layer Growth Rate Model.....	86
3.3.3	Numerical Integration Procedure:	98
3.3.4	Comparison to Experimental Data	100
3.4	Analysis	107
3.4.1	Introduction	107
3.4.2	Compressible Film Cooling Model Development	108
3.4.3	Selection of Model Parameters	115
3.4.4	Experimental Film Cooling Data	117
3.5	Results	117
3.5.1	Comparison to Experimental Data	118
3.5.2	Physical Explanation	121
3.5.3	Resolution of Discrepancies in the Literature	126
3.6	The Combined Effect of Pressure Gradients and Compressibility	128
3.6.1	Introduction	128
3.6.2	The Combined Pressure Gradient Compressible Film Cooling Model....	128
3.6.3	Comparison to Experimental Data	133
3.6.4	Resolution of Discrepancies in the Literature	135
3.7	Conclusions	136
Chapter 4:	Numerical Prediction of Subsonic Film Cooling	138
4.1	Introduction	138
4.2	Description of Loci-CHEM Navier-Stokes Solver	138
4.2.1	Governing Equations.....	138
4.2.2	Turbulence Model	144
4.2.3	Transport model	149
4.2.4	Numerical Methods	149
4.3	Quantification of Numerical Uncertainty.....	150
4.3.1	Introduction	150
4.3.2	Numerical Uncertainty	150
4.3.3	Quantifying Numerical Uncertainty.....	152
4.4	Validation of Solver	156
4.4.1	Introduction	156
4.4.2	Channel Flow	156
4.4.3	Boundary Layer Flow.....	172
4.5	Description of Subsonic Film Cooling Numerical Simulations.....	178
4.5.1	Introduction	178
4.5.2	Description of Subsonic Film Cooling Experiment	178
4.5.3	Overview of RANS methodology	182
4.5.4	Precursor Simulation Details.....	183
4.5.5	Subsonic Film Cooling Simulation Details.....	189
4.6	Subsonic Film Cooling Simulation Results	192
4.6.1	Temperature Field	192
4.6.2	Velocity Field	193
4.6.3	Vorticity Field	194
4.6.2	Thermal Mixing.....	197
4.6.2	Momentum Mixing	199
4.6.3	Skin Friction (Wall Shear Stress).....	201

4.6.4 Film Cooling Effectiveness.....	203
4.6.5 Explanation of the Discrepancies between the Simulations and Experiment	206
4.7 Conclusions.....	210
Chapter 5: Supersonic Film Heating Simulations.....	213
5.1 Introduction.....	213
5.2 Description of Supersonic Film Heating Experiment.....	213
5.3 Objectives of the Supersonic Film Heating Numerical Simulations	219
5.4 Validation of Solver.....	220
5.4.1 Introduction.....	220
5.4.2 Supersonic flow over a wedge	220
5.4.3 Supersonic flow over a blunt body.....	224
5.5 Supersonic Film Cooling Simulation Details.....	228
5.5.1 Introduction.....	228
5.5.1 Grid Details	228
5.5.2 Boundary and Initial Conditions	229
5.5.3 Turbulence Model.....	231
5.5.4 Convergence/Steady State.....	232
5.6 Results.....	233
5.6.1 Thermal mixing.....	233
5.6.2 Momentum mixing.....	235
5.6.3 Heat Flux and Film Heating Effectiveness	237
5.7 Conclusions.....	244
Chapter 6: Conclusions.....	246
6.1 Research Summary.....	246
6.2 Fundamental Contributions.....	249
Chapter 7: Extensions and Future work.....	253
Appendix.....	255
Bibliography.....	258

List of Tables

Table 2.1 Summary of empirical constants determined for the ZPG Teekaram et al. [140] data.....	71
Table 2.2 Summary of PGFM predictions.....	78
Table 2.3 Summary of 3-D hole injection data.....	79
Table 3.1 Summary of the three compressibility regimes.....	84
Table 3.2 Summary of average relative errors in the normalized growth rate predictions of the CVM and DVM for all of the experimental data examined.....	105
Table 3.3 Summary of experimental conditions used in various film cooling studies used to validate the CFM	117
Table 3.4 Summary of experimental conditions used in various compressible film cooling studies	127
Table 3.5 Summary of experimental conditions used by Teekaram et al. [140].....	134
Table 4.1 Summary of the subsonic slot-jet film cooling test conditions explored by Cruz et al. [187].....	180
Table 4.2 Summary of the uncertainties in measured and derived quantities from the subsonic slot-jet film cooling experiments performed by Cruz et al. [187].....	181
Table 4.3 Summary of the analysis of the experimental velocity data taken by Cruz et al. [187].....	209
Table 5.1 Proposed test matrix for the supersonic film heating experiment and design operating conditions for the J-2X engine nozzle extension.....	218
Table 5.2 Summary of the β , M_2 , P_2 and T_2 conditions predicted by Loci-CHEM and the exact oblique shock relations.....	223
Table 5.3 Summary of results for the standoff distance of a detached shock associated with turbulent, supersonic flow over a blunt body at various upstream Mach numbers.....	226

List of Figures

Figure 1-1 Schematic illustration of a liquid rocket engine (LRE) with staged combustion	2
Figure 1-2 Conceptual drawing of the J-2X engine showing various key components	3
Figure 1-3 Sketch showing the various fluid dynamic and geometric factors influencing the film cooling process.....	5
Figure 1-4 Schematic illustration of the pressure distribution in a rocket engine.....	7
Figure 1-5 Sketch showing: a) 3-D hole injection and b) 2-D slot injection.....	8
Figure 1-6 Schematic of a two-dimensional shear layer.....	10
Figure 1-7 Sketch illustrating examples of flow-fields with compressible shear layers.....	15
Figure 1-8 Schematic illustration of: a) A wall-jet film b) A core-driven film.....	21
Figure 1-9 a) Sketch of a film cooled combustor liner {Adapted from Naval Ships' Technical Manual [101]} b) Picture of a gas turbine blade with several rows of cooling holes {From Kaszeta et al. [102]}.....	21
Figure 1-10 Representative two-dimensional film cooling geometries: a) porous slot, b) tangential injection (step-down slot) and c) angled slot.....	22
Figure 1-11 Sketch of the angled slot-injection film cooling configuration used by Hartnett et al. [107].....	23
Figure 1-12 Sketch of the 3-D hole-injection film cooling configuration used by Mayhew et al. [11]	24
Figure 1-13 Schematic of Simon's [114] wall jet, slot film cooling model.....	26
Figure 1-14 Schematic of annular film cooling of a rocket thrust chamber.....	32
Figure 1-15 Schematic of water film cooling of a rocket engine wall.....	33
Figure 1-16 Schematic of a water-cooled conical nozzle. (b) Schematic of a water-cooled bell contour nozzle.....	35
Figure 1-17 Plot showing the three different pressure gradient profiles used by Teekaram et al. [140].....	37

Figure 1-18 Schematic illustration of the boundary layer model used by Sivrioglu [157].....	39
Figure 2-1 Sketch showing: a) An adverse pressure gradient b) A favorable pressure gradient.....	48
Figure 2-2 Pressure gradient film cooling model {adapted from Simon [114] (1986)}.....	50
Figure 2-3 Sketch of shear layer geometry. {Adapted from Abramovich [27] (1962)}.....	55
Figure 2-4 Effect of variation of: a) a_0 b) C_0 c) N and d) I_v on the predictions of the PGFM for a wall-jet film under zero pressure gradient conditions ($R = 0.63$, $\lambda = 2.22$ and $TR = 0.71$).....	63
Figure 2-5 Range of predictions obtained for different initial guesses for a_0 and N : a) using the two-variable LSQ method for a wall-jet film under zero pressure gradient conditions ($R = 0.63$, $\lambda = 2.22$ and $TR = 0.71$); and b) using the three-variable LSQ method for the core-driven film under zero pressure gradient conditions ($R = 3.53$, $\lambda = 0.33$ and $TR = 0.8590$).....	68
Figure 2-6 Film cooling efficiency, η_{eff} , as a function of non-dimensional stream-wise distance, $x/\lambda s$, for an isobaric, turbulent wall-jet film ($R=0.63$) at $\lambda=2.22$ and $TR=0.71$, as predicted by the SM and PGFM.....	69
Figure 2-7 Comparison of film cooling effectiveness, η_{eff} , as a function of non-dimensional stream-wise distance, $x/\lambda s$, predicted by the PGFM to experimental measurements by Teekaram et al. [140] for a turbulent core-driven film ($R_0 = 3.53$) in the presence of a constant zero pressure gradient, at $\lambda = 0.33$, $TR = 0.86$	70
Figure 2-8 Film cooling efficiency, η_{eff} , as a function of non-dimensional streamwise distance, $x/\lambda s$, for a turbulent wall-jet ($R_0 = 0.63$) undergoing a constant favorable pressure gradient ($C_{P_\infty} = -0.05$), a constant adverse pressure gradient ($C_{P_\infty} = +0.05$) and a constant zero pressure gradient ($C_{P_\infty} = 0.0$), at $\lambda = 2.22$ and $TR = 0.71$, as predicted by the PGFM.....	72
Figure 2-9 Film cooling efficiency, η_{eff} , as a function of non-dimensional streamwise distance, $x/\lambda s$, for a turbulent core-driven film ($R_0 = 1.58$) undergoing a constant favorable pressure gradient ($C_{P_\infty} = -0.05$), a constant adverse pressure gradient ($C_{P_\infty} = +0.05$) and a constant zero pressure gradient ($C_{P_\infty} = 0.0$), at $\lambda=0.89$ and $TR= 0.71$, as predicted by the PGFM.....	73

Figure 2-10 Non-dimensional shear layer impingement thickness, $b(x_1)/s$, versus non-dimensional initial region length x_1/s and non-dimensional pressure gradient $C_{p\infty}$, for a wall-jet film ($R_0 = 0.63$) and a core-driven film ($R_0=1.58$) at $TR = 0.71$	74
Figure 2-11 a) Change in the shear layer growth rate, ℓ , versus non-dimensional pressure gradient $C_{p\infty}$, for a wall-jet film ($R_0 = 0.63$) and a core-driven film ($R_0 = 1.58$). b) Overall shear layer growth rate, $k'+\ell$, versus non-dimensional pressure gradient $C_{p\infty}$, for a wall-jet film ($R_0 = 0.63$) and a core-driven film ($R_0=1.58$).....	75
Figure 2-12 Film cooling efficiency, η_{eff} , predicted by the PGFM as a function of non-dimensional streamwise distance, $x/\lambda s$, for a turbulent core-driven film ($R_0 = 3.53$) with a strong favorable pressure gradient ($K_p = 2.62 \times 10^{-6}$), a mild adverse pressure gradient ($K_p = -0.22 \times 10^{-6}$) and zero pressure gradient. $\lambda = 0.33$ and $TR = 0.86$	76
Figure 2-13 Peak non-dimensional film cooling effectiveness as a function of acceleration parameter (K_p) and velocity ratio (R) reported in various studies.....	77
Figure 3-1 Schematic showing the isentropic model of large-scale structure in a compressible shear layer.....	83
Figure 3-2 Compressible shear layer geometry and nomenclature.....	86
Figure 3-3 a) Mean non-dimensional velocity profile U_c/U_1 as a function of π for $r = 1/5$. b) Mean temperature profile $T_{0,c}/T_1$ as a function of π , for $\theta_0=5$	90
Figure 3-4 Effect of convective Mach number, M_c , on the proportionality constant ratio, c_{comp}/c_{inc} at a fixed density and velocity ratio, $S = 1.0$ and $R = 2.0$, for various gas mixtures. $\gamma_2/\gamma_1 = 0.8$ corresponds to an acetone-air mixture, $\gamma_2/\gamma_1 = 1.0$ corresponds to an air-air mixture and $\gamma_2/\gamma_1 = 1.2$ corresponds to a helium-air mixture.....	95
Figure 3-5 Residual (R_n) as a function of the number of points (N) associated with the Gauss-Legendre quadrature of: a) A_0 and b) A_1 for the $M_c = 0.96$ test case by Hall [198].....	99
Figure 3-6 Normalized compressible mixing layer growth rate, $\delta'_{comp}/\delta'_{inc}$, as function of convective Mach number, M_c , for a homogeneous air shear layer at a fixed density ratio, $S = 0.5$ and a velocity ratio, $R = 4.0$, as predicted by the CVM and the DVM.....	100
Figure 3-7 a)-f) Variation of normalized shear layer growth rate, $\delta'_{comp}/\delta'_{inc}$, with convective Mach number, M_c , for the conditions explored in various homogeneous (air) shear layer studies [195, 202-211].....	102

Figure 3-8 a)-d) Variation of normalized shear layer growth rate, $\delta'_{comp}/\delta'_{inc}$, with convective Mach number, M_c , for the conditions explored in various heterogeneous shear layer studies [70,199-203].....	103
Figure 3-9 Per cent Relative Error in the CVM predictions of normalized mixing layer growth rate as a function of convective Mach number, M_c , for all of the experimental data examined [70,194,198-210].....	106
Figure 3-10 Wall-jet film cooling model {Adapted from Simon [114] (1986)}.....	108
Figure 3-11 Range of predictions obtained for different initial guesses for d_0 and K using the two-variable LSQ method for: a) moderately compressible conditions ($M_c = 0.30$, $M_{HS} = 0.80$ and $\theta_0 = 0.58$) and b) highly compressible conditions ($M_c = 1.29$, $M_{HS} = 6.0$ and $\theta_0 = 0.62$).....	116
Figure 3-12 Plot of film cooling effectiveness, η_{eff} , as a function of non-dimensional streamwise distance, $x/(\lambda s)$, for a turbulent, wall-jet at $\theta_0 = 0.71$ and $M_c = 0.015$ as predicted by the CFM and the SM.....	118
Figure 3-13 Plot of film cooling effectiveness, η_{eff} , as a function of non-dimensional streamwise distance, $x/(\lambda s)$ for a turbulent, core-driven film at $\theta_0 = 0.58$ and $M_c = 0.31$ as predicted by the CFM and SM.....	119
Figure 3-14 Plot of film cooling effectiveness, η_{eff} , as a function of non-dimensional streamwise distance, $x/(\lambda s)$ for a turbulent, core-driven film at $\theta_0 = 0.62$ and $M_c = 1.29$ as predicted by the CFM and the SM.....	120
Figure 3-15 Compressible (CFM) to incompressible (SM) film cooling effectiveness (peak $\eta_{eff(comp)}/\eta_{eff(inc)}$) as a function of convective Mach number, M_c , and non-dimensional shear layer impingement length, $x_{1,comp}/x_{1,inc}$, for a turbulent, core-driven film at fixed total temperature ratios, $\theta_0 = 1.00, 0.50$ and 0.25	122
Figure 3-16 Compressible mixing layer growth rate: a) normalized (δ'_{comp}), and b) unnormalized (db/dx_{comp}), as a function of convective Mach number, M_c , for a turbulent, core-driven film at fixed total temperature ratios, $\theta_0 = 1.00, 0.50$ and 0.25	123
Figure 3-17 Plot of peak non-dimensional film cooling effectiveness, $\eta_{eff(comp)}/\eta_{eff(inc)}$, as a function of total temperature ratio, θ_0 , and non-dimensional shear layer impingement length, $x_{1,comp}/x_{1,inc}$, for a turbulent, core-driven film at fixed convective Mach numbers, $M_c = 0.50, 0.25$ and 0.00 , as predicted by the CFM and SM.....	124
Figure 3-18 Compressible mixing layer growth rate: a) normalized (δ'_{comp}), and b) unnormalized (db/dx_{comp}), as a function of total temperature ratio, θ_0 , for a turbulent,	

core-driven film at fixed total temperature ratios, $M_c = 0.50, 0.25$ and 0.00125

Figure 3-19 a) Change in the shear layer growth rate (m) versus convective Mach number (M_c) for a wall-jet film ($R_0 = 0.63$) and a core-driven film ($R_0 = 1.58$). b) Change in the shear layer growth rate (ℓ) versus non-dimensional pressure gradient ($C_{p\infty}$) for a wall-jet film ($R_0 = 0.63$) and a core-driven film ($R_0 = 1.58$). c) Contours of overall shear layer growth rate ($k'+\ell+m$) versus convective Mach number (M_c) and non-dimensional pressure gradient ($C_{p\infty}$) for a wall-jet film ($R_0 = 0.63$) d) Contours of overall shear layer growth rate ($k'+\ell+m$) versus convective Mach number (M_c) and non-dimensional pressure gradient ($C_{p\infty}$) for a core-driven film ($R_0 = 1.58$).....130

Figure 3-20 Film cooling effectiveness, η_{eff} , predicted by the CPFM as a function of non-dimensional streamwise distance, x/λ_s , for a turbulent core-driven film ($R_0 = 3.53$) with a strong favorable pressure gradient ($K_p = 2.62 \times 10^{-6}$), a mild adverse pressure gradient ($K_p = -0.22 \times 10^{-6}$) and zero pressure gradient. $\lambda = 0.33$ and $\theta_0 = 0.82$133

Figure 3-21 Peak non-dimensional film cooling effectiveness (η/η_0) as a function of acceleration parameter (K_p) and velocity ratio (R) reported in various studies [140,155,220-221].....135

Figure 4-1 Sensitivity of predicted film cooling effectiveness to the type of turbulence model used.....152

Figure 4-2 Schematic of the channel flow geometry.....156

Figure 4-3 Inlet velocity profiles for: a) developing HPF case and b) fully developed HPF case.....158

Figure 4-4 Evolution of velocity profile for developing, laminar Hagen-Poiseuille Flow in a square channel at four stream-wise locations: a) $x/H = 10$, b) $x/H = 30$, c) $x/H = 50$ and d) $x/H = 90$159

Figure 4-5 a) Streamwise evolution of the pressure for developing, laminar Hagen-Poiseuille Flow in a square channel. b) Per cent difference between the analytical solution and numerical predictions for the pressure drop along the square channel for developing, laminar Hagen-Poiseuille Flow in square channel.....160

Figure 4-6 Evolution of velocity profile for fully developed, laminar Hagen-Poiseuille Flow in a square channel at four stream-wise locations: a) $x/H = 10$, b) $x/H = 30$, c) $x/H = 50$ and d) $x/H = 90$162

Figure 4-7 a) Stream-wise evolution of the pressure in case (ii). b) Per cent difference between the analytical solution and numerical predictions for the pressure drop along the square channel for case (ii).....163

Figure 4-8 Inlet velocity profiles specified for: a) the developing turbulent channel case and b) the fully developed turbulent channel flow case.....	165
Figure 4-9 Evolution of velocity profile for developing, laminar Hagen-Poiseuille Flow in a square channel at four stream-wise locations: a) $x/H = 10$, b) $x/H = 30$, c) $x/H = 50$ and d) $x/H = 90$	167
Figure 4-10 a) Stream-wise evolution of the pressure for developing turbulent channel flow. b) Per cent difference between the analytical solution and numerical predictions for the pressure drop associated with developing turbulent channel flow.....	168
Figure 4-11 Evolution of velocity profile for fully developed, turbulent channel flow at four stream-wise locations: a) $x/H = 10$, b) $x/H = 30$, c) $x/H = 50$ and d) $x/H = 90$	169
Figure 4-12 a) Stream-wise evolution of the pressure for fully developed turbulent channel flow. b) Per cent difference between the analytical solution and numerical predictions for the pressure drop associated with fully developed turbulent channel flow.....	170
Figure 4-13 Mean velocity (a) and temperature (b) profiles in wall units predicted by LOCI-CHEM for fully developed turbulent channel flow.....	172
Figure 4-14 Schematic of the geometry used in the boundary-layer flow simulations.....	172
Figure 4-15 a) Dimensionless velocity, u/U , as a function of dimensionless vertical distance, y/δ , for a laminar, incompressible flat-plate boundary layer at $Re_x = 5.0 \times 10^5$. b) Per cent difference between the CHEM predictions and von Kármán approximation for u/U	175
Figure 4-16 a) Wall shear stress, τ_{wall} , as a function of Reynolds number based on streamwise distance, Re_x , for a laminar, incompressible flat-plate boundary layer at a free-stream velocity of 25m/s (Peak $Re_x = 5.95 \times 10^5$). b) Per cent difference between the CHEM predictions and the exact Blassius solution for the wall shear stress associated with a laminar, incompressible flat-plate boundary layer at a free-stream velocity of 25m/s (Peak $Re_x = 5.95 \times 10^5$).....	176
Figure 4-17 a) Dimensionless velocity, u/U , as a function of dimensionless vertical distance, y/δ , for a turbulent flat-plate boundary layer at $Re_x = 4.0 \times 10^7$. b) Per cent difference between CHEM's predictions and Prandtl's 1/7 th power approximation for u/U	177
Figure 4-18 a) Wall shear stress, τ_{wall} , as a function of Reynolds number based on streamwise distance, Re_x , for a turbulent flat-plate boundary layer at a free-stream velocity of 100m/s (Peak $Re_x = 4.1 \times 10^7$). b) Per cent difference between the CHEM predictions and the turbulent boundary layer correlation.....	177

Figure 4-19 Schematic of the hot wind tunnel facility used by Cruz et al. [187] to make subsonic slot-jet film cooling measurements.....	178
Figure 4-20 a) Test section used by Cruz et al. [187] to make subsonic slot-jet film cooling measurements {Adapted from Cruz et al. [187]}. b) Schematic illustration of the canonical film cooling configuration.....	180
Figure 4-21 Overview of RANS methodology.....	182
Figure 4-22 Plot of velocity (U), turbulent kinetic energy (K) and turbulent eddy viscosity (μ_t), as a function of non-dimensional wall-normal distance, y/s , obtained from the precursor coolant and core simulations at: a) $\lambda = 0.5$ b) $\lambda = 1.0$ and c) $\lambda = 3.0$	187
Figure 4-23 Schematic of the grid used for the subsonic film cooling simulations.....	189
Figure 4-24 Schematic of the subsonic film cooling computational domain showing the boundary conditions used in the numerical simulations.....	190
Figure 4-25 a) Residual drop, b) Mass conservation, c) Temperature probe output, as a function of the number of iterations performed for the $\lambda=1.3$ case.....	191
Figure 4-26 Temperature contours predicted by CHEM for the film cooling of an adiabatic wall at: a) $\lambda = 0.6$. b) $\lambda = 1.3$ and c) $\lambda = 3.0$	192
Figure 4-27 Velocity contours predicted by CHEM for the film cooling of an adiabatic wall at: a) $\lambda = 0.6$. b) $\lambda = 1.3$ and c) $\lambda = 3.0$	193
Figure 4-28 Vorticity contours predicted by CHEM for the film cooling of an adiabatic wall at: a) $\lambda = 0.6$. b) $\lambda = 1.3$ and c) $\lambda = 3.0$	194
Figure 4-29 Zoomed vorticity contours predicted by CHEM for the film cooling of an adiabatic wall at: a) $\lambda = 0.6$. b) $\lambda = 1.3$ and c) $\lambda = 3.0$	196
Figure 4-30 Profiles of normalized temperature, T/T_s , at four discrete locations downstream of the point of coolant injection, for the film cooling of an adiabatic wall at: a) $\lambda = 0.6$. b) $\lambda = 1.3$ and c) $\lambda = 3.0$	197
Figure 4-31 Profiles of normalized velocity, U/U_c , at four discrete locations downstream of the point of coolant injection, associated with the film cooling of an adiabatic wall at: a) $\lambda = 0.6$. b) $\lambda = 1.3$ and c) $\lambda = 3.0$	199
Figure 4-32 Variation of skin friction coefficient, $C_{f_{\infty}}$, with non-dimensional streamwise distance, $x/\lambda s$, associated with the film cooling of an adiabatic wall at three different blowing ratios ($\lambda = 0.6, 1.3$ and 3.0).....	201

Figure 4-33 Variation of film cooling effectiveness, η_{eff} , with non-dimensional streamwise distance, x/s , for the film cooling of an adiabatic wall at: a) $\lambda = 0.6$. b) $\lambda = 1.3$ and c) $\lambda = 3.0$	203
Figure 4-34 Change in velocity (ΔU) at a fixed measurement location as a function of non-dimensional wall-normal distance (y/s) for: a) &b) $\lambda = 0.6$ case, c) & d) $\lambda = 1.3$ and d) & e) $\lambda = 3.0$	207
Figure 5-1 Comparison of the heat flux in: a) Film cooling and b) Film heating configurations.....	213
Figure 5-2 Schematic of the UMD blow-down supersonic wind tunnel facility.....	214
Figure 5-3 Schematic of the supersonic wedge geometry.....	220
Figure 5-4 Plot showing contours of: a) x-component velocity (u), b) Mach number (M), c) pressure (P) and d) temperature (T), predicted by CHEM for Mach 3.0 flow over a 15° wedge.....	222
Figure 5-5 Schematic of the blunt body grid	224
Figure 5-6 Plot of shock standoff distance, δ/d , as a function of Mach number, M , associated with turbulent, supersonic flow over a blunt body over a range of Mach numbers between 6 and 10.....	226
Figure 5-7 Contours of a) x-component velocity, b) Mach number, c) pressure and d) temperature associated with supersonic flow over a blunt body at Mach 10.....	227
Figure 5-8 Schematic illustration of the grid used for the supersonic film heating simulations.....	228
Figure 5-9 Schematic of the supersonic film heating computational domain showing the boundary conditions used in the Off-Baseline #1 Case numerical simulations.....	229
Figure 5-10 Schematic of the supersonic film heating computational domain showing the boundary conditions used in the Off-Baseline #2 Case numerical simulations.....	230
Figure 5-11 a) Residual drop, b) Mass conservation, c) Temperature probe output, as a function of the number of iterations performed for the Off-Baseline #2 case with film heating.....	232

Figure 5-12 Profiles of normalized temperature, T/T_{wall} , at four discrete locations downstream of the point of film injection, associated with film heating of an isothermal wall under the conditions given in: a) the Off-Baseline #1 Case and b) the Off-Baseline #2 Case.....233

Figure 5-13 Profiles of normalized velocity, U/U_f , at four discrete locations downstream of the point of film injection, associated with the film heating of an isothermal wall under conditions specified in: a) the Off-Baseline #1 Case and b) the Off-Baseline #2 Case.....235

Figure 5-14 Heat flux (\dot{Q}) as a function of non-dimensional streamwise distance (x/h) along the lower and upper test section walls predicted by CHEM for the Off-Baseline #1 case with and without film injection.....237

Figure 5-15 Schematic illustration of the supersonic film heating flowfield highlighting the shockwave boundary layer interaction.....238

Figure 5-16 Contours of constant temperature associated with the Off-Baseline #1 Case: a) with film injection and b) without film injection. c) Non-dimensional thermal boundary layer thickness (δ) associated with the upper and lower walls for the Off-Baseline #1 Case.....239

Figure 5-17 Adiabatic film cooling effectiveness (η_{eff}) as a function of non-dimensional streamwise distance (x/h) along the test section wall predicted by CHEM for the Off-Baseline #1 configuration with and without film heating.....240

Figure 5-18 Heat flux (\dot{Q}) as a function of non-dimensional streamwise distance (x/h) along the test section wall predicted by CHEM for the Off-Baseline #2 case with and without film heating.....241

Figure 5-19 Contours of constant temperature associated with the Off-Baseline #2 Case: a) with film injection and b) without film injection. c) Thermal boundary layer thickness associated with the upper and lower walls for the Off-Baseline #2 Case.....242

Figure 5-20 Adiabatic film cooling effectiveness (η_{eff}) as a function of non-dimensional streamwise distance (x/h) along the test section wall predicted by CHEM for the Off-Baseline #2 configuration with and without film heating.....244

Nomenclature

a_0 : Empirical constant

b : Shear layer thickness (m)

β : Initial region factor

b_0 : Film cooling louver thickness (m)

c : Ratio of density in mixing zone I at the transition point to the coolant stream density

C_0 : Empirical constant

C_M : Turbulent mixing coefficient

$C_{P\infty}$: Hot gas stream pressure coefficient

db/dx : Shear layer growth rate

h : Heat transfer coefficient (W/m^2), slot height (m)

I_v : Overall average turbulence intensity

$I_{v,s}$: Average transverse coolant stream turbulence intensity

$I_{v,\infty}$: Average transverse hot stream turbulence intensity

J : Momentum flux ratio

L : Length of mixing passage (m)

$\{$: Characteristic length scale (m)

k : Turbulent kinetic energy (J), thermal conductivity (W/mK)

K_p : Kays acceleration parameter

\dot{m} : Mass flow rate (kg/sec)

M : Mach number

\dot{m}'_e : Entrained hot gas stream rate per unit length ($kg/m*sec$)

\dot{m}_f : Total mass flow rate of the film per unit length ($kg/m*sec$)
 \dot{m}_s : Coolant mass flow rate per unit length ($kg/m*sec$)
 N : Empirical constant
 P : Static pressure (Pa)
 p/d : Injection hole spacing
 Pr : Prandtl number
 q : Heat flux
 r : Grid refinement ratio
 R : Ratio of the local average hot stream to coolant stream velocity, U_∞/U_s
 R_0 : Ratio of the initial average hot stream to coolant stream velocity, $U_{0\infty}/U_{0s}$
 Re : Reynolds number
 Ru : Gas constant (J/kgK)
 s : Louver slot height (m)
 S : Density ratio, Strain rate
 t : Time (sec), louver thickness (m)
 T : Static temperature (K)
 T_0 : Total temperature (K)
 TR : Coolant stream to hot stream temperature ratio (T_s/T_∞)
 u : Streamwise velocity component (m/sec)
 U : Average fluid stream velocity (m/sec)
 U^* : Characteristic velocity (m/sec)
 U_∞ : Core stream velocity (m/sec)
 U_s : Coolant stream velocity (m/sec)

v : Wall-normal velocity component (m/sec)
 w : Spanwise velocity component (m/sec)
 x : Streamwise distance (m)
 x_0 : Streamwise location of the point of coolant injection (m)
 x_1 : Streamwise transition point between the initial and fully developed regions (m)
 y : Transverse distance (m)
 y_1 : Transverse location of the shear layer/coolant stream interface (m)
 y_2 : Transverse location of the shear layer/hot stream interface (m)

Greek

δ_{99} : Boundary layer thickness
 δ : Shear layer thickness
 δ' : Shear layer growth rate
 γ : Ratio of specific heats
 η_{eff} : Film cooling effectiveness $(T_\infty - T_{aw}) / (T_\infty - T_s)$
 λ : Blowing ratio, $(\rho_s U_s) / (\rho_\infty U_\infty)$
 μ : Dynamic viscosity ($N \cdot sec / m^2$)
 ν : Kinematic viscosity (m^2 / sec)
 ρ : Fluid density (kg / m^3)
 θ_0 : Total temperature ratio, $(T_{0s} / T_{0\infty})$
 τ_w : Wall shear stress (N / m^2)
 ω : Dimensionless flow-temperature grouping
 ψ : Dimensionless temperature ratio

Subscripts

0: Initial, total

l: Transition point

c: Crossflow, Convective

comp: Compressible

conv: Convective

eff: Effectiveness

f: Film

inc: Incompressible

mom: Momentum

s: Coolant stream

w: Wall

∞ : Core stream

Acronyms

AGTB: Advanced Gas Turbine Blade

AIAA: American Institute of Aeronautics and Astronautics

APG: Adverse Pressure Gradient

ASCE: American Society of Civil Engineers

ASME: American Society of Mechanical Engineers

CFD: Computational Fluid Dynamics

CPGM: Compressible Pressure Gradient Model

DES: Detached Eddy Simulations

DNS: Direct Numerical Simulation

GCI: Grid-convergence index

HPF: Hagen-Poiseuille Flow

IEEE: Institute of Electrical and Electronics Engineers

LDV: Laser Doppler Velocimetry

LEO: Low Earth Orbit

LES: Large Eddy Simulation

LOX: Liquid Oxygen

LRE: Liquid rocket engine

LSQ: Least-squares

MAPG: Mild Adverse Pressure Gradient

PF: Plug Flow

PGFM: Pressure Gradient Film Cooling Model

psi: pounds per square inch

psia: pounds per square inch absolute

RANS: Reynolds Averaged Navier-Stokes

rms: root mean squared

SFPG: Strong Favorable Pressure Gradient

SM: Simon's Film Cooling Model

URANS: Unsteady Reynolds Averaged Navier-Stokes

ZPG: Zero Pressure Gradient

Abbreviations

2-D: Two dimensional

3-D: Three dimensional

CO₂: Carbon dioxide

G-G: Gas-Gas

L-G: Liquid-Gas

psi: Pounds per square inch

rms: Root mean squared

scramjet: Supersonic combustion ramjet

Chapter 1: Introduction

1.1 Motivation: What is film cooling and why are we interested in it?

The thermal management and protection of the components and surfaces in rocket engine combustion chambers presents one of the most challenging problems for designers. Without exception, all the various types of rockets (including liquid, hybrid, solid and nuclear, etc.) have characteristic cooling problems [1]. For example, liquid-propellant rocket motors experience thermal management difficulties when the combustion pressure is raised above 2000 lb/in² [2]. Beyond this pressure conventional cooling strategies like regenerative cooling become grossly inadequate. More advanced cooling concepts are, therefore, needed to augment conventional cooling strategies. One approach, which is widely used, is film cooling.

Film cooling is an active cooling strategy, which involves the continuous injection of a thin layer of protective fluid near a wall or boundary, as shown in Figure 1-1, to insulate it from rapidly flowing hot propellant gases. Gaseous film cooling in particular is considered to be ideally suited to three types of rocket motors: large solid-propellant motors, nuclear rockets, and high-energy liquid chemical rockets. Its main advantages are that it allows for the use of much lighter-weight nozzle assemblies and it is relatively simple to implement from a fabrication standpoint [1]. The main drawback of film cooling is that it requires a large as well as continuous supply of coolant fluid. In addition, film cooling can be extremely challenging because it is hard to maintain a continuous, uninterrupted (and therefore

effective) cooling film in combustors and nozzles because of the wide range of geometric and fluid dynamic scales and the complexity of the flow fields [3].

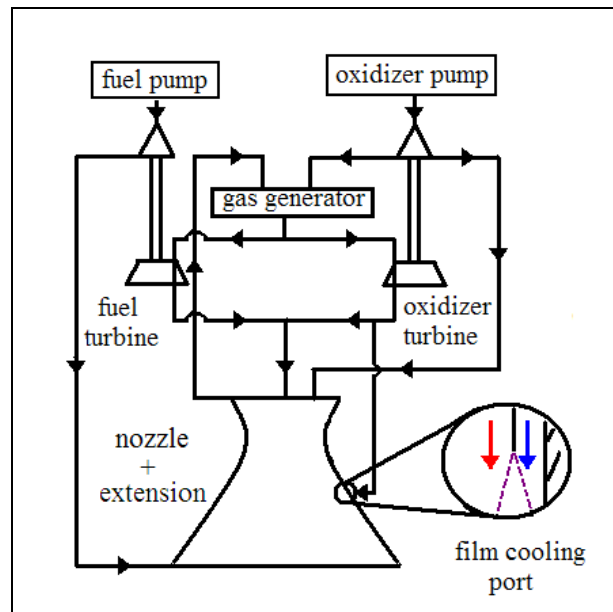


Figure 1-1 Schematic illustration of a liquid rocket engine (LRE) with staged combustion {Adapted from Bazarov et al. [15] (1998)}.

The inherent complexity of the film cooling process is underscored by the fact that, in addition to usual complicating factors (chemical reaction, high turbulence intensity, three-dimensionality, separation and recirculation, and high pressure flow [4]) associated with reacting flows in rockets, film cooling also adds the fluid dynamic influence of secondary flow injection and the imposition of a third temperature. The latter creates what is commonly referred to as the ‘three temperature problem’ [3 & 5], i.e., temperature differences between the core stream, wall and coolant stream. Not only is it difficult to design such a system, it is equally hard to predict its performance both theoretically and numerically. To compound this problem further, it has been well documented [1,6] that there are significant inconsistencies between film cooling data acquired using different experimental configurations and techniques. This can lead to appreciable differences in film

cooling performance predictions especially when the results are interpreted in terms of design considerations.

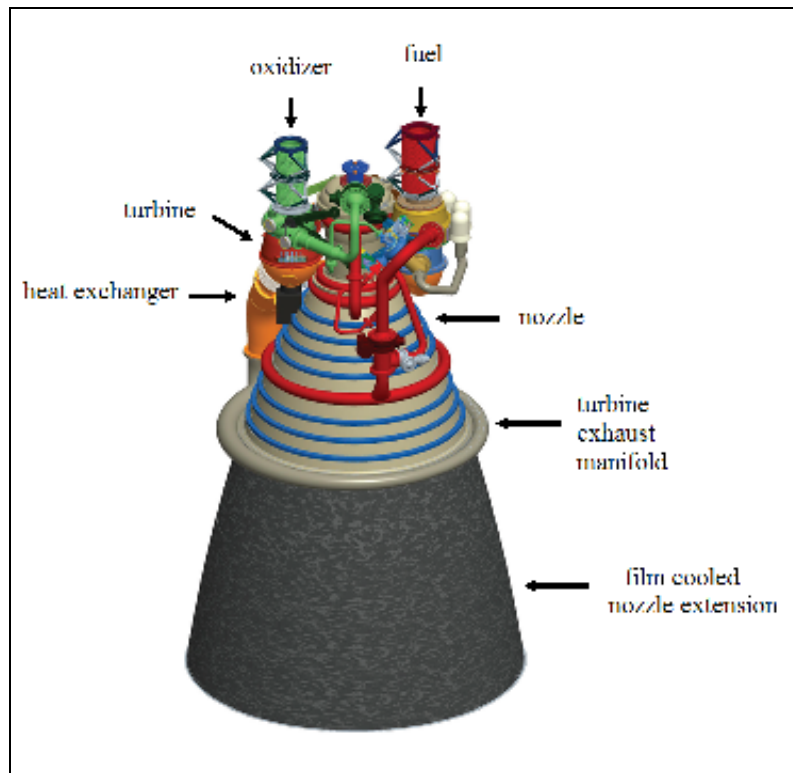


Figure 1-2 Conceptual drawing of the J-2X engine showing various key components {Adapted from NASA/MSFC [7]}.

Recently, film cooling has been selected for cooling the composite nozzle extension of the J-2X engine which is being developed for the second stage of NASA's next generation launch vehicle, the Ares I [7]. The J-2X is a derivative of the J-2 and J-2S (i.e., J-2 Simplified) rocket engines which were developed for the upper stages of the Saturn family of launch vehicles (Stages 2 and 3 on the Saturn V, and Stage 2 on the Saturn IB) [7]. Thermal management of the heat transfer in these engines was achieved using transpiration (or sweat) cooling¹ with hydrogen fuel as the coolant [8].

¹Sweat or *transpiration cooling* is an active cooling technique that involves the injection of coolant through a porous thrust chamber wall. It is a special case of film cooling [8].

A conceptual illustration of the J-2X engine is shown in Figure 1-2. The J-2X will measure approximately 185 inches in length and 120 inches in diameter at the end of its nozzle. It will weigh approximately 5,450 pounds and produce 294,000 pounds of thrust in its primary operating mode. This will enable the Ares I upper stage to place the Orion Crew Exploration Vehicle in Low-Earth Orbit (LEO). By changing the mixture ratio of liquid oxygen to liquid hydrogen, the J-2X can operate in a secondary mode producing 242,000 pounds of thrust, which will allow the Ares V Earth departure stage to leave the Earth's orbit and reach the moon.

Many different active cooling strategies for managing the heat loads on the J-2X nozzle extension were considered. These included various combinations of regenerative cooling, transpiration (or sweat) cooling, radiation cooling, ablation cooling and gaseous, as well as liquid film cooling. A description of each of these techniques and their application to rocket engines is presented in detail in Sutton [8]. However, with the decision to use a heavier Haynes metallic (stainless steel and nickel) alloy nozzle extension, a film cooling/radiative cooling combination was selected because of its weight saving advantage and ease of implementation relative to other strategies (J. Ruf, personal communication, July 31st 2009).

In the J-2X engine film cooling will be accomplished by supersonically injecting coolant at Mach 1.4, at the end of the regeneratively cooled nozzle, near the base of the 2.5m long nozzle extension. The film coolant is the LOX turbine exhaust gas which is distributed around the nozzle extension by the manifold shown in Fig. 1-2 (J. Ruf, personal communication, July 31st 2009).

However, several challenges remain to achieve effective film cooling of the J-2X engine nozzle extension. Both the film cooling effectiveness and the emissivity of the Haynes material control how much heat is absorbed by the nozzle extension walls and how much heat the structure can lose via radiation. However, the extreme complexity of the flow (three-dimensional wakes, lateral flows, vorticity, and flow separation) makes predicting cooling performance difficult and the nozzle extension could become unsafely hot. In addition, the amount of useful supersonic film cooling data available for engineers to use in engine design is very limited. While CFD can help to fill this void, at present it is not possible to quantitatively match supersonic film cooling data [9]. Therefore, numerical simulations are not ready to be used as the primary design tool.

In light of these tremendous technical challenges a deeper and more complete understanding of the film cooling process must be developed in order to achieve more efficient designs as well as more accurate performance predictions. The aforementioned provide the motivation for this thesis, which is to advance the state of the art in film cooling design and prediction.

1.2 The Key Challenges in Rocket Engine Film Cooling

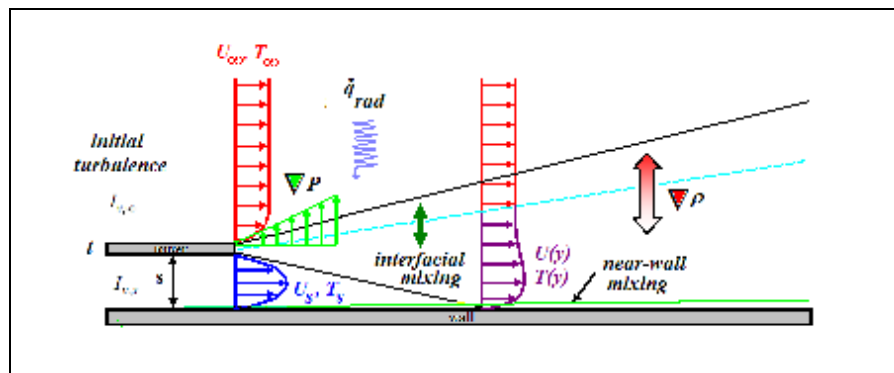


Figure 1-3 Sketch showing the various fluid dynamic and geometric factors influencing the film cooling process.

The extreme pressure and temperature conditions in modern rocket engines present a particularly challenging environment for the film cooling process. Severe thermal loads are experienced by several engine components, including the thrust chamber assembly, nozzle and nozzle extension. To design an efficient and effective film cooling system to protect these critical components a number of key challenges must be overcome. These include:

1. *Effect of initial turbulence:*

One of the most important factors affecting film cooling performance is the initial turbulent state of the coolant and core streams [4 & 10]. Increasing the initial turbulence level increases mixing and transport of hot core stream gases towards the walls. This reduces the persistence of the film thereby decreasing thermal protection. According to Bogard et al. [10] and Mayhew et al. [11] turbulence intensities on the order of 10–20% are common in regions where film cooling is employed in gas turbine and rocket engines. It is therefore important for film cooling systems to work effectively in flows that are moderately turbulent.

2. *Effect of near-wall transport and interfacial mixing:*

Zones of strong shear (mixing) exist at the interface between the coolant and core streams as well as in the region near the thrust chamber and nozzle/nozzle extension walls. This mixing is illustrated in Fig 1-3. High levels of shearing in these locations can have detrimental effects on the persistence of the film because the increase in the mixing of coolant with hotter surrounding fluid leads to an increase in the local convective heat transfer coefficients and causes the film to break down more quickly as it moves downstream. [10 & 12].

3. Pressure gradient and surface curvature effects:

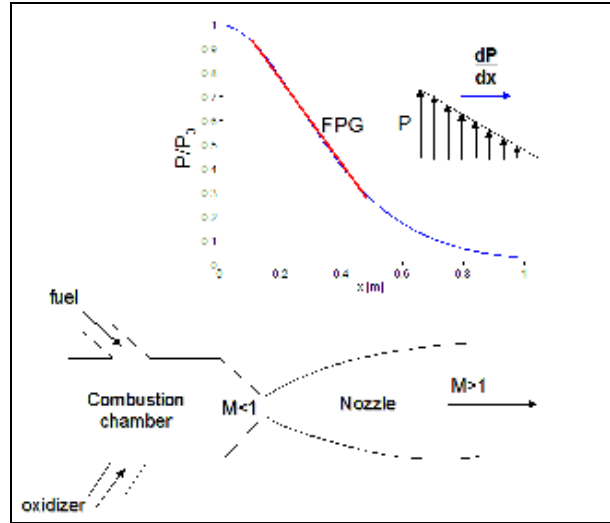


Figure 1-4 Schematic illustration of the pressure distribution in a rocket engine

The rapid expansion of the hot thrust chamber gases in a rocket nozzle and nozzle extension means that rocket engine film cooling must take place in the presence of a strong favorable pressure gradient (FPG) (i.e., an accelerating flow environment). This expansion is highlighted above in Figure 1-4, which shows a representative pressure distribution in a typical rocket engine.

4. Density gradient and compressibility effects:

The extremely large flow velocities and temperature differences present in rocket engines create significant density gradients. Coolant to core stream density ratios on the order of two or higher are typical in many rocket engines [13 & 14] and can strongly influence the protection provided by the film. Therefore, it is important to understand and to be able to predict the effect of density gradients on film behavior.

5. Mach number effects:

High flow Mach numbers are present in both the core and coolant streams in most rocket engines. They can potentially influence the protection provided by the

film because of the formation of expansion fans, coolant louver lip shocks, separation bubbles and reattachment shocks [6 & 10].

6. *Radiation effects:*

Gas temperatures in many conventional rocket engines exceed 3000K [15 & 16]. At these elevated temperatures, heat transfer via radiation can be significant [17] and also has the potential to influence the performance of the film.

7. *Unsteady flow effects:*

Unsteadiness in the core flow of a rocket motor can arise from various sources including turbulent flow in the feed lines, fluttering of pump wheel blades, vibrations of control valves, and unsteady motions in the combustion chamber and gas generator [18–20]. These variations in the core flow can in turn cause fluctuations in the pressure field external to the film-cooling injection ports. These fluctuations can thin the film and wall boundary layer, increase the overall turbulence [10 & 20], increase the heat transfer to the wall and decrease the film cooling effectiveness [21 & 22].

8. *Injection geometry:*

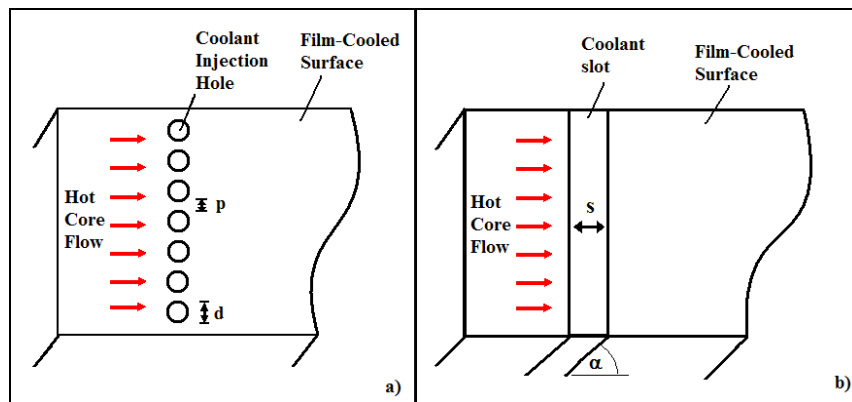


Figure 1-5 Sketch showing: a) 3-D hole injection and b) 2-D slot injection

Although both 3-D (hole) and 2-D (slot) injection configurations can be used to deliver the film as shown in Fig. 1-5 a) and b), in practice 3-D configurations are

the most common. Geometric parameters including injection angle (α), hole shape, hole spacing (p), injection hole diameter (d), louver (lip) thickness (t) and slot height (s), can greatly influence the development and decay of the film [3 & 6]. Among the consequences of poor geometric design are: flow separation, reversed flow and increased mixing, which are detrimental to film cooling performance since they accelerate the break up of the film. It is therefore vital that the geometry of the film cooling configuration utilized in a rocket engine be carefully designed to ensure optimum film cooling performance.

1.3 Review of Previous Work

1.3.1 Introduction

Having identified many of the key challenges in achieving effective rocket engine film cooling, it is now useful to review some of the literature to understand what is already known about the fundamental processes that influence film cooling performance. For example, one of the most important phenomena that must be understood is how the turbulent shear layer growth rate changes under both compressible and incompressible conditions. Therefore, a broad overview of the literature on incompressible and compressible two-dimensional free mixing layer flows is presented first. This is followed by a review of the literature focused specifically on film cooling problems. In each case the discussion is divided into three categories covering experimental, numerical and theoretical work.

1.3.2 Free mixing layer flows

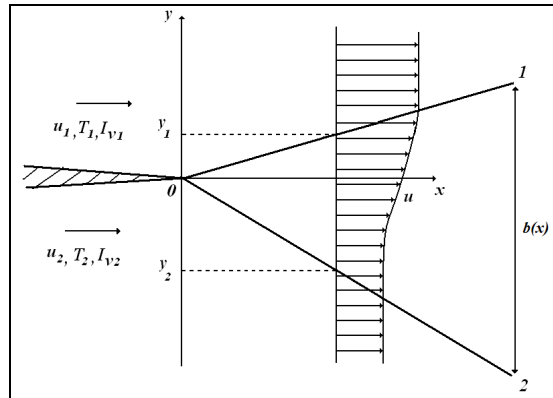


Figure 1-6 Schematic of a two-dimensional free shear layer {Adapted from Abramovich [27] (1963)}.

A free mixing layer is formed when two flows separated by a barrier merge as shown above in Figure 1-6. The interface after the flows meet is called a mixing or shear layer, and it grows as momentum is transferred from the higher speed stream to the lower speed stream. The term ‘free’ is used to indicate that the mixing layer is not bounded by walls or boundaries on any side.

Turbulent, two-dimensional, free mixing layer flows are ubiquitous in engineering. They are encountered in a wide range of practical devices such as supersonic ejectors, chemical and gas dynamic lasers, fuel injectors, scramjet engine combustors and projectile base flows [23]. As a result, they have been extensively studied over the past eight decades under both incompressible and compressible conditions [23–99].

Incompressible free mixing layers

Experimental work:

One of the earliest experimental investigations of two dimensional mixing layers was performed by Tollmien in 1926 [24]. He experimentally studied the mixing of an air stream and air jet of uniform velocity with still air. He found that the

width of the mixing zone increased linearly with streamwise distance from the point of injection. This was followed by the work of Liepmann et al. [25] in 1947, who obtained measurements of the mean velocity, the intensity and scale of turbulent fluctuations, and the turbulent shear. Their results showed that both the mixing length and the exchange coefficient vary across the mixing region. Subsequently, in the 1960's and early 1970's several experimental studies were carried out by Sabin [26], Abramovich [27], Mills [28], Baker [29] and Wygnanski [30]. These studies focused primarily on exploring the effect of velocity ratio (i.e., on the ratio of the coolant to core stream velocity) on mixing layer growth rate, as well as Reynolds number and density ratio (i.e., ratio of the coolant to core stream density) effects. In addition, several studies reported turbulence levels and the evolution of the velocity profiles with streamwise distance.

Analytical work:

Several theoretical studies of incompressible mixing layers have also been conducted. In 1942, Görtler [31] used a stream function and a similarity assumption to derive one of the earliest analytic solutions of the boundary-layer equations for the prediction of the spreading rate of an incompressible mixing layer. Subsequent work by several researchers including Golik [32], Szablewski [33], Sabin [34], Abramovich [27], Miles et al. [35], and Yule [36] produced many velocity ratio dependent mixing layer growth rate relations that were based on an eddy viscosity assumption. Later in 1975, Brown [37] developed a more sophisticated entrainment-based, unsteady (temporal) incompressible mixing layer growth rate model which accounted for the intermittent structure of the shear layer. He obtained good agreement with

experimental data over a range of density and velocity ratios at low Mach numbers ($M \leq 0.3$). A little over a decade later Dimotakis [38] proposed a modified version of Brown's model that accounted for asymmetries in spatial-growth.

Numerical work:

Numerical investigations of incompressible mixing-layers date to the advent of computational fluid dynamics in the mid-1960's. Various approaches including Direct Numerical Simulation (DNS), Large Eddy Simulation (LES), and Reynolds Averaged Navier–Stokes (RANS) simulation have been pursued [39–65] with no single method dominating the literature.

A thorough review of previous work on RANS simulations of incompressible mixing layers has been compiled previously by Birch et al. [39]. This review suggests that the most commonly used turbulence models in this area are two-equation k - ε and k - ω models. Among the first researchers to use the k - ε model was Rodi [40], who simulated a turbulent incompressible mixing layer in 1972. Rodi found that the mean-velocity predictions of the k - ε model closely agreed with experimental data, however, shear stress profiles were not well predicted. A few years later, in 1978, Pope [41] used a modified version of the k - ε model that accounted for dissipation due to vortex stretching to study the spreading rates of axisymmetric jets and planar mixing layers. However, he failed to improve agreement with experimental data relative to the standard k - ε model. Two years later, Hanjalic et al. [42] obtained an improved prediction of the growth rate for both jets and planar mixing layers by sensitizing the dissipation equation in the k - ε model to irrotational strain. In 1992, Menter [43] performed RANS simulations of an incompressible free shear layer using the k - ω

model. His results showed that the numerical predictions depended strongly on the freestream value of ω . In 1995, Robinson et al. [44] predicted growth rates as well as the corresponding velocity and shear stress similarity profiles in planar axisymmetric shear layers using RANS simulations that incorporated a newly developed two-equation turbulence model. The model was based on the exact turbulent kinetic energy and the variance of vorticity (sometimes referred to as the enstrophy) equations. Their results matched available data to within experimental uncertainty.

Many studies of incompressible shear layers have been conducted using Direct Numerical Simulation (DNS²) over the years [45–47]. One of the first studies, by Zabusky et al. [45] in 1971 used DNS to investigate the non-linear evolution of a 2-D perturbed, linearly unstable, mixing layer under inviscid (high Reynolds number) and finite Reynolds number conditions. Their results showed that after approximately two exponentiation times of the linearly most unstable mode, the flow becomes quasi-periodic from the interaction between the mean flow and the vortex states. This was followed in 1980 by the work of Riley et al. [46], who studied the evolution of forced two- and three-dimensional mixing layer using DNS. Their results showed that the addition of a perturbation based on the most unstable linear eigenmode could significantly reduce mixing layer growth. In 1985, Metcalfe et al. [47] used DNS to investigate the formation and evolution of coherent structures in a temporally growing shear layer under forced and un-forced conditions. They concluded that low

² DNS involves solving the Navier-Stokes equations on a grid that resolves all of the turbulent scales in the problem. While this is the best method available at present for simulating turbulent flows, its extreme computational demands limit its application to very simple geometries (like flows in channels) at relatively low Reynolds numbers (< 5000) [48]. Therefore, DNS is not a practical tool for realistic engineering problems. However, it can be very useful for understanding elemental processes in turbulent flows.

levels of coherent forcing can dramatically change the evolution of the mixing layer. In the absence of such forcing, the large-scale vortical structures lack regularity in transverse position, spacing, amplitude, shape and spanwise coherence. In 1990 Clarksean et al. [49] carried out direct numerical simulations of spatially developing two- and three-dimensional mixing layers using a spectral compact finite difference scheme. The two-dimensional results showed vortex shedding and pairing that closely matched experimental observations. In addition, their three-dimensional results showed that the mixing process is enhanced by the development of secondary structures.

Recently, Large Eddy Simulations (LES) have gained popularity in the engineering community due to the increased level of detail that they offer when compared to RANS simulations and their lower computational cost relative to DNS. One of the first researchers to use LES to study incompressible shear layers was Friedrich [50] in 1982. He investigated the growth rate of a turbulent wall-bounded shear layer with longitudinal curvature using LES. This was followed in 1998 by Maruyama [51] who examined the effects of variation in turbulence intensity and the application of non-isotropic turbulence on a plane turbulent shear layer using LES. The results obtained were found to agree qualitatively with some of the available experimental data when a suitable initial turbulence level was selected. This was soon followed by Claus et al. [52] who performed simulations of a temporally evolving forced shear layer based on the experiments of Oster et al. [53] and Weisbrot et al. [54]. They performed both three-dimensional DNS and two-dimensional LES simulations. Due to a lack of detailed information about the inflow boundary

conditions, their results were found to agree only qualitatively with certain aspects of the experiments. They also noted that their results were sensitive to mesh refinement and Reynolds number. In 1997 Vreman et al. [55] performed low and high Reynolds number numerical simulations of an unsteady, weakly compressible mixing layer using LES and compared their results with DNS predictions. They tested six different subgrid-scale models in their LES. These included the Smagorinsky [56], similarity [57–58], gradient [58–59], dynamic eddy-viscosity [60], dynamic mixed [61–62] and dynamic Clark [63] models. Vreman et al. concluded that the dynamic subgrid-scale models produce more accurate predictions of shear layer momentum thickness, transition to turbulence and Reynolds stresses than do the non-dynamic models. Subsequently Comte et al. [64] investigated the formation of three-dimensional vortices in spatially-growing incompressible mixing layers using LES at zero molecular viscosity, with the aid of the Filtered Structure Function subgrid-scale model proposed in Ducros et al. [65]. They found that vortex formation was highly sensitive to the nature of the random upstream perturbations and the spanwise size of the computational domain.

Compressible free mixing layers

Introduction:

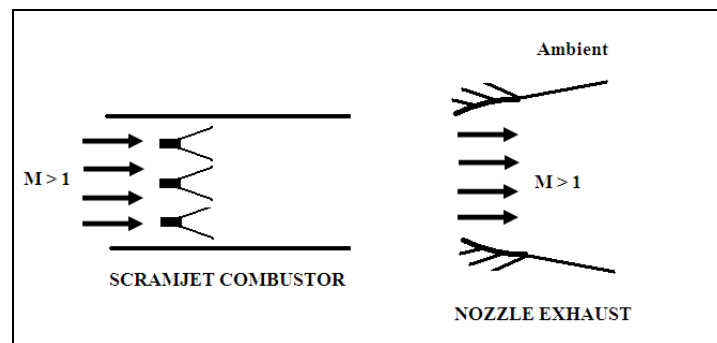


Figure 1-7 Sketch illustrating examples of flow-fields with compressible mixing layers {Adapted from Bodi [89] (2005)}

Interest in compressible mixing layers arose in the 1960's from the near wake problem in supersonic aircraft aerodynamics [66]. More recently it has been driven by challenges in supersonic combustion. At the heart of the research in this area is the well-established finding that the growth rate of compressible mixing layers is significantly smaller than that of incompressible mixing layers [66]. This has spurred a vast amount of experimental, theoretical and numerical research into understanding the mechanisms responsible for this decrease in growth rate, and into the prediction of mixing under compressible conditions [23, 37, 66–100].

As far back as 1973 Birch et al. [23] argued that the decrease in mixing layer growth rate with compressibility can be attributed to the increase in density associated with the static temperature drop as the Mach numbers of the streams comprising the shear layer are increased. However, other studies by Brown et al. [67 & 68] in 1971 and 1974 and Lu et al. [69] in 1994 have shown that density variations associated with higher flow Mach numbers are not large enough to account for the decrease in mixing layer thickness observed. For example, Brown et al. [68] found that at low Mach numbers the vorticity thickness decreased by 30% when the density ratio (ρ_1/ρ_2) was increased from 1 to 7. However, at high Mach numbers where compressibility becomes important, the shear layer growth rate decreased by 300% for the same change in density ratio. In 1988 Papamoschou et al. [70] argued that the reduction in growth rate is a compressibility effect that acts independently of density and velocity ratio effects and manifests itself in the development of large coherent turbulent structures. This argument was later refined by others [71–74] who suggested that the reduction in growth rate was directly attributable to the increase

with convective Mach number of the three-dimensionality of large turbulent structures in the mixing layer.

Analytical and Experimental work:

Among the primary objectives of many experimental and theoretical studies has been the establishment of growth rate models and correlations. A thorough review has been performed by Birch et al. [23] who found that eddy viscosity-based incompressible models like those of Abramovich [27] and Sabin [75] are inadequate for predicting mixing layer growth rates under compressible conditions. In response, Brown [37] developed a more sophisticated entrainment-based incompressible mixing layer growth rate model which accounted for the intermittent structure of the mixing layer. He obtained good agreement with experimental data over a range of density and velocity ratios, but only at low Mach numbers ($M \leq 0.3$). Ferri et al. [76] also developed a compressible model for the thickening of a turbulent jet based on a modified formulation for the eddy viscosity. This model made qualitative predictions for the change in diameter of a turbulent helium jet under compressible conditions which were consistent with the experimental data. Subsequently, Channapragada [77] developed a semi-empirical model for the spreading of a compressible jet into still air based on a representation of the density ratio in the jet in terms of mean flow properties. Channapragada's model captured experimental trends correctly over a range of Mach numbers from 0 to 3. The model matched experimental data to within less than 10% at Mach numbers below 2; however, errors of greater than 30% were obtained at higher Mach numbers.

In addition to these theoretical growth rate models, several investigators including Slessor et al. [78], Murakami et al. [79], Zhuang et al. [80] and Kline et al. [81] have developed growth rate correlations based on curve fits to experimental data. The latter by Kline et al. is commonly referred to as the “Langley Experimental Curve.” Despite the utility of such empirical correlations, they have two important drawbacks: Their predictions can vary considerably depending on the scaling parameter chosen and they do not provide much insight into the physical processes governing mixing layer growth.

Numerical work:

Numerical work on compressible mixing-layers began with solutions of the linear stability problem by Lessen et al. [82–84] in 1965 and 1966. They solved the temporal stability problem and found compressibility to have a stabilizing influence on mixing layers. They also identified ‘supersonic’ modes of instability, i.e., modes with a phase speed supersonic relative to one or other of the free streams, at high Mach numbers. This work was followed up three years later by Gropengiesser [85], who solved the spatial stability problem for realistic base profiles of velocity and temperature and noted the strong amplification rate of oblique instability waves at high Mach numbers. Numerical simulations of compressible mixing layers using RANS, LES and DNS approaches followed in subsequent years with the advent of computers.

A comprehensive review of previous RANS simulations work is presented in Birch et al. [39]. Among the most noted work in this area are studies by Sarkar et al. [86] and Vreman et al. [87]. In 1991 Sarkar et al. [86] developed a simple

compressible turbulence model with an algebraic dependence on the turbulent Mach number based on asymptotic analysis and DNS of isotropic turbulence. They performed RANS simulations of a high speed mixing layer using the new model and were able to capture dramatic reduction in mixing layer growth rate with increasing Mach number that had been observed experimentally. This was followed in 1996 by Vreman et al. [87], who performed RANS simulations of a compressible mixing layer using a compressible turbulence model based on reduced pressure fluctuations and simple anisotropy considerations obtained from a direct numerical simulation database. Their results were found to be in close agreement with DNS predictions for the variation of integrated Reynolds stresses, pressure-strain terms, and dissipation rate.

The previous DNS and LES work on compressible mixing layers has been reviewed in detail by Vreman [88] and more recently by Bodi [89]. Initially, much of the previous DNS work was limited to the early stages of vortex formation in either the temporally evolving compressible mixing layer or two-dimensional spatially developing compressible mixing layer [87–88 & 90–91]. These provided insight into changes in typical eddy structure but did not contain small scales of turbulence (i.e., Taylor and Kolmogorov microscales). Subsequent work by Luo et al. [92–93], Vreman [88], Vreman et al. [94] in the mid 90’s focused on simulating compressible mixing layers through a mixing transition to small-scale turbulence. To gain further insight into the structure and formation of coherent structures, and to overcome the computational limitations of DNS, many researchers also turned to LES in the early 1990’s. This spawned a vast amount work including research by Bodi [89], Lele [95],

Ragab [96], Vreman et al. [97], and Chalot [98]. In addition, more recently, several studies including Georgiadis et al. [99] and Simon et al. [100], have also explored hybrid RANS-LES approaches.

Summary:

In summary, there is a consensus in the literature that compressible mixing layers grow much more slowly than incompressible ones. This suggests that supersonic film cooling could be a favorable strategy in the J-2X engine. However, none of the existing work appears to be able to make quantitative predictions of mixing layer growth rates that are generalizable to other systems. This implies that additional work will be needed in order to predict film cooling effectiveness.

1.3.3 Film cooling flows (confined mixing layer flows with thermal gradients)

Introduction:

A film cooling flow is distinguished from other mixing layer flows by the fact that in addition to being confined by a wall on one side, there is also a non-negligible, wall-normal temperature gradient. The wall and thermal gradient introduce additional physics that are not present in free mixing layers and complicate the analysis. Before proceeding with a review of work in this area it is useful to provide a brief background on the different types of film cooling flows. This will be followed by a discussion of previous work on gas turbine and rocket engine film cooling with emphasis placed on their similarities and differences. Finally, a brief summary of the literature specifically highlighting investigations of the effects of pressure gradient, wall curvature, compressibility and density gradient will be presented.

Types of film cooling flows:

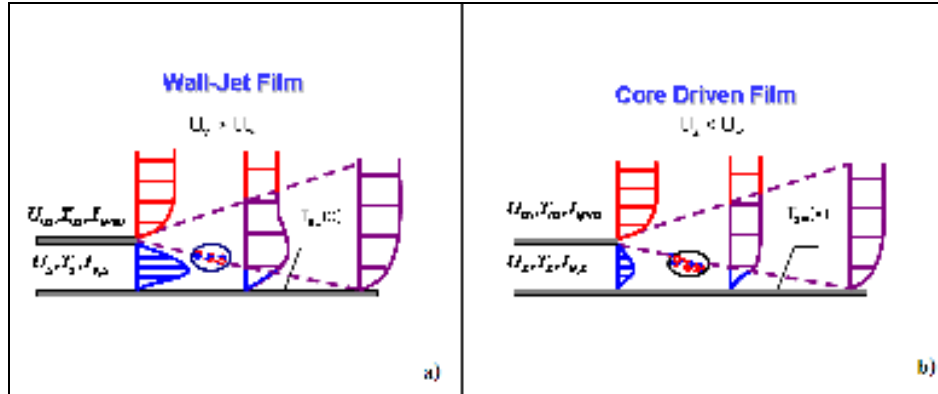


Figure 1-8 Schematic illustration of: a) A wall-jet film b) A core-driven film.

Film cooling flows are commonly categorized in two ways depending on the velocity ratio between the coolant and core streams. If the coolant stream velocity exceeds the core stream velocity (i.e., if the $R < 1$), then flow is referred to as a wall-jet film (Fig. 1-8a). Conversely, if the core stream velocity is higher than that of the coolant stream (i.e., if $R > 1$), then the flow is termed a core-driven film (Fig. 1-8b).

Gas turbine film cooling:

Introduction:

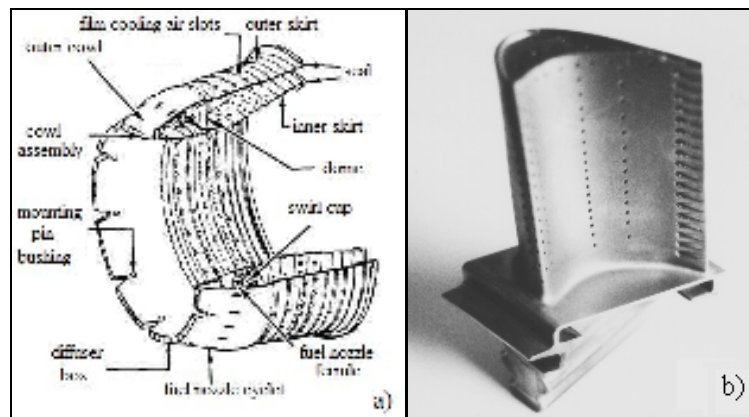


Figure 1-9 a) Sketch of a film cooled combustor liner {Adapted from Naval Ships' Technical Manual [101]} b) Picture of a gas turbine blade with several rows of cooling holes {From Kaszeta et al. [102]}.

In gas turbine engines, film cooling of turbine blades is typically accomplished by bleeding air from the compressor (usually after the last stage) and

ejecting it through a series of discrete holes on the blade surface so that it is immersed in a protective layer of cool air [103]. This allows turbine blades to operate above their normal material failure temperatures which results in greater combustor thermal efficiency. A similar approach is taken to protect combustor liners. Since the performance of the engine is very sensitive to turbine inlet temperature – increasing turbine inlet temperature increases overall efficiency – finding ways to operate the engine hotter without destroying its components is a very important problem and there is a vast literature describing film cooling in gas turbine engines spanning more than half a century [103–127].

Experimental work:

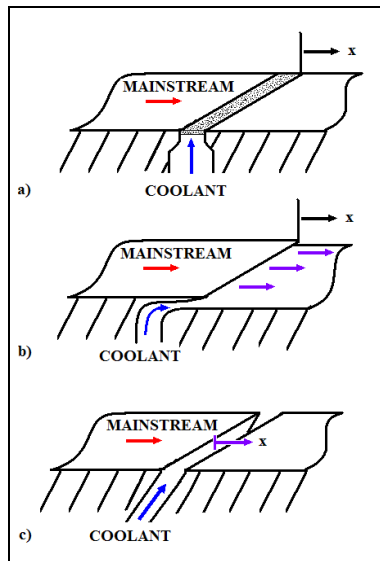


Figure 1-10 Representative two-dimensional film cooling geometries: a) porous slot, b) tangential injection (step-down slot) and c) angled slot. {Adapted from Goldstein [6] (1971)}

According to a review by Goldstein [6], the majority of experimental film cooling studies fall into two broad categories. These are geometric studies investigating the effects of hole shape, hole spacing, hole length, injection angle, slot height, surface curvature, and surface roughness [104–111] and fluid dynamic studies

investigating the influence of parameters ranging from the free-stream turbulence intensity to mainstream pressure gradient strength [112–122].

One of the earliest geometric film cooling investigations was performed by Wieghardt in 1946 [104]. He studied the effect of hot-air injection from a discrete slot into a turbulent boundary layer by measuring the adiabatic wall temperature distribution downstream of the point of injection and the development of the velocity and temperature boundary layer profiles. This work was followed in 1959 by Papell et al. [105] who experimentally investigated the characteristics of axially discharging single-slot film cooling of an adiabatic wall exposed to a hot air stream. They developed a correlation from their data covering a range of effective temperature ratios from 0.1 to 1. They also found that variation of the main-stream Mach number from 0.2–0.8 had little effect on film cooling performance. In 1960, Papell explored the effect of coolant injection angularity on gaseous film cooling effectiveness [106]. He made adiabatic wall temperature measurements at three different jet injection angles (30° , 60° and 90°) and used the data to develop a film cooling correlation. He found that increasing the injection angle had a detrimental effect on film cooling effectiveness because it increased mixing with the core stream.

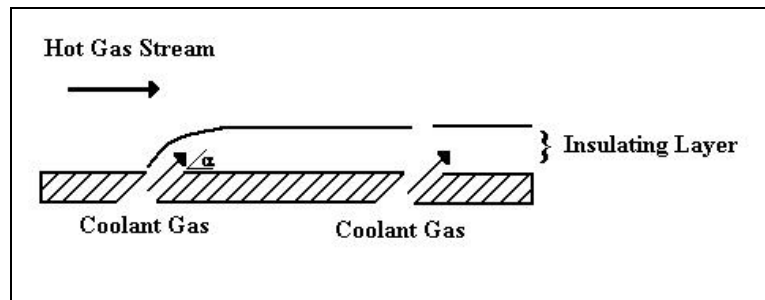


Figure 1-11 Sketch of the angled slot-injection film cooling configuration used by Hartnett et al. [94] {Adapted from Hartnett et al. [107] (1961)}

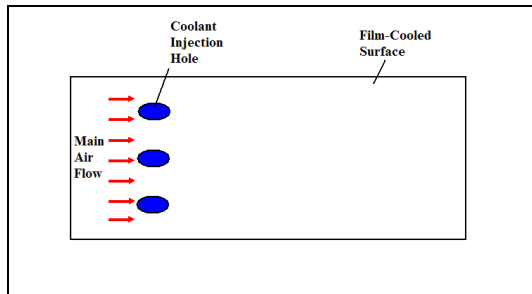


Figure 1-12 Sketch of the 3-D hole-injection film cooling configuration used by Mayhew et al. [10] {Adapted from Mayhew et al. [11] (2003)}

One year later, Hartnett et al. [107] conducted a detailed study of heat transfer associated with tangential air injection through a single, 30° angled slot into a turbulent boundary layer developing along a flat plate. A sketch of the angled-slot injection film cooling approach used by Hartnett et al. is illustrated in Fig. 1-11. Hartnett et al. measured boundary layer velocity and temperature profiles at several locations downstream of the point of injection and developed a simple model relating the film cooling effectiveness to the blowing ratio and the slot Reynolds number. The model's predictions agreed well with experimental correlations at locations far downstream from the slot.

Many experiments have also examined the impact of various fluid dynamic factors on film cooling effectiveness. Considerable work has focused on investigating the effect of turbulence in both the coolant and core streams. Among the most noted work in this area are studies by Juhasz et al. [108], Marek et al. [109], Ko et al. [110], Lebedev et al. [111] and Mayhew et al. [11].

Juhasz et al. [108] performed one of the earliest studies of turbulent effects on film cooling performance in 1971. They measured combustor liner slot-film cooling performance at a turbulence intensity of 15% using different injection configurations and compared their results with existing correlations. They found that turbulence

decreased film cooling performance and reported a simple correlation for the variation of cooling effectiveness with turbulence level. This was followed in 1975 by the work of Marek et al. [109] who measured temperatures on a slot-film cooled wall downstream of a turbulence producing blockage plate at axial turbulence intensities of 7, 14, 23 and 35 percent. Their results showed that higher turbulence intensities caused a more rapid degradation of the film cooling layer and effectiveness decreased by as much as 50 percent as the turbulence intensity was increased from 7 to 35%.

Five years later, Ko et al [110] measured the film cooling effectiveness of a turbulent flow over an adiabatic flat plate. They used a Schlieren system to visualize the flow and a hot film anemometer to measure velocity and turbulence intensity fluctuations at different streamwise locations along the plate. They concluded that turbulence was detrimental to film cooling performance and suggested a method for accounting for the turbulence effects on film cooling effectiveness using a turbulent mixing coefficient.

Later, Lebedev et al. [111] examined how elevated mainstream turbulence levels affect film cooling performance using a continuous running aerodynamic tube. Their results showed that as the turbulence level was increased from 0.2–15%, the film cooling performance deteriorated by a factor of more than 2 and the length of the initial region decreased by a factor of 2.5. More recently in 2003, Mayhew et al. [11] explored the influence of turbulence on the 3-D hole injection film cooling of a flat-plate. They found that at low coolant to core stream mass flux ratios, high core-stream turbulence decreased the area-averaged effectiveness. However, at high coolant to core stream mass flux ratios, high core-stream turbulence led to increased area-

averaged effectiveness. They attributed the increase in area-averaged effectiveness to reattachment of the coolant jets to the wall surface caused by increased mixing between the coolant and core flows. A number of other factors have been explored in other studies. These include the effects of wall-curvature, pressure gradients, density ratio and compressibility on film cooling effectiveness. These will be discussed at length later.

Analytical work:

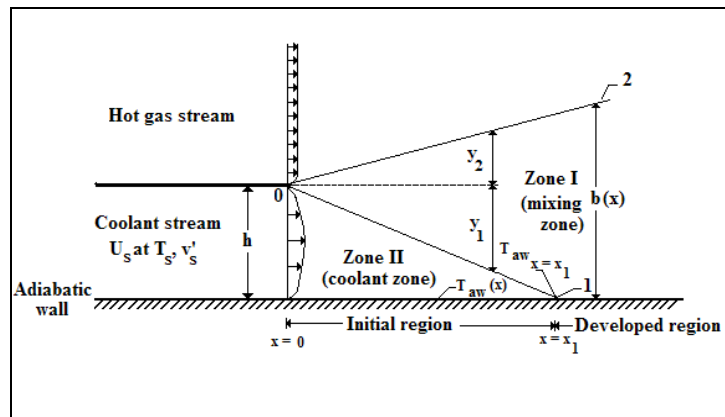


Figure 1-13 Schematic of Simon's wall jet, slot film cooling model. {Adapted from Simon [114] (1986)}

Despite the tremendous geometric and fluid dynamic complexity of gas turbine film cooling, several attempts have been made to develop simple theoretical models [107, 112–114]. They take one of two approaches: a boundary layer approach or a wall jet approach. Their relative validity depends on the velocity ratio between coolant and hot gas streams. In gas turbine engines, where velocity and blowing ratios are typically high ($\lambda > 1$), a wall jet model is often used.

One of the earliest efforts to develop an analytical model of film cooling effectiveness was by Hartnett et al. [107] in 1961. They derived a boundary layer based model relating the film cooling effectiveness to the blowing ratio and the slot Reynolds number. It agreed well with previous experimental correlations but only at

locations far downstream from the slot. This was followed in 1965 by Stollery et al. [112] who used a turbulent boundary layer model to derive a simple film cooling correlation that depended on the slot Reynolds number, slot height, and blowing ratio. The predictions were generally in agreement with experimental data. In 1971 Sturgess [113] developed a wall-jet based model which was able to correlate experimental data to within 10%. In 1986, Simon [114] formulated a semi-empirical, incompressible, wall-jet based slot film cooling model that accounted for the effects of free-stream and coolant turbulence. Turbulence effects were incorporated by accounting for an initial developing region of the jet (where mixing is generally very slow) and for a fully developed, mixing region (where mixing is very rapid) as illustrated in Fig. 1-13. The model's prediction of film cooling effectiveness were found to match experimental data to within $\pm 4\%$ for lateral free-stream turbulence intensities up to 24 per cent and blowing ratios up to 1.9.

Numerical work:

Several numerical studies of film cooling in gas turbines have also been performed [115–127]. In general, most numerical investigations have focused on three-dimensional modeling to achieve better resolution of the complex flow-fields associated with film cooling in gas turbine engines. Since Direct Numerical Simulations (DNS) are not yet practical due to the fact that they are very computationally intensive, the majority of previous numerical work in this area has involved Large Eddy Simulation (LES) or Reynolds Averaged Navier-Stokes (RANS) approaches. However, it must be noted that of these two approaches no particular simulation method appears to dominate in the literature.

One of the first RANS gas turbine film cooling studies was conducted by Zhou et al. [115] in 1993. They used the k - ε model with a near-wall low-Reynolds-number k - ω model and also a k - ε model with a wall function to explore slot-jet film cooling of an adiabatic flat plate at various blowing ratios. For blowing ratios less than 0.4, their simulation results were found to be in good agreement with measurements of velocity profiles and cooling effectiveness. One year later, Jansson et al. [116] performed two dimensional simulations of slot film cooling of an adiabatic wall using an algebraic stress model and a standard k - ε model. The numerical results matched velocity profile measurements but not temperature profiles, especially near the wall. Nearly a decade later, Lakehal [117] investigated turbulent convective heat transport associated with film cooling of turbine blades. They used a three-dimensional, finite volume, RANS approach incorporating a novel turbulence model. The model included dynamic coupling of the high-Reynolds number k - ε model with a one-equation model capable of resolving the near-wall viscosity, anisotropy of turbulent transport coefficients, and near-wall variation of the turbulent Prandtl number as a function of local Reynolds number. Comparison of the RANS model temperature field predictions with experimental data for the film cooling of a symmetrical Advanced Gas Turbine Blade (AGTB) by a row of laterally injected jets showed good agreement - especially at higher blowing rates.

In 2005, Jia et al. [118] numerically and experimentally investigated the mixing of a slot jet issuing into crossflow at three injection angles, 30°, 60° and 90°, at jet blowing ratios between 2 and 9. They solved the time-averaged Navier-Stokes equations on a collocated body-fitted grid system using three different turbulence

models (shear stress transport $k-\omega$ model, V2F $k-\varepsilon$ model and the stress- ω model), and compared their results with velocity and temperature measurements from LDV experiments. They found that the stress- ω turbulence model did the best job predicting the measured mean and rms velocity distributions. In addition, their results showed that a recirculation bubble downstream of the injection point develops for injection angles greater than 30° and that the size of the bubble decreases with increasing blowing ratio.

As a result of the extreme computational cost, only a handful of studies have applied DNS to gas turbine film cooling flows. One of the first was by Muldoon et al. [119] in 2004. They simulated a single film cooling hole inclined at 35° at a Reynolds number of approximately 3100 (based on jet diameter). They obtained statistics for the various budgets in the turbulence kinetic energy and dissipation rate equations. In addition, they used their results in to develop a new wall function for film cooling flows. Two years later, Muldoon et al [120] followed up this work with more DNS of the same configuration. From these new simulations they computed all the terms in the $k-\varepsilon$ transport equations and compared their values with those of the modeled $k-\varepsilon$ terms. They found that the Boussinesq gradient approximation [121] as used in standard $k-\varepsilon$ was a reasonable model but that the eddy viscosity contained large errors. Based on this they proposed a new damping function for the eddy-viscosity model.

Recent work on the numerical simulation of gas turbine film cooling flows has also utilized LES and hybrid RANS-LES approaches [122–127]. One of the first LES studies on film cooling was conducted by Tyagi et al. in 2003 [122]. They performed

three-dimensional, time-averaged large eddy simulations (LES) of film cooling flow from a row of inclined cylindrical jets at blowing ratios of 0.5 and 1 corresponding to jet Reynolds numbers of 11,100 and 22,200. Tyagi et al. compared their results to the film cooling flow measurements of Lavrich et al. [123] and found that LES was able to predict the flow-field dynamics with reasonable accuracy, especially at locations far downstream from the point of injection. In addition, the LES results revealed that the film cooling flow produced by the inclined cylindrical jets was dominated by packets of hairpin-shaped vortices which influence the formation of ‘hot spots.’ This was followed in 2006 by Guo et al. [124], who carried out LES of a jet in a cross-flow (JICF) problem to investigate the turbulent flow structure and the vortex dynamics in gas turbine blade film cooling. They simulated a turbulent flat plate boundary layer at a Reynolds number of 400,000 interacting with a jet issuing from a pipe at injection angles of 90° and 30° . Their results indicated that a large separation region formed at the leading edge of the jet hole for normal injection which was absent in the stream-wise injection case. Moreover, they noted that the first appearance of the counter rotating vortex pair of the jet is further downstream and weaker for the stream-wise injection case.

A number of studies have also utilized hybrid RANS-LES, sometimes referred to as Detached Eddy Simulation (DES), approaches. In 2003 and 2004, Roy et al. [125–126] implemented the DES approach to simulate film-cooling flow on a flat plate with coolant injection through a single inclined cylindrical hole. Their results showed a strong anisotropic mixing behavior not captured by RANS alone. In addition, when they compared their numerical predictions to experimental data, they

found that the centerline cooling effectiveness had a tendency to be over-predicted while the spanwise averaged effectiveness was slightly under-predicted. This was followed by the work of Martini et al [127] who performed steady DES and RANS of slot film cooling at the trailing edge of a gas turbine engine blade over a range of blowing ratios. They found that for all the blowing ratios considered, the film cooling effectiveness predicted by the DES were in closer agreement with available experimental data than the RANS predictions.

Summary:

To recap, this subsection has shown that previous experimental work in gas turbine film cooling can be classified into two key areas: geometric and fluid dynamic studies. The most widely studied geometric parameters have been hole shape and injection angle while the initial coolant and core stream turbulence are the most well-investigated fluid dynamic factors. The literature review has also revealed that reasonable predictions of film cooling effectiveness can be obtained analytically using Simon's semi-empirical model and numerically using various approaches. Specifically in the case of RANS simulations it has been revealed that good agreement with experimental data can be achieved for momentum mixing but not always for the thermal mixing. All of this information is relevant to the J-2X film cooling problem since it provides a good guide foundation for tackling not only the practical challenges from mixing and 3-D effects but also a useful starting point for the prediction of film cooling performance using both analytical and numerical techniques.

Rocket engine film cooling:

Introduction:

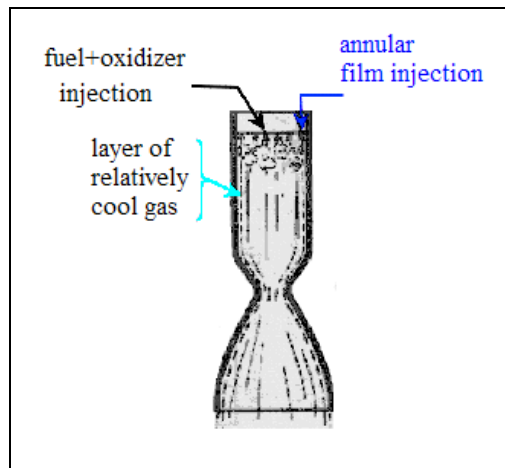


Figure 1-14 Schematic of annular film cooling of a rocket thrust chamber {Adapted from Sutton [8]}

The physics underlying rocket engine film cooling is somewhat different from that of gas turbine film cooling. So as not to reduce the rocket performance, the cooling fluid should serve dual purposes. In addition to protecting the wall, the cooling flow should also provide some propulsion. This contrasts with the gas turbine application where the sole purpose is to cool the combustor liner and turbine blades. In the rocket case, the wall cooling fluid mixes and reacts with the main propellant flow [128], whereas in the gas turbine application the cooling fluid remains chemically inert. Finally, flow velocities are significantly higher in rocket motors. This means that coolant to core stream velocity ratios, and by extension mass flux ratios are typically much less than unity in rocket motors whereas they are often greater than unity in gas turbine engines.

In rockets, film cooling is used in several ways. The face plate can be cooled by injecting coolant into the combustion chamber through a series of discrete holes or slots located in the injector face [129]. The walls of the thrust chamber can be cooled

by injecting coolant through holes in the wall. The peak heat flux at the throat can be reduced by injecting coolant immediately upstream of the throat region, through a series of orifices located in the chamber walls.

Film cooling not only extends rocket chamber life, but also reduces the pressure requirements in the chamber and the amount of coolant required when compared to other cooling techniques. However, achieving effective film cooling in a rocket combustor nevertheless is challenging since the flow-fields in rocket combustors are complex and are influenced by a wide array of geometric and fluid dynamic parameters. As result, there has been extensive experimental, numerical and theoretical research in this area for the past sixty years [129–148].

Experimental work:

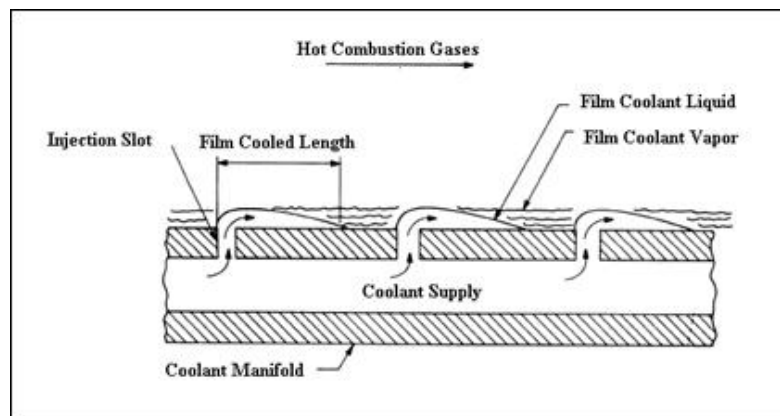


Figure 1-15 Schematic of water film cooling of a rocket engine wall. {Adapted from Emmons (1962) [131]}

One of the earliest experimental studies of rocket film cooling was performed by Boden in 1951 [130]. He investigated film and transpiration cooling of a 1000-lb-thrust rocket motor using water as the coolant in both cases. His results showed that heat transfer near the throat of a rocket could be reduced by as much as 70–75% with film cooling and by as much as 60% with sweat cooling. Boden also reported that the

least effective method of film cooling was radial injection at the entrance of the nozzle which only decreased heat transfer at the throat by 20%.

Boden's work was soon followed by the experimental work of Emmons in 1962 [131]. He conducted tests to determine the effect of different gas stream parameters and coolant physical properties on chamber wall temperatures as well as on the liquid film-cooled length. He used water, anhydrous ammonia, ethyl alcohol, and Freon 113 as coolants in the configuration illustrated in Fig. 1-15. Emmons's results indicate that the film cooled length varies linearly with flow rate and that higher coolant flow rates are required for higher combustion temperatures. He also concluded that combustion pressure (in the range of 250 to 750 psia) had almost no influence upon the flow rate of the coolant required to protect a given wall length.

In 1990, Volkmann et al. [129] performed a series of hot fire tests to determine the gas side heat flux characteristics of film-cooled LOX/RP-1 and LOX/CH₄ rocket engines at a nominal chamber pressure of 2000 psia. They also explored the effect of mixture ratio biasing and of injecting film coolant immediately upstream of the throat. Their results showed that 3.9 lb/s of coolant injected upstream of the throat reduced the gas side heat flux from 58.6 to 36.4 BTU/in²-sec. Subsequently in 1991, Volkmann et al. [132] explored the use of throat film coolant as a method to reduce peak combustion heat flux. They performed a series of hot-fire tests of a subscale LOX/Rp-1 combustor at a nominal chamber pressure of 2000 psia using a special manifold capable of injecting coolant between 4.4 and 16.4 inches upstream of the throat. Their results showed that throat film coolant can greatly reduce peak chamber heat flux even at low coolant flow rates. In addition, they found

that by moving the injection point closer to the throat they could reduce the peak throat heat flux by more than 50% when coolant flow rates exceeded 1.5lb/s.

Volkman's work was followed by Arrington et al. [133] in 1996 who tested two small rocket nozzles at two different fuel film cooling flow rates under three different chamber pressures. Sketches of the water-cooled bell and conical nozzles used in these experiments are shown in Fig. 1-16. Their results showed that film cooling increased the performance of both nozzle types with the bell nozzle producing a higher overall thrust coefficient.

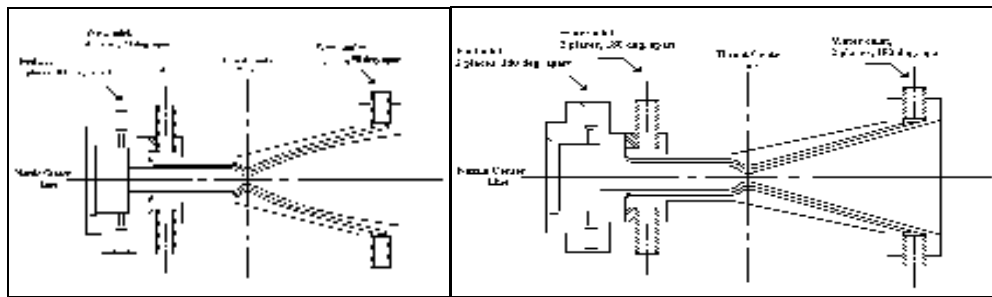


Figure 1-16 (a) Schematic of a water-cooled bell contour nozzle. (b) Schematic of a water-cooled conical nozzle. {Adapted from Arrington et al. (1996) [133]}

Analytical work:

No previous work beyond that described earlier for gas turbine engines has been undertaken to analytically investigate rocket engine film cooling.

Numerical work:

A number of investigations of rocket film cooling using RANS, DNS and LES approaches have been performed over the years.

One of the first RANS investigations of rocket film cooling was a study by Stoll et al. in 1988 [134]. They used a parabolic finite difference boundary layer code with the $k-\epsilon$ model to investigate film cooling and heat transfer in nozzles with rounded, smooth throats. They calculated wall heat fluxes and found that their results

agreed well with available experimental data even at distances far away from the throat. More recently, Zhang et al. [135] numerically studied liquid film cooling in a rocket combustion chamber by solving the mass, momentum and energy equations along with the standard k - ε model to simulate turbulent gas flow and a modified van Driest model for turbulent liquid flow. They computed the liquid film length and found good agreement with experimental data.

To date, only a small number of DNS studies of rocket engine film cooling have been performed. This is largely due to the extreme computational cost of DNS and the very high flow Reynolds numbers associated with most conventional rocket engines [136]. One of the few studies published in this area was by Matesanz et al. [137]. They reported DNS and LES of slot film cooling in a convergent divergent nozzle using a finite element Navier-Stokes solver. Their adiabatic wall temperatures and film cooling effectivenesses agreed moderately well (to within 20%) with corresponding experimental data.

Several rocket engine film cooling studies have also been carried out using LES [136–138]. In addition to the Matesanz et al. [137] study mentioned above, Cruz et al. [136] simulated 2-D slot film cooling of a flat plate using a high-order compressible LES solver. Their results over-predicted effectiveness in the developing region of the film. This was attributed to the two-dimensional domain used in the simulations which resulted in incorrect flow structure and slower mixing dynamics. Subsequent work by Cruz [138] addressed this deficiency by performing a full three-dimensional simulation. This led to a significant improvement in the film cooling and thermal mixing predictions; however, momentum mixing was not well predicted.

Summary:

In summary, it has been shown that film cooling when implemented correctly, can be highly effective in rocket engines and when implemented correctly can reduce heat transfer by as much as 75%. It was also found that RANS and LES approaches predict momentum and thermal mixing reasonably well (within 20%).

Pressure Gradient Effects:

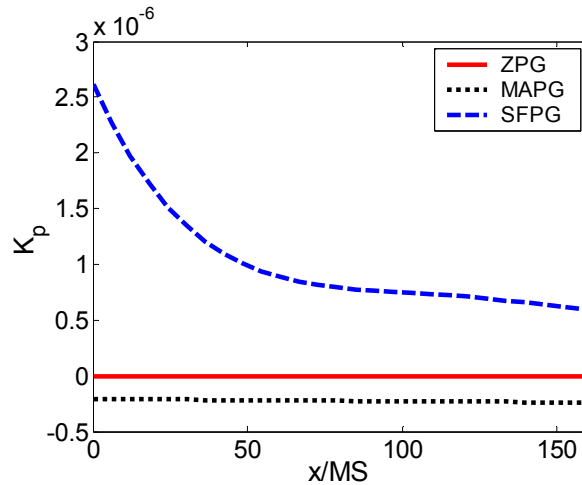


Figure 1-17 Plot showing the three different pressure gradient profiles used by Teekaram et al. [140] {Adapted from Teeekaram et al. (1991) [140]}

Pressure gradients arise on curved blade surfaces and combustor liners in gas turbine engines and along the nozzle contour in rocket motors. Film cooling in both of these cases, therefore, occurs in the presence of a streamwise pressure gradient. Previous work indicates that mainstream pressure gradients impact film cooling effectiveness [139–164] but the results are often contradictory regarding specific impacts.

Experimental work:

A comprehensive review of experimental work by Teekaram et al. [140] in 1989 suggests that the geometry determines whether pressure gradients improve or

degrade film cooling performance. Two-dimensional slot injection studies by Hartnett et al. [141], Seban et al. [142] and Pai et al. [143] suggest that the influence of the pressure gradient is limited and depends on the distance from the slot as well as the coolant to mainstream velocity and density ratios. In contrast, Hay et al.'s [144] investigation of film cooling through three-dimensional holes showed that mainstream pressure gradients have a strong influence on film cooling effectiveness - particularly at low blowing ratios and in the vicinity of coolant injection. They reported a 70 to 80% reduction in the heat transfer coefficient in the presence of a strong favorable pressure gradient (corresponding to an acceleration parameter (K_p) of 5×10^{-6}) at the point of injection. They found no significant effect when the pressure gradient was mildly adverse ($K_p = -0.85 \times 10^{-6}$). Finally, Kruse's [145] investigations of film cooling downstream of a single row of discrete circular holes over a range of blowing ratios and injection angles concluded that adverse pressure gradients improved film cooling effectiveness slightly while favorable pressure gradients degraded film cooling performance. Kruse also noted that the influence of the pressure gradient on film cooling effectiveness was most pronounced when the blowing ratio and hole spacing were small. Among the many experimental studies some of the more notable include studies by Escudier et al. [146] (1968), Zolotogorov [147] (1972), Lutum et al. [148] (2001), and Maiteh et al. [149] (2004) of pressure gradient effects; and Mayle et al. [150] (1977), Ito et al. [151] (1978), Papell et al. [152] (1979), Jung et al. [153] (2001), and Kim et al. [154] (2005) of surface curvature effects.

Analytical work:

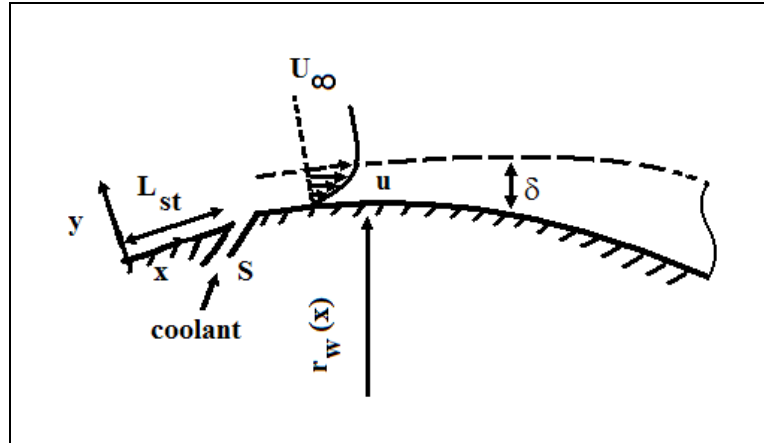


Figure 1-18 Schematic illustration of the boundary layer model used by Sivrioglu [157] {Adapted from Sivrioglu (1991) [157]}

There are only a few theoretical investigations of the effects of pressure gradients on film cooling performance. In 1968, Carlson et al. [155] derived a semi-empirical film cooling correlation based on an accelerating, compressible, turbulent boundary layer. Using their model they correlated experimental slot-film cooling data obtained at various acceleration rates and free-stream turbulence intensities. From their results they concluded that hot gas acceleration has a detrimental effect on film cooling effectiveness along converging walls, especially at locations far downstream from the point of injection. Subsequently, in 1971, Goradia et al. [156] used superposition theory to develop a model for the effect of a streamwise pressure gradient on the growth of a wall jet film without heat transfer. They compared the model's predictions to measurements in a two-dimensional turbulent wall-jet film over a range of velocity ratios in the presence of adverse and favorable pressure gradients but found that their model was not reliable in the initial jet region. Later in 1991, Sivrioglu [157] developed a simple numerical model based on the laminar, two-dimensional boundary layer equations to analyze the effects of pressure gradient and

streamline curvature on film cooling effectiveness. Comparison of the model's predictions with experimental data from Mayle et al. [150] showed reasonable agreement. The model predicted that the effectiveness over a curved surface is higher on the convex side than on the flat plate and the concave side. In addition, the model predicts that favorable pressure gradients cause a decrease in effectiveness relative to the zero pressure gradient case.

Numerical work:

Several numerical studies have focused on the effect of pressure gradients and surface curvature on film cooling performance. The overwhelmingly majority of these have taken RANS approaches. One of the first studies in this area was conducted by Camci et al. [158] in 1985. He used a two-dimensional boundary layer code called STAN5/STANCOOL, as developed by Crawford et al. [159], to model film cooling along the suction side of a gas turbine blade. The numerical predictions of the heat transfer coefficient closely matched experimental data for blowing ratios less than 0.69. At higher blowing ratios, however, the agreement was not as good, especially in the near-injection region. This was followed by Tai et al. [160] in 2002 who performed a RANS simulation of the film cooling of a gas turbine blade. Their results showed that film cooling effectiveness was better on the suction side of blade and that the velocity distribution at the exit plane of the coolant holes was not uniform. RANS simulations were also used by Undapalli et al. [161] in 2003 to investigate film cooling on concave and convex surfaces. Test cases were performed for a single row of film cooling holes at blowing ratios ranging from 1 to 2.5 with a density ratio close to 2 and an injection angle of 35°. The predictions of the

computations for the effects of curvature on mean flow quantities were consistent with measurements but the effects of turbulence on the flow-field were not well captured.

More recently in 2007 Li et al. [162] performed 2-D and 3-D RANS simulations to analyze the effect of surface curvature on mist film cooling. Their results showed that at a nominal blowing ratio of 1.33, air-only adiabatic film cooling effectiveness on the curved surface is less than on a flat surface. In addition, they found that the concave (pressure) surface had a better cooling effectiveness than the convex (suction) surface. Their results suggest that by adding 2% (by weight) mist, film cooling effectiveness can be enhanced by approximately 40% at the leading edge, 60% on the concave surface, and 30% on the convex surface.

Recent RANS simulations by Tao et al. [163] (2007) and Yang et al. [164] (2009) have focused on exploring the effects of surface curvature on film cooling under rotating conditions. Tao et al. [163] used the κ - ω turbulence model to simulate the mixing process between coolant film and a hot air core stream over a curved, rotating, high pressure turbine blade. They found that both rotation and curvature significantly influence the distribution of film coolant along a turbine blade. Rotation could lead to separation of the film while curvature on the suction (convex) side of the blade can cause decreased cooling effectiveness. In the study by Yang et al. [164], the Reynolds number based on mainstream velocity and film hole diameter was varied from 3200 to 6725, the blowing ratio ranged from 0.2 to 1.2, and the rotation number ranged from 0 to 0.0159. Both κ - ω and the shear-stress transport (SST) models were chosen for turbulence closure. Their results showed that increasing the

Rotational speed leads to a decreased effectiveness in the centerline region downstream of the film cooling hole. However, they noted that it can improve the integrated effectiveness on the pressure (concave) surface.

Compressibility and Density Ratio Effects:

Strong compressibility and large density (thermal) gradients are present in gas turbine as well as rocket engine combustors. In order to achieve effective film cooling in these environments it is necessary to be able to understand and predict the influence of these phenomena on cooling performance. Over the past fifty years, many experimental, numerical and theoretical studies of film cooling performance under compressible and large thermal gradient conditions have been conducted [165–184]. However, the results of these studies are often contradictory and a consensus regarding the importance of compressibility has not yet emerged.

Analytical and Experimental work:

Volchkov et al. [165] performed a theoretical investigation of the effect of velocity and temperature compressibility on film cooling effectiveness by deriving a film cooling correlation based on an energy and momentum analysis of a boundary layer. They compared their results with experimental data from Durgin [166] for the film cooling of a cone at Mach 3.5 and concluded that compressibility effects are very small and to first order can be ignored in practical calculations. This conclusion was corroborated by the theoretical work of Repukhov [167] who transformed the turbulent boundary layer equations to account for the effects of compressibility and non-isothermal conditions on film cooling performance. He compared his theoretical predictions with experimental data for the tangential slot film cooling of a flat plate at

a coolant injection Mach number of 0.4. Repukhov found that compressibility effects can be ignored over a wide range of velocity and temperature conditions. In contrast, experimental work by Hansmann et al. [16], suggests that compressibility can significantly influence film cooling performance. Their investigation of tangential slot film cooling of a flat plate in a high enthalpy wind tunnel ($2000\text{K} < T < 3000\text{K}$, $0.5 < M < 1.0$, air and helium working fluids) showed that film cooling performance strongly depended on the density and velocity ratios (coolant to mainstream), with higher effectiveness observed as the velocity and density ratios were increased. Similar results have also been reported by Pedersen et al. [168] who investigated the effects of large density differences between the mainstream and coolant stream on the cooling performance of three-dimensional hole injection over a flat plate. Their results showed that increasing the density ratio (by mixing various amounts of helium, carbon dioxide, refrigerant F-12 and air into the main and film streams) increases the cooling efficiency. Pedersen et al. also noted that this effect was most pronounced at large blowing ratios ($\lambda > 1$) where increases in effectiveness of greater than 200% were observed.

Other noteworthy experimental studies of the effects of compressibility on film cooling performance include the work of Stalder et al. [169] (1956), Danneberg [170] (1962), Goldstein et al. [171] (1966), Parthasarathy et al. [172] (1970), Cary et al. [173] (1972), Ferri et al. [174] (1976), Kanda et al. [175] (1994) and Schuchkin et al. [9] (2002). In addition, a number of experiments have also examined density gradient effects in film cooling flows. Among the key studies in this area are papers by Ferri et al. [176] (1956), Sinha et al. [177] (1991) and Etheridge et al. [178] (2001).

Numerical work:

There are fewer numerical simulations of density and compressibility effects in film cooling [179–184]. This is largely because of the extremely high Reynolds numbers and complex flow-field environments associated with film cooling under highly compressible or large density gradient conditions. To date, most of the studies have taken a RANS approach. Several RANS studies of compressibility effects on film cooling have been conducted including those by Aupoix et al. [179] (1998), Lushchik et al. [180] (2001), Wang et al. [181] (2007), Wang et al. [182] (2008) and Sun et al. [183] (2008) on compressibility effects in film cooling flows. Only one numerical study by Renze et al. [184] (utilizing an LES approach) has focused on density gradient effects in film cooling flows.

1.3.4 Overall Summary:

Several important lessons relevant to the design of the J-2X nozzle extension have emerged from this extensive review of the literature on mixing layer and film cooling flows. First, there is a consensus in the literature that compressible shear layers grow much more slowly than incompressible ones. This indicates that supersonic film cooling could be a favorable strategy in the J-2X engine. Second, experiments have shown that when film cooling is implemented correctly, it can be highly effective in rocket engines reducing heat transfer by as much as 75%. Third, the literature shows that reasonable predictions of film cooling effectiveness can be obtained analytically using Simon's semi-empirical model (within 5% error) and numerically using both LES and RANS approaches (within 10 to 20% error). Fourth, previous work has shown that RANS simulations can achieve good agreement with

experimental data for momentum mixing, but, not always for the thermal mixing. Fifth and finally, there appears not to be consensus in the literature on the effects of pressure gradients, wall curvature, compressibility and density gradients on film cooling effectiveness. Some researchers have suggested that favorable pressure gradients degrade effectiveness while others have shown that it enhances effectiveness. Similarly some researchers have indicated that density gradients and compressibility have a small to negligible effect on film cooling effectiveness while others have demonstrated that it can have a significant effect.

1.4 Main Objectives

The primary objectives of this thesis are to:

1. Improve the basic physical understanding and prediction of the effects of pressure gradients (caused by surface curvature) on film cooling effectiveness.
2. Advance the basic physical understanding and prediction of the effects of compressibility and density gradients on film cooling performance.
3. Identify strategies and techniques that can be used independently or in combination with existing approaches to enhance film cooling performance.
4. Develop a computationally inexpensive RANS methodology for accurately predicting momentum mixing, thermal mixing, skin friction and film cooling effectiveness measurements in a subsonic slot-jet film cooling experiment.
5. Enhance understanding of the subsonic slot-jet film cooling process.

6. Use inexpensive RANS simulations to design a supersonic film cooling experiment.

1.5 Organization of This Thesis

This chapter has introduced the concept of film cooling and outlined the main challenges and objectives associated with the implementation of this cooling strategy in a rocket engine. A comprehensive review of the literature on mixing layer and film cooling flows has also been presented.

The goal of chapter two is to improve the understanding of the influence of pressure gradients on film cooling effectiveness. A short review of the classification and quantification of pressure gradients is presented and Simon's isobaric, incompressible semi-empirical film cooling model is explained. Then, a new non-isobaric incompressible semi-empirical film cooling model is developed based on Simon's initial approach. The model's parameters are selected using a sensitivity analysis and the method of least squares. Results are presented and discussed for the zero pressure gradient, constant pressure gradient and variable pressure gradient cases. The chapter concludes with an explanation of how this model resolves some of the apparent conflicts in the open literature.

Chapter three describes a new semi-empirical model to predict the effects of density gradients on film cooling performance. This is prefaced by a brief review of the classification and quantification of density gradients and a discussion of the development and validation of a compressible shear layer growth rate model. The chapter concludes with a physical explanation for the results, a discussion of the

influence of density gradients on film cooling performance, and an explanation of how the model resolves other apparent conflicts in the open literature.

Chapter four discusses the development of a computationally inexpensive RANS methodology for the accurate numerical prediction of subsonic film cooling performance. It begins with a brief description of the loci-CHEM RANS solver along with a discussion on the quantification of numerical uncertainty and validation of the RANS solver. Next, precursor RANS simulations and full subsonic film cooling RANS simulations are presented. Results are presented and discussed.

Chapter five describes the preliminary numerical simulations that were used to support the design of a supersonic film cooling experiment. It begins with an overview of the experiment and its objectives. This is followed by an explanation of how the solutions were validated under supersonic conditions. The chapter concludes with the presentation of results and a discussion of their implications for the design of a practical supersonic film cooling experiment.

Chapter six summarizes the major conclusions and key contributions of this dissertation.

Chapter seven presents recommendations for future work. This includes a brief outline of the development of a film cooling model accounting for the effect radiative heat loss and a combined pressure gradient-density gradient film cooling model, as well as a short discussion of the application of the compressible shear layer growth rate model devised in Chapter 3 to reacting flows.

Chapter 2: The Influence of Pressure Gradients on Film Cooling Performance

2.1 Introduction

Previous work has shown that one of the key fluid dynamic factors affecting film cooling performance is the presence of a mainstream pressure gradient [139]. However, as noted in the literature review in §1.3, the results of several experimental numerical and theoretical investigations [139–164] of the influence of mainstream pressure gradient are often contradictory. In the current chapter, therefore, the focus is on providing a clearer picture of the influence of mainstream pressure gradient on film cooling and resolving some of the conflicts in the open literature. To do this, the incompressible film cooling analysis developed by Simon [114] is extended to account for the effect of main stream pressure gradients on film cooling performance.

2.2 Background

Before proceeding further it is useful to first consider how pressure gradients are typically classified and quantified.

2.2.1 Types of Pressure Gradients

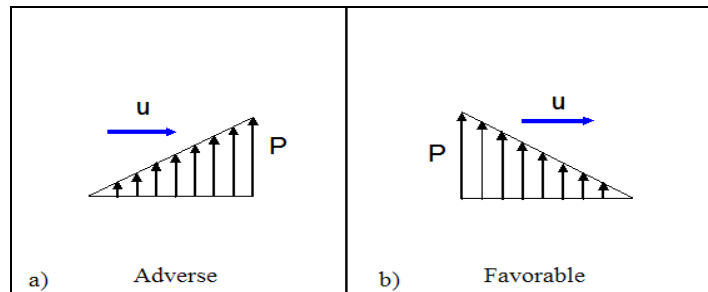


Figure 2-1 Sketch showing: a) An adverse pressure gradient b) A favorable pressure gradient.

Pressure gradients commonly fall into two categories: adverse or favorable which are illustrated in Figure 2-1. An adverse pressure gradient is associated with

increasing pressure in the streamwise direction which leads to flow deceleration. In contrast, a favorable pressure gradient is associated with decreasing pressure in the streamwise direction and flow acceleration.

2.2.2 Quantification of Pressure Gradients

Pressure gradients can be quantified in different ways depending on whether they are constant or vary with streamwise distance.

Constant Pressure Gradients

Constant pressure gradients are typically quantified using the pressure coefficient, C_p , which is given by:

$$C_p = \frac{P - P_{ref}}{q_{ref}} \quad (2.1)$$

where P is local static pressure, P_{ref} is the reference static pressure, and q_{ref} is the reference dynamic pressure, $q_{ref} = 1/2 \rho u_{ref}^2$. When C_p is > 0 (i.e., when $P > P_{ref}$) this indicates an adverse pressure gradient is present and when C_p is < 0 (i.e., when $P < P_{ref}$) this indicates a favorable pressure gradient is present.

Variable Pressure Gradients

In situations where the pressure gradient changes with downstream distance (like in a rocket nozzle) it is more common to represent pressure gradients acting on boundary or shear layers using Kay's acceleration parameter [185], K_p . It is defined as follows:

$$K_p = \frac{v_\infty}{U_{0,\infty}^2} \frac{dU_\infty}{dx} \quad (2.2)$$

where ν_∞ is the kinematic viscosity of the hot stream, $U_{0,\infty}$ and U_∞ are the initial and local hot stream velocities respectively, and x is the downstream distance. K_p is related to C_{p_∞} and the initial hot stream to coolant stream velocity ratio ($R_0 = U_{0,\infty}/U_{0,s}$) by the following expression:

$$K_p = \frac{\nu_\infty}{U_{0,\infty}} \frac{\left[\sqrt{1 - \frac{C_{p_\infty}}{R_0^2}} - 1 \right]}{x} \quad (2.3)$$

A major advantage of using Kay's acceleration parameter is that it provides a more intuitive 'feel' for pressure gradients. When K_p is positive (i.e., $K_p > 0$) this indicates a favorable (accelerating) pressure gradient is present whereas when K_p is negative (i.e., $K_p < 0$) an adverse (decelerating) pressure gradient is present.

2.3 Analysis

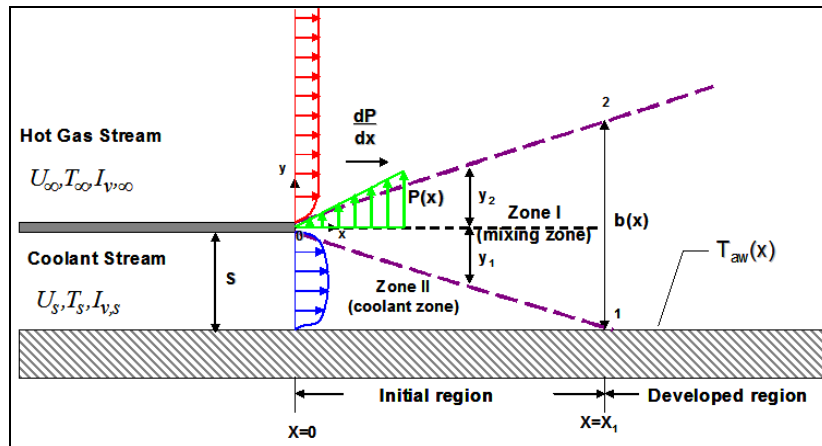


Figure 2-2 Pressure gradient film cooling model {adapted from Simon [114] (1986)}

Figure 2-2 is a schematic illustration of the wall-jet film cooling situation investigated by Simon [114] but with the addition of a streamwise pressure gradient. The figure shows a coolant stream at a temperature, T_s , and velocity, U_s , being injected near the wall, from a slot of height, s . At x_0 , the coolant stream encounters a

hot gas stream of temperature, T_∞ (with $T_\infty > T_s$), moving at a velocity, U_∞ , where $U_\infty < U_s$. Associated with this hot gas stream is a pressure gradient of magnitude dP/dx . A weakly turbulent shear layer of thickness b develops and grows with streamwise distance x at the interface between the coolant and hot gas streams. The length of the initial developing region x_I is taken to be the distance required for the inner edge of the developing mixing zone, labeled Zone I in Fig. 2-2, to reach the wall. The initial developing region is often termed the ‘potential core’ region and has been shown experimentally to provide very effective protection [113]. Following the approach of Simon, the adiabatic wall temperature in the initial region ($x < x_I$), T_{aw} , is assumed to equal the mean fluid temperature in Zone II (coolant zone), while in the developed region the adiabatic wall temperature is assumed to equal the mean fluid temperature in Zone I. Hence:

$$T_{aw} = \begin{cases} \bar{T}_{II}, & (x < x_I) \\ \bar{T}_I, & (x \geq x_I) \end{cases} \quad (2.4)$$

The following assumptions are also made:

- (1) The change in the specific heat with temperature is small. (This is justified by the fact that the specific heat capacity of air remains approximately constant over a wide temperature range [186]).
- (2) The composition of the coolant and hot streams is the same.
- (3) The hot gas stream temperature, T_∞ , is constant.
- (4) Thermal radiation from the hot gas stream is negligible. (This is a reasonable assumption since radiation only becomes important at very high temperatures due to the fourth squared dependence of radiation on temperature).

(5) The shear layer growth, b , is linear. (This has been shown experimentally to be a valid assumption [27]).

2.3.1 Film Cooling Model Development

Film-cooling effectiveness, η_{eff} , is typically defined for an incompressible flow as [108]:

$$\eta_{eff} = \frac{T_{\infty} - T_{aw}}{T_{\infty} - T_s} \quad (2.5)$$

From a mass and energy balance on the coolant stream, it can be shown following Stollery et al. [112] that the film cooling effectiveness is related to the amount of hot stream gas entrained by the coolant stream.

$$\eta_{eff} = \dot{m}_s / \dot{m}_f \quad (2.6)$$

where \dot{m}_s is the coolant mass flow rate per unit length, $\dot{m}_s = \rho_s U_s s$, and \dot{m}_f is the total mass flow rate of the film per unit length, at any arbitrary x -location downstream of the coolant slot exit. The value of \dot{m}_f includes both the coolant mass flow rate per unit length and the entrained hot gas stream rate per unit length, \dot{m}'_e . This can be expressed as follows:

$$\dot{m}_f = \dot{m}_s + \int_0^x \dot{m}'_e dx \quad (2.7)$$

Following the approach of Juhasz et al. [108] \dot{m}'_e is assumed to be directly proportional to the hot gas stream mass flux:

$$\dot{m}'_e = C'_M \rho_{\infty} U_{\infty} \quad (2.8)$$

where C'_M is an ‘effective’ turbulent mixing coefficient which is related to the average turbulence intensity, I_v .

Substitution of Eqs. (2.7) and (2.8) into Eq. (2.6) yields:

$$\eta_{eff} = (1 + (x/\lambda s)C'_M)^{-1} \quad (2.9)$$

where λ is the blowing ratio - defined as the ratio of the coolant stream to hot stream mass flux:

$$\lambda = \rho_s U_s / \rho_\infty U_\infty \quad (2.10)$$

Eq. (2.9) gives the functional form for a basic turbulent film cooling correlation. It shows that film cooling effectiveness decreases with increasing streamwise distance, with decreasing blowing ratio, with decreasing slot height, and with increasing turbulence intensity.

Following Simon’s approach, C'_M is written in terms of the turbulent mixing coefficient, C_M , and a turbulent diffusion parameter, β :

$$C'_M = \frac{C_M - \beta(x/\lambda s)^{-1}}{1 + \beta} \quad (2.11)$$

The parameter β accounts for turbulent diffusion from zone I to zone II in the initial region ($x < x_I$) only. It therefore has a value of zero in the developed region ($x \geq x_I$). C_M is a function of the shear layer entrainment rate, db/dx , which can be directly related to I_v using Abramovich’s [27] empirical assumption that db/dx is proportional to the perturbation-component of the fluctuating hot gas stream velocity, v'_0 . This leads to:

$$C_M = db/dx = \frac{a_0 v'_0}{U_0^*} \quad (2.12)$$

where a_0 is an empirical constant and U_0^* is the characteristic velocity of the shear layer given by:

$$U_0^* = \frac{\rho_\infty U_\infty + \rho_s U_s}{\rho_\infty + \rho_s} \quad (2.13)$$

Substituting Eq. (2.13) into Eq. (2.12), simplifying by noting that $I_v = v'_0/U_\infty$, and incorporating Eq. (2.10), yields an expression for C_M , which in general form can be written as:

$$C_M = a_0 (I_v \omega)^N \quad (2.14)$$

In this expression, N is an empirically determined constant, ω is a dimensionless flow temperature parameter developed by Simon, and I_v is the overall average transverse turbulence intensity. ω and I_v are given by:

$$\omega = \left(\frac{1 + 1/TR}{1 + \lambda} \right) \quad (2.15)$$

$$I_v = I_{v,\infty} + 0.4(|I_{v,\infty} - I_{v,s}|) \quad (2.16)$$

TR is the temperature ratio, which is defined as the ratio of the coolant to hot stream static temperature, T_s/T_∞ . $I_{v,s}$ is the initial average transverse coolant stream turbulence intensity and $I_{v,\infty}$ is the initial average transverse turbulence intensity of the hot gas stream; I_v is based on a turbulent correlation obtained from Ko et al. [110], which has the constraint that I_v cannot be greater than either $I_{v,\infty}$ or $I_{v,s}$. Eq. (2.14) is used by

Simon to account for turbulence in both the initial region ($x < x_l$) and in the developed region ($x \geq x_l$).

Returning to the β parameter from Eq. (2.11), Simon [114] developed the following expression for β based on empirical observation and by noting that the turbulent diffusion from zone I to zone II is a function of the initial average transverse turbulence intensity of the coolant stream, $I_{v,s}^*$:

$$\beta = \left[C_M \left(\frac{x}{\lambda s} \right) + \left(\frac{x}{x_1} \right) - C_0 I_{v,s}^* \left(T_s / T_{aw_{x=x_1}} \right) \ln \left| 1 / \left(1 - \frac{x}{x_1} \right) \right| \right] \left(\frac{T_{aw_{x=x_1}} - T_{aw}}{T_\infty - T_s} \right) \quad (2.17)$$

In Eq. (2.17), C_0 is an empirically determined constant.

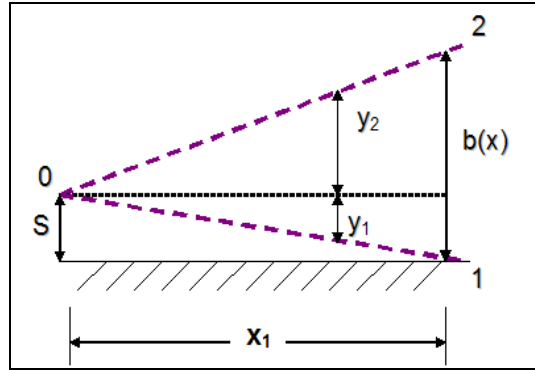


Figure 2-3 Sketch of shear layer geometry. {Adapted from Abramovich [27] (1962)}

The location of the transition point between the initial and fully developed regions, x_l , can be computed from the geometry of the shear layer, as shown in Fig. 2-3:

$$x_1 = \frac{s}{y_1} x \quad (2.18)$$

where y_l is the shear layer-coolant stream interface position. Next by noting from Fig. 2-3 that the shear layer thickness, $b = y_l + y_2$, and that the turbulent mixing coefficient, C_M , is related to the shear layer growth rate by $C_M = (b - y_1)/x$, Eq. (2.18) can be simplified to:

$$x_1 = [(C_M/s)y_1/y_2]^{-1} \quad (2.19)$$

where y_2 is the shear-layer-hot stream interface position.

Before proceeding further, it is important to note that the introduction of a pressure gradient does not change the forms of Eqs. (2.4) – (2.17) as the pressure gradient has no effect on the mass or energy balance in Zones I or II. However, the pressure gradient does affect the momentum balance in Zones I and II thereby influencing the location of the transition point between the initial and fully developed regions through y_1/y_2 in Eq. (2.19). So, the next step is to use Abramovich's [27] semi-empirical theory of incompressible, turbulent jets (or shear layers) to find y_1/y_2 . Once y_1/y_2 is known, x_1 can be determined using Eq. (2.19) and the streamwise evolution of film cooling effectiveness can be computed using Eq. (2.9) plus Eqs. (2.10) – (2.17).

2.3.2 Isobaric Case (Simon's Model)

Abramovich showed that for an incompressible shear layer formed between two co-flowing streams of different velocities in the absence of a pressure gradient, the shear layer growth rate can be expressed as:

$$db/dx = k \quad (2.20)$$

where b is the shear layer thickness and k is a constant which depends on R , the ratio of the average hot stream velocity to the average coolant stream velocity ($R \equiv \bar{U}_\infty/\bar{U}_s$):

$$k = \pm c \left(\frac{1-R}{1+R} \right) \quad (2.21)$$

c is a constant which representing the density ratio between the two streams. The negative sign is taken when $R > 1$, i.e., when $U_\infty > U_s$. This corresponds to a core-driven film situation. Integrating Eq. (2.20) yields the following expression for the shear layer thickness:

$$b = \pm c \left(\frac{1-R}{1+R} \right) x \quad (2.22)$$

Eq. (2.22) shows that the growth in the shear layer thickness, b , in the absence of a pressure gradient depends only on the velocity and density ratio. It also shows that the shear layer thickness varies linearly with streamwise distance. This expression can be related to Eq. (2.19), by performing a momentum and mass balance on the two streams to obtain an expression for y_1/b . This has been done by Abramovich [27] and yields the following result:

$$\frac{y_1}{b} = c(0.416 + 0.134R) \quad (2.23)$$

Recalling that $b = y_1 + y_2$ (see Fig. 2-3) Eq. (2.23) can be rearranged to obtain an expression for y_1/y_2 :

$$\frac{y_1}{y_2} = \left[\frac{1}{c(0.416 + 0.134R)} - 1 \right]^{-1} \quad (2.24)$$

Following the approach of Simon, c is defined to be the ratio of the fluid density in mixing zone I at the impingement point (x_I) to the coolant stream density:

$$c = T_s / T_{aw, x=x_I} \quad (2.25)$$

Eqs. (2.24) and (2.25) combined with Eqs. (2.4)- (2.19) form the Simon Model (SM) which is valid for incompressible wall-jet film cooling in the absence of a pressure gradient.

2.3.3 Non-isobaric case

An analogous approach is used to develop an expression for y_1/y_2 under non-isobaric conditions. Returning to the semi-empirical theory of incompressible, turbulent jets (or shear layers), if a longitudinal mainstream pressure gradient is present as shown in Fig. 2-2, it can be shown using Bernoulli's equation [186] that the ratio of the local hot stream velocity at a given x-location, U_∞ , to the initial hot stream velocity, $U_{0\infty}$, along an arbitrary streamline is given by:

$$\frac{U_\infty^2}{U_{0\infty}^2} = 1 - \left[\frac{P_\infty(x) - P_{0\infty}}{\frac{1}{2} \rho U_{0\infty}^2} \right] \quad (2.26)$$

where $P_\infty(x)$ is the local hot stream static pressure at a given x-location and $P_{0\infty}$ is the static pressure of the hot stream at the point of coolant injection.

Recalling from §2.2.2 that the pressure coefficient (non-dimensional pressure gradient), C_{P_∞} is defined as:

$$C_{P_\infty} = \frac{P_\infty(x) - P_{\infty,x=0}}{\frac{1}{2} \rho \bar{U}_{\infty,x=0}^2} \quad (2.27)$$

where $C_{P_\infty} > 0$ corresponds to an adverse pressure gradient while $C_{P_\infty} < 0$ corresponds to a favorable pressure gradient.

Eq. (2.26) can be simplified by substituting Eq. (2.27) and by introducing definitions for R , the local hot stream to coolant stream velocity ratio, i.e., $R = \frac{U_\infty}{U_s}$,

and for R_0 , the initial hot stream to coolant stream velocity ratio, i.e., $R_0 = \frac{U_{0\infty}}{U_{0s}}$. This

leads to an expression for R in terms of R_0 and $C_{P\infty}$ which is given by:

$$R = \sqrt{\left(\frac{R_0^2 - C_{P\infty}}{1 - C_{P\infty}} \right)} \quad (2.28)$$

Substituting Eq. (2.28) into Eqs. (2.20) and (2.21) and simplifying leads to an expression for the shear layer growth rate that is analogous to the growth rate expression for the isobaric case:

$$db/dx = k' + \ell \quad (2.29)$$

The first term, k' , corresponds directly to k in the isobaric case (Eq. 2.20) and is given by:

$$k' = \pm c \frac{1 - R_0}{1 + R_0} \quad (2.30)$$

The second term, ℓ , is new and arises because of the pressure gradient. It is given by the following expression:

$$\ell = 2c \frac{R_0 - C_{P\infty} - \sqrt{(1 - C_{P\infty})(R_0^2 - C_{P\infty})}}{1 - R_0^2} \quad (2.31)$$

As in the isobaric case, the negative sign in Eq. (2.30) is taken for a core-driven film (i.e., $R_0 > 1$) and the positive sign is taken for a wall-jet.

An expression for the shear layer thickness is obtained by integrating Eq. (2.29). Applying the boundary condition that at $x = 0$, $b = 0$ yields the following expression for the variation of the shear layer thickness with x :

$$b = \pm cx \frac{1-R_0}{1+R_0} \mp \frac{cx}{1-R_0^2} \left\{ R_0 - \frac{1}{2} C_{P\infty} - \frac{1}{4C_{P\infty}} \left[(2C_{P\infty} - 1 - R_0^2) \sqrt{K_1} + R_0 (1 + R_0^2) - 2(1 - R_0^2) \ln|K_2| \right] \right\} \quad (2.32)$$

$$K_1 = (1 - C_{P\infty}) (R_0^2 - C_{P\infty}) \quad (2.33)$$

$$K_2 = \frac{1 + R_0^2 - 2C_{P\infty} - 2\sqrt{K_1}}{1 - R_0^2} \quad (2.34)$$

Eqs. (2.32) - (2.34) show that the shear layer thickness is a function of R_0 , $C_{P\infty}$ and x .

As in the isobaric case, Abramovich [27] performed a mass and momentum balance on the two streams to obtain an expression for y_1/b :

$$\frac{y_1}{b} = \frac{(1 - C_{P\infty}) (0.416 + 0.268R + 0.316R^2) - R_0 \sqrt{1 - C_{P\infty}} (0.55 + 0.45R) + 2C_{P\infty} - (1 - R_0) (1 - \sqrt{1 - C_{P\infty}}) \frac{b_0}{b}}{(1 - R_0) \sqrt{1 - C_{P\infty}}} \quad (2.35)$$

Substituting Eqs. (2.32)- (2.34), and Eq. (2.28) into Eq. (2.35) and recalling that $b = y_1 + y_2$ (see Fig. 1) gives an expression for y_1/y_2 :

$$\frac{y_1}{y_2} = \frac{1}{1 - c \left[\frac{2C_{P\infty}}{\sqrt{1 - C_{P\infty}}} + \sqrt{1 - C_{P\infty}} \left(0.416 + \frac{0.316K_1}{(1 - C_{P\infty})^2} + 0.268 \frac{\sqrt{K_1}}{1 - C_{P\infty}} \right) - R_0 \left(0.55 + 0.45 \frac{\sqrt{K_1}}{1 - C_{P\infty}} \right) - K_3 \right]} \quad (2.36)$$

$$K_3 = \frac{b_0 (1 - R_0 - R_0^2 + R_0^3) \left(\frac{1}{\sqrt{1 - C_{P\infty}}} - 1 \right)}{c \left((1 - R_0)^2 x - \left(R_0 x - C_{P\infty} \frac{x}{2} - \frac{b_0}{4s} \left(R_0 (1 + R_0^2) + (-1 - R_0^2 + 2C_{P\infty}) \sqrt{K_1} + (-2(1 - R_0^2) \ln|K_2|) \right) \right) \right)} \quad (2.37)$$

Using Eqs. (2.36) and (2.37) to represent y_1/y_2 in Eqs. (2.4)-(2.19) gives the Pressure Gradient Film Cooling Model (PGFM), which is valid for incompressible, film

cooling in the presence of a streamwise pressure gradient. In the limit as $C_{p\infty} \rightarrow 0$, Eqs. (2.36) and (2.37) simplify to:

$$\frac{y_1}{y_2} = \left(\frac{1}{\frac{c}{1-R_0} [0.416 - 0.282R_0 - 0.134R_0^2]} - 1 \right)^{-1} \quad (2.38)$$

Factoring this equation and noting from Eq. (2.28) that when the pressure gradient tends to zero, $R_0 \rightarrow R$, yields:

$$\frac{y_1}{y_2} = \left(\frac{1}{c(0.416 + 0.134R)} - 1 \right)^{-1} \quad (2.39)$$

The PGFM is equivalent to the SM in the limit of zero pressure gradient because Eq. (2.39) is identical to Eq. (2.24).

2.4 Selection of Model Parameters

2.4.1 Introduction

To apply the film cooling model developed in §2.3, it is necessary to first select values for the model's empirical parameters C_o , a_o and N . In addition, the model also requires inputs for the initial coolant stream and hot stream turbulence intensities, $I_{v,s}$, and $I_{v,\infty}$, which historically have not been reported in previous experimental work in the open literature.

The process of determining the values for these constants and inputs to the model occurs in two parts. First, a sensitivity analysis is carried out to ascertain which parameters exert the greatest influence on the predictions of the model. Second, a

least-squares analysis is performed to find specific values for the most sensitive constants and inputs while the values used by Simon [114] were applied for the most insensitive parameters. The details of this procedure are outlined below.

2.4.2 Sensitivity Analysis

To explore the sensitivity of the PGFM's predictions to the different empirical constants and input parameters, a series of tests were performed in which each parameter was varied systematically from a baseline value for a fixed set of flow conditions in the absence of a pressure gradient present. The baseline values for the empirical constants were set to those used by Simon [114] in his model, i.e., $a_0 = 0.177$, $C_0 = 13.7$ and $N = 0.65$. Also, the initial average turbulence of the coolant and core streams, $I_{v,s}$, and $I_{v,\infty}$, were assumed to be identical and set to an arbitrary baseline value of 0.05. This allowed the turbulence intensities of both streams to be collapsed into a single parameter, I_v , (representing the initial effective lateral turbulence i.e., initial average turbulence of both streams) following Eq. (2.16). The flow conditions used in this exercise were based on the isobaric, turbulent wall-jet film cooling of experiment by Cruz et al. [187] (described in detail in §2.4.4) with velocity ratio ($R = 0.63$), blowing ratio ($\lambda = 2.22$) and temperature ratio ($TR = 0.71$). The results of this analysis are presented below in Figure 2-4. In each case, the parameters are varied by 10%, 25%, 50% and 100%. The solid red lines correspond to the predictions of the PGFM for the baseline values of the empirical constants and input parameters.

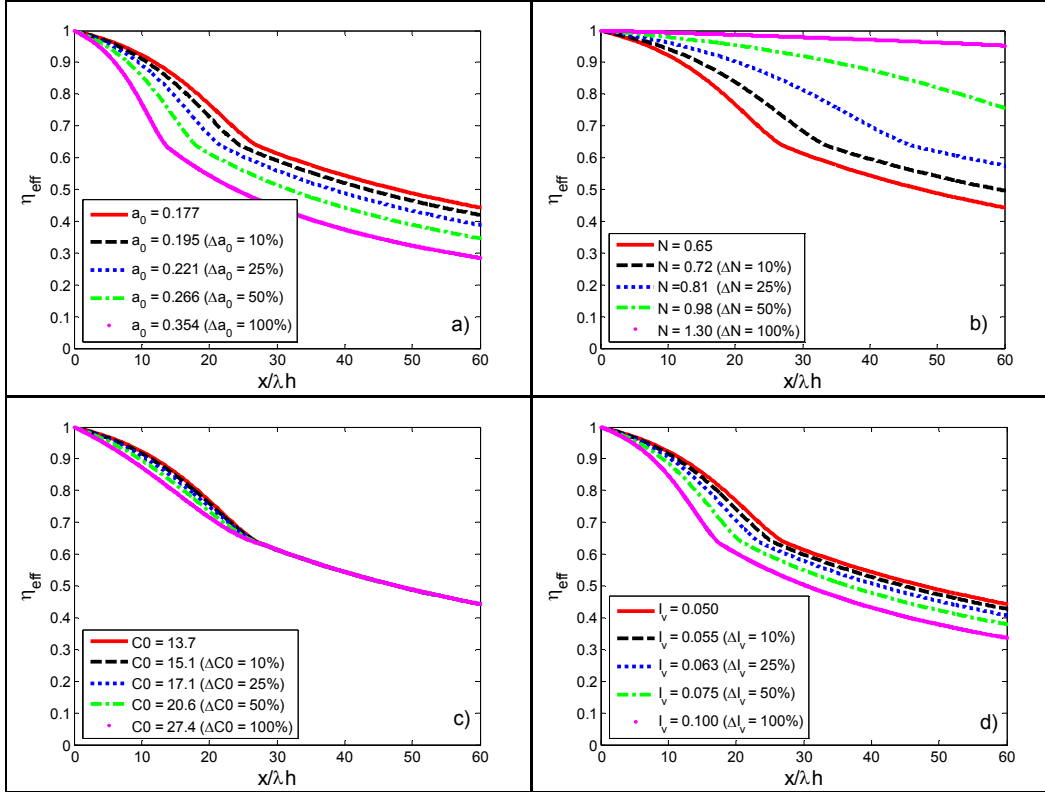


Figure 2-4 Effect of variation of: a) a_0 b) N c) C_0 and d) I_v on the predictions of the PGFM for a wall-jet film under zero pressure gradient conditions ($R = 0.63$, $\lambda = 2.22$ and $TR = 0.71$).

Figure 2-4 shows that the PGFM predictions are least sensitive to changes in the constant C_0 and most sensitive to changes in the value of the constant N . The figure also shows that the parameters a_0 and I_v have a non-negligible influence on the model's predictions. Based on these results the following conclusion can be made: In determining values for the empirical constants and input parameters, it will be important to carefully select the values for a_0 , I_v and N in order to guarantee that sensible predictions are obtained. In addition, since the model is virtually insensitive to changes in the value of C_0 , and its value appears to affect only the initial, near injection region, it is reasonable to prescribe its value *a priori* to that used by Simon [114] ($C_0 = 13.7$).

2.4.3 Least Squares Analysis Details

Simon [114] determined the value of the empirical constants a_0 and N , used in his model from experimental shear layer data. N corresponds to the slope of the log-log plot of the dimensionless shear layer growth rate ($d\phi/dx$) vs. the dimensionless grouping of flow temperature and turbulence ($I_v\omega$); a_0 corresponds to the slope of the plot of the dimensionless shear layer growth rate ($d\phi/dx$) vs. the dimensionless grouping of flow temperature and turbulence raised to the power of N i.e., $(I_v\omega)^N$. In addition, the input for initial average turbulence intensities of both coolant and core streams were measured experimentally and as a result could readily be applied in the model. This information, however, is not always included by researchers reporting their film cooling measurements.

One approach that can be used to circumvent the problem of missing or unreported empirical information, is to perform a least squares analysis to determine the values of the model parameters that allow the PGFM's predictions to agree most closely with a given set of experimental data. Having eliminated the constant C_0 as a variable, and given measured values for $I_{v,s}$ and $I_{v,\infty}$, this leads to a relatively straightforward two-variable least-squares (LSQ) analysis to determine values for a_0 and N . For cases in which $I_{v,s}$ and $I_{v,\infty}$ are unknown, a slightly more complicated three-variable LSQ analysis must be performed to find I_v in addition to a_0 and N .

Two-variable LSQ Approach:

Since η_{eff} does not depend linearly on N and a_0 , a non-linear two-variable least squares analysis must be performed. The first step in this process involves selecting initial guesses for each parameter and obtaining a preliminary prediction of the

effectiveness based on the ‘known’ empirical quantities in the model (i.e., λ , s , C_0 , T_s , and T_∞). Estimates for the impingement length, x_I , and the adiabatic wall temperature at this location, $T_{aw_{x=x_1}}$, are then obtained from this initial effectiveness prediction.

Next the method of least squares is applied to find a_0 and N , by solving:

$$\|r\| = \left\| \eta_{eff_{exp}} - \eta_{eff_{PGFM_k}} \right\| \rightarrow 0 \quad (2.40)$$

where r is the residual.

This is achieved in the following way. First the difference ($d\beta_k$) between the experimental and predicted effectiveness values at each measurement location is computed. This corresponds to a column vector given by:

$$d\beta_k = \begin{bmatrix} \eta_{eff_{exp}}(x_0) - \eta_{eff_{PGFM_i}}(x_0) \\ \eta_{eff_{exp}}(x_1) - \eta_{eff_{PGFM_i}}(x_1) \\ \vdots \\ \eta_{eff_{exp}}(x_m) - \eta_{eff_{PGFM_i}}(x_m) \end{bmatrix} \quad (2.41)$$

where the subscript k indicates the value at the current iteration and x_i are the streamwise measurement/evaluation locations.

Next, the effectiveness defined in Eq. (2.9) can be expressed as an explicit (i.e., direct function) of the parameters a_0 and N . This yields the following:

for $x < x_1$:

$$\eta_{eff} = \frac{1 + \left[a_0 (I_v \omega)^N \left(\frac{x}{\lambda s} \right) + \left(\frac{x}{x_1} \right) - C_0 I_{v,s}^* \left(\frac{T_s}{T_{aw_{x=x_1}}} \right) \ln \left| 1 / \left(1 - \frac{x}{x_1} \right) \right| \right] \psi}{1 + \left(\frac{x}{\lambda s} \right) a_0 (I_v \omega)^N} \quad (2.42)$$

for $x \geq x_1$:

$$\eta_{eff} = \left[1 + \left(x / (\lambda s) a_0 (I_v \omega)^N \right) \right]^{-1} \quad (2.43)$$

where ψ is a dimensionless flow temperature grouping given by $\psi = \left(\frac{T_{aw_{x=x_1}} - T_{aw}}{T_\infty - T_s} \right)$.

Note here that Eq. (2.42) is valid only in the initial region ($x < x_1$), while Eq. (2.41) is valid only in the developing region ($x \geq x_1$).

Following the non-linear least squares fitting procedure outlined by Bates et al. [188] Eqs. (2.42) and (2.43) are then partially differentiated with respect to each parameter. This yields the following expressions for the developed region:

$$\left. \begin{aligned} \partial \eta_{eff} / \partial a_0 &= - \left[1 + \left(x / (\lambda s) a_0 (I_v \omega)^N \right) \right]^{-2} (x / (\lambda s)) (I_v \omega)^N \\ \partial \eta_{eff} / \partial N &= - \left[1 + \left(x / (\lambda s) a_0 (I_v \omega)^N \right) \right]^{-2} (x / (\lambda s)) (a_0) (N) (I_v \omega)^{N-1} \end{aligned} \right\} \text{ for } x > x_1 \quad (2.44)$$

The partial derivatives of Eq. (2.42) are extremely complicated and cumbersome in the initial region. This necessitates the use of a numerical differentiation function.

An $m \times n$ Jacobian matrix A can then be constructed as follows:

$$A = \begin{vmatrix} \partial \eta_{eff} / \partial a_0(x_0) & \partial \eta_{eff} / \partial N(x_0) \\ \partial \eta_{eff} / \partial a_0(x_1) & \partial \eta_{eff} / \partial N(x_1) \\ \vdots & \vdots \\ \partial \eta_{eff} / \partial a_0(x_m) & \partial \eta_{eff} / \partial N(x_m) \end{vmatrix} \quad (2.45)$$

Here m is the number of stream-wise evaluation points (in both the initial and developed regions), and n is the number of parameters being considered, i.e., $n = 2$ in this case.

Now the following system of equations can be established, where $d\phi_j$ is a column vector corresponding to the two variables being evaluated (i.e., a_0 and N):

$$Ad\varphi_j = d\beta_k \quad (2.46)$$

The values of a_0 and N are then determined by solving the system for $d\varphi_j$ in the following manner:

$$A^T Ad\varphi_j = A^T d\beta_k \quad (2.47)$$

$$d\varphi_j = (A^T A)^{-1} (A^T d\beta_k) \quad (2.48)$$

Once the new values of a_0 and N are obtained, new values for $n_{effPGFM_i}$ are computed and the process is repeated until a residual convergence criterion is met.

Because of the complexity of determining and manipulating the partial derivatives of Eq. (2.42), the entire process is implemented using the MATLAB built-in function *lsqcurvefit* [189]. Further details are provided in the Appendix.

Three-Variable LSQ Approach:

The least-squares procedure outlined in the previous subsection can be extended with a minimal increase in complexity to include a third variable, I_v . One additional assumption is require, which is that $I_{v,s}$ and $I_{v,\infty}$ are equal in magnitude. In practice, it was found that the three-variable LSQ method was relatively unstable (i.e., sometimes converged to non-physical values) compared to the 2-variable method and very sensitive to the initial guesses used.

Least-squares Results

To build confidence in this non-linear LSQ approach a series of tests were performed to evaluate the effect of changing the initial guesses for the parameters on the final converged values obtained by the two- and three-variable LSQ methods developed above. This involved using a random number generator to produce a

sequence of initial guesses between 0 and 1 for each parameter, and then applying the least squares technique outlined above to obtain converged values for a_0 and N . In the case of the three variable LSQ analysis converged values were also obtained for I_v , with the additional constraint that I_v must fall between 1% and 25% i.e., $0.01 \leq I_v \leq 0.25$. The results of this exercise are presented in Figure 2-5 a) and b) for two different zero pressure gradient film cooling data sets [140&187]. The ‘o’ symbols correspond to the initial random guesses for each parameter and the ‘x’ symbols indicate the converged values. The converged values indicated by the ‘◇’ symbol, that were closest to Simon’s [114] reported values for a_0 and N ($a_0 = 0.177$ and $N = 0.65$) indicated by the ‘□’ symbol, were chosen to be most ‘realistic’ (since this would correspond to a similar incompressible shear layer growth rate to that found in the data used by Simon) and therefore used for the PGFM analysis in each case.

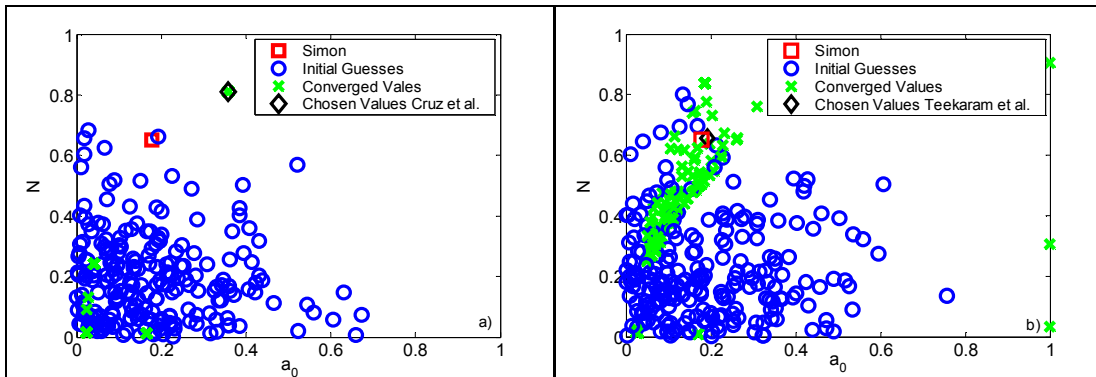


Figure 2-5 Range of predictions obtained for different initial guesses for a_0 and N : a) using the two-variable LSQ method for a wall-jet film under zero pressure gradient conditions ($R = 0.63$, $\lambda = 2.22$ and $TR = 0.71$); and b) using the three-variable LSQ method for the core-driven film under zero pressure gradient conditions ($R = 3.53$, $\lambda = 0.33$ and $TR = 0.8590$).

2.4.4 Experimental Data

Film cooling data from Cruz et al. [187] and Teekaram et al. [140] were used to validate the model’s predictions under zero pressure gradient and variable pressure gradient conditions respectively.

Isobaric Data

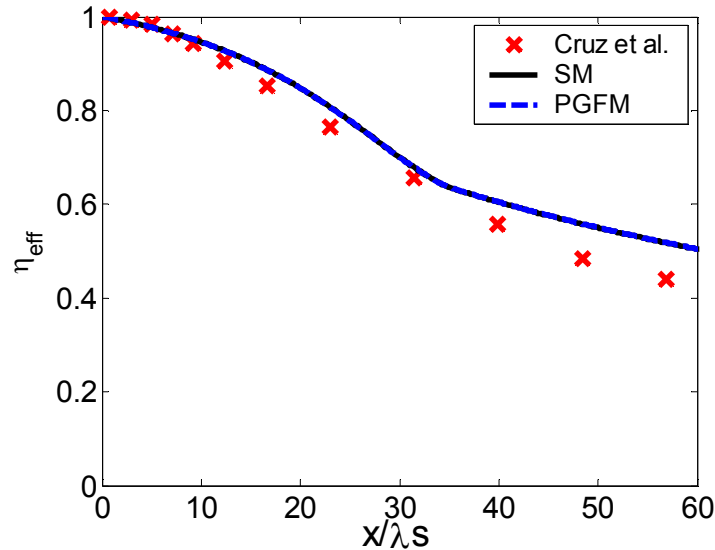


Figure 2-6 Film cooling efficiency, η_{eff} , as a function of non-dimensional stream-wise distance, x/λ_s , for an isobaric, turbulent wall-jet film ($R=0.63$) at $\lambda=2.22$ and $TR=0.71$, as predicted by the SM and PGFM.

Cruz et al. [187] reported film-cooling effectiveness as a function of downstream distance (x) in a subsonic hot wind tunnel facility. A wall-jet flow condition was used for model validation having a hot stream velocity of 20.0 m/s at a temperature of 431K and a coolant stream velocity of 31.5m/s at a temperature of 306K. LDV measurements indicated that the average coolant stream turbulence intensity, $I_{v,s}$, was 5.0% while the average hot stream turbulence intensity, $I_{v,\infty}$ was 1.6%. Using the least squares analysis described in §2.4.3, it was found that choosing $N = 0.8106$ and $a_o = 0.3585$ produced the best correspondence between the model and the experimental data. Figure 2-6 shows that with these assumptions, the SM (solid lines) and the PGFM (dashed lines) predict the experimentally measured film cooling effectiveness (symbols) to within an *rms* error of 2.1% of the experimentally measured values in the near slot region ($x/\lambda_s < 30$). The models do not perform as

well farther downstream of the slot (*rms* error of 6.8%) but are consistent with the data trend.

Non-isobaric Data

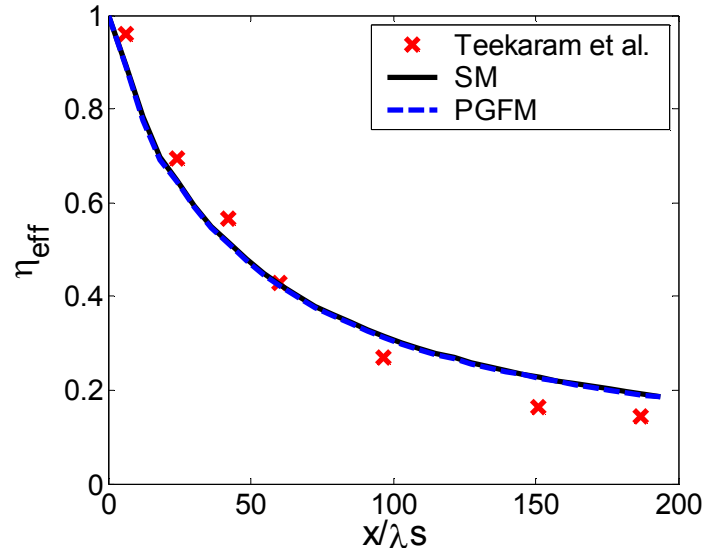


Figure 2-7 Comparison of film cooling effectiveness, η_{eff} , as a function of non-dimensional stream-wise distance, x/λ_s , predicted by the PGFM to experimental measurements by Teekaram et al. [140] for a turbulent core-driven film ($R_\theta = 3.53$) in the presence of a constant zero pressure gradient, at $\lambda = 0.33$, $TR = 0.86$.

Teekaram et al. [140] measured film cooling effectiveness under variable pressure gradient conditions using an isentropic light piston tunnel facility. Various contoured nozzles were used to produce adverse and favorable pressure gradients that varied with downstream distance. The hot stream flow Mach number was maintained between 0.5 and 0.6 near the injection point with a static temperature of 348K. The coolant injection Mach number was varied from 0.07 to 0.34 at a static temperature of 295K. This approach allowed blowing ratios between 0.15 and 0.75 to be achieved. Acceleration parameters ranging from $K_p = 2.62 \times 10^{-6}$ (favorable pressure gradient) to -0.22×10^{-6} (adverse pressure gradient) were achieved at the point of coolant injection. The average hot stream and coolant stream turbulence intensities were not reported in

this study so it was necessary to estimate $I_{v,\infty}$ and $I_{v,s}$ in addition to N and a_0 using the least square analysis procedure outlined in §2.4.3.

The results of the three-variable LSQ analysis performed for a wide range of initial guesses under zero pressure gradient conditions are summarized below in Table 2.1. The table shows that many different combinations of empirical constants and input parameters can produce close agreement between the PGFM predictions and Teekaram’s experimental findings. Therefore the values chosen to represent Teekaram et al.’s [140] data were, therefore, selected based on how consistent they were relative to Simon’s [114] empirical constants (i.e., $a_0 = 0.177$ and $N = 0.65$). This yielded a_0 , N and I_v , equal to 0.1915, 0.6567 and 0.024, respectively. The latter value for the effective average turbulence intensity is considered ‘reasonable’ since it falls well within the range $1\% \leq I_v \leq 5\%$, which is typical for experiments of this nature. Figure 2-7 shows that with these assumptions, the SM (solid lines) and the PGFM (dashed lines) predict the experimentally measured film cooling effectiveness (symbols) to within an *rms* error of 5.1% of the experimentally measured values.

I_v	a_0	N
0.0103	0.1525	0.4683
0.0109	0.2267	0.5721
0.0123	0.2216	0.5850
0.0150	0.1207	0.4524
0.0216	0.1158	0.4890
0.0235	0.1915	0.6567
0.029227	0.1456	0.6129
0.0323	0.1575	0.6605
0.0498	0.1855	0.8390

Table 2.1 Summary of empirical constants determined for the ZPG Teekaram et al. [140] data.

2.5 Results

2.5.1 Introduction

In this section the film cooling predictions of the new derived PGFM are explored under constant and variable pressure gradient conditions. In the latter case, which is more representative of conditions encountered in an actual rocket, a comparison with experimental data is also made.

2.5.2 Constant Pressure Gradient Results

Wall-jet film

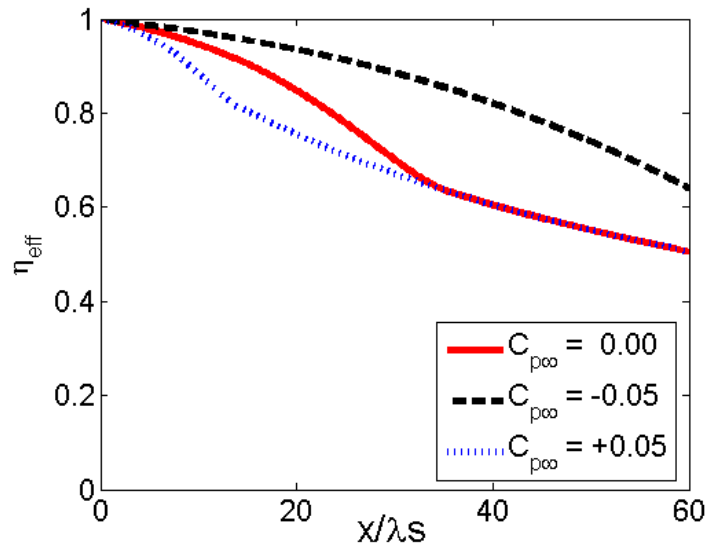


Figure 2-8 Film cooling effectiveness, η_{eff} , as a function of non-dimensional streamwise distance, x/λ_s , for a turbulent wall-jet ($R_\theta = 0.63$) undergoing a constant favorable pressure gradient ($C_{p_\infty} = -0.05$), a constant adverse pressure gradient ($C_{p_\infty} = +0.05$) and a constant zero pressure gradient ($C_{p_\infty} = 0.0$), at $\lambda = 2.22$ and $TR = 0.71$, as predicted by the PGFM.

Figure 2-8 is a plot of film cooling effectiveness predicted by the PGFM as a function of non-dimensional downstream distance for a turbulent wall-jet film in the presence of three different pressure gradients. The dashed line corresponds to a favorable pressure gradient ($C_{p_\infty} = -0.05$), the dotted line to an adverse pressure gradient ($C_{p_\infty} = +0.05$) and the solid line to the isobaric case ($C_{p_\infty} = 0.0$). The results

show that for a *wall-jet* film, the presence of an *adverse* pressure gradient *decreases* film cooling effectiveness - in this case by as much as 12.5%. In contrast, a favorable pressure gradient increases the effectiveness – in this case by as much as 30%.

Core-driven film

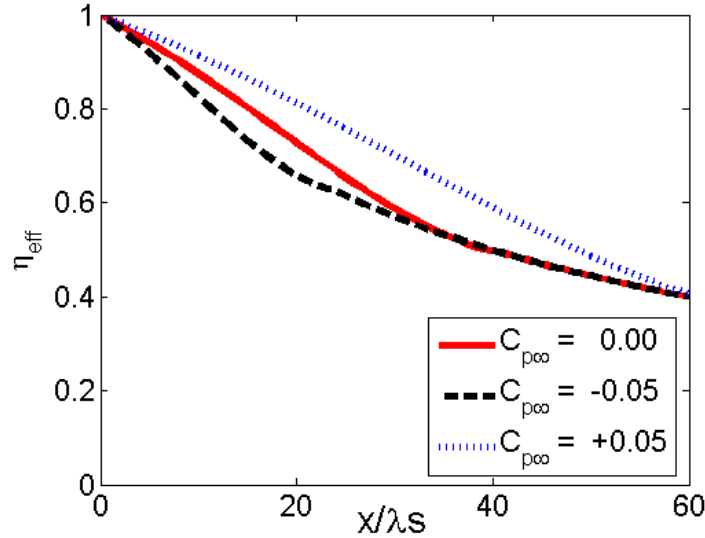


Figure 2-9 Film cooling effectiveness, η_{eff} , as a function of non-dimensional streamwise distance, x/λ_S , for a turbulent core-driven film ($R_\theta = 1.58$) undergoing a constant favorable pressure gradient ($C_{p_\infty} = -0.05$), a constant adverse pressure gradient ($C_{p_\infty} = +0.05$) and a constant zero pressure gradient ($C_{p_\infty} = 0.0$), at $\lambda=0.89$ and $TR=0.71$, as predicted by the PGFM.

Figure 2-9 is a plot of film cooling effectiveness predicted by the PGFM as a function of non-dimensional downstream distance for a turbulent core-driven film in the presence of three different pressure gradients. The dashed line corresponds to a favorable pressure gradient ($C_{p_\infty} = -0.05$), the dotted line to an adverse pressure gradient ($C_{p_\infty} = +0.05$) and the solid line to the isobaric case ($C_{p_\infty} = 0.0$). Note that the behavior reverses for a core-driven film. In this case, the presence of a favorable pressure gradient decreases the film cooling efficiency by as much as 10%. Meanwhile, the presence of an *adverse* pressure gradient actually *increases* the film cooling effectiveness, in this case by as much as 20%. Taken together, Figures 2-8 and 2-9 show that the effect of the pressure gradient reverses depending on whether

$R > 1$ or $R < 1$. This is important because it helps to explain some seemingly contradictory results in the literature. This will be addressed later. For the moment, let us consider why this reversal occurs.

2.5.3 Physical Explanation

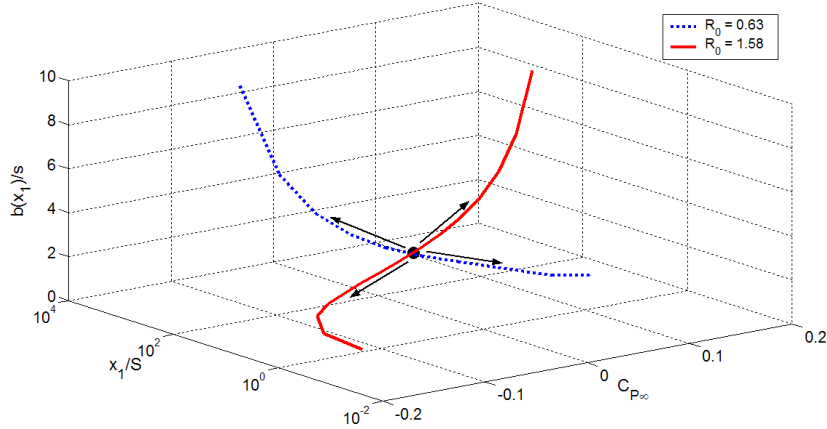


Figure 2-10 Non-dimensional shear layer impingement thickness, $b(x_1)/s$, versus non-dimensional initial region length x_1/s and non-dimensional pressure gradient C_{P_∞} , for a wall-jet film ($R_\theta = 0.63$) and a core-driven film ($R_\theta = 1.58$) at $TR = 0.71$.

Figure 2-10 shows the shear layer thickness at the impingement point, $b(x_1)/s$, as a function of the initial region length x_1/s , and the pressure gradient, C_{P_∞} , for a wall-jet film (dotted line) and a core-driven film (solid line). The figure shows that applying a favorable pressure gradient ($C_{P_\infty} < 0$) to a wall-jet film ($R < 1$) increases the length of the initial region as well as the thickness of the shear layer. The increase in x_1/s means that more of the wall is protected and an increase in $b(x_1)/s$ means that the hot free stream moves farther away from the wall. These effects combine to improve film cooling performance. In contrast, when a favorable pressure gradient is applied to a core-driven film ($R > 1$), x_1/s is reduced which means less of the wall is protected and $b(x_1)/s$ decreases which means that the hot flow is closer to the wall. Together, these

effects degrade cooling performance. The figure also shows that reducing the slot height, s , degrades performance in both types of jets by decreasing the length of the protected region and decreasing the thickness of the shear layer.

But why do the changes in x_l/s and $b(x_l)/s$ with $C_{p\infty}$ depend on whether R_θ is >1 or R_θ is <1 ? Equation (2.29) shows that the shear layer growth rate is the sum of two terms: a term k' that depends on the velocity ratio alone (Eq. (2.30)) and a term ℓ that depends on both the pressure gradient and the velocity ratio (Eq. (2.31)). k' is always positive. Figure 2-11 a) shows that ℓ can be positive or negative depending on the sign of $C_{p\infty}$ and whether or R_θ is >1 (solid line) or $R_\theta <1$ (dotted line). Figure 2-11 b) shows that the overall growth rate of the layer (i.e., $k'+\ell$) increases with $C_{p\infty}$ when $R_\theta <1$ (dotted line) and decreases when $R_\theta >1$ (solid line). Therefore, the reversal in the effect of the pressure gradient with R arises directly from the influence of the pressure gradient on the shear layer growth rate.

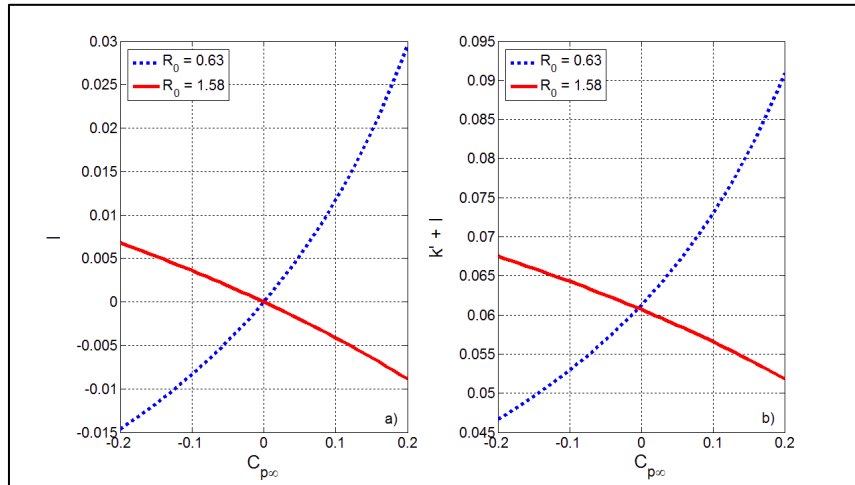


Figure 2-11 a) Change in the shear layer growth rate, ℓ , versus non-dimensional pressure gradient $C_{p\infty}$, for a wall-jet film ($R_\theta = 0.63$) and a core-driven film ($R_\theta = 1.58$). b) Overall shear layer growth rate, $k'+\ell$, versus non-dimensional pressure gradient $C_{p\infty}$, for a wall-jet film ($R_\theta = 0.63$) and a core-driven film ($R_\theta = 1.58$).

2.5.4 Variable Pressure Gradient Results

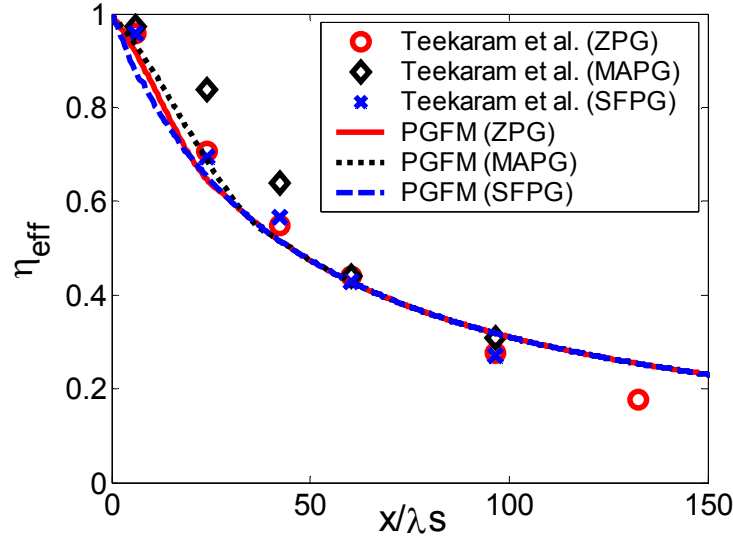


Figure 2-12 Film cooling effectiveness, η_{eff} , predicted by the PGFM as a function of non-dimensional streamwise distance, x/λ_s , for a turbulent core-driven film ($R_\theta = 3.53$) with a strong favorable pressure gradient ($K_p = 2.62 \times 10^{-6}$), a mild adverse pressure gradient ($K_p = -0.22 \times 10^{-6}$) and zero pressure gradient. $\lambda = 0.33$ and $TR = 0.86$.

Figure 2-12 shows film cooling effectiveness as a function of non-dimensional downstream distance for a turbulent core-driven film with three different acceleration parameters. $K_p = -0.22 \times 10^{-6}$ corresponds to a mild adverse variable pressure gradient (MAPG), $K_p = 2.62 \times 10^{-6}$ corresponds to a strong favorable variable pressure gradient (SFPG) and $K_p = 0$ corresponds to a constant zero pressure gradient (ZPG). The blowing ratio (λ) is 0.33 and the temperature ratio (TR) is 0.86. The solid line shows the model's predictions for a constant zero pressure gradient (ZPG); the dotted line shows the model's predictions for the mild adverse variable pressure gradient (MAPG) and the dashed line shows the predictions for the strong favorable variable pressure gradient (SFPG). The symbols show the corresponding experimental data from Teekaram et al. [140]. Despite the relatively weak influence of pressure gradient, the model captures the effect of K_p on effectiveness and matches the

magnitude with an rms error of 8.9%. Some of the discrepancy between the PGFM and the Teekaram et al.'s measurement may be attributable to the uncertainty in the turbulence conditions that were estimated earlier. A significant portion of the discrepancy, however, may be attributable to other physical effects like compressibility that are not accounted for in the PGFM. Compressibility is expected to be important here since the hot stream flow Mach numbers reported by Teekaram's experiments were between Mach 0.5 and 0.6.

2.5.5 Reconciling Anomalies in the Literature

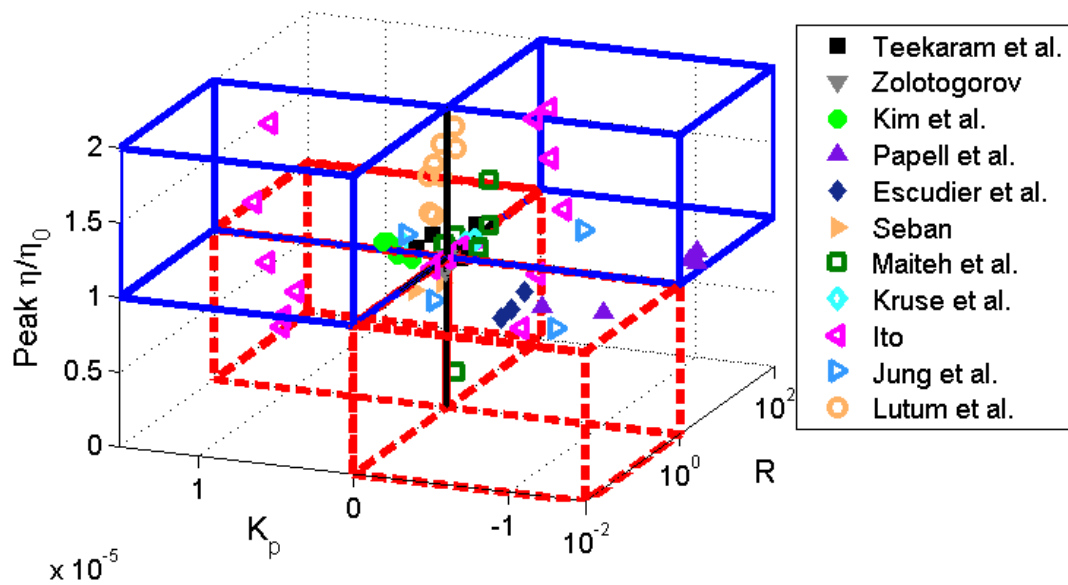


Figure 2-13 Peak non-dimensional film cooling effectiveness (η/η_0) as a function of acceleration parameter (Kp) and velocity ratio (R) reported in various studies.

One challenge in interpreting previous experimental measurements of film cooling effectiveness under variable pressure gradient conditions is reconciling apparent contradictions in the literature. For instance, Kruse [145] predicts that a favorable pressure gradient degrades film cooling performance; whereas, Kim et al. [154] predicts that it enhances performance. Which is correct? The predictions of the

PGFM model outlined above show that both are correct because Kruse’s experiment used a core-driven film ($R>1$) while Kim et al.’s experiment used a wall-jet film ($R<1$). This trend is confirmed by a more comprehensive analysis of data from ten studies [140, 145–154] presented in Fig. 2-13. The filled symbols correspond to 2-D slot injection studies, while the open symbols correspond to data from 3-D hole injection studies. The lower plane of the figure shows acceleration parameter and velocity ratio while the z-axis shows the change in film cooling performance relative to the peak effectiveness at the baseline zero pressure gradient case. According to the PGFM model whose predictions are summarized in Table 2.2, the data should group into four octants: Enhanced cooling performance when $K_p>0$ and $R<1$; enhanced cooling performance when $K_p<0$ and $R>1$; degraded cooling performance when $K_p<0$ and $R<1$; degraded cooling performance when $K_p>0$ and $R>1$.

	$K_p<0$	$K_p>0$
$R<1$	$\frac{\eta_{eff}}{\eta_{eff,0}} < 1$	$\frac{\eta_{eff}}{\eta_{eff,0}} > 1$
$R>1$	$\frac{\eta_{eff}}{\eta_{eff,0}} > 1$	$\frac{\eta_{eff}}{\eta_{eff,0}} < 1$

Table 2.2 Summary of PGFM predictions

These octants are highlighted in Fig. 2-13. The boxes outlined by the dashed red lines in Fig. 2-13 show the regions associated with degraded film cooling performance while the boxes outlined by the solid blue lines show the regions associated with enhanced film cooling performance. The PGFM model predicts that the remaining four octants should be vacant. This means that for a specified K_p and R , only an increase *or* a decrease in effectiveness is possible according to the PGFM model – not both. Since Fig. 2-13 shows that most of the experimental data lies

within the four octants predicted by the PGFM model, the model appears to capture the impact of K_p and R on film cooling effectiveness in a way that is consistent with most experimental measurements.

Interestingly, Fig. 2-13 shows that the model correlates both 2-D (solid symbols) and 3-D hole (open symbols) injection data despite the fact that the model was derived for 2-D configurations. This makes sense because the row of holes in a film cooling application is designed so that the individual fluid jets merge quickly to form an approximately two-dimensional layer that spans and protects the surface. The ability of the jets to merge to form the film depends, among other things, on the hole spacing and the number of rows. Table 2.3 shows that the hole spacing in four of the five 3-D injection studies reported in Fig. 2-13 is relatively small ($p/d \leq 4$) indicating that the jets would be able to merge quickly into an approximately 2-D film. It also shows that one of the two data sets that is not correlated by the model (Lutum et al. [148]) corresponds to a single row of holes and the largest p/d where one would expect it to be more difficult for individual jets to coalesce into a film. Therefore, this result indicates that the model can also be applied to ‘realistic’ 3-D injection geometries provided the holes are configured in a way that actually produces a film.

Study	p/d	Spacing Type	No. of Rows
Kruse et al. [145]	1.5	small	2
Maiteh et al. [149]	2	small	2
Lutum et al. [148]	3 & 6	moderate-large	1
Ito et al. [150]	3	moderate	1
Jung et al.[153]	4	moderate	2

Table 2.3 Summary of 3-D hole injection data.

Two studies [146 & 148] do not fit the pattern predicted by the PGFM. The first by Escudier et al. [146] examined film cooling effectiveness of a core-driven film under a very strong adverse pressure gradient and concluded that an adverse pressure gradient degrades film cooling performance. However, in these experiments the pressure gradients were so strong that the flow separated – a condition not accounted for in the PGFM and one that is generally avoided in film cooling applications because it substantially decreases the performance of the film. The second study by Lutum et al. [148] investigated film cooling performance of both wall-jet films and core-driven films on a concave surface with zero and favorable pressure gradients ($K_p=1.0 \times 10^{-6}$). It reported that favorable pressure gradients improved film cooling performance in both wall-jet films and core-driven films. However, different turbulence intensities were used for the zero ($I_{v,\infty} = 9\%$) and favorable pressure gradient ($I_{v,\infty} = 6\%$) cases. Since the turbulence intensity has a very strong influence on cooling performance, this fact alone could be responsible for the deviation from the model. The authors also introduced an unknown arbitrary scaling factor which further complicates interpretation of the results. Finally, as indicated earlier, the study used a single row of relatively widely spaced holes that would have more difficulty coalescing into a film that would be well-approximated by the 2-D model.

2.6 Conclusions

Simon's semi-empirical wall-jet film cooling model has been extended to include the effect of variation in the mainstream pressure gradient. The model predicts that the response of a cooling film to the pressure gradient depends upon the free stream to film velocity ratio R . For wall-jet films ($R > 1$), an adverse pressure gradient

decreases cooling performance while a favorable pressure gradient improves performance. For core-driven films ($R < 1$), the effect is reversed: An adverse pressure gradient improves performance while a favorable pressure gradient decreases it. This reversal is caused by the pressure gradient's influence on the shear layer growth rate which, in turn, influences its thickness and impingement point. In wall-jet films, a favorable pressure gradient decreases the shear layer growth rate thereby moving the impingement point downstream and increasing the shear layer thickness. This increases the cooling effectiveness. In core-driven films, a favorable pressure gradient decreases the shear layer growth rate, moves the impingement point upstream, and reduces the shear layer thickness thereby reducing cooling effectiveness. The model's predictions resolve most of the discrepancies in the literature regarding the effect of the pressure gradient on film cooling performance and correlate both 2-D slot and 3-D hole injection data. The latter is possible only when the hole injection scheme is 'well designed' i.e., when the individual jets merge into a film rapidly. This occurs when the hole spacing is small enough ($p/d \leq 4$) and/or if multiple rows of holes are used.

Chapter 3: The Influence of Density Gradients on Film Cooling Performance

3.1 Introduction

Another key fluid dynamic factor affecting film cooling performance is the presence of density gradients that arise as a result of large velocity differences and thermal gradients in the film cooling flow-field [13 & 14]. The literature review in §1.3 noted that the results of various experimental and theoretical investigations of the effects of density gradients on film cooling effectiveness are often contradictory [165–184]. Therefore this chapter will focus on understanding of the influence of density gradients on film cooling and resolving some of the disagreements in the open literature. This will be accomplished by extending the incompressible film cooling analysis developed by Simon to account for the effect of density gradients, that arise from both large velocity and thermal differences, on film cooling performance.

3.2 Background

It is useful to first consider how density gradients in film cooling flows are typically quantified and classified.

3.2.1 Quantifying Density Gradient Effects

Density gradients in film cooling flows can arise from either velocity differences, thermal differences or via some combination of the two. As a result three parameters are commonly used to quantify density gradient effects:

Average Convective Mach number

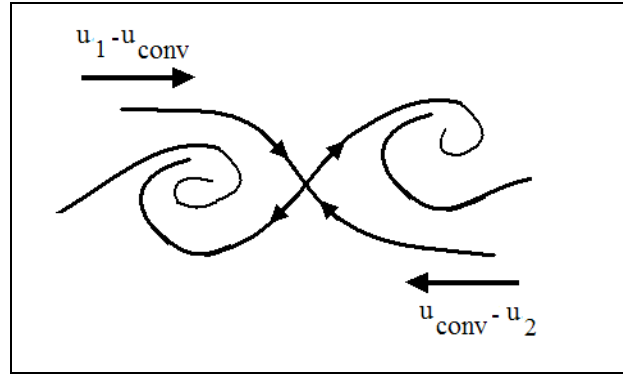


Figure 3-1 Schematic showing the isentropic model of large-scale structure in a compressible shear layer {adapted from Coles (1981) [191]}.

The convective Mach number (M_c) was proposed by Papamoschou et al. [66 & 70] as a means of correlating compressibility effects in mixing layer flows (of which film cooling flows are a subset). It is defined for each stream as follows:

$$M_{c1} = (u_1 - u_{conv})/a_1 \quad \text{Eq. (3.1)}$$

$$M_{c2} = (u_{conv} - u_2)/a_2 \quad \text{Eq. (3.2)}$$

where u_{conv} is the convective velocity of large scale structures relative to each stream (see Fig. 3-1); a_1 and a_2 are the speeds of sound in the primary and secondary streams respectively.

However, when $\gamma_1 = \gamma_2$, M_{c1} and M_{c2} are identical which leads to the following:

$$M_c = (u_1 - u_2)/(a_1 + a_2) \quad \text{Eq. (3.3)}$$

For simplicity, since the values of M_{c1} and M_{c2} only differ by a maximum of 13% for the majority of the experimental shear layer and film cooling studies that will be considered here, the 'average' convective Mach number obtained from Eq. (3.3) will be used in all cases.

Total Temperature Ratio

The total temperature ratio $\theta_0 = T_{0s}/T_{0\infty}$ was suggested by Abramovich [27] as a means of quantifying ‘thermal compressibility’ in mixing layers. Flows with total temperature ratios near unity exhibit weak thermal compressibility whereas flows with total temperature ratios far from unity exhibit strong thermal compressibility. Only studies in which $\theta_0 \leq 1$ are considered here since in practical film cooling applications, hot gas stream total temperatures are always equal to or greater than coolant stream total temperatures.

High Speed Stream Flow Mach number

The flow Mach number of the highest speed stream in the film cooling flow (M_{HS}) is another indicator of the influence of compressibility. In practice this is usually the mainstream Mach number, but in some cases it can be the coolant stream Mach number. All things being equal (i.e., if M_c and θ_0 are equal between two film cooling flows), the flow with the higher M_{HS} will experience a larger density gradient effect than the flow with the lower M_{HS} .

3.2.2 Quantifying the Magnitude of Density Gradient Effects

Regime	M_c	θ_0	M_{HS}
Weak	≤ 0.3	0.6 – 1.0	≤ 0.3
Moderate	0.3 – 1.0	0.3 – 0.6	0.3 – 1.0
Strong	>1.0	<0.3	>1.0

Table 3.1 Summary of the three compressibility regimes.

Three distinct compressibility ‘regimes’ in film cooling flows can be identified based on the values of the compressibility parameters defined previously (see Table

3.1). The ‘weak’ regime corresponds to low convective and flow Mach numbers, M_c , $M_{HS} \leq 0.3$, as well as near unity total temperature ratios, approximately in the range $0.6 \leq \theta_0 \leq 1$. In this regime, velocity and thermal compressibility effects are generally very small to negligible and the flow is essentially incompressible. The ‘moderate’ regime corresponds to convective and flow Mach numbers roughly in the range, $0.3 < M_c, M_{HS} \leq 1$ and total temperature ratios in the range $0.30 \leq \theta_0 < 0.60$. Here the effects of thermal and velocity compressibility are present and become more pronounced with increasing convective Mach number and decreasing total temperature ratio. The ‘strong’ compressibility regime corresponds to convective and flow Mach numbers greater than unity, i.e., $M_c, M_{HS} > 1$, and to total temperature ratios less than 0.3, i.e., $\theta_0 < 0.3$. In this regime compressibility effects are expected to be significant.

3.3 Effect of Density Gradients and Compressibility on Mixing Layer Growth Rate

3.3.1 Introduction

In the previous chapter, it was noted that one of the most important parameters influencing film cooling effectiveness is the mixing layer impingement length, x_l , which depends heavily on the growth rate of the mixing layer formed at the coolant-core stream interface. Consequently, the first step in the development of a model to predict the effect of density gradients and compressibility on film cooling effectiveness is to find a way to compute the growth rate of a compressible mixing layer. The second step is to extend Simon’s [114] incompressible model to account for the effect of density gradients and compressibility on film cooling performance.

3.3.2 Development of a Compressible Shear Layer Growth Rate Model

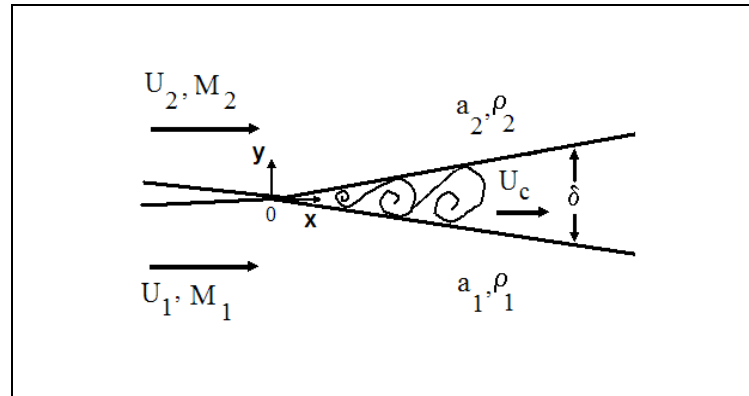


Figure 3-2 Compressible shear layer geometry and nomenclature {Adapted from Papamoschou et al. [190] (1997)}.

Figure 3-2 is a schematic illustration of the two-dimensional turbulent shear layer formed between two co-flowing streams in the absence of a streamwise pressure gradient. The figure shows a primary stream at temperature T_1 with velocity u_1 and initial average characteristic turbulent intensity I_{v1} , encountering a secondary stream at T_2 with velocity u_2 (where $u_2 < u_1$) and initial average characteristic turbulent intensity I_{v2} . The two streams meet at $x=0$ and a turbulent shear layer of thickness $b(x)$ develops and grows with streamwise distance x . This simplified physical picture is used to develop growth rate models for both incompressible and compressible shear layers.

Abramovich [27] followed the approach of Prandtl [192] to show that under incompressible conditions (and in the absence of a streamwise pressure gradient) the temporal growth rate of the shear layer $\frac{db}{dt}$ is proportional to the perturbation component of the transverse velocity v' which, in turn, is proportional to the transverse gradient of the longitudinal flow velocity:

$$\frac{db}{dt} \sim v' \sim \ell \frac{du}{dy} \quad (3.4)$$

In this expression ℓ is the turbulent mixing length. The transverse gradient of the longitudinal velocity at any point in the layer is proportional to the differences in velocities on the boundaries:

$$\frac{du}{dy} \sim \frac{u_1 - u_2}{b} \quad (3.5)$$

Assuming that the transverse velocity profiles at different downstream positions in the shear layer are self-similar [27], means that $\ell/b \sim \text{constant}$ giving the following expression for the temporal shear layer growth rate:

$$\frac{db}{dt} \sim u_1 - u_2 \quad (3.6)$$

Eq. (3.6) can be expressed in terms of the spatial growth rate ($\frac{db}{dx}$) using the chain rule:

$$\frac{db}{dt} = \frac{db}{dx} \frac{dx}{dt} \sim u_1 - u_2 \quad (3.7)$$

In this expression $\frac{dx}{dt}$ is the reference or characteristic velocity (u_c) in the shear layer, so Eq. (3.7) becomes:

$$\frac{db}{dx} = \pm \frac{c (u_1 - u_2)}{u_c} \quad (3.8)$$

The minus sign is taken when $u_2 > u_1$, c is a proportionality constant, and u_c is given by:

$$u_c = \frac{\int_{y_2}^{y_1} \rho u \, dy}{\int_{y_2}^{y_1} \rho \, dy} \quad (3.9)$$

Since the right hand side of Eq. (3.8) is a constant, the analysis predicts that the mixing layer grows linearly with downstream distance, a fact that has been confirmed experimentally in both compressible and incompressible turbulent shear layers [27].

Previous work [27] has developed expressions for incompressible shear layer growth by integrating Eq. (3.9) assuming various velocity distributions where the density is constant. In the compressible case considered here, however, one must account for both density and velocity variations across the shear layer. There are two ways to describe the velocity distribution through the shear layer.

Discontinuous Velocity Profile

An approximate expression for the characteristic velocity can be obtained using a weighted average between the two streams as proposed by Yakovlevskiy [193]:

$$u_c = \frac{\rho_1 u_1 + \rho_2 u_2}{\rho_1 + \rho_2} \quad (3.10)$$

Substituting Eq. (3.10) into Eq. (3.8) gives the following expression for the compressible shear layer growth rate:

$$\frac{db}{dx} = \pm \frac{c}{2} \frac{(1+S)(1-1/R)}{1+S/R} \quad (3.11)$$

where S is the density ratio ($S = \rho_2/\rho_1$) and R is the velocity ratio ($R = u_1/u_2$). The minus sign is taken when $R < 1$. Here u_1 is assumed to be always greater than u_2 so R will take values between 0 and 1.

Eq. (3.11) shows that the compressible shear layer growth rate depends on both the density and velocity ratio in the cross section of the shear layer. In the limit as $S \rightarrow 1$, Eq. (3.11) simplifies to Abramovich's incompressible result [27]:

$$\frac{db}{dx} = \pm c \frac{R-1}{R+1} \quad (3.12)$$

Continuous Velocity Profile

A more rigorous approach to finding the characteristic velocity is to assume that the velocity, static temperature, and total temperature profiles across the shear layer are universal [27] (i.e., independent of x) and can be expressed in terms of a similarity function $f(\xi)$. Abramovich proposed that the velocity profile through the layer is given by:

$$\frac{u_1 - u(y)}{u_1 - u_2} = f(\xi) \quad (3.13)$$

where the similarity variable ξ is defined as follows:

$$\xi = \frac{y - y_2}{y_1 - y_2} = \frac{y - y_2}{b} \quad (3.14)$$

The functional form of $f(\xi)$ is given by Schlichting [194]:

$$f(\xi) = \left(1 - \xi^{3/2}\right)^2 \quad (3.15)$$

Rearranging Eq. (3.13) leads to:

$$\frac{u(\xi)}{u_1} = \left[1 - \left(1 - \frac{1}{R} \right) f(\xi) \right] \quad (3.16)$$

At this point it is convenient to re-write Eq. (3.9) in dimensionless form.

Multiplying both sides of Eq. (3.9) by $\frac{\rho_1 b}{u_1 \rho_1 b}$ and noting that $dy = bd\xi$ leads to:

$$\frac{u_c}{u_1} = 1 - \left(1 - \frac{1}{R} \right) \frac{\int_0^1 \frac{\rho(\xi)}{\rho_1} f(\xi) d\xi}{\int_0^1 \frac{\rho(\xi)}{\rho_1} d\xi} \quad (3.17)$$

Since the static pressure is constant across the shear layer, the equation of state is used to relate the density ratio profile in Eq. (3.17) to the static temperature profile:

$$\frac{\rho(\xi)}{\rho_1} = \frac{MW(\xi)}{MW_1} \frac{T_1}{T(\xi)} \quad (3.18)$$

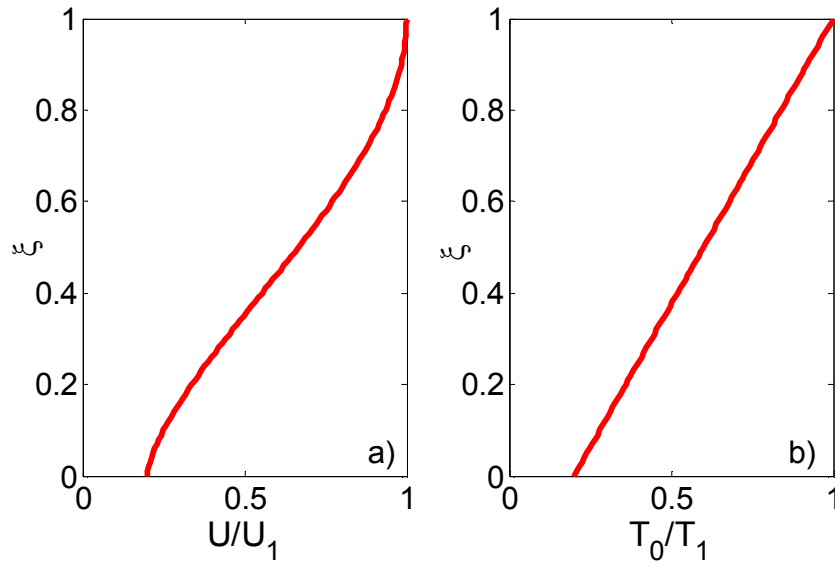


Figure 3-3 a) Mean non-dimensional velocity profile U/U_1 as a function of ξ for $r = 1/5$. b) Mean temperature profile T_0/T_1 as a function of ξ , for $\theta_0=5$.

The total temperature profile is represented using an empirical formulation by Zhestkov³:

$$\frac{T_{01} - T_0(\xi)}{T_{01} - T_{02}} = 1 - \xi \quad (3.19)$$

Rearranging Eq. (3.19) and letting $\theta_0 = \frac{T_{01}}{T_{02}}$ leads to:

$$\frac{T_0(\xi)}{T_{01}} = \frac{[1 + \xi(\theta_0 - 1)]}{\theta_0} \quad (3.20)$$

Figure 3-3 illustrates the forms of the assumed velocity and total temperature distributions through the layer as a function of the similarity coordinate.

The one-dimensional energy equation [186] is used to write the static temperature in terms of the total temperature, flow Mach number (M), and specific heat ratio (γ):

$$T = T_0 \left(1 + \frac{\gamma - 1}{2} M^2 \right)^{-1} \quad (3.21)$$

Inserting Eq. (3.20) and Eq. (3.21) into Eq. (3.18) gives:

$$\frac{\rho(\xi)}{\rho_1} = \frac{\sigma(\xi)\theta_0}{(1 + (\theta_0 - 1)\xi)} \left[\frac{1 + \frac{\gamma(\xi) - 1}{2} M(\xi)^2}{1 + \frac{\gamma_1 - 1}{2} M_1^2} \right] \quad (3.22)$$

where $\sigma(\xi) \equiv MW(\xi)/MW_1$.

Next, it is convenient to rewrite Eq. (3.22) in terms of the Mach number referenced to sonic conditions, M^* [186]. From the definition of M^* it can be shown that:

³ Unpublished work on two stream shear layer mixing (see Abramovich [27]).

$$1 + \frac{\gamma - 1}{2} M^2 = \left(1 - \frac{\gamma - 1}{\gamma + 1} M^{*2} \right)^{-1} \quad (3.23)$$

Inserting the definition of M^* into Eq. (3.22) gives:

$$\frac{\rho(\xi)}{\rho_1} = \frac{\sigma(\xi)\theta_0}{(1 + (\theta_0 - 1)\xi)} \left[\frac{1 - \frac{\gamma_1 - 1}{\gamma_1 + 1} M_1^{*2}}{1 - \frac{\gamma(\xi) - 1}{\gamma(\xi) + 1} M^*(\xi)^2} \right] \quad (3.24)$$

Writing $M(\xi)^*$ in terms of M_I^* , gives:

$$\frac{\rho(\xi)}{\rho_1} = \frac{\sigma(\xi)\theta_0}{(1 + (\theta_0 - 1)\xi)} \left[\frac{1 - \alpha_1 M_1^{*2}}{1 - \alpha(\xi) \chi(\xi) \sigma(\xi) \theta_0 M_1^{*2} \frac{\left[1 - f(\xi) \left(1 - \frac{1}{R} \right) \right]^2}{1 + (\theta_0 - 1)\xi}} \right] \quad (3.25)$$

where $\chi(\xi) \equiv \gamma_1/\gamma(\xi)$, $\alpha_1 = (\gamma_1 - 1)/(\gamma_1 + 1)$ and $\alpha(\xi) \equiv (\gamma(\xi) - 1)/(\gamma_1 + 1)$.

Next, by making the additional assumption that $\chi(\xi)$, $\gamma(\xi)$ and $\sigma(\xi)$ follow linear distributions through the shear layer as a function of ξ , as was assumed previously for the total temperature in Eq. (3.19), the following expression is obtained:

$$\frac{\rho(\xi)}{\rho_1} = \frac{[1 + \varphi(\xi)]\theta_0}{(1 + (\theta_0 - 1)\xi)} \left[\frac{1 - \alpha_1 M_1^{*2}}{1 - \frac{[1 - 1/\gamma_1 + \psi(\xi)]}{[1 + \psi(\xi)]} [1 + \varphi(\xi)] \theta_0 M_1^{*2} \frac{[1 - f(\xi)(1 - 1/R)]^2}{1 + (\theta_0 - 1)\xi}} \right] \quad (3.26)$$

where $\psi(\xi) \equiv (\xi - 1)(1 - \gamma_2/\gamma_1)$ and $\varphi(\xi) \equiv (\xi - 1)(1 - MW_2/MW_1)$.

The characteristic velocity can now be computed by substituting Eq. (3.26) into Eq. (3.17):

$$\frac{u_c}{u_1} = 1 - \left(1 - \frac{1}{R}\right) \frac{\int_0^1 \left[\frac{[1 + \varphi]\theta_0(1 - \alpha_1 M_1^{*2})}{(1 + (\theta_0 - 1)\xi) - \frac{[1 - 1/\gamma_1 + \psi]}{[1 + \psi]} [1 + \varphi]\theta_0 M_1^{*2} \left[1 - f(\xi) \left(1 - \frac{1}{R}\right)\right]^2} \right] (1 - \xi^{3/2})^2 d\xi}{\int_0^1 \frac{[1 + \varphi]\theta_0(1 - \alpha_1 M_1^{*2})}{(1 + (\theta_0 - 1)\xi) - \frac{[1 - 1/\gamma_1 + \psi]}{[1 + \psi]} [1 + \varphi]\theta_0 M_1^{*2} \left[1 - f(\xi) \left(1 - \frac{1}{R}\right)\right]^2} d\xi} \quad (3.27)$$

Unfortunately, computing the integrals in Eq. (3.27) analytically is non-trivial so we must therefore rely on numerical integration. This process is greatly simplified by treating the integrals in the numerator and denominator of the second term on the right hand side of Eq. (3.27) separately. Accordingly, two variables are defined for the denominator and numerator respectively:

$$A_0 = \int_0^1 \rho(\xi)/\rho_1 d\xi \quad (3.28)$$

$$A_1 = \int_0^1 f(\xi)\rho(\xi)/\rho_1 d\xi \quad (3.29)$$

The characteristic velocity in terms of A_0 , A_1 and u_1 is:

$$\frac{u_c}{u_1} = 1 + (1/R - 1)A_1/A_0 \quad (3.30)$$

The compressible shear layer growth rate can now be determined by substituting Eq. (3.30) into Eq. (3.8). This gives:

$$\frac{db}{dx} = \pm \frac{c}{2} \frac{(1 - 1/R)}{1 + (1/R - 1)A_1/A_0} \quad (3.31)$$

where c is the proportionality constant and the negative sign is taken when $R < 1$. In the limit as the flow becomes incompressible (i.e., $\theta_0 \rightarrow 1$ and $M_1^* \rightarrow 0$), $A_0 \rightarrow 1$, $A_1 \rightarrow 0.45$, and Eq. (3.31) simplifies (appropriately) to Abramovich's expression for the incompressible growth rate [27]:

$$\frac{db}{dx} = \pm c \frac{(1-1/R)}{1.1+0.9/R} \quad (3.32)$$

Determination of the Proportionality Constant

In the incompressible situation, it has been standard practice to adjust the value of the proportionality constant (c) to provide the best match to experimental data. Typical values for c in incompressible flows lie in the 0.1 to 0.5 range. However, we do not expect this to be the case in high Mach number flows where experiments show that compressibility effects suppresses turbulence levels [68 & 195] and hence mixing. Therefore, an inverse relationship between Mach number and c should be expected. Brown et al. [37], Korst et al. [196] and Channapragada [77] have all suggested that c is a function of the density ratio across the shear layer. Following the approach of Channapragada it can be assumed that:

$$c = c_{inc} \rho_2 / \rho_1 \quad (3.33)$$

where c_{inc} is set to Abramovich's [27] value of 0.27.

Assuming that the turbulent Prandtl number across the shear layer is near unity and following Korst et al. [196], we use Crocco's energy integral relationship to approximate the density ratio across the shear layer:

$$\rho_2 / \rho_1 \approx (1 - C_1^2) / (1 - C_2^2) \quad (3.34)$$

where C is the Crocco number which is defined as [77]:

$$C = \left[\frac{\gamma - 1}{2} M^2 \left/ \left(1 + \frac{\gamma - 1}{2} M^2 \right) \right. \right]^{1/2} \quad (3.35)$$

Inserting Eq. (3.34) and Eq. (3.35) into Eq. (3.33) yields the following expression for c :

$$c = 0.27 \left[\left(1 + \frac{\gamma_2 - 1}{2} M_2^2 \right) \left/ \left(1 + \frac{\gamma_1 - 1}{2} M_1^2 \right) \right. \right] \quad (3.36)$$

Eq. (3.36) appears to have the proper qualitative behavior: increasing the primary stream Mach number (M_1) reduces the value of c (since $M_2 < M_1$) which means that the growth rate decreases with increasing convective Mach number (as is observed experimentally). In addition, c also reduces to the incompressible value in the limit of $M_2, M_1 \rightarrow 0$.

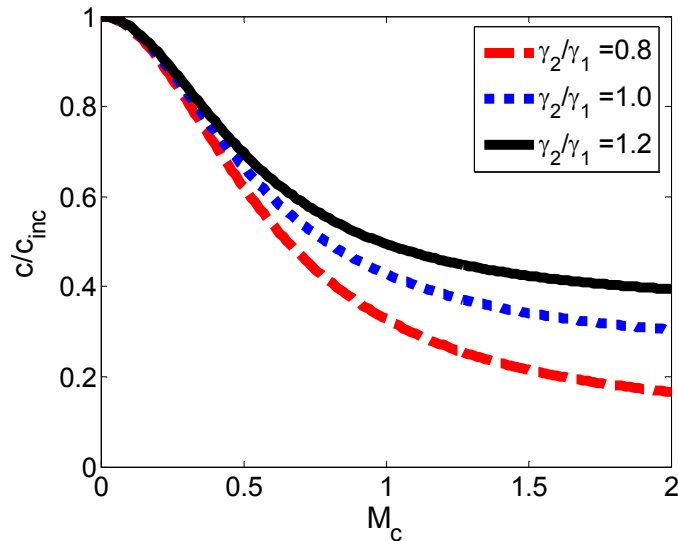


Figure 3-4 Effect of convective Mach number, M_c , on the proportionality constant ratio, c_{comp}/c_{inc} at a fixed density and velocity ratio, $S = 1.0$ and $R = 2.0$, for various gas mixtures. $\gamma_2/\gamma_1 = 0.8$ corresponds to an acetone-air mixture, $\gamma_2/\gamma_1 = 1.0$ corresponds to an air-air mixture and $\gamma_2/\gamma_1 = 1.2$ corresponds to a helium-air mixture.

Figure 3-4 shows c/c_{inc} as function of the convective Mach number, M_c , for gas streams with three different specific heat ratios at a fixed density and velocity ratio, $S = 1.0$ and $R = 2.0$. The figure shows that both the convective Mach number and the chemical composition of the streams can have significant impacts on the shear layer growth rate through the proportionality constant.

Normalized Compressible Growth Rate Model Formulation

Compressible growth rates are usually presented in non-dimensional form by normalizing the experimentally measured compressible growth rate with an estimate of the corresponding incompressible growth rate. These estimates usually come from Brown's [37] temporal incompressible growth rate model, which is given by:

$$\delta'_{inc} = \pm \frac{c}{2} \frac{(1-1/R)(1+\sqrt{S})}{(1+\sqrt{S}/R)} \quad (3.37)$$

Note that in the above equation the growth rate notation has been changed from db/dx to δ' to be consistent with the nomenclature commonly used in experimental mixing layer studies. The main difference between Eq. (3.37) and Abramovich's incompressible growth rate expressions in Eq. (3.32) and (3.12) is in the effect of the density ratio on the growth rate. In Abramovich's model density ratio effects are neglected whereas in Brown's model a weak dependence of the density ratio on the growth rate is assumed. However, in the limit as $S \rightarrow 1$ Eq. (3.37) simplifies to Abramovich's incompressible growth rate expression [27]. Therefore Eq. (3.37) will be utilized to normalize estimates of the compressible growth rate. This leads to two approaches based on the preceding analysis.

Discontinuous Velocity Model (DVM)

Combining Eq. (3.11) and Eq. (3.37) with Eq. (3.36) leads to the following expression for the shear layer growth rate when the velocity profile across the mixing layer is discontinuous:

$$\frac{\delta'_{comp}}{\delta'_{inc}} = \left[\left(1 + \frac{\gamma_2 - 1}{2} M_2^2 \right) / \left(1 + \frac{\gamma_1 - 1}{2} M_1^2 \right) \right] \frac{(1 + \sqrt{S}/R)(1 + S)}{(1 + S/R)(1 + \sqrt{S})} \quad (3.38)$$

Continuous Velocity Model (CVM)

Combining Eq. (3.31) and Eq. (3.37) with Eq. (3.36) gives an expression for the normalized compressible shear layer growth rate when the velocity profile across the mixing layer varies smoothly as per Eq. (3.16) and the temperature profile across the mixing layer is linear as per Eq. (3.20):

$$\frac{\delta'_{comp}}{\delta'_{inc}} = \left[\left(1 + \frac{\gamma_2 - 1}{2} M_2^2 \right) / \left(1 + \frac{\gamma_1 - 1}{2} M_1^2 \right) \right] \frac{(1 + \sqrt{S}/R)}{[1 + (1/R - 1)A_1/A_0](1 + \sqrt{S})} \quad (3.39)$$

Un-Normalized Growth Rate Model Formulation

Incompressible Growth Rate Model (IGM)

Eq. (3.37) with $c_{inc} = 0.27$, yields an expression for the incompressible growth rate:

$$\delta'_{inc} = 0.135 \frac{(1 - 1/R)(1 + \sqrt{S})}{(1 + \sqrt{S}/R)} \quad (3.40)$$

Compressible Growth Rate Model (CGM)

Combining Eq. (3.31) and Eq. (3.36) leads to the following expression for the compressible growth rate when the velocity profile across the mixing layer is continuous:

$$\delta'_{comp} = 0.135 \left[\left(1 + \frac{\gamma_2 - 1}{2} M_2^2 \right) / \left(1 + \frac{\gamma_1 - 1}{2} M_1^2 \right) \right] \frac{\left(1 - \frac{1}{R} \right)}{1 + \left(\frac{1}{R} - 1 \right) A_1 / A_0} \quad (3.41)$$

3.3.3 Numerical Integration Procedure:

A_0 and A_1 are determined by approximating the integrals in Eq. (3.28) and Eq. (3.29) using an N-point Gauss-Legendre quadrature rule [197]:

$$\int_0^1 f(x) dx = \frac{1}{2} \sum_{i=1}^N w_i f\left(\frac{1}{2} x_i + \frac{1}{2}\right) + R_n \quad (3.42)$$

where $f(x)$ is the function being integrated, x_i are the i^{th} roots of orthogonal Legendre polynomials $P_n(x)$, w_i are the weights for $i=1, \dots, N$ such that $w_i = 2 / \left[(1 - x_i)^2 (P'_n(x_i))^2 \right]$ and R_n is the residual. This quadrature method was selected because it is typically more accurate as well as converges more quickly than other numerical integration methods [198].

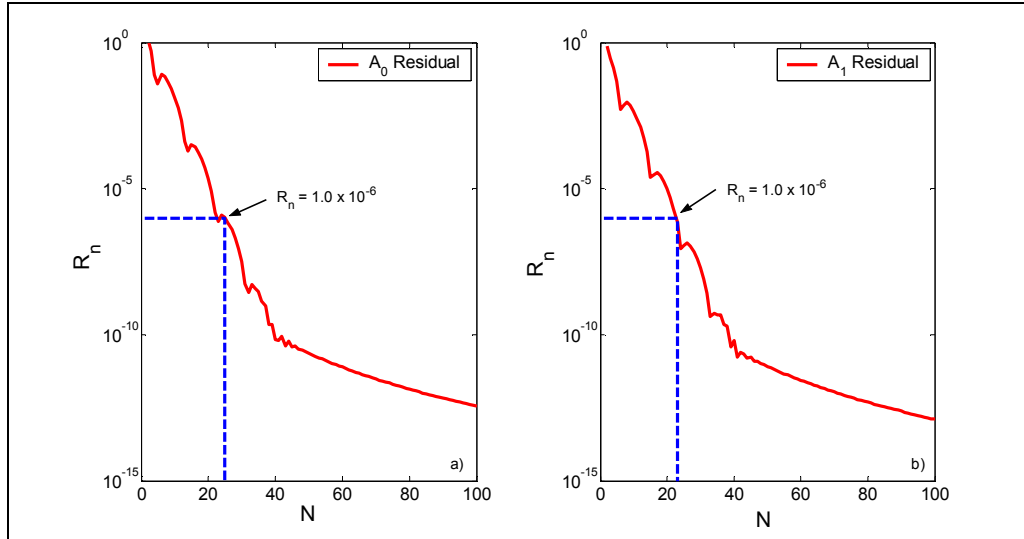


Figure 3-5 Residual (R_n) as a function of the number of points (N) associated with the Gauss-Legendre quadrature of: a) A_0 and b) A_1 for the $M_c = 0.96$ test case by Hall [199].

Figure 3-5 a) and b) show sample plots of the residual (R_n) as a function of N associated with the Gauss-Legendre quadrature of A_0 and A_1 for the $M_c = 0.96$ test case explored by Hall [199]. The residual is estimated following Stoer et al. [198], as the difference between the approximation to the integral at a given order, n and at the order $n-1$. In this work N is chosen to ensure that R_n in Eq. (3.42) is always less than 1.0×10^{-6} in each case. The figure shows $N = 25$ is sufficient to ensure convergence in the $M_c = 0.96$ test case.

3.3.4 Comparison to Experimental Data

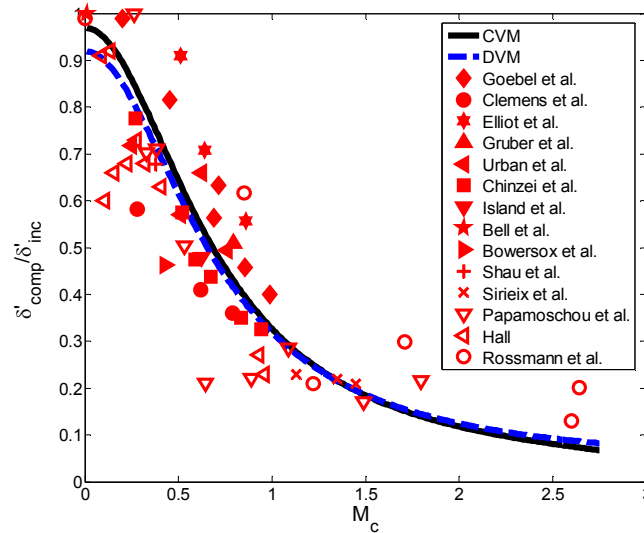


Figure 3-6 Normalized compressible mixing layer growth rate, $\delta'_{comp}/\delta'_{inc}$, as function of convective Mach number, M_c , for a homogeneous air shear layer at various density and velocity ratios. The predictions of the CVM and DVM are based on fixed density ratio, $S = 0.5$ and a constant velocity ratio, $R = 4.0$.

Figure 3-6 compares the normalized mixing layer growth rates predicted by the CVM and DVM (solid and dashed lines respectively) to experimental data from several studies [70,195,199–211] (symbols). The filled symbols correspond to data from homogeneous (air) studies, and the open symbols to data from heterogeneous (i.e., involving a mixture of two or more different gases) studies taken at various density and velocity ratios. The model predictions are based on a homogeneous air mixing layer at a fixed density and velocity ratio of 0.5 and 2.0 respectively. The model and data appear to be in reasonable qualitative agreement. Both show that increasing the convective Mach number decreases the non-dimensional shear layer growth rate and that the rate of decrease is more rapid for $0.2 < M_c < 1.0$ and more gradual for $M_c > 1.0$ and $M_c < 0.2$. This trend is also consistent with the observation that the shear layer growth rate decreases with increasing compressibility.

The scatter in the data can be attributed to several factors. First, the data were taken at different density and velocity ratios, while the predictions of the CVM and DVM are made at a fixed velocity and density ratio. Second, as pointed out by Birch et al. [23] some of the experimental data may have been taken in under-developed shear layers (i.e., transitional or developing mixing layers) in which the mean velocity profile is not self-similar and the shear stress is not constant. This can lead to inaccurate shear layer growth rate estimates. Third, as pointed out by Urban et al. [202] and Barone et al. [212], the different definitions of the mixing layer thickness (e.g., vorticity, pitot and visual thickness) used by various investigators can lead to significant differences in estimates of the non-dimensional compressible mixing layer thickness. Fourth, several researchers [213–215] have shown that the initial turbulent state of the shear layer can have a strong influence on shear layer development. Since neither the DVM nor the CVM account for this, and turbulence levels can vary considerably from one experiment to another, this may also contribute to some of the observed scatter. Fifth, there are uncertainties in the experimental data themselves which are on the order of 5% to 10%. Finally, while most of the experimental data are for homogeneous (air) mixing layers, some (open symbols) correspond to heterogeneous mixing layers.

The next step is to assess how well the models perform in a quantitative comparison with experimental data. To do this the model's predictions of the variation of non-dimensional compressible mixing layer growth rate, $\delta'_{comp}/\delta'_{inc}$, with convective Mach number are compared to homogeneous (air) mixing layer data [195,

202–211], followed by a comparison to heterogeneous mixing layer data [70,199–203].

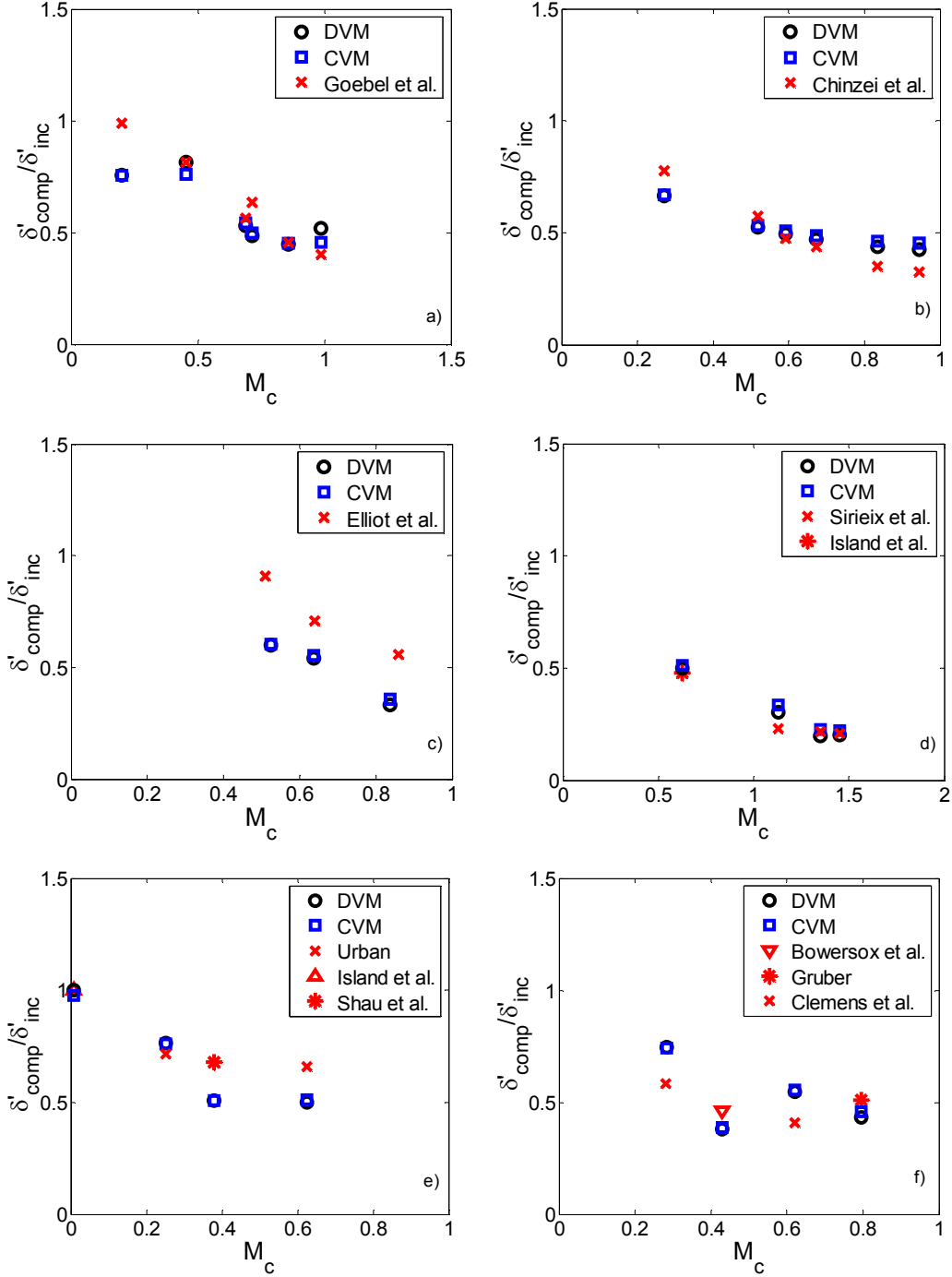


Figure 3-7 a)-f) Variation of normalized shear layer growth rate, $\delta'_{comp}/\delta'_{inc}$, with convective Mach number, M_c , for the conditions explored in various homogeneous (air) shear layer studies [195, 202-211].

The square and circular symbols in Figure 3-7 correspond to the predictions of the CVM and DVM respectively while experimental data are shown using ‘x’, ‘*’ and ‘Δ’ symbols. Figure 3-7 shows that in almost all cases the DVM and CVM predict trends in the data correctly. The quantitative differences between the model and experiment lie between 2.5% and 31.6% for the CVM and between 0.02% and 32.7% for the DVM (see Table 3.2). In addition, the overall average quantitative differences are 17.8% and 17.6% for the CVM and DVM respectively, which is considerably better than the range implies.

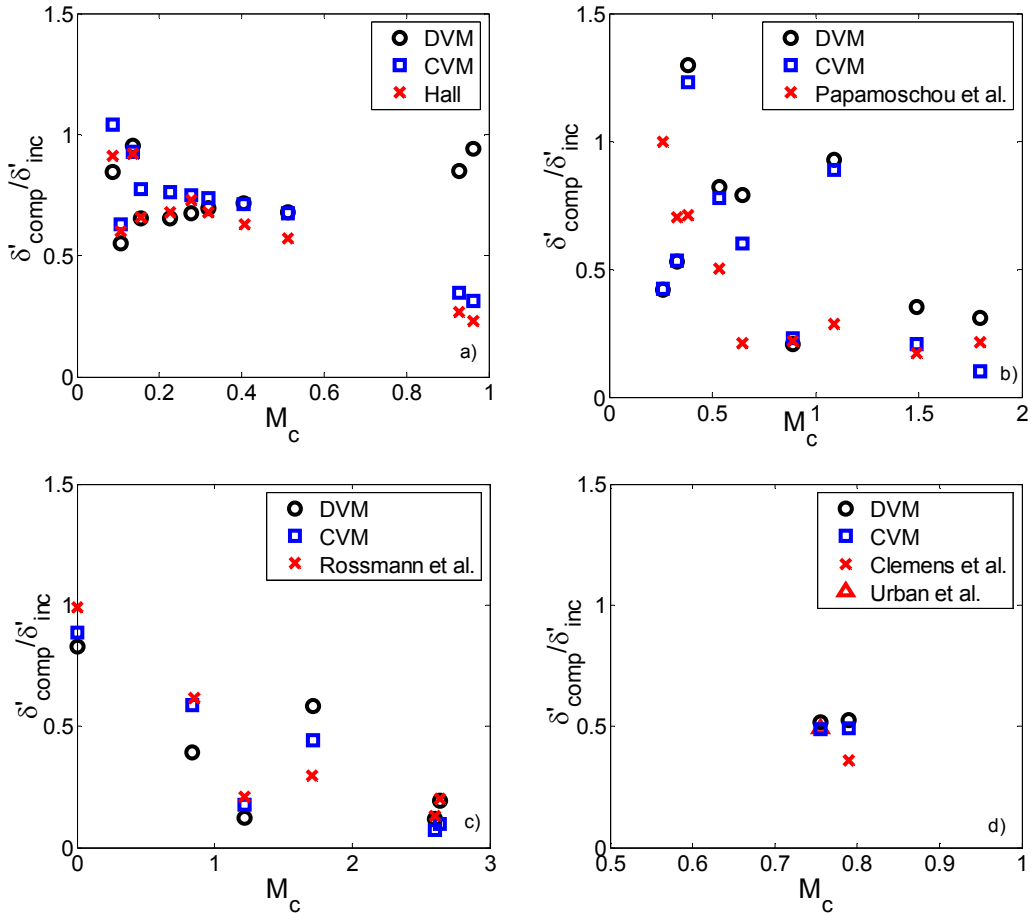


Figure 3-8 a)-d) Variation of normalized shear layer growth rate, $\delta'_{comp}/\delta'_{inc}$, with convective Mach number, M_c , for the conditions explored in various heterogeneous shear layer studies [70,199-203].

Figure 3-8 a)-d) compares predicted normalized growth rates to experimental measurements from various heterogeneous shear layer studies [70,199–203]. The square symbols correspond to the CVM predictions, the circular symbols to those of the DVM, and the ‘x’, and ‘Δ’ symbols to the experimental data. Figures 3-8 a) and c) show good qualitative and quantitative agreement between the CVM and the data with average differences of 14.1% and 28.2%, respectively. In contrast, the DVM shows only fair quantitative agreement with the data, yielding average differences of 52.7% and 46.6% respectively for the same studies. The main reason for the difference between the CVM and DVM models is the fact that the CVM accounts for the distribution of specific heat and molecular weight ratio across the shear layer (by assuming a linear profile), whereas the DVM neglects this variation. In Figure 3-8 d) the agreement between the models and data is only fair, while in Figure 3-8 b) the models fail completely.

The poor agreement with experimental data in this latter case may be partly as a result of the presence of an adverse streamwise pressure gradient in the near-field of the test section, which the authors of the study also noted became more adverse with increasing primary stream Mach number. Since previous work has shown that shear layer growth rates are very sensitive to pressure gradients [216–217] this may be a plausible explanation for the difference. Other factors contributing to the discrepancies are experimental uncertainty and the initial turbulent state of the shear layer. Also, while most studies report normalized growth rate (i.e., measured growth rate normalized by incompressible growth rate), the correlation used to estimate the

incompressible growth rate is rarely described in detail which makes it hard to back out absolute growth rates that can be compared to the model's predictions.

Study	Gas Combinations Used	Growth Rate Definition	No. Data Points	DVM Avg. Relative Error %	CVM Avg. Relative Error %
Papamoschou et al. [70]	argon-argon helium-nitrogen helium-argon nitrogen-nitrogen nitrogen-argon	Pitot thickness	9	97.5	53.8
Hall [199]	helium-nitrogen helium-argon nitrogen-nitrogen nitrogen-argon-helium	Visual thickness	11	52.7	14.1
Rossmann et al. [200-201]	argon-helium argon-carbon dioxide	Visual thickness	6	46.6	28.2
Urban et al. [202]	air-air argon-air	Energy thickness	2 1	15.5 4.3	14.1 1.5
Clemens et al. [203]	air-air argon-air	Visual thickness	2 1	30.9 45.2	31.6 36.4
Sirieux et al. [204]	air-air	Vorticity thickness	3	15.5	17.8
Goebel et al. [205]	air-air	vorticity thickness	6	14.1	11.7
Chinzei et al. [206]	air-air	energy thickness	6	15.3	18.4
Island et al. [207]	air-air	Visual thickness	1	4.0	6.8
Bell et al. [208]	air-air	Energy thickness	1	0.02	2.5
Bowersox et al. [209]	air-air	Energy thickness	1	17.9	16.2
Shau et al. [210]	air-air	Pitot thickness	1	25.4	25.3
Gruber [211]	air-air	Vorticity thickness	1	15.0	10.3
Elliot et al. [195]	air-air	vorticity thickness	3	32.7	30.5
Overall [69,195,199-211]	homogeneous studies heterogeneous studies all studies	Various Methods	27 28(19 [†]) 55(46 [†])	17.6 63.8(47.9 [†]) 41.1(30.1 [†])	17.8 30.2(19.1 [†]) 24.1(18.3 [†])

Table 3.2 Summary of average relative errors in the normalized growth rate predictions of the CVM and DVM for all of the experimental data examined [70,195,199-211]. [†]without data from [70].

Table 3.2 summarizes the comparison of the model predictions to experimental data. The overall average relative difference between the experimental data and the CVM and DVM is 24.1% and 41.1%, respectively. However, if the data by Papamoschou et al. [70] is omitted, the average difference drops to 18.3% and 30.1% respectively. Figure 3-9 summarizes these results graphically where the dashed lines bound the space corresponding to relative discrepancies of $\pm 20\%$ or less with respect to experimental data.

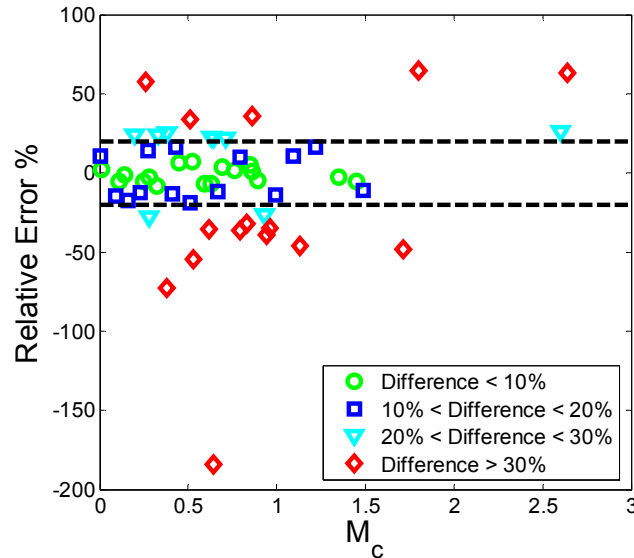


Figure 3-9 Per cent Relative Error in the CVM predictions of normalized mixing layer growth rate as a function of convective Mach number, M_c , for all of the experimental data examined [70,194,198-210].

Figure 3-9 shows that the majority of the data fall within the $\pm 20\%$ range. While at first glance the discrepancies between the CVM's predictions and experimental data may appear relatively large, upon reflection they are not so bad. First, uncertainties in the experimental data themselves are on the order of 5% to 10%. Second, there is no 'agreed upon' standard for measuring shear layer growth rate so a wide variety of growth rate definitions are used (e.g., visual thickness, pitot thickness, etc., see Table 3.2). This makes it difficult to make quantitative

comparisons between different data sets. While reporting the normalized growth rate is one way to try to overcome this, it seems inevitable that different studies will measure different growth rates under otherwise identical conditions. Third, in most studies the incompressible growth rate used to normalize the measured compressible growth rate is estimated using a growth rate correlation. As a result, the normalized growth rate depends heavily upon the choice of growth rate constant and correlation used. Fourth, the overall average relative error between the CVM predictions and experiment of 24.1% is consistent with errors reported from numerical simulations of compressible shear layers [212 & 218]. Taken together therefore, the CVM appears to be a useful tool for predicting normalized compressible shear layer growth rates.

3.4 Analysis

3.4.1 Introduction

Having established a reasonable method for predicting the compressible mixing layer growth rate, attention is now placed on the development of a film cooling model that is capable of accounting for the effects of density gradients and compressibility on film cooling effectiveness. As a starting point for this analysis, it is useful return to the physical picture of the film cooling flow proposed by Simon [114] in his incompressible film cooling analysis.

3.4.2 Compressible Film Cooling Model Development

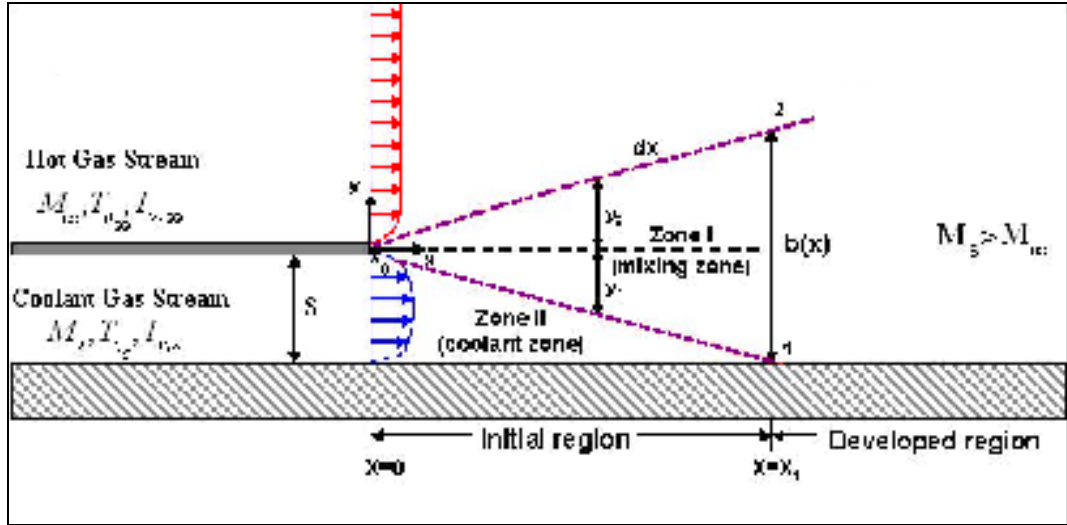


Figure 3-10 Wall-jet film cooling model {Adapted from Simon [114] (1986)}.

Figure 3-10 is a schematic illustration of the wall-jet film cooling model proposed by Simon [114]. The figure shows a coolant stream at a temperature, T_{0s} , and Mach number, M_s , being injected near the wall, from a slot of height, s . At x_0 , the coolant stream encounters a hot gas stream of temperature, $T_{0\infty}$ (with $T_{0\infty} > T_{0s}$), moving at a velocity, M_{∞} , where $M_{\infty} < M_s$. A weakly turbulent shear layer of thickness b develops and grows with streamwise distance x at the interface between the coolant and hot gas streams. The length of the initial developing region, x_1 , is once again taken to be the distance required for the inner edge of the developing mixing zone, labeled Zone I in Fig. 3-10, to reach the wall.

Following the approach of Simon [114], the adiabatic wall temperature in the initial region ($x < x_1$), T_{aw} , is assumed to equal the mean fluid total temperature in Zone II (coolant zone) while in the developing region the adiabatic wall temperature is assumed to equal the mean fluid total temperature in Zone I. Hence:

$$T_{aw} = \begin{cases} \bar{T}_{0II}, & (x < x_1) \\ \bar{T}_{0I}, & (x \geq x_1) \end{cases} \quad (3.43)$$

The following assumptions are also made:

- 1) The change in the specific heat with temperature is small.
- 2) The hot gas stream total temperature, $T_{0\infty}$, is constant.
- 3) Thermal radiation from the hot gas stream is negligible.
- 4) The shear layer growth, b , is linear.
- 5) No pressure gradient is present.

Under compressible conditions, the film cooling effectiveness is typically defined in terms of the recovery temperature [6]:

$$\eta_{eff} = \frac{T_{r\infty} - T_{aw}}{T_{r\infty} - T_{rs}} \quad (3.44)$$

Since the recovery temperature is usually very close to the stagnation temperature, it is common practice to approximate the effectiveness as [172]:

$$\eta_{eff} \approx \frac{T_{0\infty} - T_{aw}}{T_{0\infty} - T_{0s}} \quad (3.45)$$

As in the pressure gradient and incompressible cases, a mass and energy balance on the coolant stream shown in Fig. 3-10 following Stollery et al. [112] shows that the film cooling effectiveness is related to the amount of hot stream gas entrained by the coolant stream:

$$\eta_{eff} = \frac{\dot{m}_s}{\dot{m}_f} \quad (3.46)$$

In this expression, \dot{m}_s is the coolant mass flow rate per unit length, $\dot{m}_s = \rho_s U_s s$, and \dot{m}_f is the total mass flow rate of the film per unit length at any arbitrary x -location downstream of the coolant slot exit. Note that \dot{m}_f is the sum of

both the coolant mass flow rate per unit length and the entrained hot gas stream rate per unit length, \dot{m}'_e :

$$\dot{m}_f = \dot{m}_s + \int_0^x \dot{m}'_e dx \quad (3.47)$$

Following Juhasz et al. [108], \dot{m}'_e is assumed to be directly proportional to the hot gas stream mass flux:

$$\dot{m}'_e = C'_{M_0} \rho_\infty a_\infty M_\infty \quad (3.48)$$

C'_{M_0} is an 'effective' turbulent mixing coefficient which is a function of the average flow-field turbulence intensity, I_v .

Substitution of Eqs. (3.47) and the definition of \dot{m}_s into Eq. (3.46) yields the correlation:

$$\eta_{eff} = \left[1 + \left(\frac{x}{\lambda s} \right) C'_{M_0} \right]^{-1} \quad (3.49)$$

λ is the blowing ratio which is defined as the ratio of the coolant stream to hot stream mass flux:

$$\lambda = \rho_s M_s a_s / \rho_\infty M_\infty a_\infty \quad (3.50)$$

Equation (3.49) gives the functional form for a basic turbulent film cooling correlation. It shows that film cooling effectiveness decreases with increasing streamwise distance, with decreasing blowing ratio, with decreasing slot height, and with increasing turbulence intensity.

The ‘effective’ turbulent mixing coefficient C'_{M_0} , is defined following Simon’s [114] approach in terms of a turbulent mixing coefficient, C_{M_0} , and a turbulent diffusion parameter, χ :

$$C'_{M_0} = \frac{C_{M_0} - \chi \left(\frac{x}{\lambda_s} \right)^{-1}}{1 + \chi} \quad (3.51)$$

The parameter χ in Eq. (3.51) accounts for turbulent diffusion from zone I to zone II in the initial region ($x < x_1$) only and $\chi=0$ in the developed region ($x \geq x_1$). The turbulent diffusion parameter is given by:

$$\chi = \left\{ C_{M_0} \left(\frac{x}{\lambda_s} \right) + \left(\frac{x}{x_1} \right) - E_0 I_{v,s}^* \left(T_{0s} / T_{aw_{x=x_1}} \right) \ln \left[1 / \left(1 - x / x_1 \right) \right] \right\} \left(\frac{T_{aw_{x=x_1}} - T_{aw}}{T_{0\infty} - T_{0s}} \right) \quad (3.52)$$

where E_0 is an empirically determined constant.

Continuing in an analogous manner to Simon [114], an expression for C'_{M_0} in terms of C_{M_0} and χ can be found by assuming that C_{M_0} is a function of the shear layer growth rate (db/dx). This growth rate can be directly related to I_v by utilizing Abramovich’s [27] empirical assumption that db/dx is proportional to the perturbation-component of the fluctuating hot gas stream velocity (v'_i). This leads to:

$$C_{M_0} = db/dx = d_0 v'_i / u_c \quad (3.53)$$

where d_0 is an empirical constant and u_c is the characteristic velocity of the shear layer given by:

$$u_c = \frac{\int_{y_2}^{y_1} \rho u \, dy}{\int_{y_2}^{y_1} \rho \, dy} \quad (3.54)$$

An approximate expression for u_c can be obtained by using a weighted average between the two streams as proposed by Yakovlevskiy [193]:

$$u_c = \frac{\rho_\infty a_\infty M_\infty + \rho_s a_s M_s}{\rho_\infty + \rho_s} \quad (3.55)$$

It is important note here that Eq. (3.55) is essentially identical to Eq. (3.10), which underscores the fact that a similar approach is used here to that applied earlier for the shear layer analysis. Next, by substituting Eq. (3.55) into Eq. (3.53), simplifying by utilizing the fact that $I_v = \frac{v'_i}{M_\infty a_\infty}$, and incorporating Eq. (3.50) yields an expression for C_{M_0} which can be written as:

$$C_{M_0} = d_0 (I_v \sigma)^K \quad (3.56)$$

In this expression, K is an empirically determined constant, σ is a dimensionless flow temperature parameter developed by Simon, and I_v is the overall average transverse turbulence intensity. σ and I_v are given by:

$$\sigma = (1 + 1/\theta)/(1 + \lambda) \quad (3.57)$$

$$I_v = I_{v,\infty} + 0.4(|I_{v,\infty} - I_{v,s}|) \quad (3.58)$$

Here θ is the temperature ratio which is defined as the ratio of the coolant to hot stream static temperature (T_s/T_∞). $I_{v,s}$ is the initial average transverse coolant stream turbulence intensity, and $I_{v,\infty}$ is the initial average transverse turbulence intensity of the hot gas stream. I_v is based on a turbulent correlation obtained from Ko et al. [110] which has the constraint that I_v cannot be greater than either $I_{v,\infty}$ or $I_{v,s}$.

The final step in the development of a useful compressible film cooling model is determining x_l in Eq. (3.52) which is typically referred to as the impingement or persistence length. From the geometry of the shear layer in Fig. 3-10:

$$x_l = x(s/y_1) \quad (3.59)$$

where y_l is the shear layer-coolant stream interface position.

Since the mixing layer thickness is given by $b = y_1 + y_2$, and the turbulent mixing coefficient (C_{M_0}) is related to the mixing layer growth rate by $C_{M_0} = (b - y_1)/x$, Eq. (3.59) can be re-written as:

$$x_l = \left[(C_{M_0}/s)(y_1/y_2) \right]^{-1} \quad (3.60)$$

To determine y_1/y_2 in Eq. (3.60) the compressible mixing layer growth rate model that was developed in §3.3 can be utilized.

Referring back to Eq. (3.31), it can be seen that the growth in the compressible mixing layer thickness is solely a function of the velocity ratio (between the coolant and core streams), density ratio and chemical composition of the two mixing streams and that the shear layer thickness varies linearly with streamwise distance. By integrating Eq. (3.31) and performing a mass and momentum balance on the two streams an expression for y_l/b can be obtained. Abramovich [27] did this for the case when both streams are homogenous and isothermal (i.e., $\theta_0 = 1$) yielding the following result:

$$y_l/b = A_0 - 2A_1 + A_2 + R(A_1 - A_2) \quad (3.61)$$

Here R is the ratio of the core stream velocity to the coolant stream velocity. The parameters A_0 , A_1 , and A_2 in Eq. (3.61) are expressed in terms of dimensionless

density and velocity ratios ($\rho/\rho_s(\xi)$ and $f(\xi)$), which were defined in §3.3 using a similarity parameter ξ , defined in Eq. (3.14). A_0 and A_1 were defined previously in Eq. (3.28) and Eq. (3.29). The additional parameter A_2 is defined as follows:

$$A_2 = \int_0^1 \rho(\xi)/\rho_s f(\xi)^2 d\xi \quad (3.62)$$

Note that in the isothermal, homogeneous case explored by Abramovich [27], the non-dimensional density ratio, in Eq. (3.26) simplifies to:

$$\frac{\rho}{\rho_s}(\xi) = \frac{1 - \alpha_s M_s^{*2}}{1 - \alpha_s M_s^{*2} [1 - U(\xi)/U_s(\xi)(1 - R)]^2} \quad (3.63)$$

For the more general problem where the total temperature and chemical composition also vary through the mixing layer, an analogous analysis to Abramovich's shows that Eq. (3.63) should be replaced by Eq. (3.26). A solution for y_1/b can be obtained by substituting Eq. (3.26) and Eq. (3.15) into Eqs. (3.62), (3.28) and (3.29). Note that Eq. (3.62) will also need to be integrated numerically. Once A_0 , A_1 , and A_2 are found, Eq. (3.61) is rearranged to obtain an expression for y_1/y_2 (recall that $b = y_1 + y_2$ as illustrated in Fig. 3-10):

$$y_1/y_2 = \{-1 + 1/c[A_0 - 2A_1 + A_2 + R(A_1 - A_2)]\}^{-1} \quad (3.64)$$

Following Simon's approach [114], c is defined to be a function of the fluid density ratio in mixing zone I at the impingement point. Assuming that the pressure is constant across the layer and ignoring variations in chemical composition across the mixing layer gives the following expression for c :

$$c = \left(T_{0s}/T_{aw_{x=x_1}}\right) \left(1 + \frac{\gamma-1}{2} M_s^2\right)^{-1} \quad (3.65)$$

Equations (3.64) and (3.65), combined with Eqs. (3.49-3.52) and Eq. (3.60) form a compressible film cooling model (CFM) which is valid for both homogeneous and heterogeneous wall-jet film cooling in the absence of a pressure gradient under compressible flow conditions.

3.4.3 Selection of Model Parameters

In order to apply the film cooling model developed in §3.4.2, it is necessary to first select values for the model's empirical parameters E_o , d_o and K , as well as inputs for the initial coolant stream and hot stream turbulence intensities, $I_{v,s}$, and $I_{v,\infty}$. The same two-step process described previously in §2.4 is used. First, a sensitivity analysis is carried out to ascertain which parameters exert the greatest influence on the predictions of the model. Second, a least-squares analysis is performed to find specific values for the most sensitive constants and inputs that produce the best agreement with a particular set of experimental data. The values used by Simon [114] were retained for the least sensitive parameters. Since the sensitivity of the model to the coefficients is unchanged by compressibility, the results of the sensitivity analysis completed in §2.4 remain valid and it is therefore convenient to proceed directly to the least-squares analysis by following the same approach described in §2.4.3.

Least-squares Results

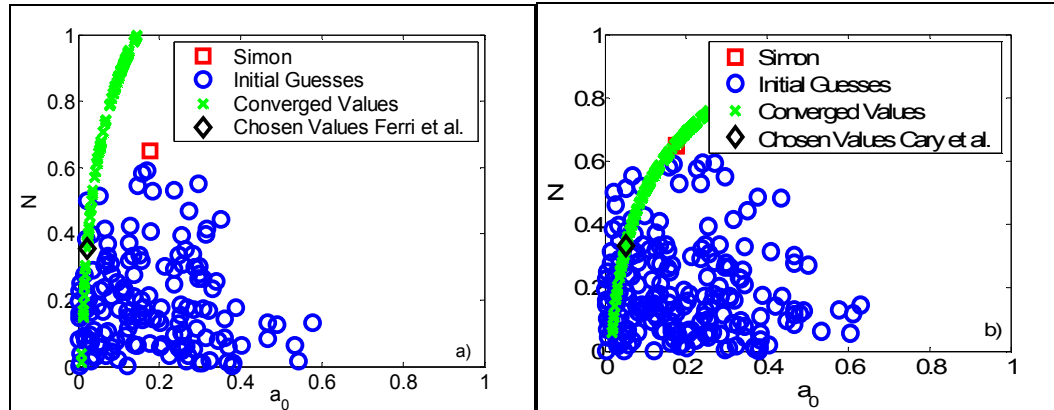


Figure 3-11 Range of predictions obtained for different initial guesses for d_0 and K using the two-variable LSQ method for: a) moderately compressible conditions ($M_c = 0.30$, $M_{HS} = 0.80$ and $\theta_0 = 0.58$) and b) highly compressible conditions ($M_c = 1.29$, $M_{HS} = 6.0$ and $\theta_0 = 0.62$).

As with the pressure gradient data, a random number generator was used to produce a sequence of initial guesses between 0 and 1 for each parameter and the two-variable least squares technique was applied to obtain converged values for d_0 and K . The results of this exercise are presented in Figure 3-11 a) and b) for two different compressible film cooling data sets from Cary et al. and Ferri et al. [173–174]. The ‘o’ symbols correspond to the initial random guesses for each parameter and the ‘x’ symbols indicate the converged values. The ‘□’ symbol corresponds to Simon’s [114] reported values for a_0 and N ($a_0 = 0.177$ and $N = 0.65$) and the ‘◇’ symbol indicates the converged value with the lowest residual (which is taken to be most “realistic”) and therefore used for the CFM analysis in each case. Note that in this case the converged values closest to Simon’s reported values were not considered to be the most realistic since they are for an incompressible film cooling situation where the shear layer growth rate is much higher than under compressible conditions. Note d_0 and K are parameters related to the shear layer growth rate as noted in [114].

3.4.4 Experimental Film Cooling Data

Values for d_0 , E_0 , and K were determined for data from three film cooling studies [173-174,187]. These studies were chosen because they reported turbulence intensity measurements and covered a broad range of compressible conditions. A summary of the experimental conditions and the results from the least squares analysis are given in Table 3.3.

Study	λ	M_s	M_∞	M_c	θ_0	R	S	Iv [%]	d_0	E_0	K
Cary et al. [173]	0.08	1.00	6.00	1.29	0.62	2.91	0.24	2.0	0.05	13.7	0.33
Ferri et al. [174]	0.50	0.32	0.80	0.30	0.58	3.13	1.57	3.0	0.02	13.7	0.35
Cruz et al. [187]	2.22	0.09	0.05	0.02	0.71	0.64	1.41	3.0	0.36	13.7	0.81

Table 3.3 Summary of experimental conditions from various film cooling studies [173-174,187] used to validate the CFM.

3.5 Results

In the following sub-sections, the effects of density gradients and compressibility on film cooling performance are explored in each of the regimes identified in §3.2.2 by comparing the model's prediction of the downstream variation of effectiveness to those of Simon's incompressible model (SM) [114] and various experimental measurements. The values of the model parameters used in each case are summarized in Table 3.3. A detailed summary of Simon's incompressible film cooling model has been presented in §2.3.

3.5.1 Comparison to Experimental Data

Weak Regime

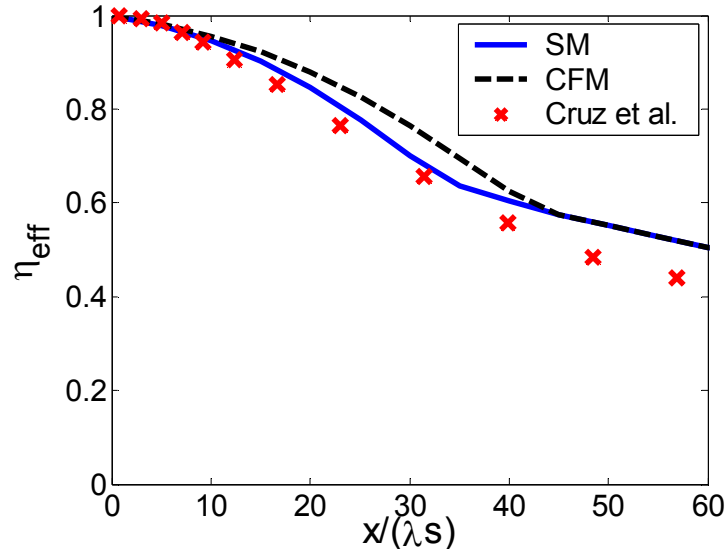


Figure 3-12 Plot of film cooling effectiveness, η_{eff} , as a function of non-dimensional streamwise distance, $x/(\lambda s)$, for a turbulent, wall-jet at $\theta_0 = 0.71$ and $M_c = 0.015$ as predicted by the CFM and the SM.

Fig. 3-12 shows film cooling effectiveness as a function of non-dimensional stream-wise distance for a turbulent, weakly compressible wall-jet where $\theta_0 = 0.71$, $M_c = 0.015$ and $M = 0.09$. The mainstream Mach number in this case is 0.05, the coolant stream Mach number is 0.09, and the slot height is 4.2 mm. The ‘x’ symbols correspond to experimental data from Cruz et al. [187], the solid line corresponds to the predictions of the SM, and the dashed line corresponds to the CFM predictions under identical conditions. The figure shows that under weakly compressible conditions, the predictions of the CFM in the near injection region ($x/\lambda s < 10$) agree to within an rms error of 0.7% with those of the SM. This makes sense because the CFM approaches the SM in the limit that $M_c, M \rightarrow 0$, since from Eq. (20) $T_0 \rightarrow T$. The CFM also matches measurements by Cruz et al. [187] to within an rms error of 5.5% compared to 3.9% for the SM. The small difference between the SM and CFM

curves is due to the fact that the total temperature ratio is less than unity and therefore there is a very weak thermal compressibility effect present. This causes a slight drop in the growth rate of the mixing layer at the coolant-mainstream interface which pushes the impingement point further downstream thereby leading the CFM to predict a slightly higher effectiveness than the SM. Beyond the impingement point, the film mixes rapidly driving the total temperature ratio to 1 and eliminating the difference between the SM and CFM in the far-field region ($x/\lambda_s > 40$).

Moderate Regime

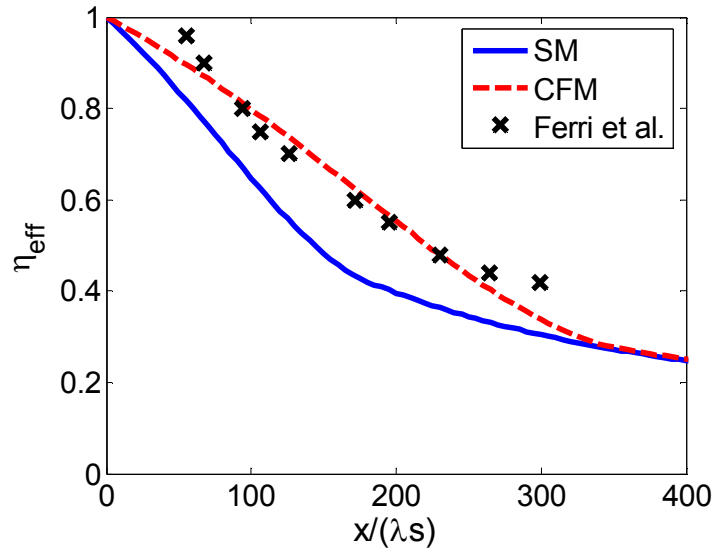


Figure 3-13 Film cooling effectiveness, η_{eff} , as a function of non-dimensional streamwise distance, $x/(\lambda_s)$ for a turbulent, core-driven film at $\theta_0 = 0.58$ and $M_c = 0.31$ as predicted by the CFM and SM.

Figure 3-13 shows the variation of film cooling effectiveness with non-dimensional stream-wise distance for a turbulent, weakly compressible wall-jet where $\theta_0 = 0.58$, $M_c = 0.31$ and $M = 0.80$. The coolant stream Mach number is 0.32 and the slot height is 0.89 mm. The ‘x’ symbols correspond to experimental data from Ferri et al. [174], the solid lines correspond to the predictions of the SM, and the dashed lines correspond to the CFM predictions under identical conditions. The figure shows that

the CFM correlates the experimental measurements much better than the SM: The rms error between the CFM and experiment is 4.0% compared to nearly 13.3% for the SM. The significant improvement in the correlation with experimental data demonstrates the importance of compressibility in this regime.

Strong Regime:

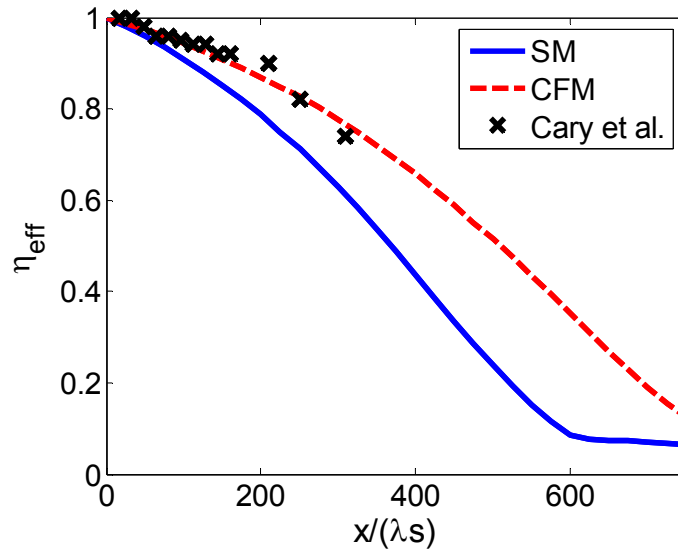


Figure 3-14 Plot of film cooling effectiveness, η_{eff} as a function of non-dimensional streamwise distance, $x/(\lambda s)$ for a turbulent, core-driven film at $\theta_0 = 0.62$ and $M_c = 1.29$ as predicted by the CFM and the SM.

Figure 3-14 shows film cooling effectiveness as a function of non-dimensional stream-wise distance, for a turbulent, highly compressible wall-jet with $\theta_0 = 0.62$, $M_c = 1.29$ and $M = 6.00$. Experimental data from Cary et al. [173] is shown using ‘x’ symbols, while the solid lines and dashed lines correspond to the predictions of the SM and the CFM respectively. The figure highlights the importance of incorporating compressibility effects when convective Mach numbers are high and temperature ratios deviate significantly from unity. The rms error between the CFM predictions and experimental data is less than 1.6% whereas the SM fails completely. Taken

together, the results from §3.5.1 indicate that compressibility can have important and sometimes dramatic effects on film cooling performance.

3.5.2 Physical Explanation

In order to understand how density gradients (or compressibility) affect film cooling performance, it is useful to consider the effects of convective and flow Mach number (i.e., ‘velocity’ or convective compressibility) as well as total temperature ratio (i.e., ‘temperature’ or thermal compressibility) separately. However, this is difficult because film cooling performance varies with downstream distance. Therefore the strategy used here is to plot the maximum value of the ratio of the compressible to incompressible film cooling effectiveness (which will be referred to as the non-dimensional film cooling effectiveness, $\eta_{eff(comp)}/\eta_{eff(inc)}$) and the ratio of the compressible to incompressible shear layer impingement distance (which will be called the non-dimensional impingement distance $x_{1,comp}/x_{1,inc}$) as a function of the average convective Mach number and total temperature ratio. The results are presented below.

Effect of Velocity Difference

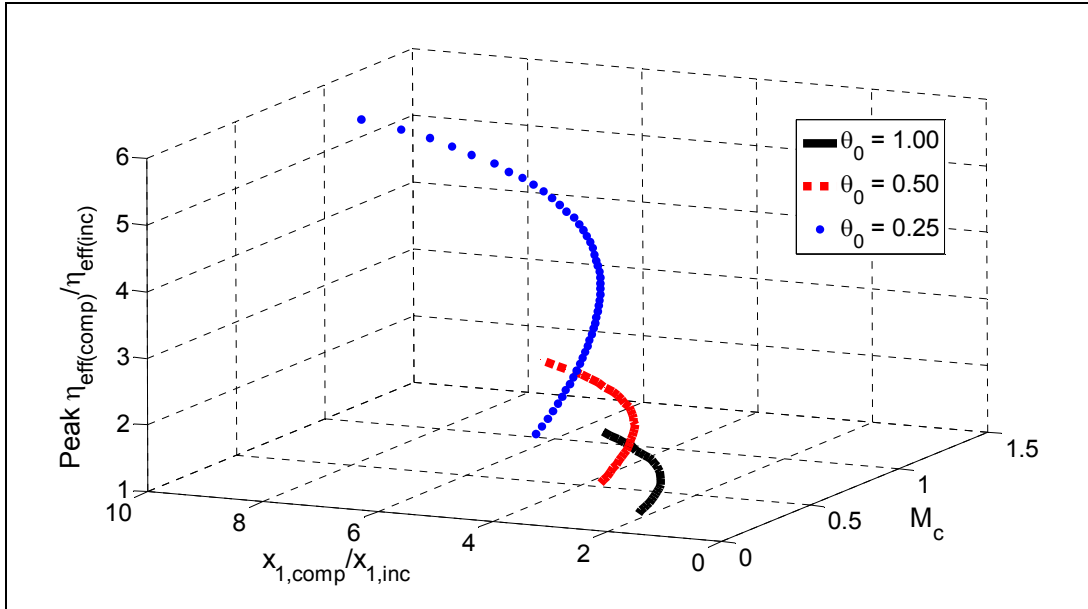


Figure 3-15 Compressible (CFM) to incompressible (SM) film cooling effectiveness (peak $\eta_{eff(comp)}/\eta_{eff(inc)}$) as a function of convective Mach number, M_c , and non-dimensional shear layer impingement length, $x_{1,comp}/x_{1,inc}$, for a turbulent, core-driven film at fixed total temperature ratios, $\theta_0 = 1.00, 0.50$ and 0.25 .

Figure 3-15 shows peak non-dimensional film cooling effectiveness ($\eta_{eff(comp)}/\eta_{eff(inc)}$) and non-dimensional impingement length ($x_{1,comp}/x_{1,inc}$) as a function of the convective Mach number for three different total temperature ratios: $\theta_0 = 1.00$, $\theta_0 = 0.50$ and $\theta_0 = 0.25$. The figure shows that increasing the compressibility (by increasing M_c) increases effectiveness by pushing the impingement point further downstream and increasing the length of the protected area. Similarly, decreasing the total temperature of the coolant stream or increasing the total temperature of the core flow (i.e., driving θ_0 farther < 1) also moves the impingement point downstream leading to improved film cooling effectiveness. For the case in which $\theta_0 = 1$, it is important to note that $\eta_{eff(comp)}/\eta_{eff(inc)}$ and $x_{1,comp}/x_{1,inc}$ do not equal the expected incompressible value of 1 because there are still density variations across the layer associated with the different coolant and mainstream flow Mach numbers. These are

varied between Mach 0.4 and 5.5 to achieve the range of convective Mach numbers shown in the figure. This highlights the influence of the high speed stream flow Mach number, M_{HS} , on the overall velocity compressibility of a film cooling flow.

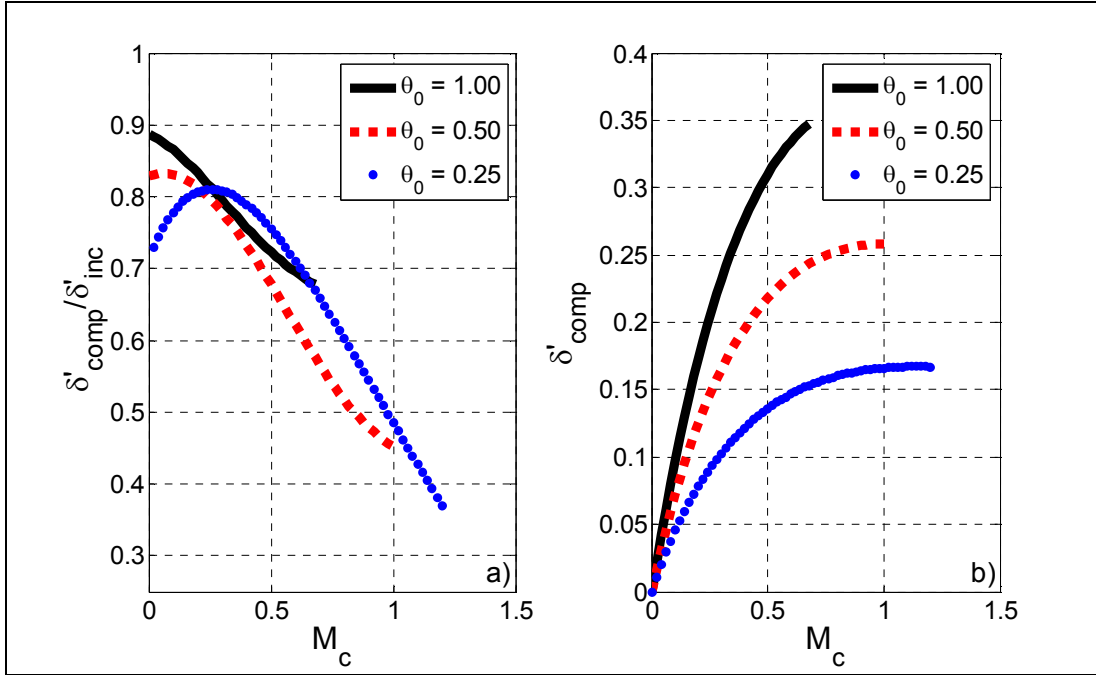


Figure 3-16 Compressible mixing layer growth rate: a) normalized ($\delta'_{comp} / \delta'_{inc}$) and b) un-normalized (δ'_{comp}) as a function of convective Mach number, M_c , for a turbulent, core-driven film at fixed total temperature ratios, $\theta_0 = 1.00, 0.50$ and 0.25 .

The reasons why the non-dimensional impingement length increases with increasing convective and flow Mach number as well as decreasing total temperature ratio can be inferred from Figure 3-16. Figure 3-16 a) shows the normalized compressible shear layer growth rate ($\delta'_{comp} / \delta'_{inc}$) as a function of convective Mach number, M_c , for the same conditions explored in Fig. 3-15. Here, the normalized growth rate is computed from Eq. (3.39). Figure 3-16 a) shows that increasing M_c decreases the normalized shear layer growth rate for most values of θ_0 - a well-established finding in compressible shear layer theory and experiments. [32-34]. Figure 3-16 b) shows the variation of the un-normalized compressible shear layer

growth rate (δ'_{comp}) with convective Mach number (M_c). Decreasing the total temperature ratio decreases the compressible growth rate thereby indicating that the shear layer is thinning. This is why the non-dimensional impingement length increases as θ_0 is decreased from 1.00 to 0.25. Finally, the $\theta_0 = 0.25$ curve shows that for $M_c < 0.25$, increasing M_c actually increases the non-dimensional growth rate. This corresponds to a situation where $M_s > M_\infty$. However, it has a negligible impact on film cooling effectiveness because the un-normalized shear layer growth rate is relatively small in this region. Taken together, these results suggest that both thermal and velocity compressibility enhance film cooling effectiveness and do so via the same mechanism: thinning of the shear layer formed at the coolant-hot gas stream interface.

Effect of Temperature Difference

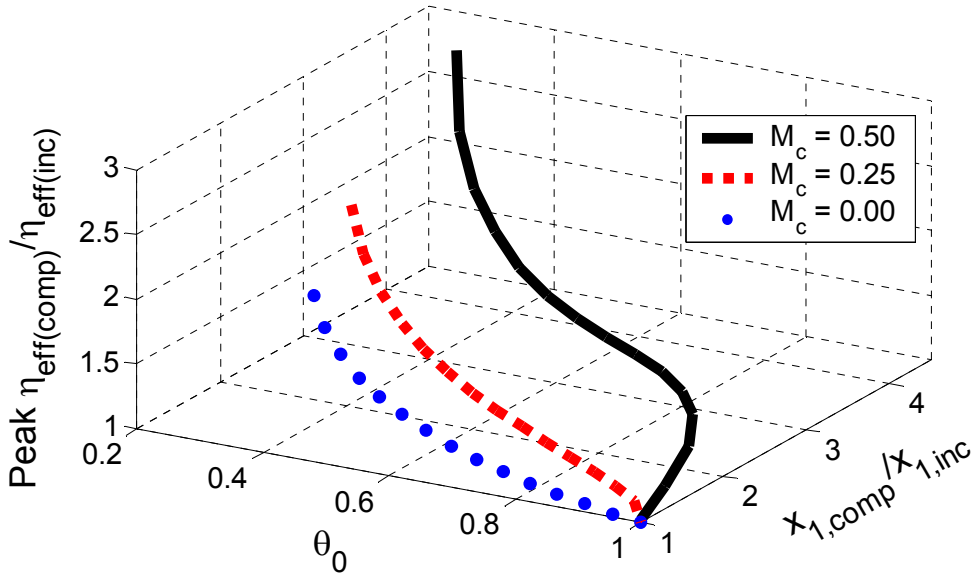


Fig. 3-17 Plot of peak non-dimensional film cooling effectiveness, $\eta_{eff(comp)}/\eta_{eff(inc)}$, as a function of total temperature ratio, θ_0 , and non-dimensional shear layer impingement length, $x_{1,comp}/x_{1,inc}$, for a turbulent, core-driven film at fixed convective Mach numbers, $M_c = 0.50, 0.25$ and 0.00 , as predicted by the CFM and SM.

Figure 3-17 shows peak non-dimensional film cooling effectiveness ($\eta_{eff(comp)}/\eta_{eff(inc)}$) and non-dimensional impingement distance ($x_{1,comp}/x_{1,inc}$) as a

function of the total temperature ratio for three different convective Mach numbers: $M_c = 0.00$, $M_c = 0.25$ and $M_c = 0.50$. Increasing the compressibility (by decreasing θ_0) increases effectiveness by thinning the shear layer which causes the impingement point to move downstream. Similarly, increasing the convective Mach number moves the impingement point downstream leading to improved film cooling effectiveness. Note that Fig. 3-17 tells essentially the same story as Fig. 3-15 except that M_c is held fixed and the total temperature varied.

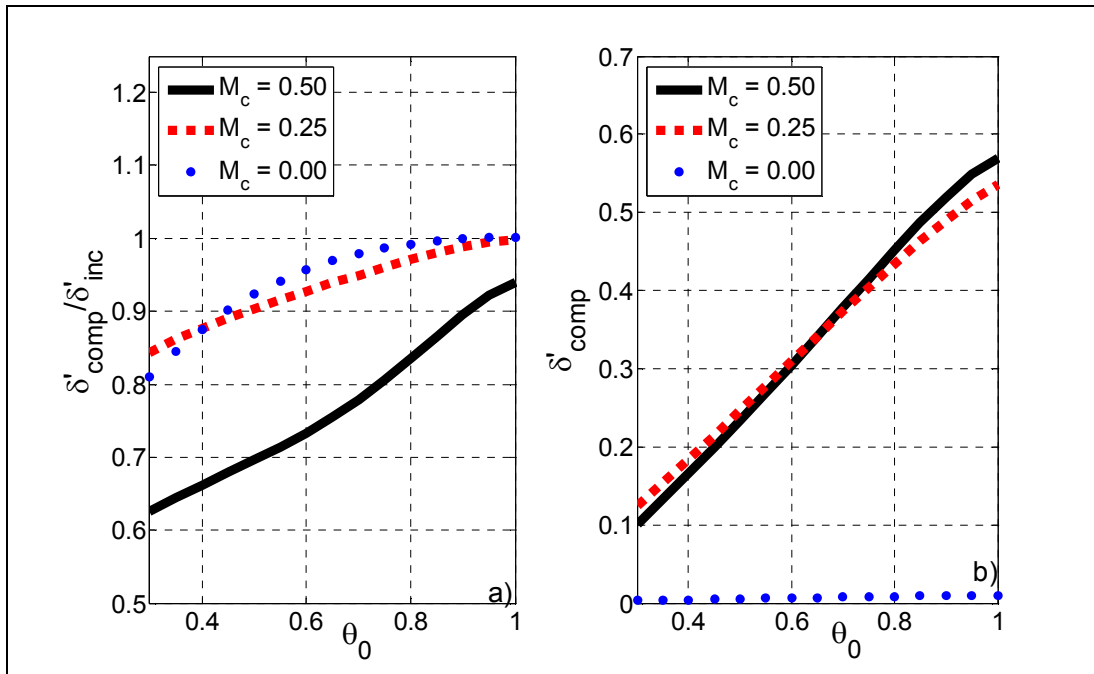


Figure 3-18 Compressible mixing layer growth rate predicted by the CVM: a) normalized ($\delta'_{comp} / \delta'_{inc}$), and b) un-normalized (δ'_{comp}), as a function of total temperature ratio, θ_0 , for a turbulent, core-driven film at fixed convective Mach numbers, $M_c = 0.50, 0.25$ and 0.00 .

The explanation of Fig. 3-17 is also analogous to that of Fig. 3-15. Figure 3-18 a) shows the normalized compressible shear layer growth rate, δ'_{comp} , as a function of total temperature ratio, θ_0 , for the same conditions explored in Fig. 3-17. As before, the increase in non-dimensional impingement length with decreasing total temperature ratio is associated with a reduction in the normalized compressible shear

layer growth rate which causes the shear layer to impinge further downstream leading to a longer persistence length of the film and therefore higher effectiveness. Fig 3-18 a) also shows that lower total temperature ratios are required to realize compressibility effects when the convective Mach number is low. This is even more apparent in the un-normalized growth rates illustrated in Fig 3-18 b). Taken together, this explains why the non-dimensional effectiveness is *maximum* at the lowest total temperature ratio and at the highest convective Mach number.

3.5.3 Resolution of Discrepancies in the Literature

One major challenge in evaluating the importance of compressibility to film cooling performance is reconciling the apparent contradictions in the literature mentioned in the introduction. To recap, Repukhov [167] predicts that compressibility can be ignored over a wide range of velocity and temperature conditions whereas Hansmann et al. [16] predict that it can have a significant effect. Who is correct? The CFM model shows that both are right. The reason for this is that the data Repukhov used to validate his theoretical predictions, despite being associated with a fairly low total temperature ratio ($\theta_0 < 0.4$), were taken at convective Mach numbers close to zero and at flow Mach numbers ($M < 0.4$) where the CFM shows that compressibility effects are weak. In contrast, Hansmann et al. [16] conducted experiments at convective Mach numbers in the range $0.3 < M_c < 1.0$, with flow Mach numbers in the range $0.1 < M < 1.0$ and at very low total temperature ratios ($\theta_0 < 0.2$) where the CFM model predicts compressibility to play a stronger role. This is illustrated below in Table 3.4 which compares Repukhov's and Hansmann's experimental conditions and the respective peak non-dimensional film cooling effectiveness predicted using

the incompressible and the compressible models. Data from other studies where compressibility is strong (Cary et al. [173]), moderate (Sinha et al. [177]) and weak (Cruz et al. [187]) are also included for comparison.

Study	M_s	M_∞	θ_0	R	S	M_c	Peak	Regime
							$\eta_{eff(comp)}/\eta_{eff(inc)}$	
Hansmann et al. [16]	0.10	0.92	0.13	23.81	6.45	0.63	3.80	Strong
	0.05	0.45	0.15	22.72	6.59	0.31	3.30	
	0.10	0.90	0.13	24.39	6.58	0.62	3.89	
Repukhov [167]	0.38	0.23	0.36	0.99	2.86	0.001	1.52 [†]	Weak-Moderate
	0.40	0.22	0.34	0.96	3.04	0.006	1.55 [†]	
Cary et al. [172]	1.00	6.00	0.62	2.92	0.24	1.29	1.84	Strong
	1.00	6.00	0.47	3.35	0.31	1.51	3.28	
	1.00	6.00	0.34	3.94	0.43	1.77	5.33	
Sinha et al. [177]	0.052	0.06	0.83	1.20	1.20	0.005	1.00	Weak-Moderate
	0.045	0.06	0.62	1.60	1.60	0.012	1.63	
	0.041	0.06	0.50	2.00	2.00	0.016	2.63	
Cruz et al. [187]	0.06	0.05	0.66	1.16	1.52	0.004	1.12	Weak
	0.03	0.06	0.66	2.30	1.52	0.018	1.29	
	0.09	0.05	0.71	0.63	1.41	0.015	1.09	

Table 3.4 Summary of experimental conditions used in various compressible film cooling studies [16,167,173,177,187].[†]Since no turbulence information is available, I_v is assumed to be equal to the value used in Hansmann et al. [16] of 5.0%.

3.6 The Combined Effect of Pressure Gradients and Compressibility

3.6.1 Introduction

In a real rocket engine, one would not expect the effects of compressibility and pressure gradients to be independent. Therefore it is useful to take the current semi-empirical modeling approach one step further, by integrating the pressure gradient and compressibility film cooling models. This will allow us to explore how these phenomena interact to set film cooling performance under more realistic '*rocket-like*' conditions.

3.6.2 The Combined Pressure Gradient Compressible Film Cooling Model

To first order the combined effects of pressure gradients and compressibility on film cooling effectiveness can be estimated by simply evaluating how these phenomena impact the length of initial region (i.e., persistence length) through the mixing layer growth rate.

The mixing layer growth rate under conditions in which both compressibility and pressure gradients are significant can be estimated by combining the growth rate expressions that were derived previously for the individual effects of pressure gradients and compressibility (i.e., by using Eqs. (2.29) - (2.31) and Eqs.(3.40) – (3.41)). Following the approach used in Eq. (2.29) the un-normalized mixing layer growth rate can be expressed as a sum of the compressible, isobaric growth rate, m' , combined with the change in growth rate due to the presence of a pressure gradient, ℓ . This can be written as follows:

$$\frac{db}{dx} = m' + \ell \quad (3.66)$$

The first term m' corresponds to the compressible growth rate which was defined earlier in Eq. (3.11) and Eq. (3.31) for discontinuous and continuous velocity profiles respectively, while the second term ℓ accounts for the influence of a pressure gradient on the shear layer growth rate and was defined previously in Eq. (2.31). This leads to the following expressions for the combined effect of pressure gradients and compressibility on the shear layer growth:

$$\frac{db}{dx} = \frac{c}{2} \left\{ \pm \frac{(1+S_0)(1-1/R_0)}{1+S_0/R_0} + 4 \frac{R_0 - C_{P,1} - \sqrt{(1-C_{P,1})(R_0^2 - C_{P,1})}}{1-R_0^2} \right\} \quad (3.67)$$

$$\frac{db}{dx} = \frac{c}{2} \left\{ \pm \frac{(1-1/R_0)}{(1/R_0 - 1) \frac{A_1}{A_0} \Big|_{x=0}} + 4 \frac{R_0 - C_{P,1} - \sqrt{(1-C_{P,1})(R_0^2 - C_{P,1})}}{1-R_0^2} \right\} \quad (3.68)$$

Here R_0 and S_0 indicate the initial velocity and density ratio (i.e. before application of the streamwise pressure gradient). The growth rate constant c was defined earlier for compressible shear layers in Eq. (3.36). Equation (3.67) accounts for discontinuous velocity profiles while Eq. (3.68) accounts for continuous profiles across the shear layer. Both equations show that the mixing layer growth rate under the combined effects of pressure gradients and compressibility depends on the velocity ratio, the type and magnitude of the pressure gradient applied, the density ratio, as well as the Mach number and chemical composition of the streams forming the mixing layer.

In the limit as the flow becomes incompressible and isobaric (i.e., $\theta_0 \rightarrow 1$, $S_0 \rightarrow 1$, $M \rightarrow 0$ and $C_{P_\infty} \rightarrow 0$), Eq. (3.67) and Eq. (3.68) simplify (appropriately) to Abramovich's incompressible result [27] given earlier in Eq. (3.12) and Eq.(3.32).

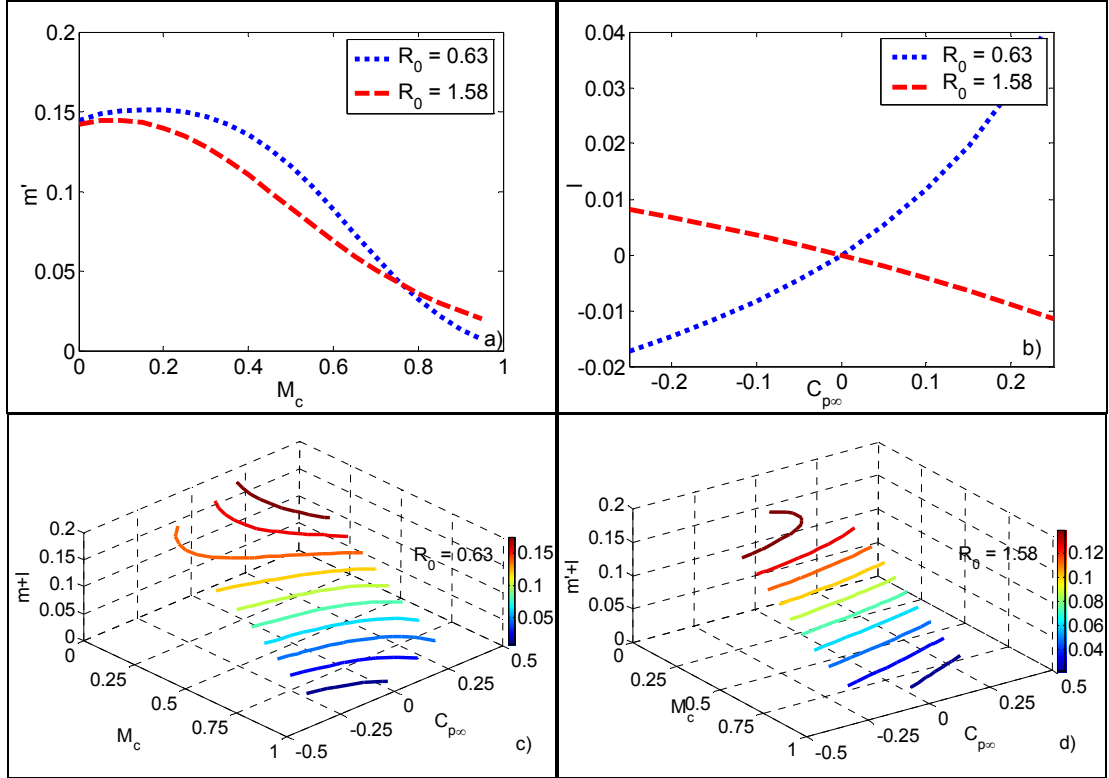


Figure 3-19 a) Change in the shear layer growth rate (m') versus convective Mach number (M_c) for a wall-jet film ($R_0 = 0.63$) and a core-driven film ($R_0 = 1.58$). **b)** Change in the shear layer growth rate (l) versus non-dimensional pressure gradient (C_{P_∞}) for a wall-jet film ($R_0 = 0.63$) and a core-driven film ($R_0 = 1.58$). **c)** Contours of overall shear layer growth rate ($m'+l$) versus convective Mach number (M_c) and non-dimensional pressure gradient (C_{P_∞}) for a wall-jet film ($R_0 = 0.63$) **d)** Contours of overall shear layer growth rate ($m'+l$) versus convective Mach number (M_c) and non-dimensional pressure gradient (C_{P_∞}) for a core-driven film ($R_0 = 1.58$). The growth rate predictions are made using Eq. (3.68) at a fixed secondary stream Mach number, $M_2 = 3.0$ and total temperature, $T_{02} = 300\text{K}$.

Figure 3-19 a) shows that m is always decreases with increasing convective Mach number, while Figure 3-19 b) shows that l can be positive or negative depending on the sign of C_{P_∞} and whether or R_0 is >1 (solid line) or $R_0 <1$ (dotted line). The overall growth rate ($m'+l$) for the wall-jet film ($R_0 = 0.63$) plotted in Figure 3-19 c) increases with C_{P_∞} and decreasing M_c , while it decreases with decreasing

$C_{P\infty}$ and increasing M_c . A different trend is observed in Figure 3-19 d) which shows the overall growth rate ($m'+l$) for the core-driven film ($R_0 = 1.58$) as a function of M_c and $C_{P\infty}$. The overall growth rate ($m'+l$) increases with decreasing $C_{P\infty}$ and M_c , while it decreases with increasing $C_{P\infty}$ and M_c .

These results show that the reversal in the effect of the pressure gradient with R which was observed under incompressible conditions is also present under compressible conditions. This suggests that the combined impact of compressibility and pressure gradients on the impingement length and therefore the film cooling effectiveness should be qualitatively similar to that predicted for film cooling flow with pressure gradients under incompressible conditions.

Having established how compressibility and pressure gradients influence the mixing layer growth rate the development of a compressible pressure gradient model (CGPM) to predict the film cooling effectiveness under non-isobaric, compressible conditions can now be continued.

To first order, the combined effects of pressure gradients and compressibility on film cooling effectiveness can be estimated by simply evaluating how these phenomena impact the length of initial region (i.e., persistence length), x_l , relative to a situation in which no pressure gradient and no compressibility effects are present (i.e., incompressible, zero pressure gradient flow). Using the incompressible persistence length, $x_{l,inc}$, as a reference, the new persistence length, x_l , can be estimated by simply summing the change in the persistence length due to the presence of a pressure gradient, $dx_{l,pg}$, and the change in the persistence length due to

compressibility effects, $dx_{1,comp}$, with the reference length, $x_{1,inc}$. This can be expressed as follows:

$$x_1 = x_{1,inc} + dx_{1,pg} + dx_{1,comp} \quad (3.68)$$

Here $dx_{1,pg}$ is obtained by applying Eq. (2.19), Eq. (2.25), Eqs. (2.33-2.37) which account for the effect of pressure gradients on the persistence length, while $dx_{1,comp}$ can be computed from Eq. (3.60), and Eqs. (3.64-3.65) which account for compressibility effects on the persistence length.

Next, by recognizing that the film cooling correlations derived previously in Eq. (3.49) and Eq. (2.9) remain valid since the effectiveness should behave qualitatively in an identical manner (i.e., decrease with increasing streamwise distance, with decreasing blowing ratio, with decreasing slot height, and with increasing turbulence intensity) when both compressibility and pressure gradient effects are present, we can avoid having to perform a new mass, momentum and energy balance. A new compressible pressure gradient film cooling model (CPGM) can be obtained by simply combining the compressible film cooling correlation from Eq. (3.49) with Eq. (3.68) and the following equations:

$$T_{aw_{x=x_1}} = \left(T_{aw_{x=x_1,pg}} + T_{aw_{x=x_1,comp}} \right) / 2 \quad (3.69)$$

$$c = c_{inc} + dc_{pg} + dc_{comp} \quad (3.70)$$

Here $T_{aw_{x=x_1}}$ is the adiabatic wall temperature at the impingement point, and c , is the ratio of the fluid density in mixing zone I at the impingement point (x_1) to the coolant stream density.

With these equations a new semi-empirical model is obtained which can predict to first order the combined effect of pressure gradients and compressibility on film cooling effectiveness. The next step is to compare the model's predictions with experimental data.

3.6.3 Comparison to Experimental Data

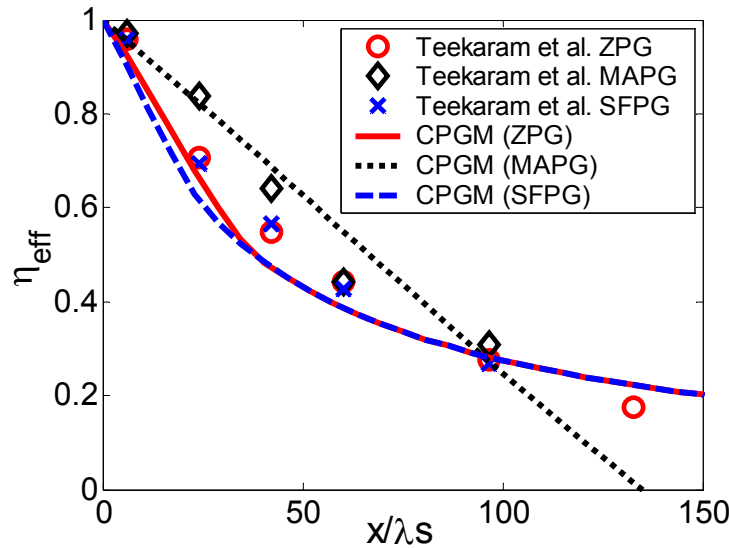


Figure 3-20 Film cooling effectiveness, η_{eff} , predicted by the CPFM as a function of non-dimensional streamwise distance, $x/\lambda s$, for a turbulent core-driven film ($R_0 = 3.53$) with a strong favorable pressure gradient ($K_p = 2.62 \times 10^{-6}$), a mild adverse pressure gradient ($K_p = -0.22 \times 10^{-6}$) and zero pressure gradient. $\lambda = 0.33$ and $\theta_0 = 0.82$.

Figure 3-20 shows film cooling effectiveness as a function of non-dimensional downstream distance for a turbulent core-driven film with three different acceleration parameters. $K_p = -0.22 \times 10^{-6}$ corresponds to a mild adverse variable pressure gradient (MAPG), $K_p = 2.62 \times 10^{-6}$ corresponds to a strong favorable variable pressure gradient (SFPG) and $K_p = 0$ corresponds to a constant zero pressure gradient (ZPG). The blowing ratio (λ) is 0.33 and the total temperature ratio (θ_0) is 0.82. In the SFPG and ZPG cases the convective Mach number (M_c) is 0.18 and the high speed stream Mach number (M_{HS}) is 0.5; while in the MAPG case the convective Mach number (M_c) is

0.22 and the high speed stream Mach number (M_{HS}) is 0.6. These conditions are summarized below in Table 3.5.

Study	M_s	M_∞	θ_0	M_c	K_p	Case
Teekaram	0.18	0.50	0.82	0.17	0	ZPG
et al.	0.18	0.60	0.82	0.22	-0.22×10^{-6}	MAPG
[140]	0.18	0.50	0.82	0.17	2.62×10^{-6}	SFPG

Table 3.5 Summary of experimental conditions used by Teekaram et al. [140]

The solid line shows the compressible pressure gradient model's predictions for a constant zero pressure gradient (ZPG); the dotted line shows the model's predictions for the mild adverse variable pressure gradient (MAPG) and the dashed line shows the predictions for the strong favorable variable pressure gradient (SFPG). The symbols show the corresponding experimental data from Teekaram et al. [140]. Figure 3-20 shows that the model captures the effect of K_p on effectiveness and matches the magnitude within an rms error of less than 5.9%. This represents a significant improvement in quantitative agreement with the data, when compared with PGFM (Pressure Gradient Film Cooling Model) results presented in Fig. 2-12 in Chapter 2. This result confirms that compressibility is significant and must be accounted for when correlating Teekaram's data. It is also interesting to note that compressibility appears to exert a greater effect in the MAPG case than in the SFPG case. This can be attributed to two things. First, in the MAPG case both compressibility and flow deceleration (due to the adverse pressure gradient) increase the persistence length of the film and therefore couple together to significantly enhance effectiveness relative to the ZPG case. In contrast, in the SFPG case compressibility increases the persistence length, while flow acceleration (due to the favorable pressure gradient) decreases the persistence length, which consequently leads to a small a decrease in effectiveness relative to the ZPG case, despite the fact

that a strong pressure gradient was applied. The second factor to take into account is that the high speed stream Mach number and convective Mach number are slightly higher in the MAPG case than in the other cases, which means that the effect of compressibility is more pronounced in this case. Overall, these results demonstrate how pressure gradient and compressibility effects can either add together or subtract from each other to influence film cooling effectiveness.

3.6.4 Resolution of Discrepancies in the Literature

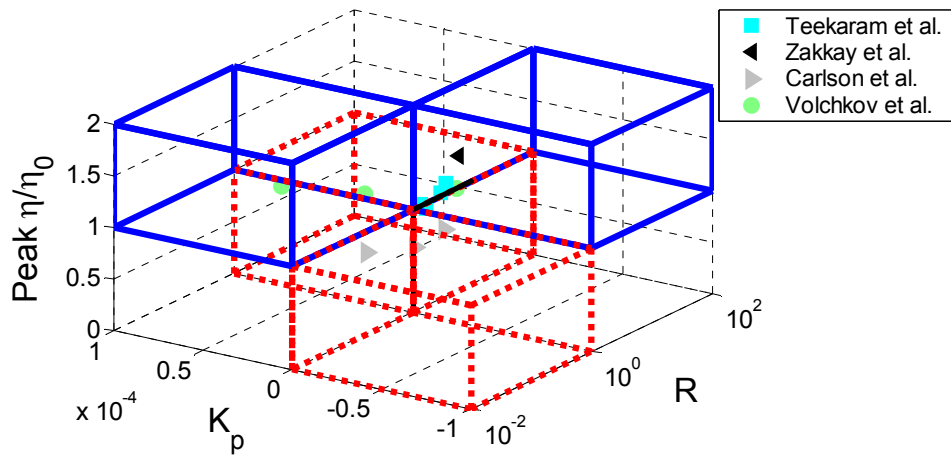


Figure 3-21 Peak non-dimensional film cooling effectiveness (η/η_0) as a function of acceleration parameter (K_p) and velocity ratio (R) reported in various studies [139,154,220-221].

In a further effort to validate the predictions of the CPGM we can examine how data from several experimental studies [140,155,220-221] in which both compressibility and pressure gradient effects are significant, matches up with the four octants predicted by the PGFM in §2.5.5. The lower plane of Figure 3-21 shows acceleration parameter and velocity ratio while the z-axis shows the change in film cooling performance relative to the peak effectiveness at the baseline zero pressure gradient case. According to the PGFM (and CPGM) model whose predictions are summarized in Table 2.2, the data should group into four octants: Enhanced cooling

performance when $K_p > 0$ and $R < 1$; enhanced cooling performance when $K_p < 0$ and $R > 1$; degraded cooling performance when $K_p < 0$ and $R < 1$; degraded cooling performance when $K_p > 0$ and $R > 1$. The figure shows that all of the data falls into the octants predicted by the PGFM. This suggests that the CPGM can be used to capture the impact of K_p and R on film cooling effectiveness under compressible conditions.

3.7 Conclusions

The influence of compressibility and density gradients on film cooling effectiveness have been explored by extending Simon's incompressible, wall-jet film cooling model to account for the effects of convective and thermal compressibility. Comparisons to experimental data show that the new model is capable of predicting film cooling performance in three different flow regimes: weakly compressible ($M_c, M_{HS} \leq 0.3$ and $0.6 \leq \theta_0 \leq 1$), moderately compressible ($0.3 < M_c, M_{HS} \leq 1.0$ and $0.30 \leq \theta_0 < 0.60$) and highly compressible ($M_c, M_{HS} > 1.0$ and $\theta_0 < 0.3$). The model shows that compressibility influences film cooling performance by changing the growth rate of the shear layer between the hot gas and coolant streams. In general, increasing the velocity difference (by increasing M_c) and the temperature difference (by decreasing θ_0) between the main flow and the cooling film decreases the growth rate of the shear layer, moves the wall-shear layer impingement point farther downstream, and therefore leads to an increase in film cooling effectiveness because more of the wall is protected. The model also resolves disagreements in the literature over whether or not compressibility is important in film cooling problems: Compressibility effects can be important, if the convective and flow Mach numbers are high enough (> 0.3) and the total temperature ratio is low enough (< 0.6). The combined effects of compressibility

and pressure gradients on film cooling effectiveness have also been explored by coupling the pressure gradient film cooling model developed in Chapter 2 with the compressible film cooling model. This model suggests that the effects of compressibility and pressure gradients can either add or subtract to change the persistence length of the film, which can lead to either enhanced or degraded film cooling performance relative to zero pressure gradient conditions. Comparison of the model's predictions to experimental data in which both compressibility and pressure gradient effects are significant shows good qualitative and quantitative agreement.

Chapter 4: Numerical Prediction of Subsonic Film Cooling

4.1 Introduction

Chapter 4 presents the development of a computationally inexpensive Reynolds Averaged Navier-Stokes (RANS) methodology for the accurate prediction of film cooling effectiveness, skin friction, thermal mixing and momentum mixing under subsonic conditions. Loci-CHEM, a developmental NASA code, is used to implement this methodology by simulating a subsonic film cooling experiment [222]. Insights into subsonic film cooling physics are obtained from the results and the limitations of the RANS methodology are established.

4.2 Description of Loci-CHEM Navier-Stokes Solver

4.2.1 Governing Equations

Loci-CHEM uses a finite volume method to discretize the Navier-Stokes equations which govern the conservation of mass, momentum and energy in a fluid flow [222-224]. In conservative form these equations are written as follows [225]:

$$\frac{\partial(\rho)}{\partial t} + \nabla \cdot (\rho \vec{V}) = 0 \quad (4.1)$$

$$\begin{aligned} & \frac{\partial(\rho u)}{\partial t} + \left(\frac{\partial(\rho u^2)}{\partial x} + \frac{\partial(\rho uv)}{\partial y} + \frac{\partial(\rho uw)}{\partial z} \right) \\ & = -\frac{\partial P}{\partial x} + \frac{\partial}{\partial x} \left(-\frac{2}{3} \mu \nabla \cdot \vec{V} + 2\mu \frac{\partial u}{\partial x} \right) + \frac{\partial}{\partial y} \left[\mu \left(\frac{\partial v}{\partial x} + \frac{\partial u}{\partial y} \right) \right] + \frac{\partial}{\partial z} \left[\mu \left(\frac{\partial w}{\partial x} + \frac{\partial u}{\partial z} \right) \right] + \rho f_x \end{aligned} \quad (4.2)$$

$$\begin{aligned}
& \frac{\partial(\rho v)}{\partial t} + \left(\frac{\partial(\rho uv)}{\partial x} + \frac{\partial(\rho v^2)}{\partial y} + \frac{\partial(\rho vw)}{\partial z} \right) \\
&= -\frac{\partial P}{\partial y} + \frac{\partial}{\partial x} \left[\mu \left(\frac{\partial v}{\partial x} + \frac{\partial u}{\partial y} \right) \right] + \frac{\partial}{\partial y} \left(-\frac{2}{3} \mu \nabla \cdot \vec{V} + 2\mu \frac{\partial v}{\partial y} \right) + \frac{\partial}{\partial z} \left[\mu \left(\frac{\partial w}{\partial y} + \frac{\partial v}{\partial z} \right) \right] + \rho f_y,
\end{aligned} \tag{4.3}$$

$$\begin{aligned}
& \frac{\partial(\rho w)}{\partial t} + \left(\frac{\partial(\rho uw)}{\partial x} + \frac{\partial(\rho vw)}{\partial y} + \frac{\partial(\rho w^2)}{\partial z} \right) \\
&= -\frac{\partial P}{\partial z} + \frac{\partial}{\partial x} \left[\mu \left(\frac{\partial u}{\partial z} + \frac{\partial w}{\partial x} \right) \right] + \frac{\partial}{\partial y} \left[\mu \left(\frac{\partial w}{\partial y} + \frac{\partial v}{\partial z} \right) \right] + \frac{\partial}{\partial z} \left(-\frac{2}{3} \mu \nabla \cdot \vec{V} + 2\mu \frac{\partial w}{\partial z} \right) + \rho f_z
\end{aligned} \tag{4.4}$$

$$\begin{aligned}
& \frac{\partial}{\partial t} \left[\rho \left(e + \frac{V^2}{2} \right) \right] + \nabla \cdot \left[\rho \left(e + \frac{V^2}{2} \vec{V} \right) \right] \\
&= \rho \dot{q} + \frac{\partial}{\partial x} \left(\kappa \frac{\partial T}{\partial x} \right) + \frac{\partial}{\partial y} \left(\kappa \frac{\partial T}{\partial y} \right) + \frac{\partial}{\partial z} \left(\kappa \frac{\partial T}{\partial z} \right) - \frac{\partial(uP)}{\partial x} - \frac{\partial(vP)}{\partial y} - \frac{\partial(wP)}{\partial z} \\
&+ \frac{\partial}{\partial x} \left[u \left(-\frac{2}{3} \mu \nabla \cdot \vec{V} + 2\mu \frac{\partial u}{\partial x} \right) \right] + \frac{\partial}{\partial y} \left[\mu u \left(\frac{\partial v}{\partial x} + \frac{\partial u}{\partial y} \right) \right] + \frac{\partial}{\partial z} \left[\mu u \left(\frac{\partial w}{\partial x} + \frac{\partial u}{\partial z} \right) \right] \\
&+ \frac{\partial}{\partial x} \left[\mu v \left(\frac{\partial v}{\partial x} + \frac{\partial u}{\partial y} \right) \right] + \frac{\partial}{\partial y} \left[v \left(-\frac{2}{3} \mu \nabla \cdot \vec{V} + 2\mu \frac{\partial v}{\partial y} \right) \right] + \frac{\partial}{\partial z} \left[\mu v \left(\frac{\partial w}{\partial y} + \frac{\partial v}{\partial z} \right) \right] \\
&+ \frac{\partial}{\partial x} \left[\mu w \left(\frac{\partial w}{\partial x} + \frac{\partial u}{\partial z} \right) \right] + \frac{\partial}{\partial y} \left[\mu w \left(\frac{\partial w}{\partial y} + \frac{\partial v}{\partial z} \right) \right] + \frac{\partial}{\partial z} \left[w \left(-\frac{2}{3} \mu \nabla \cdot \vec{V} + 2\mu \frac{\partial w}{\partial z} \right) \right] \\
&+ \rho \vec{f} \cdot \vec{V}
\end{aligned} \tag{4.5}$$

where the density, pressure, velocity, shear stress and temperature of the gas mixture, are denoted by ρ , P , V and T respectively. $V^2/2$ is the kinetic energy per unit mass, e is the internal energy per unit mass and f is the body force per unit mass. Also, the x-, y- and z-components of velocity are denoted by u , v and w , while the time, dynamic viscosity and thermal diffusivity are indicated by t , μ and κ .

In order to predict turbulent flows via numerical solution of the Navier-Stokes equations it is common to first convert them into ‘Reynolds averaged form’ before making closure assumptions.

In the conventional Reynolds averaging procedure, a time averaged quantity (\bar{f}) is defined as [226]:

$$\bar{f} \equiv \frac{1}{\Delta t} \int_{t_0}^{t_0+\Delta t} f dt \quad (4.6)$$

Here Δt is the time change which is assumed to be large compared to the period of the random fluctuations associated with turbulence, but small with respect to the time constant of any slow variations in the flow associated with ‘ordinary’ unsteady motion.

Using the definition in Eq. (4.6) the flow variables are decomposed into a mean or time-averaged component plus a fluctuating component. This can be expressed as:

$$\begin{aligned} u &= \bar{u} + u', v = \bar{v} + v', w = \bar{w} + w' \\ \rho &= \bar{\rho} + \rho', P = \bar{P} + P', T = \bar{T} + T' \end{aligned} \quad (4.7)$$

where f' denotes a fluctuating quantity.

It is important to note here that fluctuations in other fluid properties such as viscosity, thermal conductivity and specific heat are assumed to be small and are therefore usually neglected.

In the treatment of compressible flows and mixtures of gases, mass-weighted averaging of the Navier-Stokes equations is typically performed. In this approach mass-averaged variables are defined as:

$$\tilde{f} \equiv \overline{\rho f} / \bar{\rho} \quad (4.8)$$

where \tilde{f} denotes a mass averaged quantity.

This leads to the following mass-averaged Reynolds decomposition for the flow variables:

$$u = \tilde{u} + u'', v = \tilde{v} + v'', w = \tilde{w} + w'', T = \tilde{T} + T'' \quad (4.9)$$

where \tilde{u} , \tilde{v} , \tilde{w} , \tilde{P} and \tilde{T} are given by:

$$\tilde{u} = \overline{\rho u} / \bar{\rho} \quad \tilde{v} = \overline{\rho v} / \bar{\rho} \quad \tilde{w} = \overline{\rho w} / \bar{\rho} \quad \tilde{T} = \overline{\rho T} / \bar{\rho} \quad \tilde{P} = \overline{\rho P} / \bar{\rho} \quad (4.10)$$

The approach used in Loci-CHEM (which is a compressible solver) is to mass-average the governing equations over time [222], which results in the following Reynolds Averaged Navier-Stokes (RANS) formulation for the mass, momentum and energy equations [226]:

$$\frac{\partial(\bar{\rho})}{\partial t} + \nabla \cdot (\bar{\rho} \tilde{\vec{V}}) = 0 \quad (4.11)$$

$$\begin{aligned} & \frac{\partial(\bar{\rho u})}{\partial t} + \left(\frac{\partial(\bar{\rho u}^2)}{\partial x} + \frac{\partial(\bar{\rho u} \tilde{v})}{\partial y} + \frac{\partial(\bar{\rho u} \tilde{w})}{\partial z} \right) \\ &= -\frac{\partial \bar{P}}{\partial x} + \frac{\partial}{\partial x} \left(-\frac{2}{3} \mu \nabla \cdot \tilde{\vec{V}} + 2\mu \frac{\partial \tilde{u}}{\partial x} \right) + \frac{\partial}{\partial y} \left[\mu \left(\frac{\partial \tilde{v}}{\partial x} + \frac{\partial \tilde{u}}{\partial y} \right) \right] + \frac{\partial}{\partial z} \left[\mu \left(\frac{\partial \tilde{w}}{\partial x} + \frac{\partial \tilde{u}}{\partial z} \right) \right] \\ &+ \underbrace{\frac{\partial}{\partial x} \left(-\frac{2}{3} \mu \nabla \cdot \vec{V}'' + 2\mu \frac{\partial u''}{\partial x} \right) + \frac{\partial}{\partial y} \left[\mu \left(\frac{\partial v''}{\partial x} + \frac{\partial u''}{\partial y} \right) \right] + \frac{\partial}{\partial z} \left[\mu \left(\frac{\partial w''}{\partial x} + \frac{\partial u''}{\partial z} \right) \right]}_{\text{apparent Reynolds stress}} \quad (4.12) \\ & - \underbrace{\left(\frac{\partial(\overline{\rho u''^2})}{\partial x} + \frac{\partial(\overline{\rho u'' v''})}{\partial y} + \frac{\partial(\overline{\rho u'' w''})}{\partial z} \right)}_{\text{apparent Reynolds stress}} + \bar{\rho} f_x \end{aligned}$$

$$\begin{aligned}
& \frac{\partial(\overline{\rho v})}{\partial t} + \left(\frac{\partial(\overline{\rho u v})}{\partial x} + \frac{\partial(\overline{\rho v^2})}{\partial y} + \frac{\partial(\overline{\rho v w})}{\partial z} \right) \\
&= -\frac{\partial \bar{P}}{\partial y} + \frac{\partial}{\partial x} \left[\mu \left(\frac{\partial \tilde{v}}{\partial x} + \frac{\partial \tilde{u}}{\partial y} \right) \right] + \frac{\partial}{\partial y} \left(-\frac{2}{3} \mu \nabla \cdot \tilde{\vec{V}} + 2\mu \frac{\partial \tilde{v}}{\partial y} \right) + \frac{\partial}{\partial z} \left[\mu \left(\frac{\partial \tilde{w}}{\partial y} + \frac{\partial \tilde{v}}{\partial z} \right) \right] \\
&+ \frac{\partial}{\partial x} \left[\mu \left(\frac{\partial \bar{v}''}{\partial x} + \frac{\partial \bar{u}''}{\partial y} \right) \right] + \frac{\partial}{\partial y} \left(-\frac{2}{3} \mu \nabla \cdot \bar{\vec{V}}'' + 2\mu \frac{\partial \bar{v}''}{\partial y} \right) + \frac{\partial}{\partial z} \left[\mu \left(\frac{\partial \bar{w}''}{\partial y} + \frac{\partial \bar{v}''}{\partial z} \right) \right] \quad (4.13)
\end{aligned}$$

apparent Reynolds stress

$$- \left(\frac{\partial(\overline{\rho u'' v''})}{\partial x} + \frac{\partial(\overline{\rho v''^2})}{\partial y} + \frac{\partial(\overline{\rho v'' w''})}{\partial z} \right) + \bar{\rho} f_y$$

apparent Reynolds stress

$$\begin{aligned}
& \frac{\partial(\overline{\rho w})}{\partial t} + \left(\frac{\partial(\overline{\rho u w})}{\partial x} + \frac{\partial(\overline{\rho v w})}{\partial y} + \frac{\partial(\overline{\rho w^2})}{\partial z} \right) \\
&= -\frac{\partial \bar{P}}{\partial z} + \frac{\partial}{\partial x} \left[\mu \left(\frac{\partial \tilde{u}}{\partial z} + \frac{\partial \tilde{w}}{\partial x} \right) \right] + \frac{\partial}{\partial y} \left[\mu \left(\frac{\partial \tilde{w}}{\partial y} + \frac{\partial \tilde{v}}{\partial z} \right) \right] + \frac{\partial}{\partial z} \left(-\frac{2}{3} \mu \nabla \cdot \tilde{\vec{V}} + 2\mu \frac{\partial \tilde{w}}{\partial z} \right) \\
&+ \frac{\partial}{\partial x} \left[\mu \left(\frac{\partial \bar{u}''}{\partial z} + \frac{\partial \bar{w}''}{\partial x} \right) \right] + \frac{\partial}{\partial y} \left[\mu \left(\frac{\partial \bar{w}''}{\partial y} + \frac{\partial \bar{v}''}{\partial z} \right) \right] + \frac{\partial}{\partial z} \left(-\frac{2}{3} \mu \nabla \cdot \bar{\vec{V}}'' + 2\mu \frac{\partial \bar{w}''}{\partial z} \right) \quad (4.14)
\end{aligned}$$

apparent Reynolds stress

$$- \left(\frac{\partial(\overline{\rho u'' w''})}{\partial x} + \frac{\partial(\overline{\rho v'' w''})}{\partial y} + \frac{\partial(\overline{\rho w''^2})}{\partial z} \right) + \bar{\rho} f_z$$

apparent Reynolds stress

$$\begin{aligned}
& \frac{\partial}{\partial t} [\bar{\rho} C_p \tilde{T}] + \nabla \cdot [\bar{\rho} C_p \tilde{T} \tilde{\mathbf{V}}] \\
&= \frac{\partial \bar{P}}{\partial t} + \bar{\rho} \dot{q} + \frac{\partial}{\partial x} \left(\kappa \frac{\partial \tilde{T}}{\partial x} \right) + \frac{\partial}{\partial y} \left(\kappa \frac{\partial \tilde{T}}{\partial y} \right) + \frac{\partial}{\partial z} \left(\kappa \frac{\partial \tilde{T}}{\partial z} \right) \\
&+ \frac{\partial}{\partial x} \left(\kappa \frac{\partial \bar{T}''}{\partial x} \right) + \frac{\partial}{\partial y} \left(\kappa \frac{\partial \bar{T}''}{\partial y} \right) + \frac{\partial}{\partial z} \left(\kappa \frac{\partial \bar{T}''}{\partial z} \right) \\
&- \frac{\partial(\tilde{u}\bar{P})}{\partial x} - \frac{\partial(\tilde{v}\bar{P})}{\partial y} - \frac{\partial(\tilde{w}\bar{P})}{\partial z} - \frac{\partial(\bar{u}''\bar{P})}{\partial x} - \frac{\partial(\bar{v}''\bar{P})}{\partial y} - \frac{\partial(\bar{w}''\bar{P})}{\partial z} \\
&\quad - \nabla \cdot \underbrace{[\bar{\rho} C_p \bar{T}'' \bar{\mathbf{V}}'']}_{\text{apparent Reynolds heat flux}} + \frac{\partial}{\partial x} \left[\tilde{u} \left(-\frac{2}{3} \mu \nabla \cdot \tilde{\mathbf{V}} + 2\mu \frac{\partial \tilde{u}}{\partial x} \right) \right] \\
&+ \frac{\partial}{\partial y} \left[\mu \tilde{u} \left(\frac{\partial \tilde{v}}{\partial x} + \frac{\partial \tilde{u}}{\partial y} \right) \right] + \frac{\partial}{\partial z} \left[\mu \tilde{u} \left(\frac{\partial \tilde{w}}{\partial x} + \frac{\partial \tilde{u}}{\partial z} \right) \right] \\
&+ \frac{\partial}{\partial x} \left[\bar{u}'' \left(-\frac{2}{3} \mu \nabla \cdot \bar{\mathbf{V}}'' + 2\mu \frac{\partial \bar{u}''}{\partial x} \right) \right] + \frac{\partial}{\partial y} \left[\mu \bar{u}'' \left(\frac{\partial \bar{v}''}{\partial x} + \frac{\partial \bar{u}''}{\partial y} \right) \right] + \frac{\partial}{\partial z} \left[\mu \bar{u}'' \left(\frac{\partial \bar{w}''}{\partial x} + \frac{\partial \bar{u}''}{\partial z} \right) \right] \\
&\quad \underbrace{\hspace{10em}}_{\text{apparent Reynolds stress}} \\
&+ \frac{\partial}{\partial x} \left[\mu \tilde{v} \left(\frac{\partial \tilde{v}}{\partial x} + \frac{\partial \tilde{u}}{\partial y} \right) \right] + \frac{\partial}{\partial y} \left[\tilde{v} \left(-\frac{2}{3} \mu \nabla \cdot \tilde{\mathbf{V}} + 2\mu \frac{\partial \tilde{v}}{\partial y} \right) \right] + \frac{\partial}{\partial z} \left[\mu \tilde{v} \left(\frac{\partial \tilde{w}}{\partial y} + \frac{\partial \tilde{v}}{\partial z} \right) \right] \\
&+ \frac{\partial}{\partial x} \left[\mu \bar{v}'' \left(\frac{\partial \bar{v}''}{\partial x} + \frac{\partial \bar{u}''}{\partial y} \right) \right] + \frac{\partial}{\partial y} \left[\bar{v}'' \left(-\frac{2}{3} \mu \nabla \cdot \bar{\mathbf{V}}'' + 2\mu \frac{\partial \bar{v}''}{\partial y} \right) \right] + \frac{\partial}{\partial z} \left[\mu \bar{v}'' \left(\frac{\partial \bar{w}''}{\partial y} + \frac{\partial \bar{v}''}{\partial z} \right) \right] \\
&\quad \underbrace{\hspace{10em}}_{\text{apparent Reynolds stress}} \\
&+ \frac{\partial}{\partial x} \left[\mu \tilde{w} \left(\frac{\partial \tilde{w}}{\partial x} + \frac{\partial \tilde{u}}{\partial z} \right) \right] + \frac{\partial}{\partial y} \left[\mu \tilde{w} \left(\frac{\partial \tilde{w}}{\partial y} + \frac{\partial \tilde{v}}{\partial z} \right) \right] + \frac{\partial}{\partial z} \left[\tilde{w} \left(-\frac{2}{3} \mu \nabla \cdot \tilde{\mathbf{V}} + 2\mu \frac{\partial \tilde{w}}{\partial z} \right) \right] \\
&+ \frac{\partial}{\partial x} \left[\mu \bar{w}'' \left(\frac{\partial \bar{w}''}{\partial x} + \frac{\partial \bar{u}''}{\partial z} \right) \right] + \frac{\partial}{\partial y} \left[\mu \bar{w}'' \left(\frac{\partial \bar{w}''}{\partial y} + \frac{\partial \bar{v}''}{\partial z} \right) \right] + \frac{\partial}{\partial z} \left[\bar{w}'' \left(-\frac{2}{3} \mu \nabla \cdot \bar{\mathbf{V}}'' + 2\mu \frac{\partial \bar{w}''}{\partial z} \right) \right] \\
&\quad \underbrace{\hspace{10em}}_{\text{apparent Reynolds stress}} \\
&+ \bar{\rho} \vec{f} \cdot \bar{\mathbf{V}}
\end{aligned} \tag{4.15}$$

Here C_p is the specific heat capacity. Note that in Eq. (4.15) the internal energy per unit mass, e , and the kinetic energy per unit mass, $V^2/2$, have been replaced by an expression in terms of the enthalpy per unit mass h , given by:

$$e + V^2/2 = h - P/\rho + V^2/2 \tag{4.16}$$

The enthalpy per unit mass is in turn expressed as:

$$h = \int_{T_0}^T C_p(T')dT' \quad (4.17)$$

The highlighted expressions in Eqs. (4.12)-(4.15) represent the terms that correspond to apparent turbulent stress and heat flux quantities which arise due to transport of momentum and enthalpy by turbulent fluctuations in the flow [226].

The RANS equations cannot be solved in the form presented in Eqs.(4.12)-(4.15) since the new apparent turbulent stresses and heat flux quantities introduce new unknowns. They can, however, be solved if additional equations involving these new unknowns are applied or by making additional assumptions regarding the relationship between the new apparent turbulent quantities and the mean flow variables. This is commonly known as the ‘closure problem,’ which is typically handled by using a turbulence model. This is the subject of the next section.

4.2.2 Turbulence Model

All of the subsonic film cooling and precursor simulations are performed using Menter’s Shear Stress Transport (SST) two-equation turbulence model [227]. The SST model is obtained by blending the Wilcox $k-\omega$ and $k-\varepsilon$ models. In these equations k represents the mean turbulent kinetic energy associated with eddies in the flow (i.e., this corresponds physically to the root mean squared velocity fluctuations), ε is the turbulent dissipation rate which corresponds to the rate of dissipation of turbulent kinetic energy per unit mass due to viscous stresses and ω is the specific turbulent dissipation rate which corresponds to the rate of dissipation of turbulence kinetic energy.

The idea behind the SST model is to retain the robust and accurate formulation of the Wilcox $k-\omega$ model in the near wall region while taking advantage of the freestream independence of the $k-\varepsilon$ model in the outer part of the boundary-layer. The SST model is formed by transforming the $k-\varepsilon$ model into a $k-\omega$ formulation which leads to the creation of an additional term, called the cross diffusion term, which appears in the ω -equation. The original $k-\omega$ equations are then multiplied by a blending function F_l , the transformed $k-\varepsilon$ equations by a function $(1-F_l)$ before they are added together. The blending function F_l is designed so that it is one in the near wall region (activating the original $k-\omega$ model) and zero away from the surface (where the $k-\varepsilon$ model is applied). The blending between the models occurs in the wake region of the boundary-layer.

The defining equations of the original $k-\omega$ model (in conservative form) are:

$$\frac{\partial \rho k}{\partial t} + \frac{\partial \rho u_j k}{\partial x_j} = \tau_{ij} \frac{\partial u_i}{\partial x_j} - \beta^* \rho \omega k + \frac{\partial \left[(\mu + \sigma_{k1} \mu_t) \frac{\partial k}{\partial x_j} \right]}{\partial x_j} \quad (4.18)$$

$$\frac{\partial \rho \omega}{\partial t} + \frac{\partial \rho u_j \omega}{\partial x_j} = \frac{\gamma_1}{\nu_t} \tau_{ij} \frac{\partial u_i}{\partial x_j} - \beta_1 \rho \omega^2 + \frac{\partial \left[(\mu + \sigma_{\omega 1} \mu_t) \frac{\partial \omega}{\partial x_j} \right]}{\partial x_j} \quad (4.19)$$

The transformed $k-\varepsilon$ equations are given by:

$$\frac{\partial \rho k}{\partial t} + \frac{\partial \rho u_j k}{\partial x_j} = \tau_{ij} \frac{\partial u_i}{\partial x_j} - \beta^* \rho \omega k + \frac{\partial \left[(\mu + \sigma_{k2} \mu_t) \frac{\partial k}{\partial x_j} \right]}{\partial x_j} \quad (4.20)$$

$$\frac{\partial \rho \omega}{\partial t} + \frac{\partial \rho u_j \omega}{\partial x_j} = \frac{\gamma_2}{\nu_t} \tau_{ij} \frac{\partial u_i}{\partial x_j} - \beta_2 \rho \omega^2 + \frac{\partial \left[(\mu + \sigma_{\omega 2} \mu_t) \frac{\partial \omega}{\partial x_j} \right]}{\partial x_j} + 2 \frac{\rho \sigma_{\omega 2}}{\omega} \frac{\partial k}{\partial x_j} \frac{\partial \omega}{\partial x_j} \quad (4.21)$$

By multiplying Eqs.(4.18) and (4.19) by F_l and Eqs. (4.20) and (4.21) by $(1-F_l)$, and then adding together the corresponding k - and ω -equations, Menter's SST model is obtained [227]:

$$\frac{\partial \rho k}{\partial t} + \frac{\partial \rho u_j k}{\partial x_j} = \tau_{ij} \frac{\partial u_i}{\partial x_j} - \beta^* \rho \omega k + \frac{\partial \left[(\mu + \sigma_k \mu_t) \frac{\partial k}{\partial x_j} \right]}{\partial x_j} \quad (4.22)$$

$$\frac{\partial \rho \omega}{\partial t} + \frac{\partial \rho u_j \omega}{\partial x_j} = \frac{\gamma \tau_{ij}}{\nu_t} \frac{\partial u_i}{\partial x_j} - \beta \rho \omega^2 + \frac{\partial \left[(\mu + \sigma_{\omega} \mu_t) \frac{\partial \omega}{\partial x_j} \right]}{\partial x_j} + 2(1-F_1) \frac{\rho \sigma_{\omega 2}}{\omega} \frac{\partial k}{\partial x_j} \frac{\partial \omega}{\partial x_j} \quad (4.23)$$

Equations (4.22) and (4.23) are the turbulent kinetic energy and turbulent dissipation equations respectively. Physically speaking these equations govern the overall kinetic energy balance in the computational flowfield. Eq. (4.22) controls the rate at which kinetic energy is produced while Eq. (4.23) controls the rate at which it is dissipated (which takes place mostly at the smallest turbulence scales, i.e., the Kolmogorov microscale).

Letting ϕ_l represent any constant in the original k - ω model (σ_{k1}, \dots), ϕ_2 represent any constant in the transformed k - ε model (σ_{k2}, \dots) and ϕ the corresponding constant of the new model (σ_k, \dots), then the relation between them is given by:

$$\phi = F_1 \phi_1 + (1 - F_1) \phi_2 \quad (4.24)$$

This leads to two sets of constants:

Set 1 (ϕ_l) are associated with Wilcox's k - ω model:

$$\sigma_{k_1} = 0.85, \sigma_{\omega_1} = 0.5, \beta_1 = 0.0750 \quad (4.25)$$

$$\beta^* = 0.09, \kappa = 0.41, \gamma_1 = \frac{\beta_1}{\beta^*} - \sigma\omega_1\kappa^2 / \sqrt{\beta^*} \quad (4.26)$$

And set 2 (ϕ_2) are associated with the transformed k - ε model:

$$\sigma_{k_2} = 1.0, \sigma_{\omega_2} = 0.856, \beta_2 = 0.0828 \quad (4.27)$$

$$\beta^* = 0.09, \kappa = 0.41, \gamma_1 = \frac{\beta_2}{\beta^*} - \sigma\omega_2\kappa^2 / \sqrt{\beta^*} \quad (4.28)$$

The turbulent stress tensor (τ_{ij}) in Eqs. (4.22) and (4.23) is computed from:

$$\tau_{ij} = \mu_t \left(\frac{\partial \tilde{u}_i}{\partial x_j} + \frac{\partial \tilde{u}_j}{\partial x_i} - \frac{2}{3} \frac{\partial \tilde{u}_k}{\partial x_k} \delta_{ij} \right) - \frac{2}{3} \rho k \delta_{ij} \quad (4.29)$$

It is also necessary to define the blending function, F_1 . Starting from the surface, the function should be equal to 1 in the near wall region so that k - ω model is used, and it must go to zero in the freestream to ensure the k - ε model is applied.

Menter defined the blending function in terms of the variable arg_1 as:

$$F_1 = \tanh(arg_1^4) \quad (4.30)$$

where arg_1 is given by:

$$arg_1 = \min \left[\max \left(\frac{\sqrt{k}}{0.09\omega y}, \frac{500\nu}{y^2\omega} \right), \frac{4\rho\sigma_{\omega_2}k}{CD_{\omega k}y^2} \right] \quad (4.31)$$

Here y is the distance to the closest point away from the wall surface and $CD_{\omega k}$

corresponds to the cross-diffusion term in Eq.(4.21) (i.e., $2 \frac{\rho\sigma_{\omega_2}}{\omega} \frac{\partial k}{\partial x_j} \frac{\partial \omega}{\partial x_j}$):

$$CD_{\omega k} = \max \left(2 \frac{\rho\sigma_{\omega_2}}{\omega} \frac{\partial k}{\partial x_j} \frac{\partial \omega}{\partial x_j}, 10^{-20} \right) \quad (4.32)$$

The SST model must also be supplemented by the definition for the turbulent eddy viscosity, μ_t :

$$\mu_t = \frac{\rho a_1 k}{\max(a_1 \omega; \sqrt{2S} \cdot F_2)} \quad (4.33)$$

In Eq. (4.33) a_1 is a constant, typically assumed to be 0.31 [227]. S is the absolute strain rate and ω is the turbulent dissipation rate. F_2 is a blending function which allows the SST to transition between an eddy-viscosity model (used in the freestream) and Reynolds stress model (used in the wake region⁴ of the boundary layer where adverse pressure gradients are strongest).

F_2 is defined in a similar manner to F_1 in Eq. (4.30) as:

$$F_2 = \tanh(\arg_2^2) \quad (4.34)$$

$$\arg_2 = \max\left(2 \frac{\sqrt{k}}{0.09 \omega y}; \frac{500 \nu}{y^2 \omega}\right) \quad (4.35)$$

Boundary Conditions:

At a no-slip wall, all of the turbulent quantities, except ω , are set to 0. At the wall ω satisfies the following equation [227]:

$$\omega = 10 \frac{6\nu}{\beta_1 (\Delta y_1)^2} \quad (4.36)$$

where Δy_1 is the distance to the first grid point away from the wall.

At inflow boundaries, the turbulence quantities (k and ω) must be specified, while at outflow boundaries a zero gradient is assumed.

⁴The wake region is the part of the boundary layer where separation or reattachment occurs.

4.2.3 Transport model

Two models are applied to compute species transport properties. At temperature lower than 1000 K, Sutherland's law is used. This is given by:

$$t_i = T^{3/2} \frac{F_{t,i}}{T + G_{t,i}} \quad (4.37)$$

where t_i stands for either μ_i or k_i , and $F_{t,i}$, $G_{t,i}$ are empirical constants.

At temperatures higher than 1000K a more accurate model based on curve fit tabulation proposed by Gupta [228] is utilized:

$$\mu_i = \exp(C_{\mu,i}) T^{A_{\mu,i} \ln T + B_{\mu,i}} \quad (4.38)$$

$$k_i = \exp(E_{f,i}) T^{\left(A_{\mu,i} (\ln T)^3 + B_{f,i} \ln(T)^2 + C_{f,i} \ln T + D_{f,i} \right)} \quad (4.39)$$

where $A_{\mu,i}$, $B_{\mu,i}$, $C_{\mu,i}$, $A_{f,i}$, $B_{f,i}$, $C_{f,i}$, $D_{f,i}$ and $E_{f,i}$ are tabulated curve fit coefficients.

4.2.4 Numerical Methods

The numerical solution of the governing mass, momentum and energy equations is accomplished by using a finite-volume approach with a generalized grid formulation (i.e., both structured and unstructured grids can be handled) in which conservative variables are computed at cell centers. The turbulent equations are solved decoupled (i.e., separately) from the mean flow solver. According to Luke et al., [223] decoupled solvers have improved numerical stability when compared with coupled solvers since the coupling terms between turbulent and mean flow in the Jacobian are more likely to make the matrix ill-conditioned and lead to numerical instability. A more in depth discussion of the numerical methods used in Loci-CHEM can be found in Luke [222].

4.3 Quantification of Numerical Uncertainty

4.3.1 Introduction

Before performing numerical simulations it is important to understand how numerical uncertainty arises and how it is typically quantified.

4.3.2 Numerical Uncertainty

Uncertainty in numerical simulations may arise from three different sources: (i) input uncertainty, (ii) model uncertainty, and (iii) numerical uncertainty [229].

Input uncertainty results from the fact that some input parameters such as the Universal gas constant, the gas thermal conductivity, etc. are not well defined. For example, input uncertainties can arise if the wrong value for the gas thermal diffusivity is specified. This type of uncertainty exists independent of the model or computer code. Input uncertainty can be eliminated or made a second order effect by improving the definition of the input parameter, for example by using a better measured value.

Model uncertainty arises from alternative model formulations, structure, or implementations independent of discretization [229]. For example, a suite of numerical solvers that are using the same stated formulations of different time-averaged turbulence models with similar discretization schemes may produce different predictions for the wall shear stress. Model uncertainty arises in this situation since each code implements these turbulence models differently and was written by different teams. Model uncertainty can be minimized or eliminated by using a different model or even code.

Numerical uncertainty primarily occurs from the influence of discretization and iterative convergence errors, i.e., using finite length, discrete methods to represent a continuum system [229]. Unlike input and model uncertainties which can be mitigated, numerical uncertainty cannot be eliminated but can only be minimized or bounded in a simulation. For example, input uncertainty can be eliminated or made a second-order effect by an improvement of the definition of the input parameter (i.e., a better-measured value). Similarly model uncertainty can be minimized, or potentially eliminated by the use of an enhanced or improved model or even code. It is therefore crucial to be able to minimize and quantify numerical uncertainty.

In the current work an effort was made to ensure that both input and model uncertainties were minimized. This involved specifying all input constants and parameters to a high level of accuracy as well as verifying that the solvers predictions were insensitive to the turbulent and transport models used. Since it was computationally prohibitive to do this for each individual input value or parameter, input and model uncertainty were assessed on a global level by assessing the sensitivity of the numerical predictions to perturbations in key input parameters or to changes in the turbulence or transport model used. For example Figure 4-1 shows the sensitivity of the predicted film cooling effectiveness to the type of turbulence model used. The blowing ratio (λ) is one in this case and the turbulent Prandtl number (Pr_t) is 0.7. The dashed lines corresponds to the Spalart-Allmaras (S-A) model [230], the solid line to Baseline (BSL) turbulence model [227] and the dotted lines correspond to Menter's Shear Stress Transport (SST) model [227]. The figure clearly shows that

numerical predictions are independent of the turbulence model used. This suggests that model uncertainty is not significant in the current simulations.

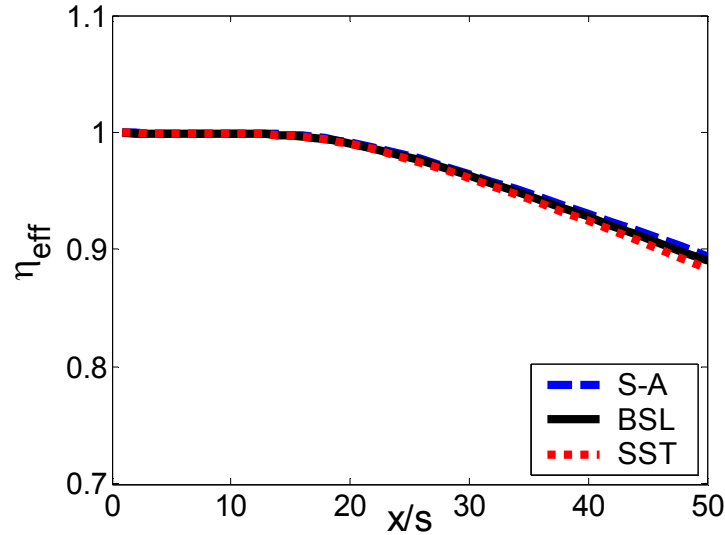


Figure 4-1 Sensitivity of predicted film cooling effectiveness to the type of turbulence model used.

4.3.3 Quantifying Numerical Uncertainty

Several different approaches have been proposed by various authors to quantify uncertainty in numerical simulations [229&231-239]. Of these, the most widely used and well established method was developed by Roache [239] in 1993. Roache proposed a simple method for uniform reporting of grid-convergence studies and numerical errors using the grid-convergence index (GCI). The GCI is based on the generalized Richardson Extrapolation and involves the comparison of discrete solutions at two different grid spacings. It is a method for obtaining a higher-order estimate of the continuum value (i.e., value at zero grid spacing) for a given quantity f from a series of lower-order discrete values.

Richardson Extrapolation, which is also known as ‘ h^2 ,’ or ‘iterated extrapolation,’ or the ‘deferred limit approach,’ was first proposed by Richardson in 1911 [240] and extended in 1927 [241].

A simulation will yield a quantity $f(x,y,z,t)$ that can be expressed in terms of the grid spacing (h) in a general form by the series expansion:

$$f(x,y,z,t) = f(x,y,z,t)_{exact} + g_1 h + g_2 h^2 + g_3 h^3 + \dots \quad (4.40)$$

where the functions g_1 , g_2 , and g_3 are defined in the continuum (i.e., independent of discretization) and $f(x,y,z,t)_{exact}$ is the continuum value at zero grid spacing. Note that for infinitely differentiable solutions, these functions are related to all orders of the solution derivatives through the elementary Taylor series expansions, but this is not a necessary assumption for Richardson Extrapolation. It is only necessary that Eq. (4.40) be a valid definition for the order of the discretization [239].

If a second order solution is assumed (i.e., $g_1 = 0$) and two separate discrete solutions, f_1 and f_2 , are computed on two different grids with uniform discrete spacings, h_1 and h_2 , corresponding to a fine and coarse grid spacing, the leading-order error terms in the error expansion can be eliminated (i.e., by solving for g_2 at the grid points in Eq. (4.40) and substituting this value into Eq. (4.40) to obtain a more accurate estimate of $f(x,y,z,t)_{exact}$). This yields:

$$f(x,y,z,t) = f(x,y,z,t)_{exact} + \frac{(h_2^2 f_1 - h_1^2 f_2)}{(h_2^2 - h_1^2)} + \text{high order terms} \quad (4.41)$$

Letting r equal the grid refinement ratio h_2/h_1 , Eq. (4.41) can be simplified by assuming h is small (which allows the high order terms to be neglected), which yields an approximate expression in the form of a correction to the fine grid solution, f_1 , given by:

$$f[exact] \cong f_1 + \frac{(f_1 - f_2)}{(r^2 - 1)} \quad (4.42)$$

Traditionally, the Richardson method has been applied to grid ‘doubling’ or ‘halving’ (i.e., moving from a coarser to finer grid by a grid refinement ratio of 2), which allows Eq. (4.42) to be expressed as:

$$f[exact] \cong 4/3 f_1 + 1/3 f_2 \quad (4.43)$$

The GCI approach advocated by Roache [239] is based on the generalized theory of Richardson Extrapolation outlined above. The first step in this approach is to approximate the error in a fine grid solution, f_1 , using a fine-grid Richardson error estimate. This is given by:

$$E_1^{fine} = \frac{\varepsilon}{1 - r^p} \quad (4.44)$$

Where $\varepsilon = f_2 - f_1$, and p = the formal order of accuracy of the algorithm. In a similar manner, the error in the coarse grid solution can also be approximated as:

$$E_2^{coarse} = \frac{r^p \varepsilon}{1 - r^p} \quad (4.45)$$

The actual error A_1 of the fine-grid solution can now be expressed following Roache [239] as:

$$A_1 = E_1^{fine} + O(h^{p+l}, E_1^2) \quad (4.46)$$

where $l = 1$ generally or 2 if centered differences are used. E_l is therefore an ordered error estimator (i.e., a good approximation of the discretization error on the fine grid if f_1 and f_2 were obtained with good accuracy ($E_l \ll 1$)).

Following Roache we can account for uncertainty in the generalized Richardson-based error estimates and put all grid convergence studies on a standardized basis, by incorporating a safety factor, F_s , into these estimators. This

leads to the following definitions for the grid convergence indices (GCI) for the fine and coarse grids:

$$GCI_1^{fine} = F_s |E_1| \quad (4.47)$$

$$GCI_2^{coarse} = F_s |E_2| \quad (4.48)$$

When $F_s = 1$ the $GCI_1^{fine} = |E_1|$ and $GCI_2^{coarse} = |E_2|$. This corresponds to an error band associated with the best estimate of the error, which in most instances may be too optimistic. In practice Roache [239] recommends a more conservative safety factor in the range, $1.25 \leq F_s \leq 3$. $F_s = 1.25$ should be used when 3 or more different grids are used to determine convergence, while $F_s = 3$ is recommended when a less rigorous two grid convergence study is performed. It is important to note here that the GCI is a measure of the percentage the computed value for a given quantity is away from the value of the asymptotic numerical value (i.e., it indicates an error band on how far the solution is from the asymptotic value and how much the solution would change with a further refinement of the grid). A small value of GCI indicates that the computation is within the asymptotic range.

Having outlined the GCI method, it is critical to recognize two key underlying assumptions. The first assumption is that accurate application of the generalized Richardson based grid-error estimator requires that the observed and theoretical⁵ convergence rates are equal. As a direct result of this first assumption Roache's GCI method further assumes that the leading-order truncation error term in the error

⁵ A CFD code uses a numerical algorithm that will provide a *theoretical order of convergence*; however, the boundary conditions, numerical models, and grid will reduce this order so that the *observed or actual order of convergence* is in practice lower.

expansion, {see Eq. (4.40)}, dominates the error. This latter assumption implies that the main source of error is due to discretization.

4.4 Validation of Solver

4.4.1 Introduction

Before tackling the problem of simulating the complex mixing and heat transfer occurring in the film cooling process, a series of ‘building block’ exercises was performed in order to validate and build confidence in the performance of the Loci-CHEM solver under subsonic conditions. This has been done by modeling two simple ‘canonical’ flow geometries: a channel flow and a boundary layer flow under both laminar and turbulent conditions. In addition to validating the solver, these exercises are relevant to the actual film cooling problem since both of these flow types are present in the film cooling geometry being simulated (i.e., the flow in the coolant louver is a channel flow, while the core flow is a boundary layer flow).

4.4.2 Channel Flow

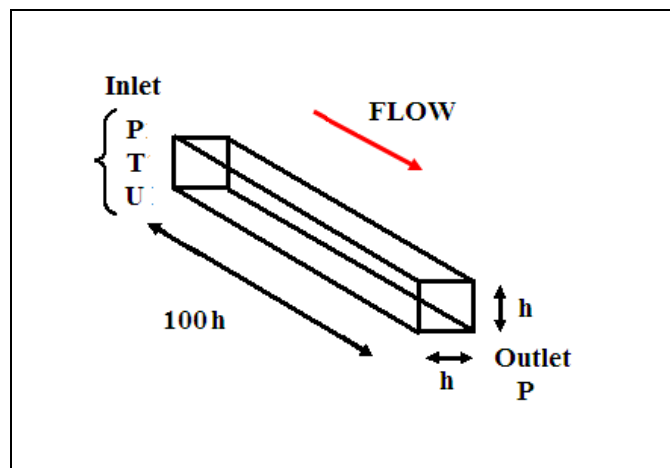


Figure 4-2 Schematic of the channel flow geometry

Laminar as well as turbulent Hagen-Poiseuille Flow (HPF) and Plug Flow (PF) (i.e., developing HPF) simulations were performed using a simple 4.0 mm square-channel geometry shown above in Figure 4-2. The channel is 100 passage heights (i.e., 0.4 m) long. A grid based on this geometry was constructed with the following dimensions: 751 grid points in the stream-wise direction, 61 grid points in the wall-normal and 25 grid points in the spanwise direction. The Reynolds number based on hydraulic diameter was 644 in the laminar case and 5833 in the turbulent case.

Laminar Flow:

Two cases were explored: (i) A developing HPF flow in which a plug flow boundary conditions is applied at the inlet and (ii) a fully developed HPF flow in which a fully developed velocity profile is specified at the inlet. The former case verifies that the solver can correctly capture the development of the velocity profile as it transitions from a flat plug flow profile to a fully developed parabolic profile. The latter case checks that the solver does not predict any evolution in the velocity profile once the flow is laminar and fully developed. In both cases a constant pressure boundary condition is specified at the outlet and all of the cells in the domain are initialized to the inlet conditions. In addition, a no slip boundary condition is applied at the walls, which are also set to be adiabatic. A reflecting boundary condition is applied along the side walls.

The boundary conditions applied in case (i) can be summarized as follows:

$$\begin{aligned}
\text{inlet : } & \begin{cases} P = 101528 Pa \\ U = \bar{U} = 10 m/s \\ T = 300 K \end{cases} \\
\text{outlet : } & P = 101325 Pa \\
\text{upper \& lower walls : } & \text{no slip (adiabatic)} \\
\text{side walls : } & \text{reflecting}
\end{aligned} \tag{4.49}$$

Similarly, the boundary conditions applied in case (ii) can be expressed as follows:

$$\begin{aligned}
\text{inlet : } & \begin{cases} P = 101491 Pa \\ U = \text{profile} \\ \bar{U} = 10 m/s \\ T = 300 K \end{cases} \\
\text{outlet : } & P = 101325 Pa \\
\text{upper \& lower walls : } & \text{no slip (adiabatic)} \\
\text{side walls : } & \text{reflecting}
\end{aligned} \tag{4.50}$$

The velocity profiles specified in each case are shown below in Figure 4-3.

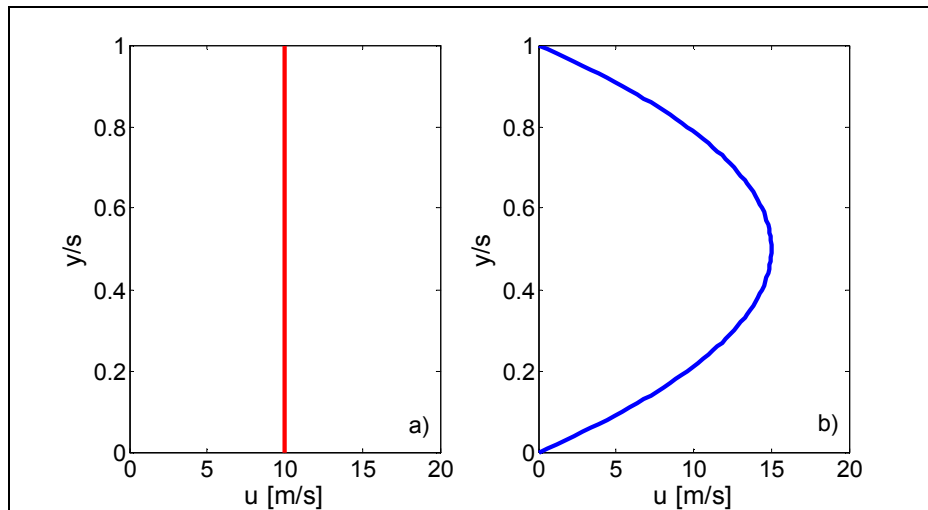


Figure 4-3 Inlet velocity profiles for: a) developing HPF case and b) fully developed HPF case.

Results:

The predictions of the loci-CHEM solver were verified in both the developing and fully developed cases by comparison to the exact Hagen-Poiseuille Flow (i.e., incompressible and laminar channel flow) analytical solution for the velocity and

pressure drop through a constant-area square channel [242]. The pressure drop is given by:

$$\Delta P = \frac{12L\mu Q}{H^4} \quad (4.51)$$

where Q is the volumetric flow rate, $Q = \bar{U} * H^2$, L is the channel length, μ is the dynamic viscosity of the fluid and H is the channel height.

The cross-sectional velocity profile in the channel is:

$$U(y) = \left(\frac{\Delta P}{2\mu L} \right) \left[\left(y - \frac{H}{2} \right)^2 - \left(\frac{H}{2} \right)^2 \right] \text{ for } 0 \leq y \leq H; \quad (4.52)$$

The entrance or development length for the flow in the PF case can be estimated from an empirical correlation from Schlichting [194]:

$$L_e \approx 0.06 Re_{D_h} D_h \quad (4.53)$$

(i) Developing HPF Case:

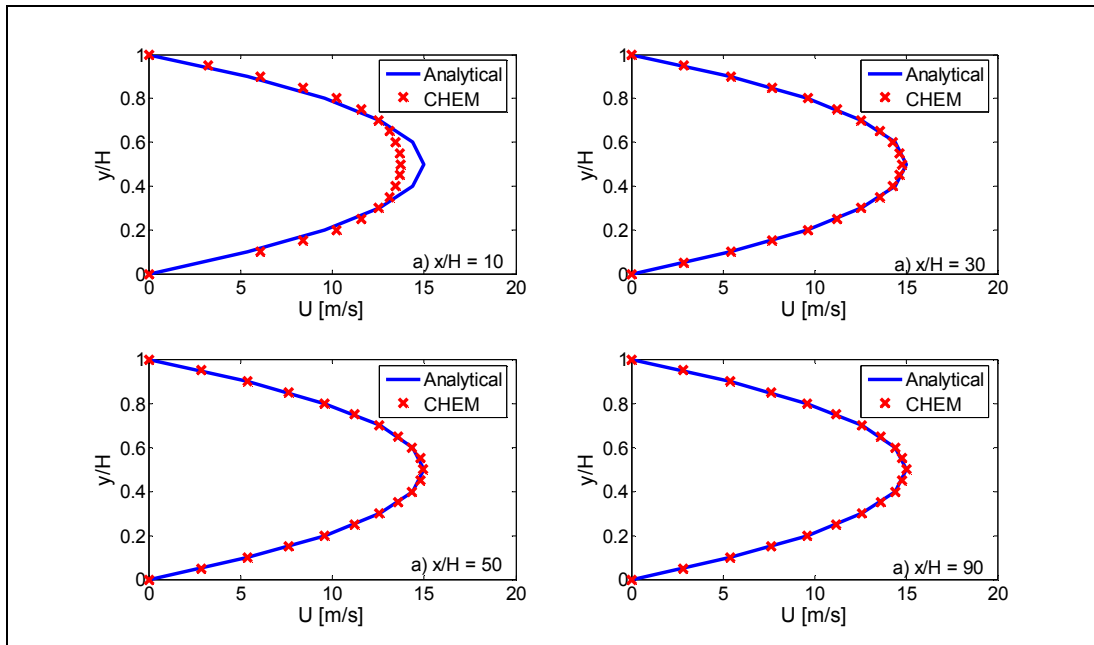


Figure 4-4 Evolution of velocity profile for developing, laminar Hagen-Poiseuille Flow in a square channel at four stream-wise locations: a) $x/H = 10$, b) $x/H = 30$, c) $x/H = 50$ and d) $x/H = 90$.

Figure 4-4 a) – d) show the evolution of the velocity profile for developing HPF at four different down stream locations. The solid line corresponds to the exact analytical solution while the ‘x’ symbols correspond to the predictions of loci-CHEM. Figure 4-4 a) shows that at $x/H=10$, the velocity profile has evolved from the initial plug flow shape shown in Figure 4-3 a), but has not become fully developed. By $x/H=30$, shown in Figure 4-4 b) the velocity profile has developed considerably and is almost matching the exact, fully developed analytical solution. At $x/H=50$ and $x/H=90$, shown in Fig. 4-4 c) and d) respectively, the velocity profiles are both fully developed. This is confirmed by the fact that they match the analytical solution to within an rms error of 0.01% once the flow becomes fully developed. To gain further insight into the development of the flow it is useful to also look at the evolution of the pressure along the length of the channel.

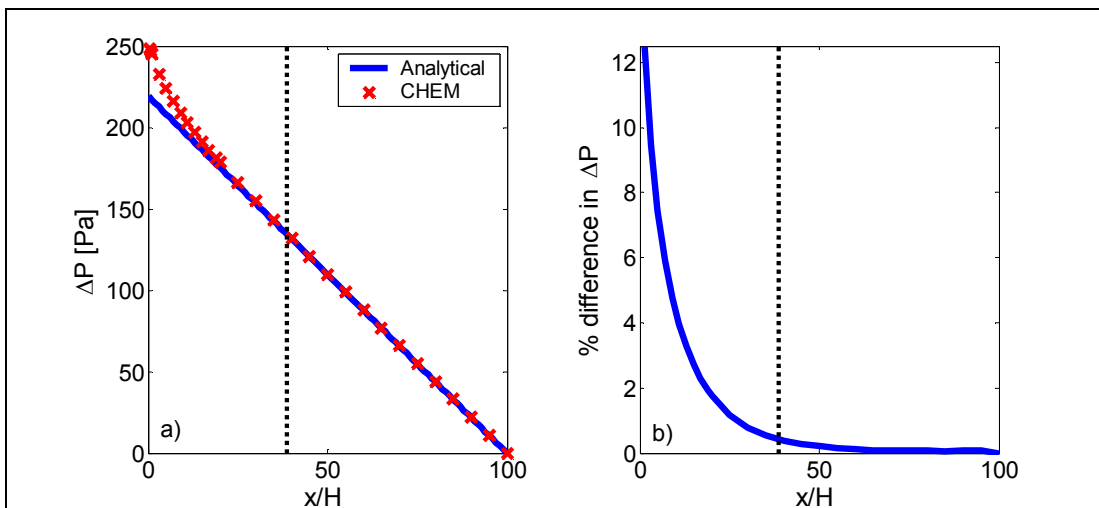


Figure 4-5 a) Streamwise evolution of the pressure for developing, laminar Hagen-Poiseuille Flow in a square channel. b) Per cent difference between the analytical solution and numerical predictions for the pressure drop along the square channel for developing, laminar Hagen-Poiseuille Flow in square channel.

Figure 4-5 a) shows the streamwise evolution of the pressure for developing, laminar Hagen-Poiseuille Flow in a square channel. The solid line corresponds to the

analytical solution for fully developed laminar flow, while the ‘x’ symbols correspond to the predictions of loci-CHEM. The plot shows that near the start of the channel ($x/H = 0$) the pressure drop exceeds the exact solution by roughly 30 Pa, however, by $x/H \approx 40$ the pressure distribution predicted by CHEM matches the exact solution. This region in which the pressure is transitioning from its initial value to the analytically predicted value is often termed the ‘*entrance region*’. It corresponds to the growth and development of the boundary layer along the upper and lower channels walls. When the boundary layers merge, the flow is then said to be fully developed. For the conditions explored in this case, the empirical correlation in Eq. (4.53) predicts that the entrance length should occur at $x/H \approx 38.6$ (indicated by the dashed lines in Figure 4-5 a) and b)). Figure 4-5 b) shows the per cent difference between the analytical solution and CHEM’s predictions for the pressure drop along the square channel. In the entrance region corresponding to $x/H < 38.6$ the difference between CHEM’s predictions and the exact solution is as high as 12.5%. However, once the flow becomes fully developed the difference drops to less than 0.5%. These results confirm that the Loci-CHEM solver can correctly capture the development of laminar flow in a channel as it transitions to being fully developed.

(i) Fully Developed HPF Case:

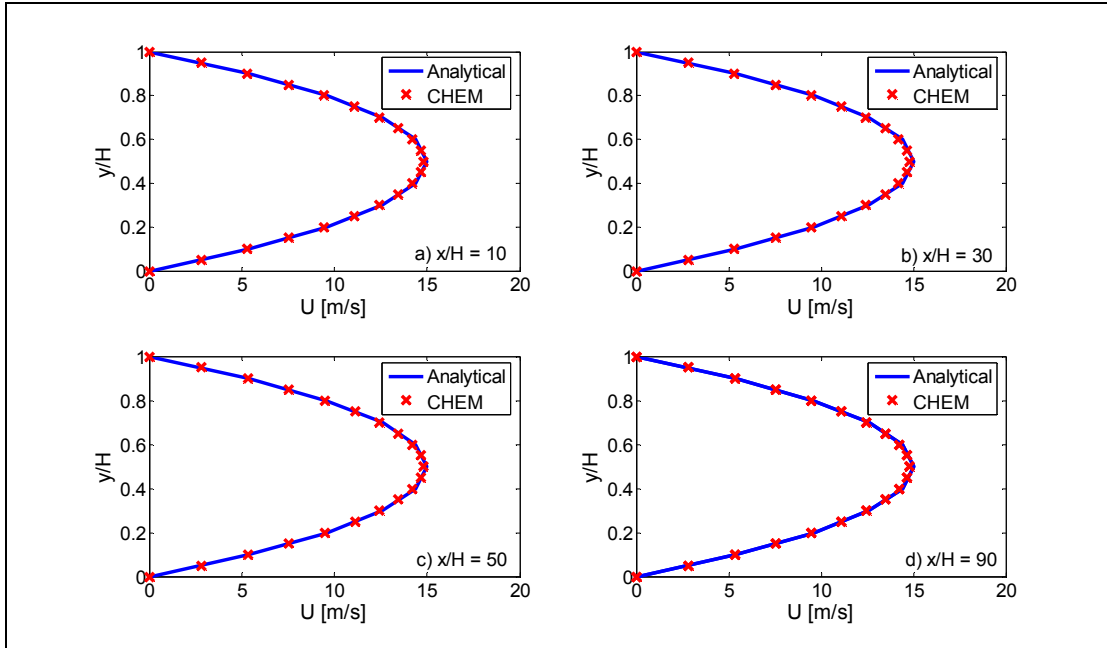


Figure 4-6 Evolution of velocity profile for fully developed, laminar Hagen-Poiseuille Flow in a square channel at four stream-wise locations: a) $x/H = 10$, b) $x/H = 30$, c) $x/H = 50$ and d) $x/H = 90$.

Figure 4-6 a) – d) are plots showing the evolution of the velocity profile for the case of fully developed HPF at four different down stream locations. The solid line corresponds to the analytical solution for fully developed flow while the ‘x’ symbols correspond to the predictions of loci-CHEM. Figure 4-6 a) shows that at $x/H=10$, the velocity profile has not evolved from the initial fully developed profile shown in Figure 4-3 b). At $x/H=30$, $x/H=50$ and $x/H=90$ Figure 4-6 b), c) and d) respectively show that the velocity profile, as expected, does not evolve along the length of the channel and remains within an rms error of 0.15% of the analytical solution throughout. This occurs because the flow at the inlet is already fully developed and therefore there is no development region as there was in the previous case. Further evidence for the absence of flow development can be gleaned from the evolution of the pressure along the length of the channel, shown in Figure 4-7 a). The

figure shows that the pressure drop predicted by CHEM closely matches the exact analytical solution along the entire length of the channel. Figure 4-7 b) shows that the difference between the analytical solution and CHEM's predictions for the pressure drop is less than 0.5% over the entire length of the channel. These results show that the Loci-CHEM solver does not predict any evolution in a fully developed, laminar channel flow.

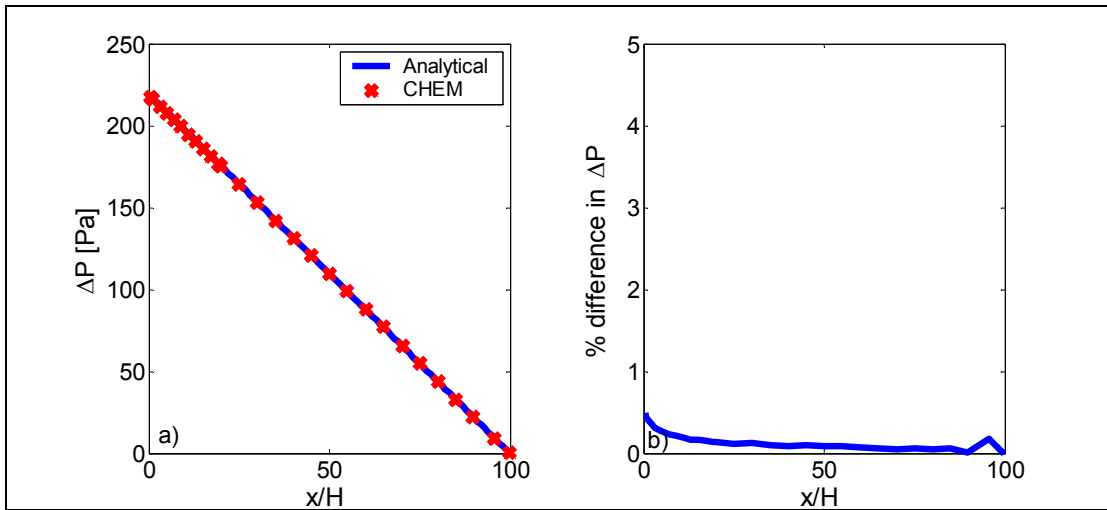


Figure 4-7 a) Stream-wise evolution of the pressure in case (ii). b) Per cent difference between the analytical solution and numerical predictions for the pressure drop along the square channel for case (ii).

Turbulent Flow:

Having verified that Loci-CHEM produces physically reasonable solutions for laminar channel flows, the next step is to examine the solver's performance under turbulent conditions. As before, two cases are explored: (i) A developing turbulent flow in which a plug flow boundary condition is applied at the inlet and (ii) a fully developed turbulent flow in which a fully developed velocity profile is specified at the inlet. In both cases a constant pressure is specified at the outlet and all of the cells in the domain are initialized to the inlet conditions. A no slip boundary condition is applied at the upper and lower walls which are also set to be adiabatic. A reflecting

boundary condition is applied along the side walls. Menter's Shear Stress Transport (SST) turbulence model [227] was used in both cases. Estimates for the values of the turbulent kinetic energy, k , and, the turbulent eddy viscosity, μ_t , at the inlets were made by assuming an initial turbulence intensity, $I_v = 0.05$, and by applying the following formulae [243]:

$$k = \frac{3}{2}(I_v \bar{U})^2 \quad (4.54)$$

$$\mu_t = \frac{\rho k}{\omega} \quad (4.55)$$

ω is the specific turbulent dissipation rate, which is given by $\omega = C_\mu^{-1/4} \sqrt{k}/\ell$. C_μ is a turbulent model constant typically assumed to be 0.09, and ℓ is a characteristic turbulent length scale assumed to be equal to the channel half height.

The boundary conditions applied in case (i) are:

$$\begin{aligned} \text{inlet} : & \begin{cases} P = 101664 \text{ Pa} \\ U = \bar{U} = 23 \text{ m/s} \\ T = 296 \text{ K} \end{cases} \\ \text{outlet} : & P = 101134 \text{ Pa} \\ \text{upper \& lower walls} : & \text{no slip (adiabatic)} \\ \text{side walls} : & \text{reflecting} \end{aligned} \quad (4.56)$$

Similarly, the boundary conditions applied in case (ii) are:

$$\begin{aligned} \text{inlet} : & \begin{cases} P = 101600 \text{ Pa} \\ U = \text{profile} \\ \bar{U} = 23 \text{ m/s} \\ T = 296 \text{ K} \end{cases} \\ \text{outlet} : & P = 101134 \text{ Pa} \\ \text{upper \& lower walls} : & \text{no slip (adiabatic)} \\ \text{side walls} : & \text{reflecting} \end{aligned} \quad (4.57)$$

The velocity profiles specified in each case are shown below in Figure 4-8.

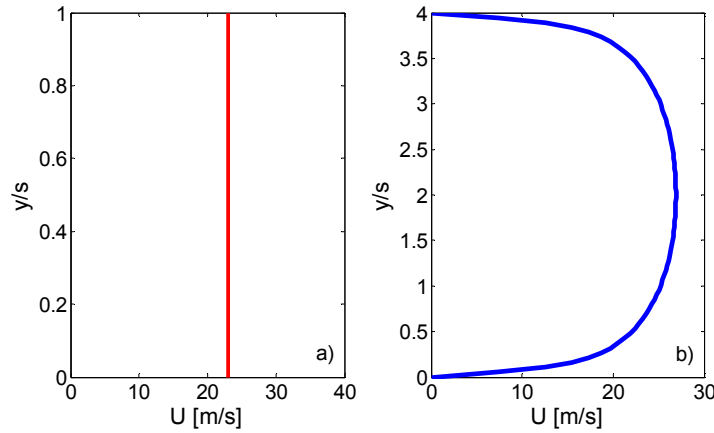


Figure 4-8 Inlet velocity profiles specified for: a) the developing turbulent channel case and b) the fully developed turbulent channel flow case.

Results:

The numerical predictions were verified in both the developing and fully developed cases by comparison to empirical correlations for turbulent channel flow. The pressure drop along the channel can be estimated using the Darcy-Weisbach equation [242]:

$$h_f = f \frac{L}{D_h} \frac{\bar{U}^2}{2g} \quad (4.58)$$

where h_f is the ‘head loss,’ f is the Darcy friction factor, L is the length of the channel, D_h is the hydraulic diameter, \bar{U} is the average velocity, and g is the acceleration due to gravity. The head loss is defined as:

$$h_f = \frac{\Delta P}{\rho g} \quad (4.59)$$

where ρ is the fluid density.

Substituting Eq. (4.59) into Eq. (4.58) yields an expression for the pressure drop, ΔP , along the channel:

$$\Delta P = f \frac{L}{D_h} \frac{\rho \bar{U}^2}{2} \quad (4.60)$$

The friction factor in Eq. (4.60) can be computed by using an approximate, explicit formula proposed by Haaland [244]:

$$f = \left[\left(1 / \left(-1.8 \log \left[\frac{6.9}{Re_{D_h}} + \left(\frac{\varepsilon/D_h}{3.7} \right)^{1.11} \right] \right) \right)^{-1} \right]^2 \quad (4.61)$$

ε/D_h is the relative roughness, which is assumed to be 0.0001. This corresponds to a very smooth pipe.

The entrance length in the developing turbulent flow case is estimated from an empirical correlation from White [242]:

$$L_e \approx 4.4 D_h Re_{D_h}^{1/6} \quad (4.62)$$

The fully developed turbulent velocity is approximated using the 1/7th power law from Schlichting [194]:

$$U = \begin{cases} U_{max} \left(\frac{y}{H/2} \right)^{1/7} & \text{for } 0 < y \leq H/2 \\ U_{max} \left(\frac{H-y}{H/2} \right)^{1/7} & \text{for } H/2 < y \leq H \end{cases} \quad (4.63)$$

Here U_{max} is the maximum centerline velocity in the channel.

(i) Developing Turbulent Channel Flow Case:

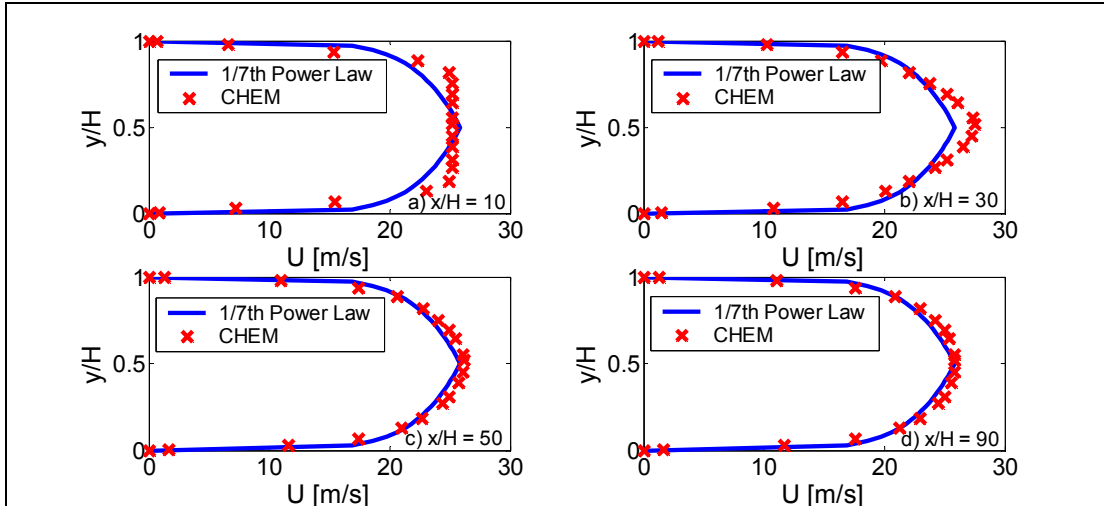


Figure 4-9 Evolution of velocity profile for developing, turbulent flow in a square channel at four stream-wise locations: a) $x/H = 10$, b) $x/H = 30$, c) $x/H = 50$ and d) $x/H = 90$.

Figure 4-9 a) – d) shows the evolution of the velocity profile for developing turbulent channel flow at four different downstream locations. The solid line corresponds to the 1/7th power law correlation from Schlichting [194] while the ‘x’ symbols correspond to the predictions of loci-CHEM at $x/H = 10, 30, 50$ and 90 . Figure 4-9 a) shows that at $x/H=10$, the velocity profile has evolved from the initial plug flow shape shown in Figure 4-8 a) but has not become fully developed. By $x/H=30$ (Figure 4-9 b)) the velocity profile has developed considerably but it still has not reached a fully developed state. By $x/H=50$ and $x/H=90$, shown in Fig. 4-9 c) and d) respectively, the velocity profiles are both fully developed with the CHEM predictions agreeing with the analytical solution to within an rms error of 1.6%. As before it is useful to also check the evolution of the pressure along the length of the channel.

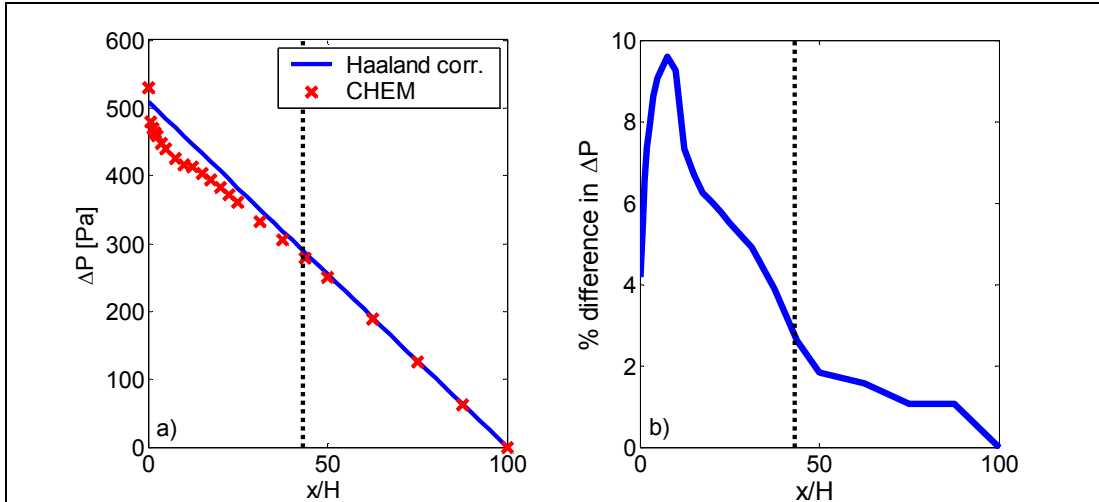


Figure 4-10 a) Stream-wise evolution of the pressure for developing turbulent channel flow. b) Per cent difference between the analytical solution and numerical predictions for the pressure drop associated with developing turbulent channel flow.

Figure 4-10 a) shows the streamwise evolution of the pressure for the developing turbulent channel flow case. The solid line corresponds to the pressure drop computed using Eq. (4.60) and Eq. (4.61) and the 'x' symbols correspond to the predictions of CHEM. The plot shows that at the channel entrance ($x/H = 0$), the pressure predicted by CHEM exceeds the correlation by roughly 15 Pa ($\sim 4\%$). However, thereafter it decreases at a faster rate than estimated by the correlation until $x/H \approx 15$. The pressure then declines at a much slower rate until it asymptotes to the value predicted by the correlation near $x/H \approx 45$. Beyond this point, the correlation and numerical predictions match to within 2.7% as shown in Fig. 4-10 b). As in the laminar case, the region in which the pressure changes rapidly (and does not match the correlation) corresponds to the 'entrance' or 'development' region. For the conditions explored here, the entrance length predicted by CHEM is within 5% of the value predicted by Eq. (4.48) of $x/H \approx 43.2$. These results indicate that Loci-CHEM correctly captures the development of turbulent flow in a channel.

(i) Fully Developed Turbulent Channel Flow Case:

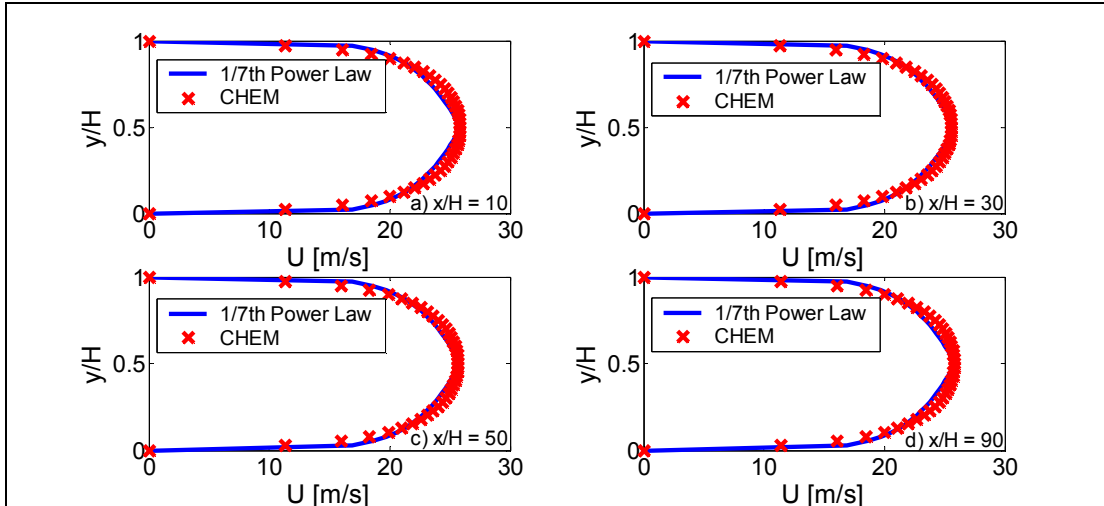


Figure 4-11 Evolution of velocity profile for fully developed, turbulent channel flow at four stream-wise locations: a) $x/H = 10$, b) $x/H = 30$, c) $x/H = 50$ and d) $x/H = 90$.

Figure 4-11 a) – d) show the evolution of the velocity profile for the case of fully developed HPF at four different downstream locations. The solid line corresponds to the 1/7th power law correlation from Schlichting [194] while the ‘x’ symbols correspond to the predictions of loci-CHEM at $x/H = 10, 30, 50$ and 90 . Figure 4-11 a) shows that at $x/H=10$, the velocity profile has not evolved from the initial fully developed profile shown in Figure 4-8 b). At $x/H = 30, x/H = 50$ and $x/H = 90$ Figure 4-11 b), c) and d) all show that the velocity profile, as expected, does not evolve along the length of the channel and remains within an rms error of 1.5% of the analytical solution throughout. This occurs because the flow at the inlet is already fully developed.

Figure 4-12 a) and b) provide further evidence that the flow is fully developed. The figures show that the pressure drop predicted by CHEM matches the empirical correlation to within 2% along the entire length of the channel. Based on

these results it can be concluded that the Loci-CHEM solver correctly predicts fully developed turbulent channel flow.

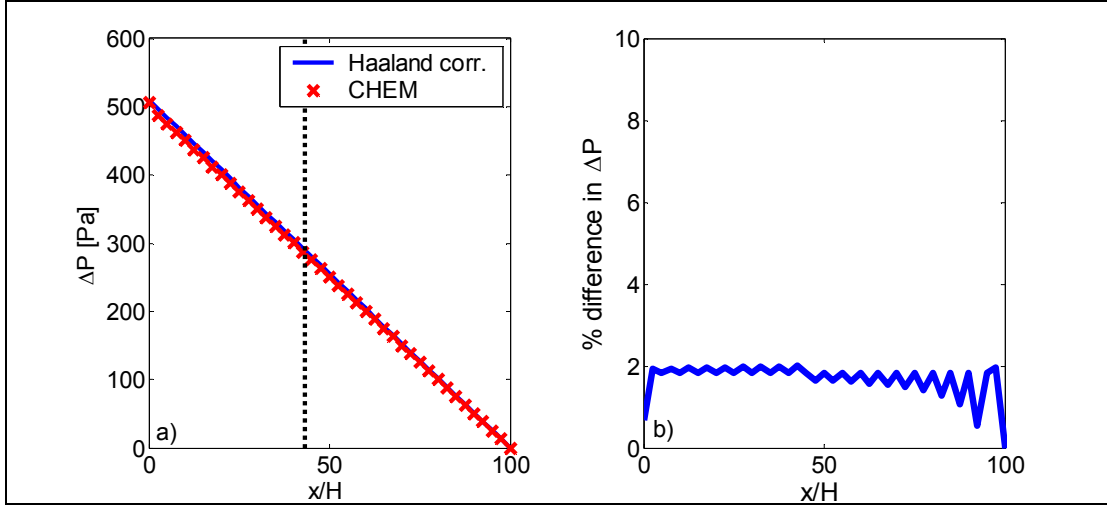


Figure 4-12 a) Stream-wise evolution of the pressure for fully developed turbulent channel flow. b) Per cent difference between the analytical solution and numerical predictions for the pressure drop associated with fully developed turbulent channel flow.

An additional validation exercise is to check whether the fully developed turbulent flow predicted by the solver obeys the ‘Law of the wall’ for both the predicted, mean velocity and temperature profiles. In order to do this the velocity, temperature and wall-normal distance must be put into dimensionless form [245]:

$$y^+ = \frac{U_\tau y}{\nu} \quad (4.64)$$

$$u^+ = \frac{U}{U_\tau} \quad (4.65)$$

$$\theta^+ = \frac{T_w - T}{T_r} \quad (4.66)$$

Here T_w is the wall surface temperature, U_τ and T_r are the friction velocity and friction temperature respectively. The latter are defined as follows:

$$U_\tau = \sqrt{\frac{\tau_{wall}}{\rho}} \quad (4.67)$$

$$T_r = \frac{\dot{q}_w}{\rho C_p U_\tau} \quad (4.68)$$

According to the “Law of the Wall”, the flow near the wall can be divided into three distinct regions. The viscous sublayer, the buffer layer and the logarithmic or ‘log’ layer. The velocity and temperature profiles scale as follows in the viscous sublayer ($y^+ \leq 5$):

$$u^+ = y^+ \quad (4.69)$$

$$\theta^+ = Pr y^+ \quad (4.70)$$

Pr is the Prandtl number, which was 0.75 in this case.

In the log layer which spans the range $30 \leq y^+ \leq 200$ the velocity and temperature scale as:

$$u^+ = \frac{1}{\kappa_1} \ln(y^+) + C_1 \quad (4.71)$$

$$\theta^+ = \frac{1}{\kappa_2} \ln(y^+) + C_2 \quad (4.72)$$

In these expressions $\kappa_1 = 0.302$ for the mean velocity profile, $\kappa_2 = 0.254$ for the mean temperature profile, $C_1 = 2.458$ for the mean velocity profile and $C_2 = -0.633$ for the mean temperature profile.

The buffer layer is located in between the viscous sublayer and the log layer ($5 \leq y^+ \leq 30$). In this region none of the previous wall laws apply.

Figure 4-13 shows mean velocity and temperature profiles expressed in terms of wall units for fully developed turbulent channel flow. The solid lines show the predictions of the loci-CHEM solver, while the dotted lines correspond to the wall laws for the viscous sublayer and log layers. Figure 4-13 a) and b) show that the mean

velocity and temperature profiles predicted by CHEM closely follow the wall law formulae in the viscous sublayer and the log layer. These results indicate that the numerical solver provide further confirmation that the numerical solver gives reasonable predictions of the mean velocity and temperature profiles under turbulent conditions.

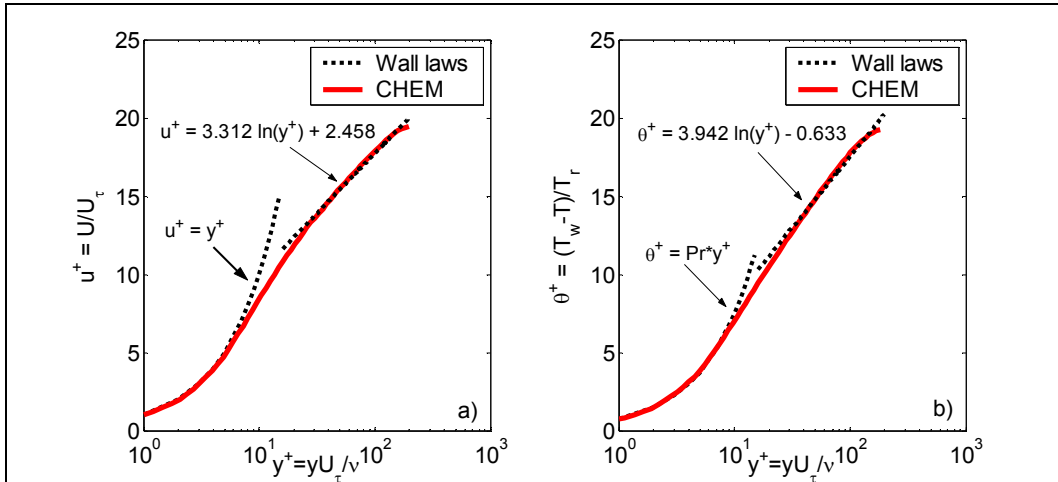


Figure 4-13 Mean velocity (a) and temperature (b) profiles in wall units predicted by LOCI-CHEM for fully developed turbulent channel flow. Note for these simulations the wall temperature (T_w) was fixed at 300K.

4.4.3 Boundary Layer Flow

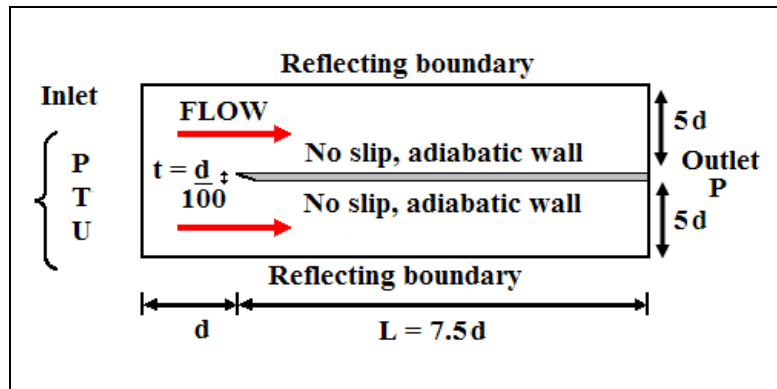


Figure 4-14 Schematic of the geometry used in the boundary-layer flow simulations.

Laminar and turbulent boundary layer simulations were performed using the simple flat-plate geometry illustrated in Figure 4-14 to check the solver's performance on subsonic external flows. The dimensions of the plate are $L = 0.75$ m

and $t = 0.001$ m. The width of the plate into the plane is 0.001 m. Also, a separation distance, $d = 0.1$ m was specified between the inflow plane and the start of the plate to allow the flow to develop ‘naturally’ over the plate. The computational grid has the following dimensions: 501 grid points in the stream-wise direction, 151 grid points in the wall-normal and 2 grid points in the spanwise direction. The grid spacing was carefully chosen to ensure that the near wall velocity and temperature gradients were adequately resolved (i.e., that $y^+ < 1$). The peak Reynolds number based on streamwise distance, Re_x , was 5.95×10^5 for the laminar case and 4.1×10^7 for the turbulent case.

In both cases a uniform velocity was applied along the entrance of the domain while a constant pressure boundary condition was specified at the outlet. All of the cells were initialized to the conditions at the inlet. A no slip boundary condition was applied at the walls which are also set to be adiabatic. Reflecting boundary conditions were applied along the side walls and outer boundaries. Menter’s Shear Stress Transport (SST) turbulence model [227] was used for the turbulent case. Estimates for the values of the turbulent kinetic energy, k , and the turbulent eddy viscosity, μ_t , at the inlets were made by assuming an initial turbulence intensity, $I_v = 0.05$, and by applying the formulae in Eq. (4.54) and Eq. (4.55). The boundary conditions applied in the laminar and turbulent cases are summarized in Eq. (4.73) and Eq. (4.74):

$$\begin{aligned}
 & \text{inlet : } \begin{cases} P = 101311 Pa \\ U = \bar{U} = 25 m / s \\ T = 300 K \end{cases} \\
 & \text{outlet : } P = 101071 Pa \\
 & \text{upper \& lower plate walls : no slip (adiabatic)} \\
 & \text{side walls \& outer boundaries : reflecting}
 \end{aligned} \tag{4.73}$$

$$\begin{aligned}
& \text{inlet : } \begin{cases} P = 101311Pa \\ U = \bar{U} = 100m/s \\ T = 100K \end{cases} \\
& \text{outlet : } P = 101071Pa \\
& \text{upper \& lower plate walls : no slip (adiabatic)} \\
& \text{side walls \& outer boundaries : reflecting}
\end{aligned} \tag{4.74}$$

Results:

The loci-CHEM results were validated by comparing to analytical solutions and empirical correlations for the skin friction and velocity profile

The Blassius solution [242] for a laminar, incompressible, flat-plate boundary layer was used to validate the numerical predictions in the laminar case. The laminar wall shear stress, $\tau_{wall,lam}$, and dimensionless velocity profile, u/U , are given by :

$$\tau_{wall,lam} = \frac{0.332\rho^{1/2}\mu^{1/2}U^{3/2}}{x^{1/2}} \tag{4.75}$$

where Re_x is the Reynolds number based on streamwise position.

$$\frac{u}{U} \approx \left[\frac{2y}{\delta} - \left(\frac{y}{\delta} \right)^2 \right], 0 \leq y \leq \delta(x) \tag{4.76}$$

Here δ is the boundary layer thickness, y is the wall-normal distance, and U is the free-stream velocity. Equation (4.76) is a correlation by von Karman [246].

In the turbulent case, the turbulent wall shear stress, and dimensionless velocity profile are given by the following correlations:

$$\tau_{wall,turb} = \frac{0.0135\rho^{6/7}\mu^{1/7}U^{13/7}}{x^{1/7}} \tag{4.77}$$

$$\frac{u}{U} \approx \left(\frac{y}{\delta} \right)^{1/7}, 0 \leq y \leq \delta(x) \tag{4.78}$$

Here Eq. (4.78) is an approximation suggested by Prandtl [242].

In the numerical simulations, the wall shear stress was output directly from the solver, while, the boundary layer thickness, δ , was computed by finding the wall-normal locations at which the velocity was 99% of the free-stream velocity:

$$\delta = y|_{u=0.99U} \quad (4.79)$$

(i) *Laminar Boundary Layer Case:*

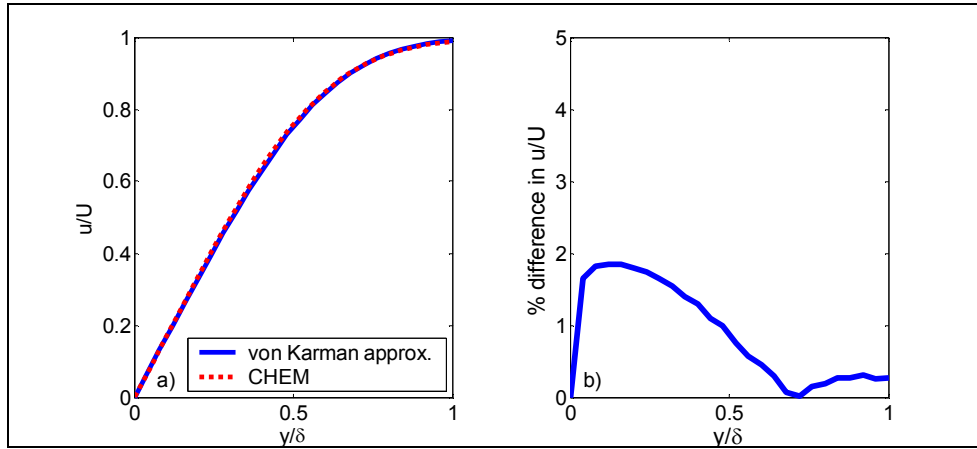


Figure 4-15 a) Dimensionless velocity, u/U , as a function of dimensionless vertical distance, y/δ , for a laminar, incompressible flat-plate boundary layer at $Re_x = 5.0 \times 10^5$. b) Per cent difference between the CHEM predictions and von Kármán approximation for u/U .

Figure 4-15 a) compares the dimensionless velocity profile predicted by CHEM (dotted line) to the von Kármán approximation [246] (solid line) for a laminar, incompressible flat-plate boundary layer under the conditions given by Eq. (4.73). Figure 4-15 b) shows that the velocity profile predicted by CHEM matches the approximation to within a maximum difference of 1.9%.

To further evaluate CHEM's performance in this flow regime, the wall shear stress distribution along the length of the flat plate can be examined. Figure 4-16 a) shows wall shear stress as a function of Re_x for the same conditions explored in Figure 4-15. Figure 4-16 b) shows that when $Re_x > 2.0 \times 10^5$ CHEM's prediction of

the wall shear stress (dotted line) matches the exact Blasius solution (solid line) to within 5%. The large discrepancy (>40%) near the leading edge of the plate (i.e., $0 < Re_x < 2.0 \times 10^5$) is probably due to the fact that at the leading edge of the plate some of the assumptions in the Blasius model are not valid. In particular the assumption that the x -component of the velocity is much larger than the y -component of the velocity (i.e., $u \gg v$) is likely invalid. It is also important to note that the plate has a finite thickness which created a stagnation point at the leading edge of the plate in the simulation which is not accounted for in Blasius's solution. Overall these results suggest that Loci-CHEM can be used to obtain reasonable predictions of laminar boundary layer flows.

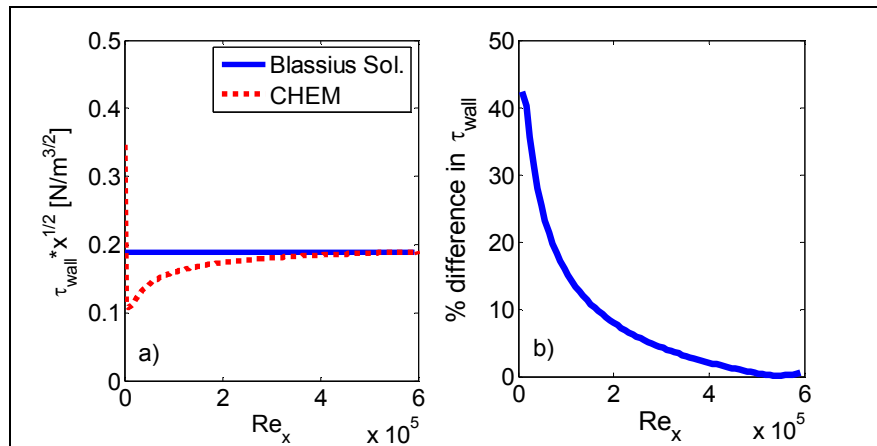


Figure 4-16 a) Wall shear stress multiplied by the square root of the streamwise distance, $\tau_{wall} * x^{1/2}$, as a function of Reynolds number based on streamwise distance, Re_x , for a laminar, incompressible flat-plate boundary layer at a free-stream velocity of 25m/s (Peak $Re_x = 5.95 \times 10^5$). b) Per cent difference between the CHEM predictions and the exact Blasius solution for the wall shear stress associated with a laminar, incompressible flat-plate boundary layer at a free-stream velocity of 25m/s (Peak $Re_x = 5.95 \times 10^5$)

(ii) Turbulent Boundary Layer Case:

Figures 4-17 and 4-18 show similar comparisons for turbulent flows. Once again, the solid lines correspond to the correlations (Eqs. 4.77 and 4.78) while the dotted lines show the numerical results. The figures show that the numerical

predictions match the correlations to within 2.8% in the regions far downstream from the leading edge ($Re_x > 1.5 \times 10^7$) of the plate where the flow is fully developed. As before, the large discrepancy near the beginning of the plate is likely due to the finite thickness of the plate, which created a stagnation point at the leading edge of the plate. Taken together, the channel flow and boundary layer simulations indicate that Loci-CHEM produces solutions that are consistent with established understanding of these flows. This gives us confidence that Loci-CHEM is an appropriate tool for investigating subsonic film cooling problems.

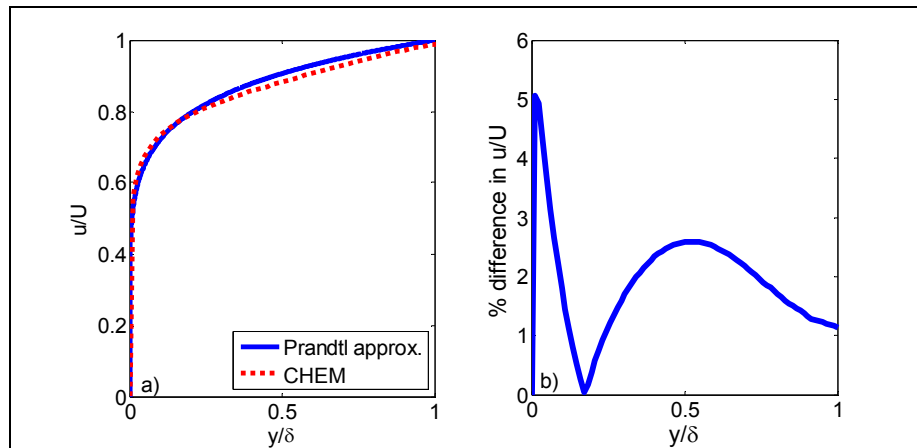


Figure 4-17 a) Dimensionless velocity, u/U , as a function of dimensionless vertical distance, y/δ , for a turbulent flat-plate boundary layer at $Re_x = 4.0 \times 10^7$. b) Per cent difference between CHEM's predictions and Prandtl's $1/7^{\text{th}}$ power approximation for u/U .

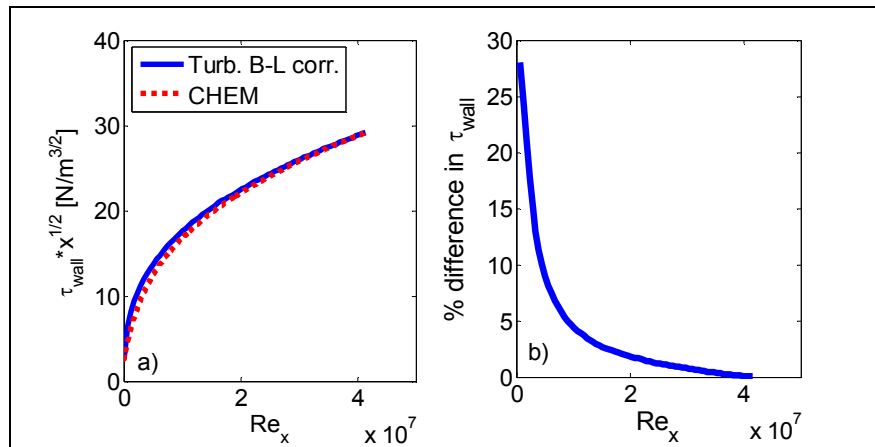


Figure 4-18 a) Wall shear stress multiplied by the square root of the streamwise distance, $\tau_{wall} * x^{1/2}$, as a function of Reynolds number based on streamwise distance, Re_x , for a turbulent flat-plate boundary layer at a free-stream velocity of 100m/s (Peak $Re_x = 4.1 \times 10^7$). b) Per cent difference between the CHEM predictions and the turbulent boundary layer correlation.

4.5 Description of Subsonic Film Cooling Numerical Simulations

4.5.1 Introduction

Having validated the Loci-CHEM solver using simple canonical flow problems, the next step was to apply it to the film cooling problem. This was done by simulating the subsonic slot-jet film cooling experiment performed by Cruz et al. [187]. To minimize computational expense, a methodology, employing RANS precursor simulations to obtain detailed turbulence information for the inlets, was devised. The numerical predictions are then compared to experimental measurements of various quantities including the film cooling effectiveness and the skin friction.

4.5.2 Description of Subsonic Film Cooling Experiment

Hot Wind Tunnel Facility and Test Section

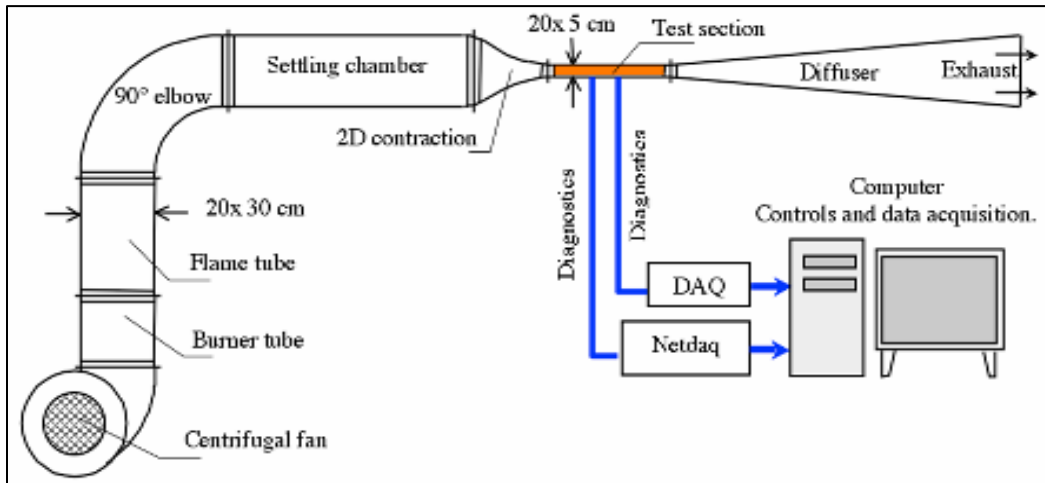


Figure 4-19 Schematic of the hot wind tunnel facility used by Cruz et al. [187] to make subsonic slot-jet film cooling measurements {From Cruz et al. [187]}.

Figure 4-19 is a schematic diagram of the hot wind tunnel facility used by Cruz et al. [187] in their subsonic slot-jet film cooling measurements. The wind tunnel is an open circuit system in which a centrifugal fan drives air through an in-

line methane burner to produce a hot ($T \approx 450\text{K}$) stream of gas. This hot stream passes through a 90-degree elbow with turning vanes (necessary to remove some of the swirl from the fan) and a settling chamber with flow control devices before passing through a two-dimensional convergent section with a 6:1 contraction ratio and into the test section illustrated in Figure 4-20 a). Compressed air injected parallel to the test-section wall through a louver that creates the film cooling flow. The flow exits the test section via an optimized two-dimensional diffuser which exhausts into a fume hood equipped with its own fan.

The velocity of the core flow in the tunnel is regulated by a controller which allows the speed of the centrifugal fan to be varied. The wind tunnel produces velocity ratios U_c/U_∞ ranging from 0.5 to 3 and maximum absolute temperature ratios T_∞/T_c up to 2. Blowing ratios, λ , ranging from 0.75 to 5 can be achieved. In addition, the experimental slot injection Reynolds numbers Re_s , are in range from 2000 to 6000.

The idea is to simulate the canonical film cooling configuration illustrated in Figure 4-20 b) in which a developing shear layer separates flow along the wall from the core flow. A CaF_2 window opposite the film cooled wall provides optical access for infrared wall temperature measurements. The test section is also equipped with access ports at various downstream locations for thermocouple and pitot probes. These probes can be traversed to measure velocity and temperature profiles above the film cooled wall. Velocity profiles above the film cooled wall are also measured using particle image velocimetry. The laser sheet illuminates the flow through a quartz window that replaces the CaF_2 window and the camera views the flow through

another window that is perpendicular to the film cooled wall. A much more detailed description of the diagnostics is presented elsewhere [187&247].

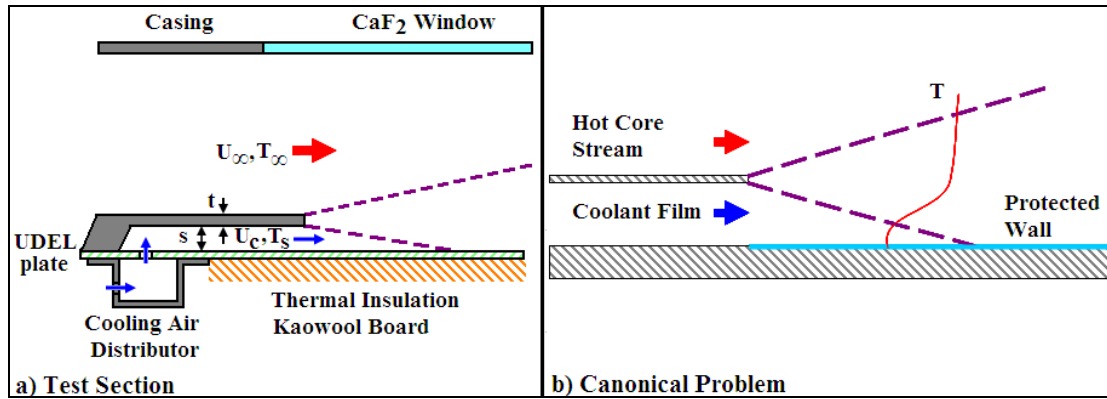


Figure 4-20 a) Test section used by Cruz et al. [187] to make subsonic slot-jet film cooling measurements {Adapted from Cruz et al. [187]}. b) Schematic illustration of the canonical film cooling configuration.

Test Matrix

Three different blowing ratios were investigated by Cruz et al. [187]: a wall-wake flow ($\lambda = 0.6$), a minimum shear flow ($\lambda = 1.3$) and a wall jet flow ($\lambda = 3.0$). A detailed summary of these test conditions is given below in Table 4.1.

λ	R	s [mm]	$I_{v,c}$	$I_{v,\infty}$	U_c [m/s]	U_∞ [m/s]	T_s [K]	T_∞ [K]	Re_s
0.66	2.30	4.0	0.0249	0.0366	10.82	24.86	304.78	462.02	2631
1.34	1.16	4.0	0.0593	0.0412	19.13	22.10	298.88	454.33	4698
2.98	0.52	4.0	0.1018	0.0427	21.20	11.10	296.33	462.92	5297

Table 4.1 Summary of the subsonic slot-jet film cooling test conditions explored by Cruz et al. [187].

Here Re_s is the slot Reynolds number which is defined by the bulk slot exit velocity, the slot height and the kinematic viscosity at the temperature of the coolant,

$$Re_s = \frac{U_c s}{\nu(T_s)} \text{ and } R \text{ is the core-to-coolant stream velocity ratio, } R = \frac{U_\infty}{U_s}.$$

Measurement Uncertainties

Uncertainty in the flow temperatures are small +/- 0.25 K, and are nearly independent of the temperature. The uncertainty in the PIV measurements, based on an analysis of the particle response time is approximately 1%. The wall and casing temperatures have higher uncertainties of +/- 0.5 K because of possible radiation effects. Based on the uncertainties in these parameters, uncertainties in the derived quantities (λ , η , C_f) were calculated by Cruz et al. [187] and are reported below in Table 4.2.

Q	$\Delta Q/Q$, %
C_f	≤ 10.00
η	≤ 0.76
λ	≤ 1.42
T, T_w	$\leq 2.0-3.0$
U	≤ 1.00

Table 4.2 Summary of the uncertainties in measured and derived quantities from the subsonic slot-jet film cooling experiments performed by Cruz et al. [187].

4.5.3 Overview of RANS methodology

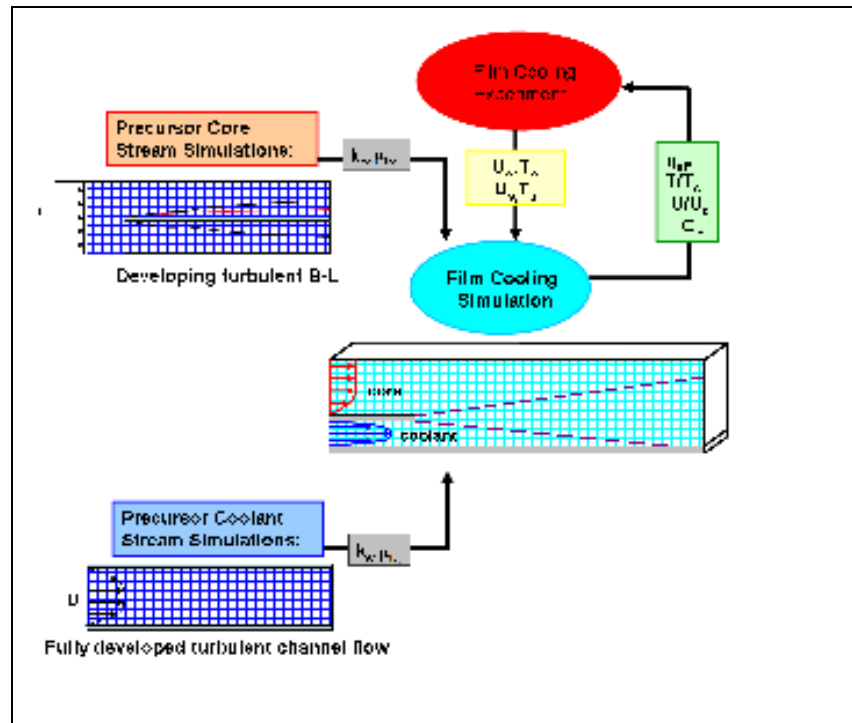


Figure 4-21 Overview of RANS methodology

Previous work by Cruz et al. [138] showed that predictions of momentum and thermal mixing were very sensitive to the turbulent state of the flow at the inflow boundaries. Since this turbulence information was not readily available from the experimental data, it was necessary to develop a numerical methodology for generating it. The basic idea was to perform precursor RANS simulations with Menter's SST turbulence model and then combine this turbulent information with experimental measurements for the velocity and temperature, to establish the inflow boundary conditions in the film cooling simulations. A schematic illustration of this methodology is shown above in Figure 4-21. An additional challenge was the need to specify inflow boundary conditions that captured the flow structures associated with the vortex shedding from the louver tip. The main film cooling grid was therefore

extended upstream by ten slot heights (i.e., 10s) to enable the boundary layer upstream of the louver to develop.

A RANS methodology was favored over LES or DNS approaches because of its computational efficiency and its simplicity of implementation in Loci-CHEM. Both LES and DNS are significantly more computationally intensive than RANS and more complex in terms of implementation. LES is currently not fully implemented in Loci-CHEM, which therefore eliminated the viability of this approach. It is also important to point out that based on the literature review in Chapter 1 no clear picture emerged as to the dominance of either LES or RANS approaches.

4.5.4 Precursor Simulation Details

Introduction

A key factor in setting up the precursor simulations for each stream was ensuring that the proper flow physics was captured. In the case of the coolant stream, the experimental measurements indicated that the coolant stream was turbulent and fully developed by the louver exit for all blowing ratios. Therefore, a fully developed turbulent channel flow precursor simulation was performed to obtain k and μ_t for the coolant stream inlet. Turbulence information was extracted from the precursor simulation where the simulated velocity profile at the channel matched the measured velocity profile at the louver exit.

In the case of the core stream, the boundary layer forming over the louver was turbulent but not fully developed (i.e., the shear stress was not constant) at the louver exit. Therefore the core stream precursor simulations were based on a developing turbulent boundary layer over a flat plate. The velocity profile in the turbulent

boundary layer precursor simulation that best matches the experimentally measured profile at the louver exit is found. The inflow boundary conditions (velocity profile, temperature profile, k profile, μ_t profile) are taken at a plane 10 slot heights upstream.

Once the core and coolant stream inlet conditions were determined from the precursor simulations, they were fed into the main film cooling simulation, which produced predictions for the film cooling performance, thermal and momentum mixing as well as the skin friction. The numerical results were then compared with experimental data from Cruz et al. [187] to assess their accuracy.

Another important point to note is that the RANS methodology outlined here is still computationally efficient relative to an LES or DES or DNS approach in spite of the fact that additional precursor simulations are required. This is because the RANS simulations do not require as highly resolved grids.

Precursor Simulation Grid Descriptions

The precursor coolant channel simulations were run using the square channel geometry shown previously in Figure 4-2 and the configuration used for the precursor core simulations was identical to that used for boundary layer validation simulations, shown earlier in Figure 4-14.

Coolant Channel Precursor Simulation Boundary Conditions

The pressure, velocity and temperature profiles were prescribed at the inlet of coolant channel grid based on experimental measurements from Cruz et al. [187] taken at the louver exit. The turbulent kinetic energy and eddy viscosity were also set to zero at the inlet. A no slip boundary condition was applied at the upper and lower channels walls, which were also set to be adiabatic, while a reflecting boundary

condition was applied at the sidewalls. A constant pressure boundary condition was specified at the outlet. All of the cells in the computational domain were initialized to the inlet conditions before running each simulation. Menter’s Shear Stress Transport (SST) turbulence model, with a turbulent Prandtl number of 0.7 was used for all blowing ratios.

The boundary conditions applied in the coolant precursor simulations can be summarized as follows:

$$\begin{aligned}
 & \left. \begin{array}{l}
 \text{inlet : } \\
 \end{array} \right\} \begin{array}{l}
 P = \text{profile} \\
 U = \text{profile} \\
 T = \text{profile} \\
 k = 0 \\
 \mu_t = 0
 \end{array} \qquad (4.80) \\
 & \text{outlet : } P = 101325 Pa \\
 & \text{upper \& lower walls : no slip (adiabatic)} \\
 & \text{side walls : reflecting}
 \end{aligned}$$

Core Boundary Layer Precursor Simulation Boundary Conditions

A uniform velocity profile was prescribed at the inlet of the core boundary layer grid, along with profiles of the temperature and pressure based on experimental measurements from Cruz et al. [187] taken at the exit of the louver. As in the coolant precursor simulations, the turbulent kinetic energy and eddy viscosity were set to zero at the inlet and no slip boundary conditions were applied at the upper and lower plate walls which were also set to be adiabatic. In addition, a reflecting boundary condition was applied at the side walls with a constant pressure boundary condition specified at the outlet. All of the cells in the computational domain were initialized to the inlet conditions before running each simulation. Menter’s Shear Stress Transport (SST)

turbulence model [227], with a turbulent Prandtl number of 0.7 was used for all simulations.

The boundary conditions used in the core precursor simulations are summarized below in Eq. (4.81):

$$inlet : \begin{cases} P = profile \\ U = constant \\ T = profile \\ k = 0 \\ \mu_t = 0 \end{cases} \quad (4.81)$$

outlets : $P = 101325 Pa$

upper & lower walls : no slip (adiabatic)

side walls : reflecting

Pecursor Simulation Results

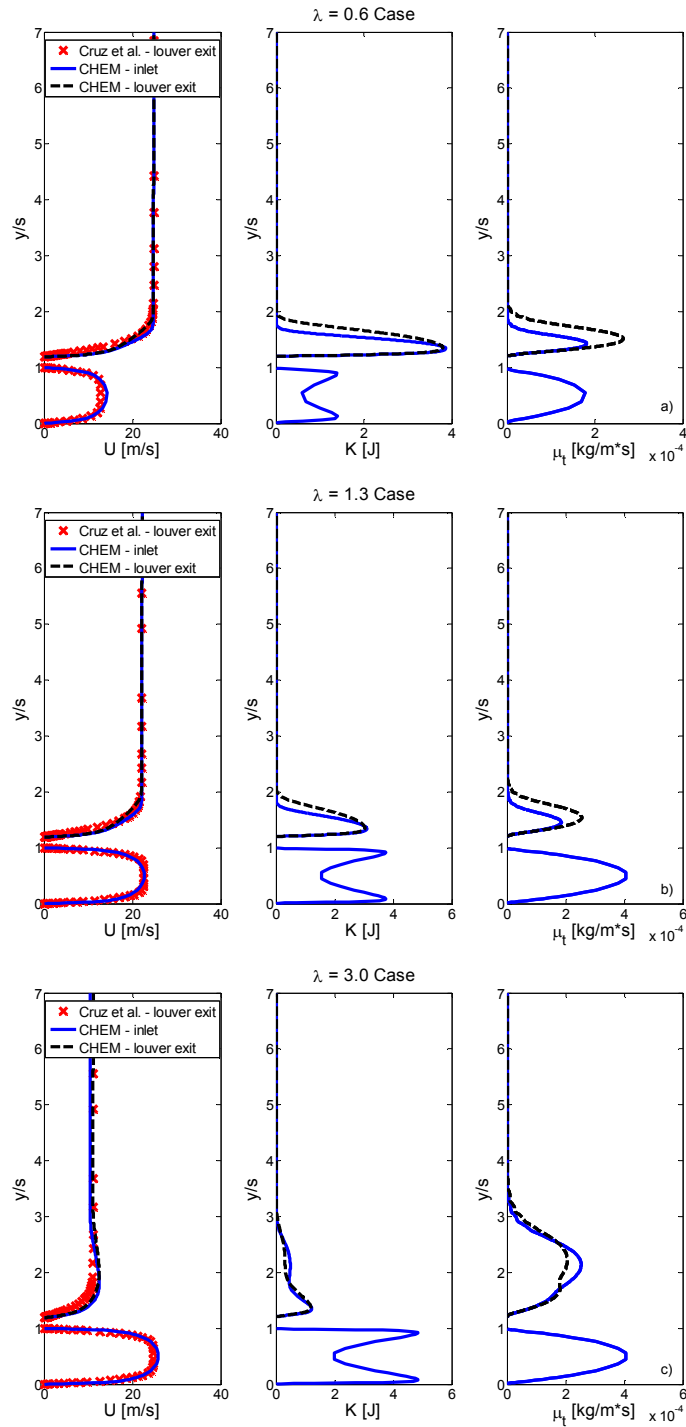


Figure 4-22 Plot of velocity (U), turbulent kinetic energy (K) and turbulent eddy viscosity (μ_t), as a function of dimensionless wall-normal distance (y/s) obtained from the precursor coolant and core simulations at: a) $\lambda = 0.5$ b) $\lambda = 1.0$ and c) $\lambda = 3.0$.

The results of the precursor coolant and core simulations for the three different film cooling cases ($\lambda = 0.6, 1.3$ and 3.0) are shown in Figure 4-22. The figure shows plots of the velocity (U), the turbulent kinetic energy (K) and the turbulent eddy viscosity, (μ_t), as a function of the dimensionless wall normal distance (y/s). The symbols in the figure correspond to experimental velocity measurements taken at the louver exit by Cruz et al. [187]. The solid lines correspond to numerical predictions from the core flow precursor simulations for the upstream inlet conditions of the core flow in the film cooling simulations (recall that the inlet plane in the film cooling simulations is located 10 slot heights upstream of the louver exit), while the dashed lines correspond to the core precursor simulation predictions for the core flow at the louver exit plane. Figure 4-22 shows that the velocity predictions for the coolant flow (indicated by U when $y/s \leq 1$), in all cases, closely matches (to within an rms error of $< 2.7\%$) the experimental data from Cruz et al. [187]. For the core flow velocity (indicated by U when $1 < y/s \leq 7$), however, the agreement is slightly worse (to within an rms error $< 3.8\%$). Based on these results it can be concluded that the velocities predicted by the precursor simulations are sensible and in good agreement with experimental measurements. From this it can be inferred that the numerical predictions for the turbulent kinetic energy and turbulent eddy viscosity obtained from the precursor RANS simulations are reasonable and can be readily applied to establish the inflow conditions for the main subsonic film cooling simulations.

4.5.5 Subsonic Film Cooling Simulation Details

Grid Description

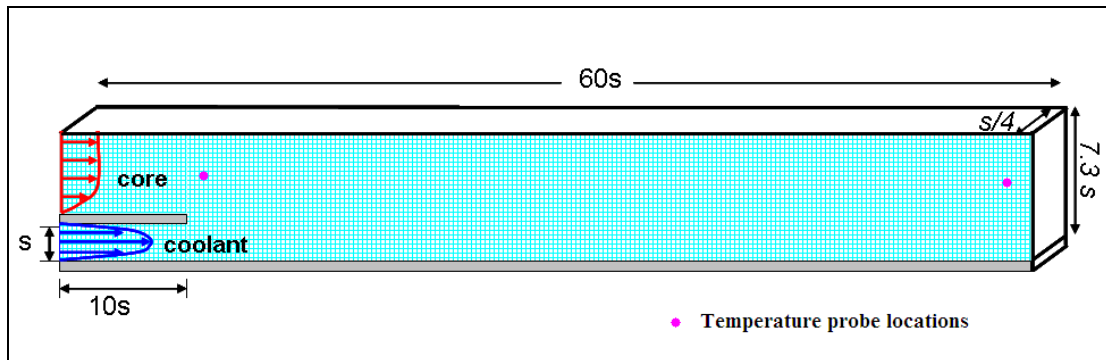


Figure 4-23 Schematic of the grid used for the subsonic film cooling simulations.

Figure 4-23 shows a schematic of the grid that was used for the main subsonic film cooling simulations. The computational domain extends $60s$ in the streamwise direction (from $10s$ upstream of the louver exit to $50s$ downstream of the louver exit), $7.3s$ in the wall normal direction and $0.25s$ in the spanwise direction. Of particular importance in generating a grid suitable for simulating the turbulent film cooling problem was ensuring that both temperature and velocity gradients were resolved in the viscous sub-layer at the wall boundary and also in the shear region located at the interface between the mainstream and the coolant stream. Based on a grid independence test it was determined that the minimum number of grid cells needed to produce a resolved solution (with $y^+ < 1$) for all blowing ratios was 494,000 cells, with 1201 grid points in the streamwise direction, 427 grid points in the wall normal direction and 2 grid points in the spanwise direction. It is important to note here that three-dimensional effects are ignored.

Boundary Conditions

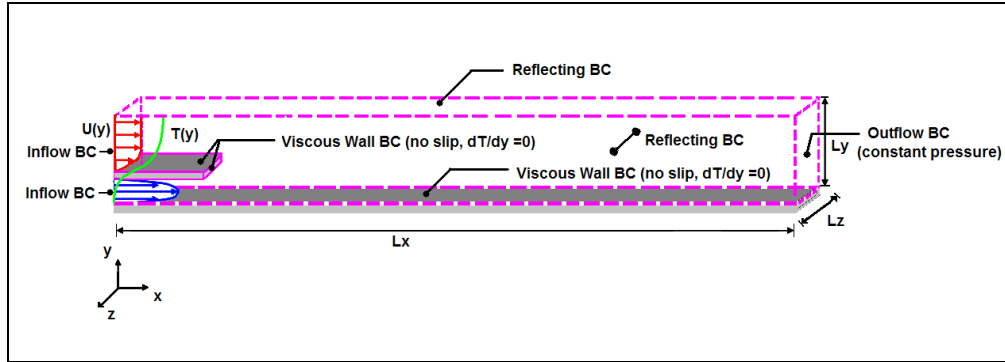


Figure 4-24 Schematic of the subsonic film cooling computational domain showing the boundary conditions used in the numerical simulations. {Adapted from Cruz et al. [187]}

Figure 4-24 is a schematic illustrating the boundary conditions that are applied in the main subsonic film cooling numerical simulations. At the coolant and core inlets respectively, the temperature, velocity, turbulent kinetic energy and turbulent eddy viscosity are prescribed using the profiles obtained from the precursor simulation results shown earlier in Figures 4-22. A reflecting boundary condition was applied along the side and upper walls, while a constant pressure boundary condition was specified at the outlet. Before running each simulation all of the cells in the computational domain were initialized to the core inlet conditions. Menter's Shear Stress Transport (SST) turbulence model with a turbulent Prandtl number of 0.7 was used for all simulations. The boundary conditions can be summarized as follows:

$$\text{inlets : } \begin{cases} P = \text{constant} \\ U = \text{constant} \\ T = \text{profile} \\ k = \text{profile} \\ \mu_t = \text{profile} \end{cases} \quad (4.82)$$

outlet : $P = 101325 \text{ Pa}$

lower walls : no slip (adiabatic)

side & upper walls : reflecting

Convergence/Steady State

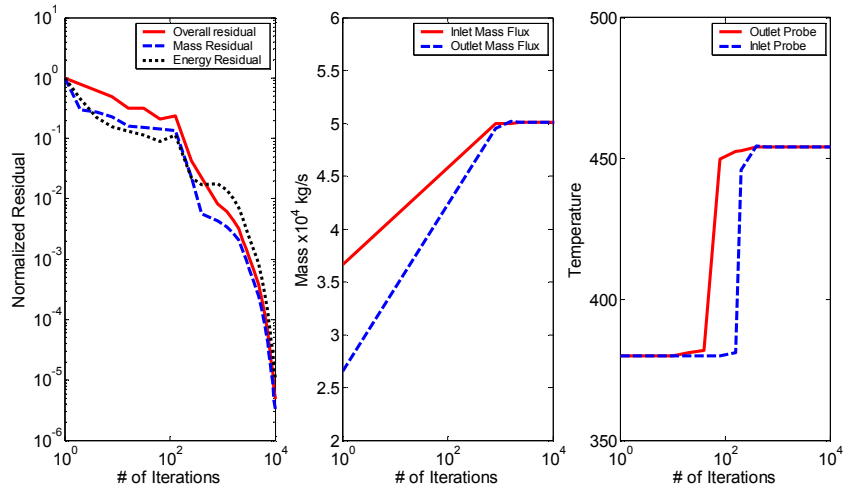


Figure 4-25 a) Residual drop, b) Mass conservation, c) Temperature probe output, as a function of the number of iterations performed for the $\lambda = 1.3$ case.

Convergence of the numerical solutions was established by observing the decrease in the overall, mass and energy residuals, comparing the total mass flow at the inlet to the outlet, and by examining the behavior of the temperature as a function of solution iteration number at selected probe point locations throughout the flow-field (see Figure 4-23). Figure 4-25 is a representative plot for the $\lambda=1.3$ film cooling case that illustrates this approach. Figure 4-25 a) shows the variation of the overall, mass and energy residuals with iteration number. Figure 4-25 b) shows inlet and outlet mass flows as a function of iteration number. Figure 4-25 c) shows how the temperature at two probe points - located in the mainstream near the inlet and outlet boundaries respectively - varies with increasing iteration number. Figures 4-25 a) and c) show that approximately 500 iterations are required to approach steady state in mass flow and mainstream temperature while 7500 iterations are needed to achieve a normalized residual drop of at least 4 orders of magnitude. Figure 4-25 b) shows that mass conservation is always satisfied to within 0.1 percent of the total mass flow after

1600 iterations. Therefore, running to at least 7500 iterations was considered adequate for ensuring convergence.

4.6 Subsonic Film Cooling Simulation Results

4.6.1 Temperature Field

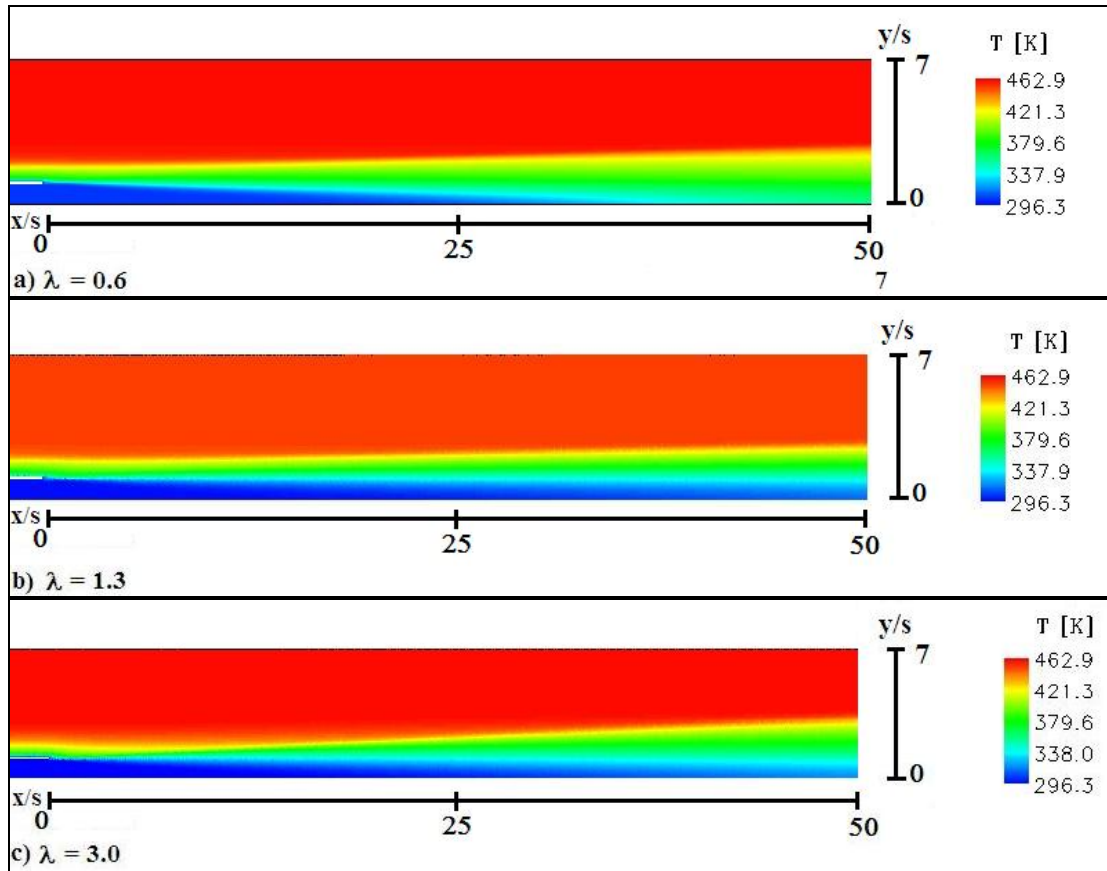


Figure 4-26 Temperature contours predicted by CHEM for the film cooling of an adiabatic wall at: a) $\lambda = 0.6$. b) $\lambda = 1.3$ and c) $\lambda = 3.0$.

Figure 4-26 shows a comparison of the temperature fields predicted by CHEM for the three blowing ratio cases ($\lambda = 0.6, 1.3$ and 3.0). In the $\lambda = 0.6$ case shown in Figure 4-26 a) the thermal shear grows steadily from the louver tip at $x/s = 0$ until it impinges the wall near $x/s \approx 30$. In the other two cases shown in Figure 4-26 b) and c) the thermal shear layer grows steadily from the point of injection at $x/s = 0$, but at a

slower rate than in the $\lambda = 0.6$ case which does not result in wall impingement by $x/s = 50$. Based on these results it can be inferred that the $\lambda = 0.6$ case will have a lower effectiveness than the $\lambda = 1.3$ and 3.0 cases because it has the lowest thermal shear layer impingement length.

4.6.2 Velocity Field

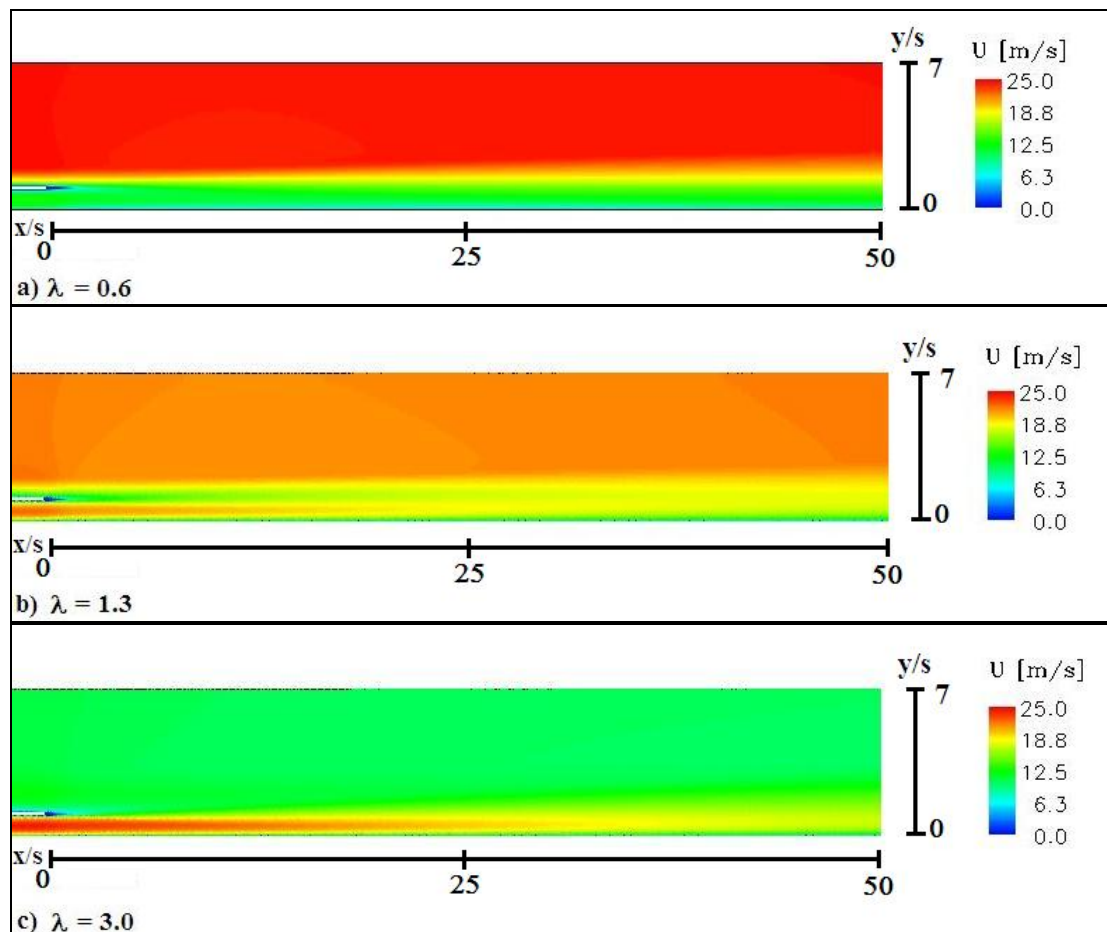


Figure 4-27 Velocity contours predicted by CHEM for the film cooling of an adiabatic wall at: a) $\lambda = 0.6$. b) $\lambda = 1.3$ and c) $\lambda = 3.0$.

Figure 4-27 shows a comparison of the velocity fields predicted by CHEM for the three blowing ratio cases ($\lambda = 0.6, 1.3$ and 3.0). In the $\lambda = 0.6$ case shown in Figure 4-27 a) the velocity maintains a boundary layer-like profile, with low speed fluid near the wall and high speed fluid far from the wall, throughout the entire length

of the computational domain. The figure also shows that the film rapidly mixes. In the $\lambda = 1.3$ case, shown in Figure 4-27 b), at the louver exit ($x/s = 0$) the velocity of the film and core stream are almost equal with a region of low velocity fluid separating them just downstream of the louver. As x/s increases the film and core stream gradually mix until by $x/s \approx 40$ the velocity profile resembles a boundary layer. In the $\lambda = 3.0$ case (Figure 4-27 c)) the film is injected at twice the velocity of the core stream. As x/s increases momentum gradually diffuses from the film to the core until by $x/s \approx 35$ the velocity profile takes on the shape of the boundary layer. These results suggest that the film persists the longest in $\lambda = 1.3$ and 3.0 cases, since the momentum mixing in these cases is much slower than in the $\lambda = 0.6$ case

4.6.3 Vorticity Field

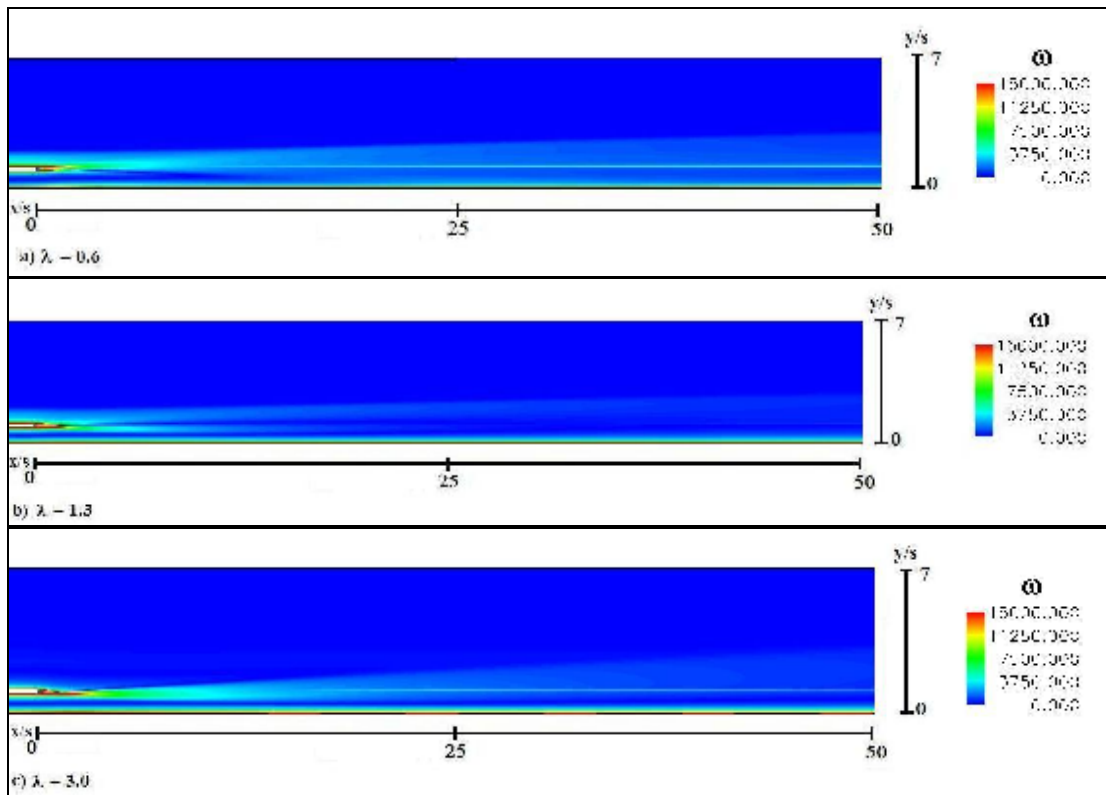


Figure 4-28 Vorticity contours predicted by CHEM for the film cooling of an adiabatic wall at: a) $\lambda = 0.6$. b) $\lambda = 1.3$ and c) $\lambda = 3.0$.

The vorticity fields for the three blowing ratio cases explored in the subsonic film cooling simulations are shown above in Figure 4-28. The figure shows that in each case the highest vorticity occurs immediately downstream of the louver lip and in the boundary layer on the lower test section wall. Also as x/s increases the vorticity is observed to rapidly decrease in intensity. The peak vorticity near the louver lip is likely due to vortices being shed off the louver as the core stream and coolant stream encounter each at the louver exit. Vorticity decreases with increasing x/s due to entrainment (diffusion of vorticity) as the shear layer formed at coolant-core stream interface grows.

A comparison of the three blowing ratio cases reveals that the $\lambda = 0.6$ case produces the most vorticity, while the $\lambda = 1.3$ case yields the least amount of vorticity. This can be explained by the fact that the $\lambda = 0.6$ case has the highest shear and hence highest vorticity since the velocity ratio (R) is 2.30 (see Table 4.1), while the $\lambda = 1.3$ case has the lowest shear and vorticity since the velocity ratio is 1.16. From these results it can be inferred that the highest effectiveness will be produced in the minimum vorticity case (i.e., $\lambda = 1.3$), while the lowest effectiveness will occur in the wall-wake case ($\lambda=0.6$).

Further insight into the mixing occurring near the point of film injection can be obtained by zooming in on the vorticity contours near the louver tip. This has been done for each blowing ratio in Figure 4-29 a) – c) for a domain measuring $12s \times 7s$ in the streamwise and wall-normal directions. Figure 4-29 a) ($\lambda = 0.6$) shows that the most intense vorticity occurs on the core side of the coolant-core stream interface.

This can be explained by the fact that the core velocity is higher than the coolant velocity in this case which leads to entrainment of coolant by the core flow.

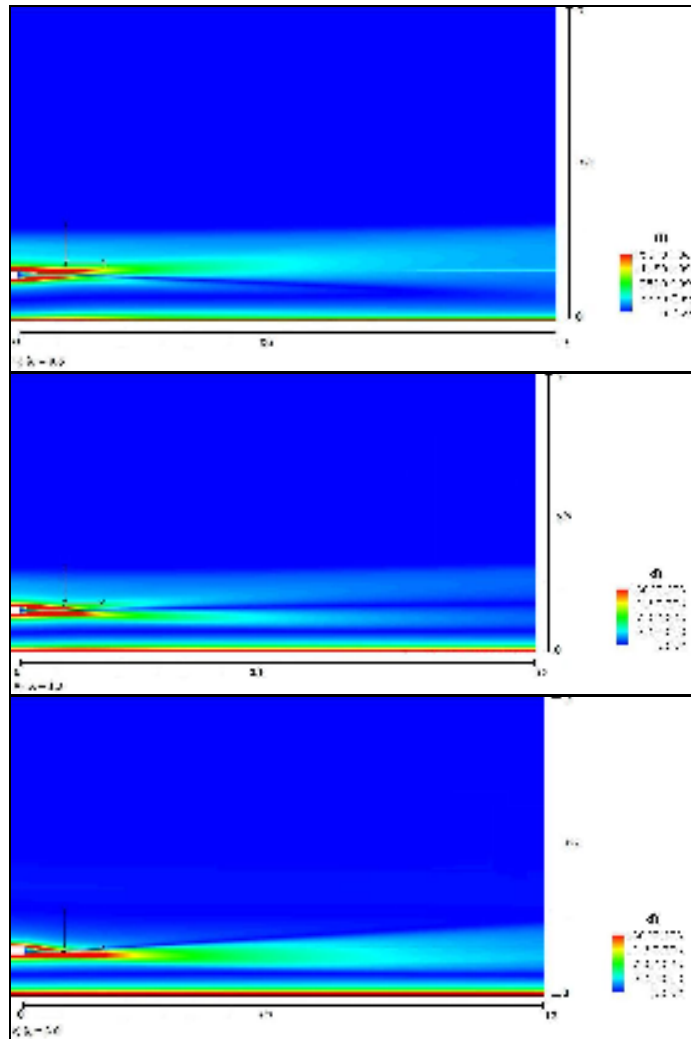


Figure 4-29 Zoomed vorticity contours predicted by CHEM for the film cooling of an adiabatic wall at: a) $\lambda = 0.6$. b) $\lambda = 1.3$ and c) $\lambda = 3.0$.

In Figure 4-29 c), the reverse occurs. The coolant stream velocity is higher than the core stream velocity which leads to higher vorticity on the coolant side of the coolant-core stream interface. This indicates entrainment of core fluid by the coolant stream. In contrast to the previous cases, in Figure 4-29 b) ($\lambda = 1.3$ case), the intensity of the vorticity of the coolant and core streams is almost equal. Since the velocity ratio is almost unity this indicates that less entrainment (mixing) is occurring.

4.6.2 Thermal Mixing

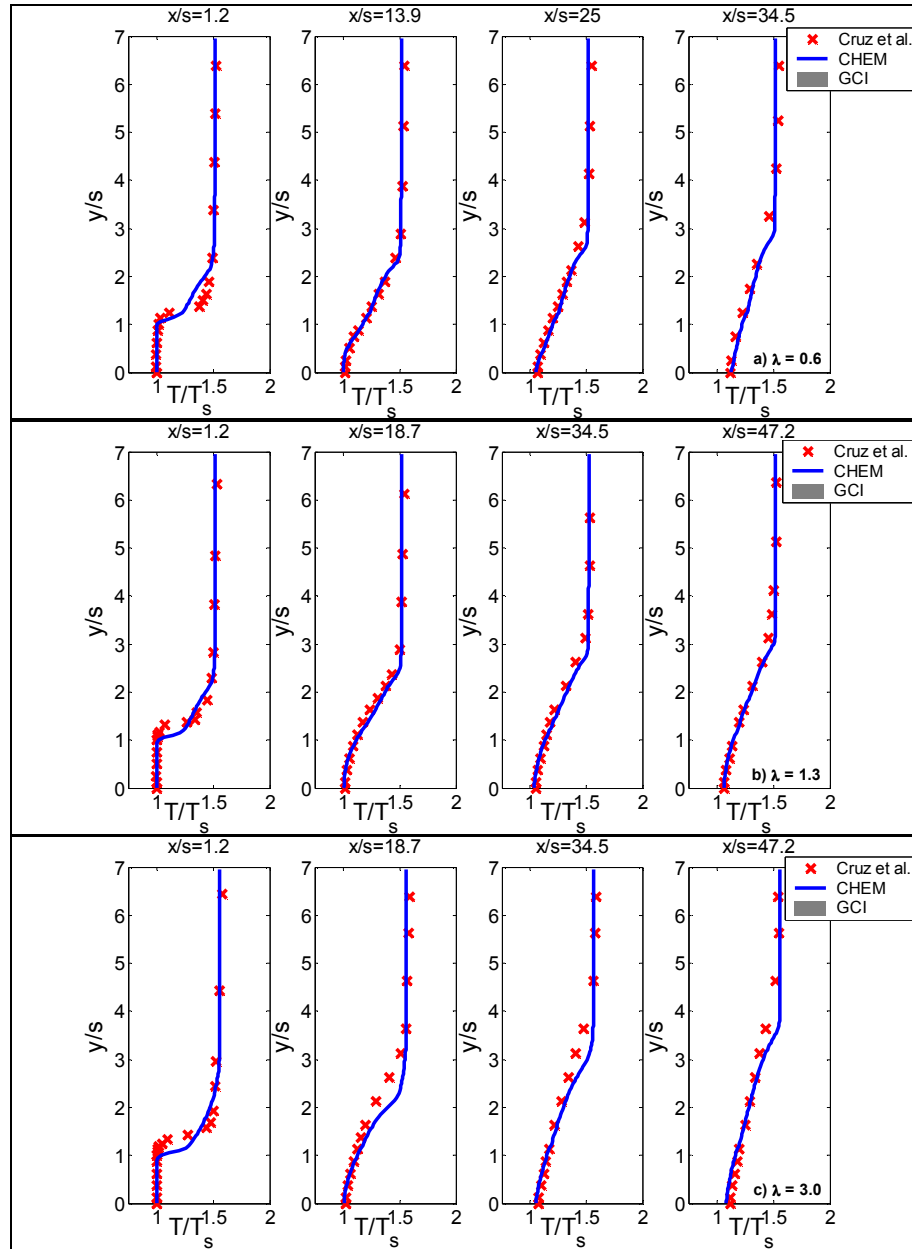


Figure 4-30 Profiles of normalized temperature, T/T_s , at four discrete locations downstream of the point of coolant injection, for the film cooling of an adiabatic wall at: a) $\lambda = 0.6$. b) $\lambda = 1.3$ and c) $\lambda = 3.0$.

Figure 4-30 a)-c) show the evolution of normalized temperature profiles, T/T_s , at four locations downstream of the point of coolant injection. The wall is adiabatic and three different blowing ratios ($\lambda = 0.6, 1.3$ and 3.0) are considered. The solid lines correspond to predictions of Loci-CHEM, the 'x' symbols correspond to experimental

data from Cruz et al. [187] which have uncertainties on the order of 2-3% and the shaded region corresponds to the Grid Convergence Index (GCI) which was computed using the approach outlined in §4.3 with a factor of safety, $F_s = 1.25$. It is important to note here that the shaded region corresponding to the GCI is not visible since the grid used in these simulations is very highly resolved. Figure 4-30 a) shows the development of the temperature profile for the $\lambda = 0.6$ case. At $x/s = 1.2$ which is near the point of coolant injection, the temperature profile remains very close to the coolant temperature, for $y/s \leq 1.0$ and then gradually increases to the hot mainstream temperature by $y/s = 2.0$. As x/s increases from 13.9 to 34.5, the penetration of the hot mainstream into the coolant stream increases steadily as indicated by the gradual increase in the slope of the temperature profile near the wall. This indicates a decrease in film cooling effectiveness with downstream distance. Comparison to the experimental data shows very good quantitative (to within an rms error of 2.9%) and qualitative agreement along the entire test section length. Similar trends are also observed in Fig. 4-30 b) and c) where rms errors of less than 2.5% and 5.9% are produced for the $\lambda = 1.3$ and 3.0 cases respectively. In the latter case ($\lambda = 3.0$), a slight under-prediction of the temperature profile is observed at the $x/s = 1.2$ and $x/s = 18$ stations. However, this discrepancy becomes negligible further downstream (by $x/s = 34.5$). It is also important to observe to note that the GCI in all cases was very small, which suggests that numerical uncertainty does not contribute significantly to the disagreement between the numerical predictions and experimental data. Most of the differences between simulations and measurements are within the uncertainty of the measurements which suggests that the current RANS approach based on Menter's

SST turbulence model is capable of making reasonable predictions of the temperature profile in the near-wall region.

4.6.2 Momentum Mixing

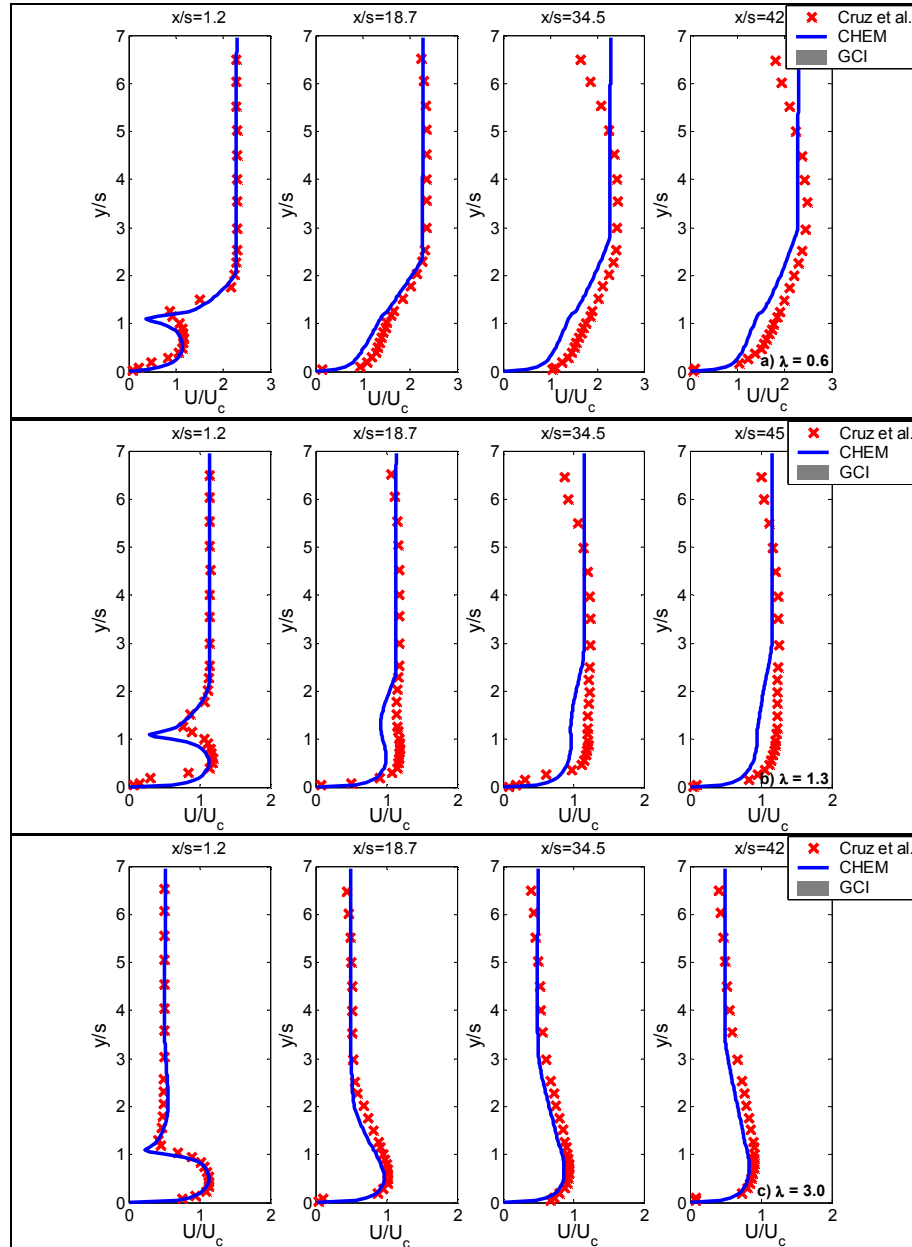


Figure 4-31 Profiles of normalized velocity, U/U_c , at four discrete locations downstream of the point of coolant injection, associated with the film cooling of an adiabatic wall at: a) $\lambda = 0.6$. b) $\lambda = 1.3$ and c) $\lambda = 3.0$.

Figure 4-31 a -c) show the development of normalized velocity profiles over an adiabatic wall at four discrete locations downstream of the point of coolant injection

and at three different blowing ratios ($\lambda = 0.6, 1.3$ and 3.0). As before, the solid lines correspond to predictions of CHEM, the 'x' symbols correspond to experimental data from Cruz et al. [187] which have uncertainties on the order of 1% and the shaded region corresponds to the Grid Convergence Index (GCI) which was computed using the approach outlined in §4.3 with a factor of safety, $F_s = 1.25$. The shaded region corresponding to the GCI is not visible due to the fact that the grid used was very highly resolved. Figure 4-31 a) shows velocity profiles in the $\lambda = 0.6$ case. Near the point of coolant injection at $x/s = 1.2$, there are steep velocity gradients near the wall ($y/s = 0$) and at the coolant-mainstream interface ($y/s \approx 1.3$). As x/s increases, these velocity gradients become shallower as momentum diffuses from the higher speed mainstream towards the lower speed coolant stream. By $x/s = 34.5$, the velocity profile has evolved sufficiently to resemble a boundary layer velocity profile. At these large values of x/s , the simulations and experiment agree within an rms error of 33.1%. This large discrepancy is due to a problem with the experiment reported by Cruz et al. [187], where a leak in the outer wall of the test section introduced mild and favorable pressure gradients into the flowfield. Inspection of Fig. 4-31 b) and c), corresponding to the $\lambda = 1.0$ and $\lambda = 3.0$ cases, shows that the leak is also present in these cases but appears to be less severe than in the wall-wake ($\lambda = 0.6$) case. In addition, both cases show similar trends in the development of the velocity profile with increasing non-dimensional streamwise distance compared to the wall-wake case ($\lambda = 0.6$). The CHEM predictions in both of these cases match the experimental data slightly better (to within an rms error of 20.4% and 13.8% for $\lambda = 1.3$ and $\lambda = 3.0$ cases respectively) in the near wall region. While the simulations show the same

trends as experiments, the differences between them cannot be attributed entirely to uncertainties in the velocity measurements or numerical simulations (the GCI is very small). One important factor may be the effect of leakage on the experimental measurements. This will be addressed later in §4.6.5.

4.6.3 Skin Friction (Wall Shear Stress)

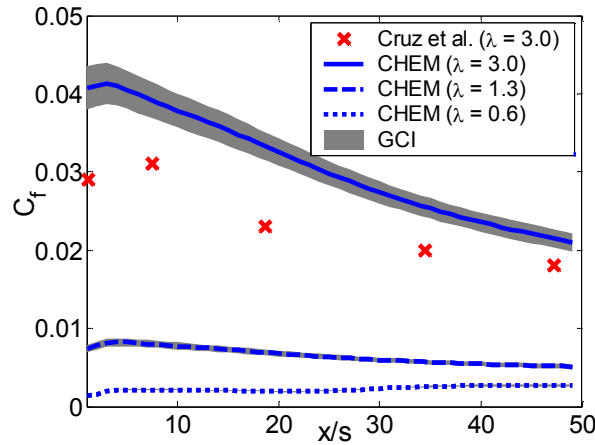


Figure 4-32 Variation of skin friction coefficient (C_{f_c}) with non-dimensional streamwise distance (x/s) associated with the film cooling of an adiabatic wall at three different blowing ratios ($\lambda = 0.6, 1.3$ and 3.0).

Figure 4-32 shows the variation of skin friction coefficient (C_{f_c}) with non-dimensional streamwise distance (x/s) for the three blowing ratio cases ($\lambda = 0.6, 1.3$ and 3.0). The solid lines correspond to predictions of Loci-CHEM, the ‘x’ symbols correspond to experimental data from Cruz et al. [187] and the shaded region corresponds to the Grid Convergence Index (GCI) which was computed using the approach outlined in §4.3 with a factor of safety, $F_s = 1.25$. The experimental data are only available for the high blowing ratio ($\lambda = 3.0$) case since a wall-jet correlation based on the similarity theory of Kruka et al. [248] was used to estimate the skin

friction coefficient. The skin friction coefficient is defined in terms of the wall shear stress and the dynamic pressure of the mainstream as:

$$C_{f\infty} = \frac{2\tau_{wall}}{\rho U_{\infty}^2} \quad (4.83)$$

Similar trends in the skin friction coefficient are observed when comparing CHEM's predictions for the wall-jet ($\lambda = 3.0$) case with those for the minimum shear ($\lambda = 1.3$) cases. In both cases, there is a slight increase in the skin friction coefficient in the near-injection region ($x/s < 5$) (suggesting that the flow is adapting to the shear induced by the inflow velocity profile) followed by a gradual decrease in skin friction with downstream distance. In the wall-wake ($\lambda = 0.6$) case the skin friction initially increases near the injection point then decreases slightly between $5 < x/s < 20$, before gradually increasing again. This is likely due to the fact that the flow transport properties at the wall are dominated by the core stream far downstream from the point of injection.

Comparison of the RANS (LocI-CHEM) results with the experimental data shows poor agreement in the near injection region ($x/s < 10$) and fair agreement (within an average error of 23.5%) far downstream from the injection point ($x/s > 30$). The discrepancy between the simulation and experiment can be partly explained by the fact that the skin friction correlation used by Cruz et al. [187] is based on the assumption of self-similar flow which is not valid over the entire length of the flow-field in Cruz's experiment and especially not near the point of injection. In addition, the error in the skin friction measurements is relatively high ($\pm 10\%$). The maximum GCI for the numerical predictions is fairly high ($\approx 5\%$) in the $\lambda = 3.0$ case since $C_{f\infty}$ is

a derived quantity based on several variables (the density, core stream velocity and wall shear stress as shown in Eq. (4.83)) .

4.6.4 Film Cooling Effectiveness

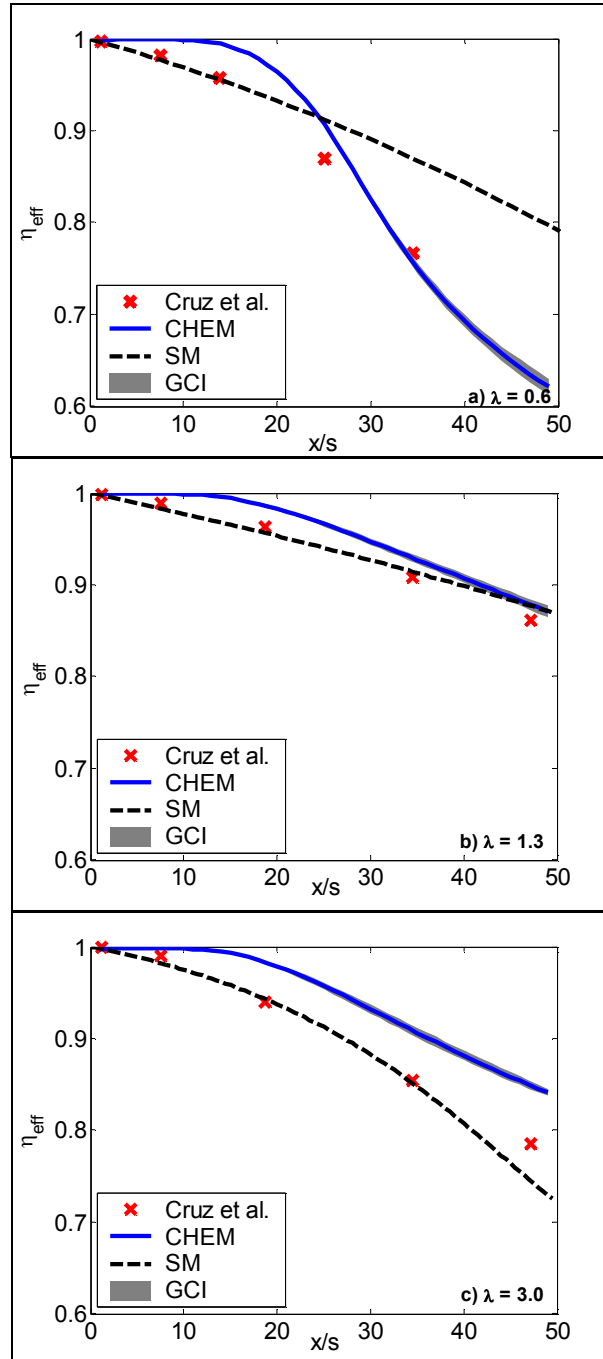


Figure 4-33 Variation of film cooling effectiveness, η_{eff} , with non-dimensional streamwise distance, x/s , for the film cooling of an adiabatic wall at: a) $\lambda = 0.6$. b) $\lambda = 1.3$ and c) $\lambda = 3.0$.

Figure 4-33 a) - c) show film cooling effectiveness (computed from the adiabatic wall temperature using Eq. (2.5)) as a function of non-dimensional streamwise distance, x/s , for the three blowing ratio cases explored by Cruz et al. [187]. The solid line shows Loci-CHEM's prediction of the variation of film cooling effectiveness with non-dimensional streamwise distance. The dashed line shows the predictions of Simon's semi-empirical model (SM) and the 'x' symbols show experimental measurements by Cruz et al. [187]. The estimated uncertainty in these measurements is $< 1\%$. The shaded region corresponds to the Grid Convergence Index (GCI) which was computed using the approach outlined in §4.3 with a factor of safety, $F_s = 1.25$. Comparison of Figs. 4-33 a) - c) shows that the effectiveness decays most rapidly in the wall-wake ($\lambda = 0.5$) case indicating the poorest protection of the wall occurs in this case. In contrast, the best protection is provided by the near unity blowing ratio case ($\lambda = 1.3$) shown in Fig. 4-33 b) where the interfacial shear between the core and coolant streams is minimal.

These results are consistent with the temperature, velocity and vorticity fields shown earlier in Figs. 4-26 – 4-29. In Fig. 4-26 it can be seen that the thinnest thermal shear layer is predicted for the $\lambda=1.3$ case, which means that the impingement distance is the longest of the three cases and explains why the film persists the furthest in this case. In Fig. 4-28 and Fig. 4-29 it also clear that CHEM predicts the least amount vorticity in the $\lambda=1.3$ case and the most in the $\lambda=0.6$ case. Less vorticity means slower mixing of fluid from the core and coolant streams which leads to slower breakdown of the film (i.e., longer persistence of the film), while high vorticity produces more rapid mixing which breaks the film up more quickly.

In all cases, the agreement between CHEM and the experiment is best immediately downstream of the injection point and far downstream when $x/s > 20$. However, the CFD slightly over-predicts effectiveness in the intermediate region $10 < x/s < 20$ where the flow transitions from the initial discontinuity to being fully developed. The rms errors are within 2.6%, 1.7% and 4.3% for the $\lambda = 0.6$, 1.3 and 3.0 cases respectively. Part of the discrepancy between the CHEM predictions and the data appears to be attributable to the under-prediction of mixing in the initial region of the film. This may be due to the fact that RANS turbulence models are overly dissipative of turbulence since they assume isotropy of turbulence (i.e., turbulence is dissipated equally in the x-, y- and z-directions). As a result RANS simulations are less accurate in scenarios where anisotropic behavior of turbulent stresses dominates. This assertion is supported by the fact that the best agreement between CHEM's predictions and the experimental data was obtained for the minimum shear case ($\lambda=1.3$), which has the least mixing and was therefore likely to have the most isotropic turbulence. In contrast, the other two cases ($\lambda = 0.6$ and 3.0) have much higher shearing (i.e., mixing) which results in more anisotropy in the turbulence and poorer agreement between simulation and experiment. Another important source of discrepancy is the presence of the leak in experiment which may have influenced the measured effectiveness. This will be discussed in greater detail in the next subsection.

Comparison to the SM reveals that the CHEM predictions match the data more closely than the SM in the $\lambda = 0.6$ case. In the $\lambda = 1.3$ case the numerical results and the SM predictions show comparable performance, while in the $\lambda = 3.0$ case, the SM models outperforms CHEM. This latter result is due to the fact that the SM model

parameters have been tuned to closely match the data. Taken together the RANS simulations using Menter's SST turbulence model appears to provide reasonable (to within an rms error < 4.3%) prediction of subsonic film cooling performance.

4.6.5 Explanation of the Discrepancies between the Simulations and Experiment

In an effort to better understand the root causes of the discrepancies between the numerical predictions and the experimental measurements, the experimental velocity data was analyzed to determine the impact of leak on the experimental readings. Since the leak is not modeled in the simulations, it was speculated that if the pressure gradients associated with the leak are non-negligible this would influence the film cooling measurements and therefore partly explain the discrepancies.

The first step in this analysis involved re-plotting the raw velocity data for all blowing ratios ($\lambda = 0.6, 1.3$ and 3.0) to reveal the local changes in velocity between: a) the inlet velocity profile and the velocity profile at a given measurement location and b) the velocity profiles at a given measurement location and the profile at the previous measurement location.

Figure 4-34 a) – f) are plots showing the change in streamwise velocity, ΔU , as a function non-dimensional wall-normal distance, y/s for the three blowing ratios explored in Cruz's [187] subsonic film cooling experiment. The solid lines correspond to ΔU values at $x/s = 18.7$, the dashed lines to ΔU values at $x/s = 34.5$ and the dotted lines to ΔU values at $x/s = 42$ or 45 . For the $\lambda = 0.6$ case shown in a) and b) recent data with the leak 'fixed' is also plotted, with the 'o' symbols corresponding to ΔU values at $x/s = 18.7$, the '□' symbols to ΔU values at $x/s = 34.5$ and the '◇' symbols to ΔU values at $x/s = 45$. Plots a), c) and e) correspond to ΔU values which

were computed by taking the difference between the inlet velocity profile and the velocity profile at the given measurement location. Plots b), d) and f) correspond to ΔU values determined by finding the difference between the velocity profiles at the given measurement location and the previous measurement location (N.B. - in the case of $x/s = 18.7$ the previous measurement location is $x/s = 1.2$).

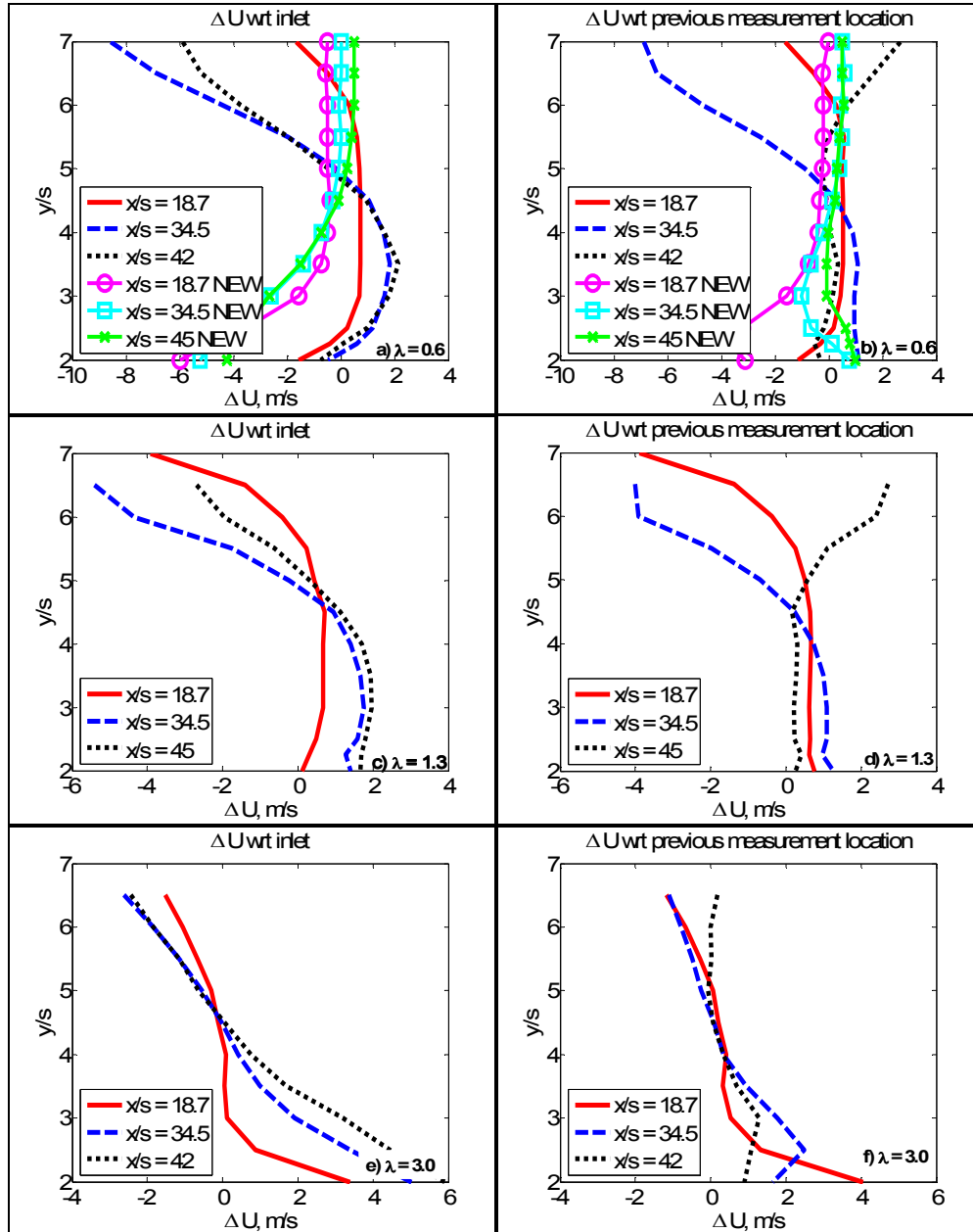


Figure 4-34 Change in streamwise velocity (ΔU) at a fixed measurement location as a function of non-dimensional wall-normal distance (y/s) for: a) & b) $\lambda = 0.6$ case, c) & d) $\lambda = 1.3$ and d) & e) $\lambda = 3.0$.

Figure 4-34 shows that in all cases there are large changes in velocity due to the presence of the leak. A significant deceleration in the velocity occurs in the range $5 < y/s < 7$ which is consistent with the presence of an adverse pressure gradient. In addition, a noticeable acceleration in the velocity occurs between $3 < y/s < 4$ which is associated with a favorable pressure gradient. The figure also clearly shows that in all cases the leak influences the velocity profile very close to the wall and therefore may have affected the performance of the film.

The next step is to evaluate the strength of the pressure gradients at each of the discrete measurement locations observed above in Figure 4-34. To do this, it is necessary to first choose a height range over which to analyze the velocity data. A wall normal height range between $3 < y/s < 7$ was therefore selected in order to minimize the influence of momentum mixing in the shear layer, formed at the coolant-core stream interface, on the velocity profiles. In addition, it is assumed in this analysis that if no leak were present the velocity above $y/s > 3$ would be identical to the velocity at the inflow plane, i.e., that there would be no acceleration or deceleration of the outer wall velocity and that the penetration of the mixing occurring at the coolant-core stream interface would not reach above $y/s > 3$.

The magnitude of the pressure gradients in the experiment were estimated using Eq. (2.2) which computes the acceleration parameter, K_p , from the streamwise velocity gradient, dU/dx . The velocity gradient was determined by finding the change in velocity between measurement locations, ΔU , and dividing it by the separation distance, dx . A maximum adverse pressure gradient (APG) was estimated when the velocity decrease relative to the inlet velocity profile was at its peak; while a

maximum favorable pressure gradient (FPG) was estimated when the velocity increase relative to the inlet velocity profile was maximum. It is important to note here that this is a crude estimate of the pressure gradients present in the test section, since the velocity profiles are measured at discrete locations far apart. It is more likely that the pressure gradients are variable in the streamwise direction.

A summary of the results of this analysis for all blowing ratios is given below in Table 4.3. Recent data for the $\lambda = 0.6$ case with the leak ‘fixed’ has also been included for comparison. The results suggest that the pressure gradients in the experimental flowfield were non-negligible and may therefore have exerted an influence on the shear layer formed at the coolant-core stream interface, which in turn may have influenced the film cooling effectiveness. It also evident that since both adverse (APG) and favorable (FPG) pressure gradients were present, the flowfield was very complex and therefore not reflective of the simple canonical film cooling problem that was simulated numerically.

λ	0.6	1.3	3.0	0.6 (fixed leak)
U_∞ (m/s)	24.86	22.1	11.1	24.86
FPG: Max +ve ΔU (m/s)	2.00	1.34	4.39	0.00
APG: Max -ve ΔU (m/s)	-8.70	-5.53	-2.69	-1.56
FPG: Max +ve $\Delta U/\Delta x$ (/s)	66.52	31.82	62.75	0.00
APG: Max -ve $\Delta U/\Delta x$ (/s)	-137.67	-87.51	-38.44	-24.63
FPG: K_p	3.58×10^{-6} MODERATE	2.11×10^{-6} MODERATE	1.70×10^{-5} STRONG	0
APG: K_p	-7.40×10^{-6} MODERATE	-5.79×10^{-6} MODERATE	-1.04×10^{-5} STRONG	-1.32×10^{-6} MODERATE
y/s location of Max FPG	3.5	3.0	3.5	-
y/s location of Max APG	7	6.5	6.5	3.5
x/s location of Max FPG	18.7-34.5	18.7-34.5	1.2-18.7	18.7-34.5
x/s location of Max APG	42-34.5	45-34.5	1.2-18.7	42-34.5

Table 4.3 Summary of the analysis of the experimental velocity data taken by Cruz et al. [187].

4.7 Conclusions

Numerical simulations of the subsonic film cooling of an adiabatic wall at three different blowing ratios were performed using loci-CHEM, a RANS solver. A comparison of the simulation results with experimental data from Cruz et al. [187] showed that CHEM is capable of predicting the evolution of temperature and velocity profiles through the film to within rms errors of 2.9% and 33.1% respectively and skin friction coefficients to within 23.5%. The film cooling effectiveness predicted by CHEM was also found to match experimental measurements to within an rms error 4.3%. This is comparable to Simon's semi-empirical film cooling model for blowing ratios of 1.3 and 3.0, and substantially better for a blowing ratio of 0.6. The highest effectiveness was predicted for the near unity blowing ratio case ($\lambda=1.3$) since the least interfacial shear between the mainstream and coolant stream occurs in this case. This was supported by the temperature, velocity and vorticity fields predicted by CHEM. The thinnest thermal shear layer was predicted for the $\lambda=1.3$ case, which means that the impingement distance was the longest of the three cases and explains why the film persists the furthest in this case. CHEM also predicted the least amount vorticity in the $\lambda=1.3$ case and the most in the $\lambda=0.6$ case. Less vorticity means slower mixing of fluid from the core and coolant streams which leads to slower breakdown of the film (i.e., longer persistence of the film), while high vorticity produces more rapid mixing which degrades the breaks the film up more quickly.

The poor prediction of the velocity profiles was in part due to a leak in the outer wall of the test section which introduced mild and favorable pressure gradients into the flowfield. The results of a pressure gradient analysis of the velocity data

suggested that the pressure gradients in the experimental flowfield were non-negligible and may therefore have exerted an influence on the shear layer formed at the coolant-core stream interface. This in turn may have influenced the film cooling effectiveness. It also evident that both adverse (APG) and favorable (FPG) pressure gradients were present. This made the flowfield very complex and may not have been reflective of the simple canonical film cooling problem that was simulated numerically.

Part of the discrepancy between the CHEM predictions and the experimental data is also attributable to the under-prediction of mixing in the initial region of the film. This may be due to the fact that RANS turbulence models are overly dissipative of turbulence since they assume isotropy of turbulence (i.e., turbulence is dissipated equally in the x-, y- and z-directions). As a result RANS simulations are less accurate in scenarios where anisotropic behavior of turbulent stresses dominates. This assertion is supported by the fact that the best agreement between CHEM's predictions and the experimental data is obtained for the minimum shear case ($\lambda=1.3$), which has the least mixing and is therefore likely to have the most isotropic turbulence. In the $\lambda = 0.6$ and $\lambda = 3.0$ cases much higher shearing (i.e., mixing) occurs which results in more anisotropy in the turbulence and poorer agreement between simulation and experiment.

Taken together, these results suggest that relatively computationally inexpensive RANS simulations can be used to obtain reasonable (to within an rms error of 4.3%) predictions of subsonic film cooling performance provided inlet boundary conditions are specified with care. This means that profiles of inlet velocity,

temperature, and modified eddy viscosity must be specified and an appropriate turbulent Prandtl number must be chosen.

Chapter 5: Supersonic Film Heating Simulations

5.1 Introduction

In this chapter the computationally inexpensive RANS methodology developed in Chapter 4 to model a subsonic film cooling experiment is applied to aid in the design of a supersonic film heating experiment. The results obtained are used to establish the viability of the experiment under subsonic and supersonic ‘coolant’ injection, as well as to guide the layout of instrumentation.

5.2 Description of Supersonic Film Heating Experiment

Introduction

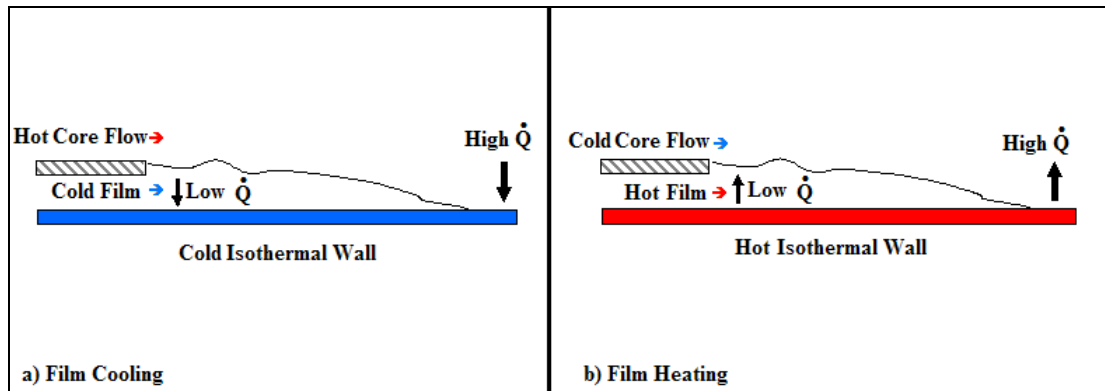


Figure 5-1 Comparison of the heat flux in: a) Film cooling and b) Film heating configurations.

To further explore more realistic conditions relevant to the film cooling of the J-2X engine nozzle extension, a supersonic film ‘heating’ experiment was designed. The term film ‘heating’ refers to the fact that the film in this case will be hotter than the core flow, which means that the direction of the heat flux will be opposite to that found in the actual J-2X engine nozzle extension, which will be film cooled. A film ‘heating’ approach was chosen for the experiment due to challenges involved in heating a high-speed flow. Nevertheless, since the test section walls will also be

heated, the essential physics of the film cooling process will be retained as illustrated above in Figure 5-1.

Hot Wind Tunnel Facility and Test Section

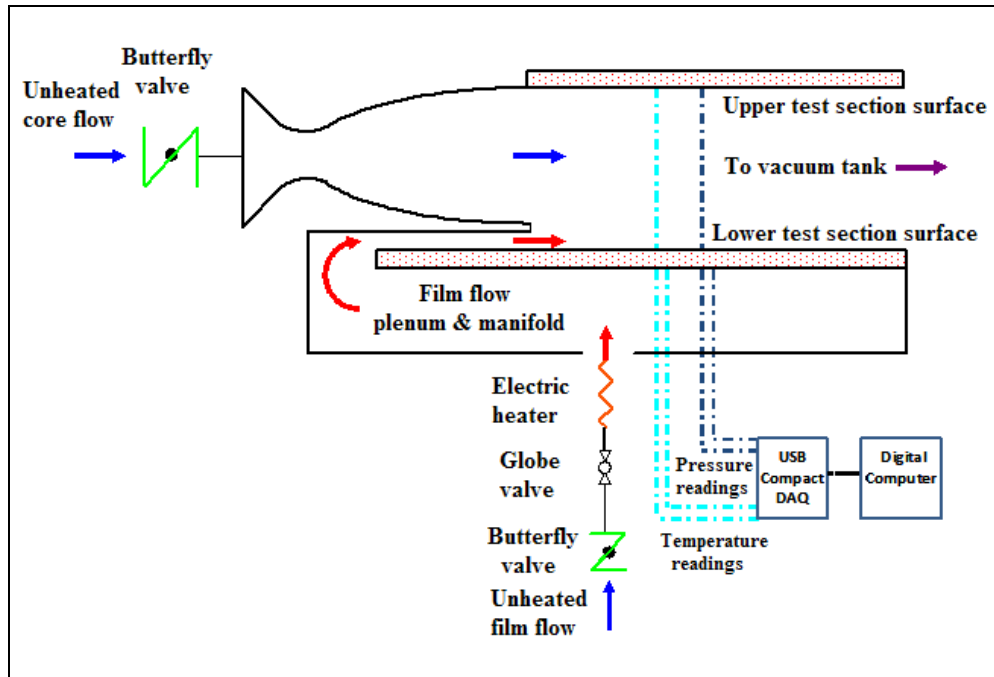


Figure 5-2 Schematic of the UMD blow-down supersonic wind tunnel facility.

Figure 5-2 is a schematic diagram of the UMD supersonic wind tunnel. It is an atmospheric total pressure blow-down facility controlled by a butterfly valve. The nozzle contour and test section are rectangular in cross-section so that the flows are quasi-two-dimensional. The film is controlled by a second butterfly valve, passes through a globe valve (for throttling), an electric heater, a plenum, and a manifold, and a secondary supersonic nozzle contour that controls the mach number of flow that is injected tangentially into the test section. Downstream of the test section is a two-dimensional diffuser.

The Mach number of the core flow in the tunnel is fixed by the nozzle design at 2.4 and can be sustained for about 6 seconds with film injection and considerably

longer (> 12 seconds) without. The film flow can be throttled using the globe valve to produce pressure-matched (i.e., at the louver exit the static pressure of the film matches that of the core) and hence shock-free subsonic flows up to Mach 0.67 or a Mach 1.4 supersonic flow. The wind tunnel can produce film to core stream velocity ratios (U_f/U_c) in the range of 0.3 to 0.75, film to core stream static temperature ratios (T_f/T_c) up to 2, and convective Mach numbers (M_c) in the range of 0.27 to 0.69.

The rectangular test section is 0.152 m wide, 0.098 m high and 0.445 m long. The film slot exit marks the beginning of the test section and occupies the lower 6.35 mm (i.e., the slot height, $h = 6.35\text{mm}$). It is separated from the core flow nozzle by a 1.27mm thick louver. The lateral walls of the test section are made of glass for optical access. The upper and lower test section walls are made from 0.016 m thick plates of MACOR, a high temperature ceramic with a low thermal diffusivity of $7.3 \times 10^{-7} \text{ m}^2/\text{s}$. Each MACOR plate is backed by a 0.016 m thick copper plate with embedded cartridge heaters to uniformly heat the MACOR plates prior to running the experiment.

Before starting each test run, the cartridge heaters will be turned on to warm the MACOR test section walls. Once the walls reach the prescribed temperature, the cartridge heaters will be turned off. Next the core and film flow butterfly valves will be opened simultaneously by means of electrically operated solenoid valves. The pre-adjusted settings of the film flow throttle valve and electric heater determine the film Mach number and total temperature. Thermocouples embedded in the MACOR plate provide a temperature-time history as the test section walls are cooled by the air flow on the surface. The surface heat flux and surface temperature will be backed inferred

from the time response of the thermocouples. The adiabatic film-heating effectiveness will be computed by applying the following equation [10]:

$$\eta_{eff} = 1 - \frac{\dot{Q}_f}{\dot{Q}_0} \quad (5.1)$$

where \dot{Q}_f = the measured heat flux on the film heated (or cooled) wall and \dot{Q}_0 = the measured heat flux on the wall with no film heating.

Typically \dot{Q}_0 is determined on the wall when no film injection takes place [6]. This corresponds to a situation in which no blowing is occurring along the lower test section wall. However, given the current experimental film heating configuration it is more advantageous to measure \dot{Q}_0 on the upper test section wall simultaneously as \dot{Q}_f is measured on the lower wall. Since there is no louver slot present along the upper wall, it is important to note that in this case \dot{Q}_0 and \dot{Q}_f will be determined using slightly different geometries. As a result of this two definitions for the film cooling effectiveness arise based on the different approaches used to determine \dot{Q}_0 , described above:

$$\eta_{eff} = 1 - \frac{\dot{Q}_f}{\dot{Q}_{0, LOWER WALL}} \quad (5.2)$$

$$\eta_{eff} = 1 - \frac{\dot{Q}_f}{\dot{Q}_{0, UPPER WALL}} \quad (5.3)$$

Both of these definitions will be used to analyze the results from the supersonic film heating numerical simulations in §5.6.

Test Matrix

Since the experimental facility cannot duplicate the conditions found in the J-2X nozzle extension, it was necessary to decide which aspects of the problem were most important and could be investigated in our facility in a reasonable amount of time. Extensive discussions with NASA and Pratt & Whitney Rocketdyne concluded that it would be most useful to study the effects of convective Mach number and streamwise pressure gradients on film cooling performance. This led to the four experiment test matrix summarized below in Table 5.1. In the Baseline case, the pressure gradient is zero (ZPG) and the film flow is adjusted to match the velocity ratio in the J-2X engine ($r = 0.45$). In the first Off-Baseline case, the pressure gradient is zero and the film is adjusted to produce a convective Mach number that is close to the design convective Mach number of the J-2X engine ($M_c = 1.08$). In the second Off-Baseline case, the pressure gradient is zero and the film flow is adjusted so that the injection Mach number matches that found in the J-2X engine ($M_f = 1.4$). In the third Off-Baseline case, the injection conditions correspond to the Baseline case but a favorable pressure gradient (FPG) is introduced by allowing the test section area to increase with downstream distance. This condition is most like those found in the actual J-2X engine.

Tests	J-2X Engine	Baseline	Off-Baseline #1	Off-Baseline #2	Off-Baseline #3
Pressure Gradient	FPG	ZPG	ZPG	ZPG	FPG
h (m)	6.35×10^{-3}	6.35×10^{-3}	6.35×10^{-3}	6.35×10^{-3}	6.35×10^{-3}
Core Film	H ₂ /O ₂ H ₂ /H ₂ O*	Air Air	Air Air	Air Air	Air Air
M_∞ M_f	3.74 1.40	2.40 0.73	2.40 0.50	2.40 1.40	2.40 0.73
$T_{0,\infty}$ (K) $T_{0,f}$ (K)	3767 539	300 340	300 340	300 340	300 340
U_∞ (m/s) U_f (m/s)	4117.2 1833.3	568.0 255.6	568.0 180.4	568.0 438.6	568.0 255.6
T_w (K) T_∞ (K) T_f (K)	- 1667.6 323.9	340.0 139.4 307.5	340.0 139.4 323.8	340.0 139.4 244.3	340.0 139.4 307.5
$\Delta T_{f \rightarrow \infty} = T_f - T_\infty$ (K) $\Delta T_{w \rightarrow f} = T_w - T_f$ (K)	1343.8 -	168.1 32.5	184.4 16.2	104.8 95.8	168.1 32.5
$s = \rho_f / \rho_c$	1.39	0.45	0.43	0.57	0.45
$\lambda = \rho_f U_f / \rho_\infty U_\infty$	0.62	0.20	0.14	0.44	0.20
$R = U_\infty / U_f$	2.22	2.22	3.13	1.30	2.22
$M_c = (U_\infty - U_f) / (a_\infty + a_f)$	1.08	0.53	0.65	0.24	0.53

Table 5.1 Proposed test matrix for the supersonic film heating experiment and design operating conditions for the J-2X engine nozzle extension. (*The film is composed of fuel (H₂) rich exhaust gas from an H₂/O₂ turbine).

Measurement techniques

The UMD supersonic wind tunnel is fitted with total pressure gauges for the core and film stream. The core stream gauge faces the oncoming stream of air before the nozzle contraction, while the film stream total pressure is measured inside the plenum below the test section. In addition, there are twelve ports to measure static pressures at the nozzle exits and along the test section walls. All measurements of the pressure, temperature and surface heat flux will be made using pressure transducers,

thermocouples and heat flux gages. In addition, Schlieren imaging will be used to visualize the shear layer growth and any shock patterns formed in the test section. Particle Image Velocimetry (PIV) will also be used to further understand the fluid mechanics of the supersonic film heating process.

5.3 Objectives of the Supersonic Film Heating Numerical Simulations

The main objective of the supersonic film heating numerical simulations was to provide some preliminary calculations to assess the viability of the proposed experimental test matrix and to identify any problems that may arise so that modifications can be made to the experimental setup. Among the key questions that were expected to be answered by the simulation results are:

1. Will the mixing layer growth rate be large enough within the axial distance available in the test section?
2. Will the temperature differences in the plate be large enough to be measured with reasonable accuracy?
3. Will there be significant variation in effectiveness with downstream distance?
4. Will the film break up in an area that is accessible optically and to the sensors?
5. How should the sensors be configured to ensure that they resolve the key features of the flow?

5.4 Validation of Solver

5.4.1 Introduction

In order to be able to apply the RANS methodology developed in Chapter 4 to model the supersonic film cooling experiment outlined in §5.2, it is necessary to validate the loci-CHEM solver under supersonic conditions. This has been done using two simple ‘canonical’ flows: supersonic flow over an angled wedge and supersonic flow over a blunt body

5.4.2 Supersonic flow over a wedge

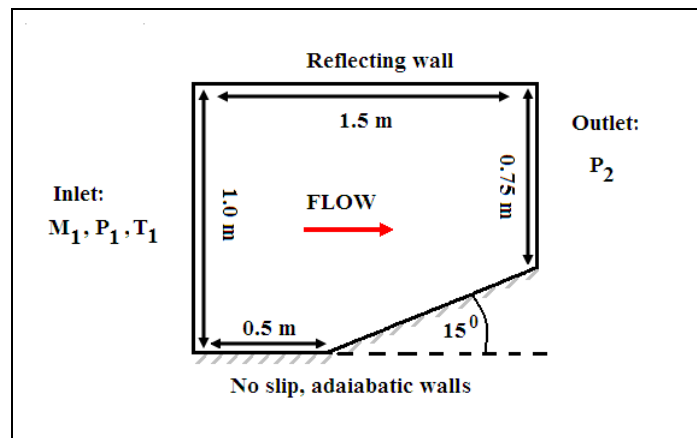


Figure 5-3 Schematic of the supersonic wedge geometry.

Inviscid supersonic simulations were performed using the simple 15° wedge geometry shown above in Figure 5-3. The wedge shown is 1.5m long, with an inlet height of 1.0m and exit height of 0.75m. The grid consists of a total of 15,400 cells, with 154 cells in the x-direction, 100 cells in the y-direction and 1 cell in the z-direction.

The inlet Mach number (M_1) was varied between 2.0 and 8.0. The wave angle (β), the pressure (P_2), static temperature (T_2) and the Mach number (M_2) behind the

oblique shock predicted by CHEM were compared to those predicted using the simple quasi-1-D analytical theory [186]:

$$\tan(\theta) = 2 \cot(\beta) \left[\frac{M_1^2 \sin^2(\beta) - 1}{M_1^2 (\gamma + \cos(2\beta) + 2)} \right] \quad (5.4)$$

$$P_2 = P_1 \left[1 + \frac{2\gamma}{\gamma + 1} (M_1^2 \sin^2(\beta) - 1) \right] \quad (5.5)$$

$$T_2 = T_1 \left[\left(1 + \frac{2\gamma}{\gamma + 1} (M_1^2 \sin^2(\beta) - 1) \right) \frac{(\gamma - 1)M_1^2 \sin^2(\beta) + 2}{(\gamma + 1)M_1^2 \sin^2(\beta)} \right] \quad (5.6)$$

$$M_2 = \frac{\left[\frac{M_1^2 \sin^2(\beta) + [2/(\gamma - 1)]}{[2\gamma/(\gamma - 1)]M_1^2 \sin^2(\beta) - 1} \right]^{1/2}}{\sin(\beta - \theta)} \quad (5.7)$$

where θ is the deflection angle, M_1 is the mach number ahead of the shock and γ is the ratio of specific heats.

Boundary and Initial conditions:

A constant Mach number, pressure and temperature boundary condition is specified at the inlet while a constant pressure boundary condition is specified at the outlet. Also, a no slip boundary condition is applied at the lower wall, which is also set to be adiabatic, and a reflecting boundary condition is applied along the side and walls while gradients in velocity, temperature and pressure are set to zero at the upper wall boundary. All of the cells in the domain are initialized to the inlet conditions. No viscosity or turbulence model is specified in this case as the flow is inviscid.

These boundary conditions are illustrated above in Fig. 5-3 and can be summarized as follows:

$$\begin{aligned}
& \left. \begin{aligned} & P = 120000 Pa \\ & M = \text{constant} \\ & T = 300 K \end{aligned} \right\} \text{inlet} \\
& \text{outlet} : P = 120000 Pa \text{ (farfield)} \\
& \text{lower walls} : \text{no slip (adiabatic)} \\
& \text{side walls} : \text{reflecting} \\
& \text{upper wall} : \frac{\partial U}{\partial y} = 0, \frac{\partial P}{\partial y} = 0, \frac{\partial T}{\partial y} = 0
\end{aligned} \tag{5.8}$$

Results:

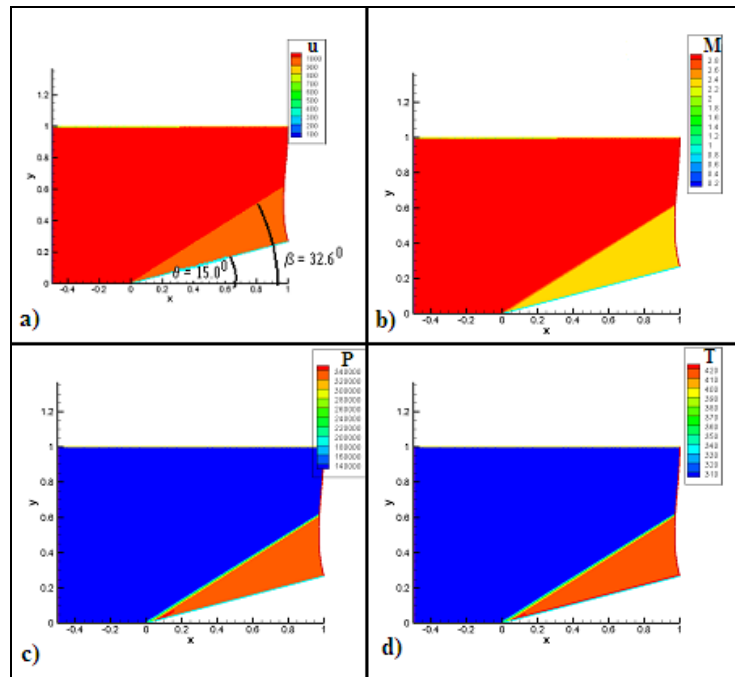


Figure 5-4 Plot showing contours of: a) x-component velocity (u), b) Mach number (M), c) pressure (P) and d) temperature (T), predicted by CHEM for Mach 3.0 flow over a 15° wedge.

Figure 5-4 shows contours of a) x-component velocity (u), b) Mach number (M), c) pressure (P) and d) temperature (T) predicted by Loci-CHEM for Mach 3.0 flow over a 15.0° wedge. The figure clearly shows that an oblique shock with a wave angle (β) of 32.6° is formed. This is within 1% of the value predicted using quasi-one dimensional theory ($\beta = 32.2^\circ$).

To further assess CHEM's performance the predicted wave angle (β), pressure (P_2), Mach number (M_2) and temperature (T_2) behind the shock can be compared with exact values from oblique shock theory. For Mach 3.0 upstream conditions, CHEM predicts $M_2 = 2.255$, $T_2 = 380.6$ K and $P_2 = 0.339 \times 10^6$ Pa. These values are within 0.2 % of the exact solution as indicated in Table 5.2, which further suggests that CHEM is capable of accurately predicting supersonic flows. To build further confidence in the numerical solver, the numerical predictions for β , M_2 , T_2 and P_2 , can also be compared with the exact solution at other upstream Mach numbers between 2.0 and 8.0 and under identical conditions. As shown in Table 5.2 the CHEM predictions for β , M_2 , T_2 and P_2 closely match (to within <2.7%) the exact solution over the entire range of upstream Mach numbers explored. This confirms that Loci-CHEM can be used to accurately simulate supersonic flows.

M_1	β			T_2 [K]			$P_2 \times 10^6$ [Pa]			M_2		
	CHEM	<i>I-D</i>	% Error	CHEM	<i>I-D</i>	% Error	CHEM	<i>I-D</i>	% Error	CHEM	<i>I-D</i>	% Error
2	45.3 ⁰	45.3 ⁰	< 0.2	380.9	380.8	< 0.1	0.263	0.263	<0.1	1.445	1.446	<0.1
3	32.6 ⁰	32.2 ⁰	< 1.1	416.3	416.5	< 0.1	0.339	0.338	<0.3	2.255	2.255	<0.1
4	26.8 ⁰	27.1 ⁰	< 1.0	463.6	463.9	< 0.1	0.444	0.443	<0.3	2.931	2.929	<0.1
5	24.3 ⁰	24.3 ⁰	< 0.2	519.6	520.8	< 0.3	0.576	0.573	<0.6	3.510	3.50	<0.2
6	22.8 ⁰	22.7 ⁰	< 0.4	584.4	587.5	< 0.6	0.731	0.728	<0.5	4.100	3.99	<2.7
7	21.7 ⁰	21.6 ⁰	< 0.6	657.7	664.4	<1.1	0.906	0.908	<0.3	4.510	4.40	<2.5
8	21.0 ⁰	20.9 ⁰	<0.5	737.6	751.6	<1.9	1.099	1.114	<1.4	4.924	4.75	<1.4

Table 5.2 Summary of the β , M_2 , P_2 and T_2 conditions predicted by Loci-CHEM and the exact oblique shock relations.

5.4.3 Supersonic flow over a blunt body

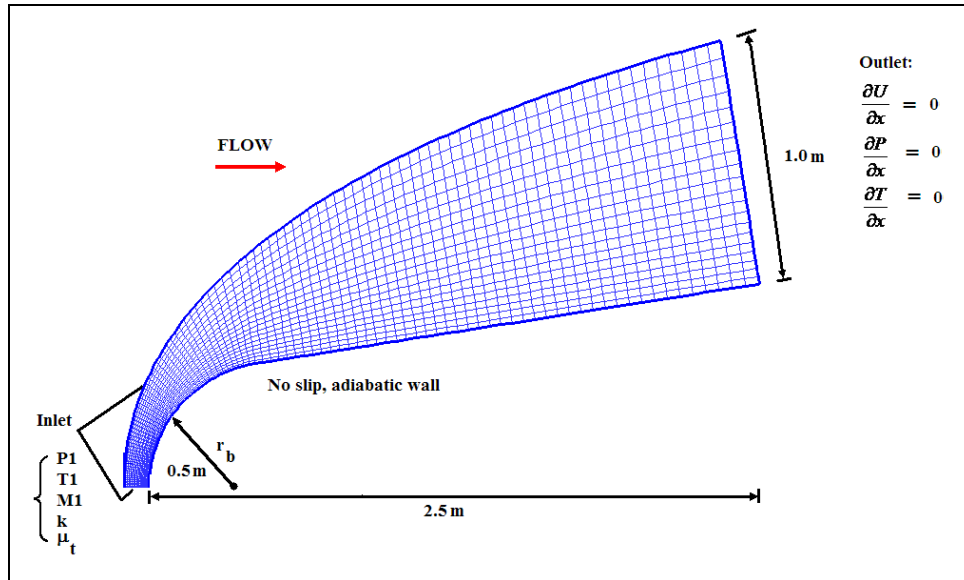


Figure 5-5 Schematic of the blunt body grid.

Turbulent supersonic simulations were performed using the blunt body geometry shown above in Figure 5-5. The grid shown is 2.5m long, with an inner radius of 0.5m and an exit height of 1.0m. The grid consists of 2000 cells, with 100 cells in the x-direction, 20 cells in the y-direction and 1 cell in the z-direction. The Reynolds number (based on the blunt body radius) for these simulations varied between 9.3×10^7 and 1.56×10^8 as the Mach number was changed from 6.0 to 10.0.

The objective of this test case was to examine whether Loci-CHEM solver can accurately capture the characteristics of a mixed subsonic-supersonic, turbulent flowfield. This is relevant to the supersonic film cooling simulations since some test cases involve subsonic coolant injection into the supersonic core flow. The standoff distance of the curved, detached shock will be compared to experimental measurements from Liepmann et al. [249] over a range of flow Mach numbers between 6.0 and 10.0. The predictions will also be evaluated qualitatively to assess

whether they accurately capture the stagnation point, as well as the subsonic and supersonic regions in the flow behind the curved shock.

Boundary and Initial conditions:

Constant Mach number, pressure, temperature, turbulent kinetic energy and dissipation rate were specified at the inlet (along the upper wall surface); while a constant pressure boundary condition was specified at the outlet. All of the cells in the domain were initialized to the inlet conditions. A no slip boundary condition was also applied along the lower wall, which was set to be adiabatic, while a symmetry boundary condition was applied along the sidewalls.

Menter's Shear Stress Transport (SST) turbulence model was used, along with a fixed turbulent Prandtl number of 0.7. Estimates for the values of the turbulent kinetic energy (k) and the turbulent eddy viscosity (μ_t) at the inlets were made by assuming an initial turbulence intensity, $I_v = 0.05$, and by applying Eq. (4.35) and (4.36).

The boundary conditions applied in this case are illustrated above in Figure 5-5 and can be summed up as follows:

$$\begin{aligned}
 & \left. \begin{aligned}
 & P = 29,500 \text{ Pa} \\
 & M = \text{constant} \\
 & T = 223 \text{ K} \\
 & k = \text{constant} \\
 & \mu_t = \text{constant}
 \end{aligned} \right\} \text{inlet} : \tag{5.9} \\
 & \text{outlet} : \frac{\partial U}{\partial x} = 0, \frac{\partial P}{\partial x} = 0, \frac{\partial T}{\partial x} = 0 \\
 & \text{lower wall} : \text{no slip (adiabatic)} \\
 & \text{side walls} : \text{symmetry}
 \end{aligned}$$

Results:

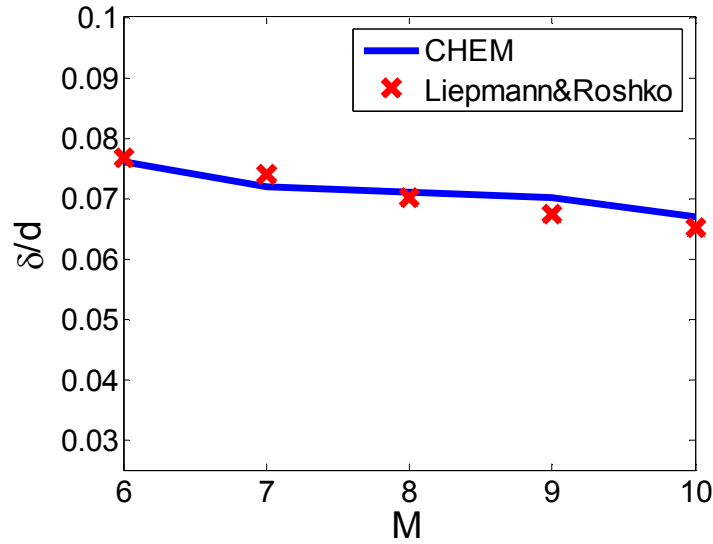


Figure 5-6 Plot of shock standoff distance, δ/d , as a function of Mach number, M , associated with turbulent, supersonic flow over a blunt body over a range of Mach numbers between 6 and 10.

The numerical predictions were compared with experimental measurements from Liepmann et al. [244] of the non-dimensional shock standoff distance, δ/d , where d is the diameter of the blunt body (i.e. $d = 2r_b$). The results of this comparison are shown above in Figure 5-6 which plots non-dimensional shock standoff distance (δ/d) as a function of Mach number (M), and below in Table 5.3. The numerical predictions match the experimental data to within less than 5% difference.

M	δ/d		
	CHEM	Data	%Difference
6	0.076	0.077	<1.3%
7	0.072	0.074	<2.7%
8	0.071	0.070	<1.5%
9	0.070	0.068	<2.9%
10	0.067	0.065	<3.1%

Table 5.3 Summary of results for the standoff distance of a detached shock associated with turbulent, supersonic flow over a blunt body at various upstream Mach numbers.

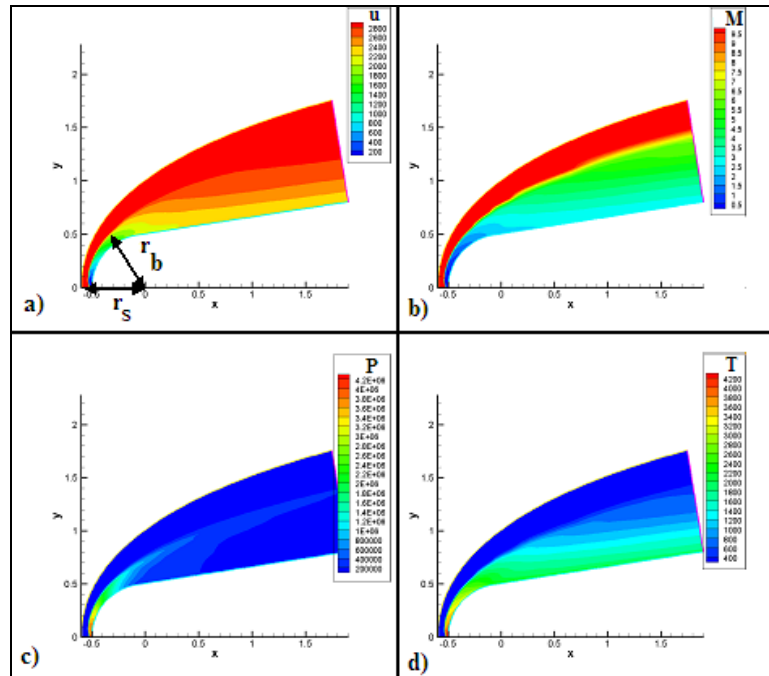


Figure 5-7 Contours of a) x-component velocity (u), b) Mach number (M), c) pressure (P) and d) temperature (T) associated with supersonic flow over a blunt body at Mach 10.

To gain insight into the flow structure under highly compressible conditions the Mach number, pressure, temperature and velocity contours associated with the blunt body flow can be examined. These are illustrated in Figure 5-7 a)-d) for Mach 10 flow over a blunt body. Figure 5-7 a) shows velocity magnitude as well as the relationship between r_b , the radius of the spherical blunt body, and r_s , the radius corresponding to the shock location. The figure clearly shows the presence of a stagnation point at the front of the body (as indicated by the high temperature and pressure at that location), as well as the high pressure and low Mach number, subsonic region, located just above the stagnation point. This gives way to a lower pressure and temperature supersonic region with increasing streamwise distance. This result is consistent with the mixed subsonic-supersonic flow regime expected for a blunt body. Taken together these results suggest that Loci-CHEM can be used to

provide reasonable predictions of mixed subsonic-supersonic flows under turbulent conditions.

5.5 Supersonic Film Cooling Simulation Details

5.5.1 Introduction

Having validated the Loci-CHEM solver's performance under supersonic conditions using simple canonical flow problems, the next step is to use the solver to predict the more complicated physics present in the supersonic film 'heating' experiment. As in the subsonic case, a RANS methodology was used to minimize computational expense. Two cases were selected for modeling: the subsonic film injection (Off-Baseline #1 Case) and the supersonic film injection (Off-Baseline #2 Case). A detailed description of the grid, boundary and initial conditions, and the convergence criterion used is provided in the following subsections.

5.5.1 Grid Details

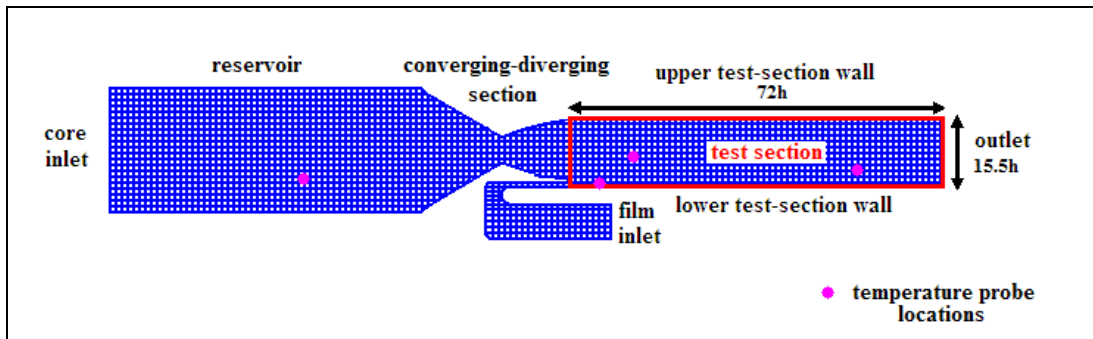


Figure 5-8 Schematic illustration of the grid used for the supersonic film heating simulations.

Figure 5-8 shows a schematic illustration of the two-dimensional grid that was used for the supersonic film heating numerical simulations. The computational domain is composed of the core stream diffuser inlet, a converging-diverging section, the main test section, and the coolant stream inlet manifold with a half nozzle

integrated into a louver. The test section extends 72 slot heights in the streamwise direction from the exit of the louver and 15.5 slot heights in the wall normal direction. Of paramount importance in generating a grid suitable for simulating turbulent, supersonic film cooling flow was ensuring that both temperature and velocity gradients were adequately resolved in the viscous sub-layer at the wall boundary and also in the shear region located at the interface between the mainstream and the coolant stream. Since isothermal (not adiabatic as in the subsonic simulations) boundary conditions are applied at the test section walls, it is also necessary to resolve the heat flux into the wall. This requires a grid resolution which is an order of magnitude greater than what is needed to resolve temperature and velocity gradients. A grid independence study found that the minimum number of grid cells needed to produce a resolved solution with $y^+ < 0.1$ was 250,330 cells.

5.5.2 Boundary and Initial Conditions

Off-Baseline #1 Case

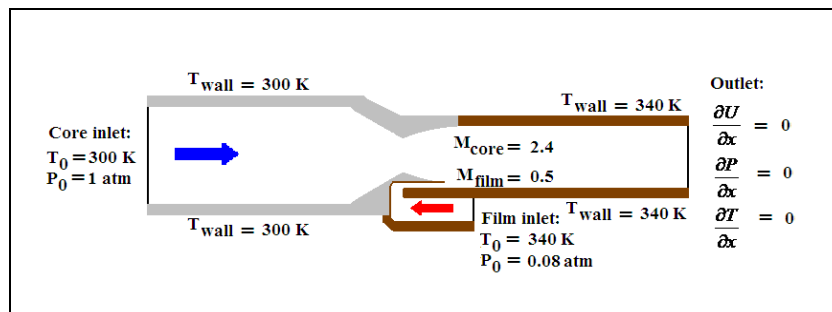


Figure 5-9 Schematic of the supersonic film heating computational domain showing the boundary conditions used in the Off-Baseline #1 Case numerical simulations.

A schematic illustration of the boundary conditions applied in the Off-Baseline #1 Case supersonic film heating numerical simulations is shown in Figure 5-9. At the film and core inlets, the total temperature and pressure are prescribed to be 340K and 0.08atm and 300K and 1atm respectively. Gradients in velocity,

temperature and pressure are set to zero at the outlet boundary. No slip, isothermal boundary conditions are applied along the upper and lower test section walls, the film manifold walls and the core converging-diverging section walls. The wall temperatures are set to 340K in the test section and manifold, and 300K in the core converging-diverging section. A reflecting boundary condition is specified along the side walls. The cells in the core and test section are initialized to the core inlet conditions while the louver cells are initialized to the film inlet conditions. These boundary conditions can be summarized as follows:

$$\begin{aligned}
 \text{core inlet : } & \begin{cases} P_0 = 1 \text{ atm} \\ T_0 = 300 \text{ K} \end{cases} \\
 \text{coolant inlet : } & \begin{cases} P_0 = 0.08 \text{ atm} \\ T_0 = 340 \text{ K} \end{cases} \\
 \text{outlet : } & \frac{\partial U}{\partial x} = 0, \frac{\partial P}{\partial x} = 0, \frac{\partial T}{\partial x} = 0 \\
 \text{lower \& upper test section \& film manifold walls : } & \text{no slip, } T_{\text{wall}} = 340 \text{ K} \\
 \text{side walls : } & \text{reflecting} \\
 \text{core converging - diverging section walls : } & \text{no slip, } T_{\text{wall}} = 300 \text{ K}
 \end{aligned} \tag{5.10}$$

Off-Baseline #2 Case

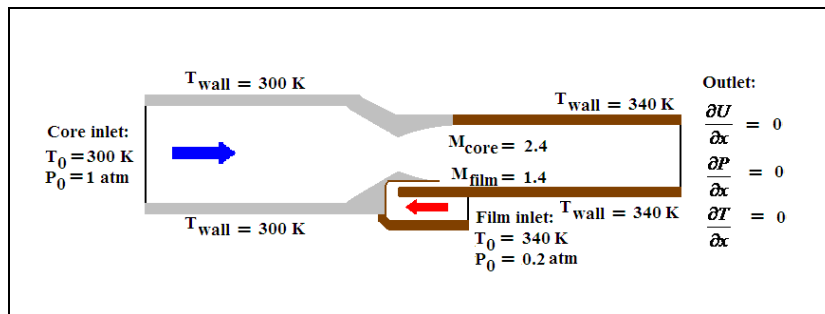


Figure 5-10 Schematic of the supersonic film heating computational domain showing the boundary conditions used in the Off-Baseline #2 Case numerical simulations.

Figure 5-10 is a schematic illustration of the boundary conditions applied in the Off-Baseline #2 Case supersonic film heating numerical simulations. At the film

and core inlets the total temperature and pressure are prescribed to be 340K and 0.2atm and 300K and 1atm respectively. Gradients in velocity, temperature and pressure are set to zero at the outlet boundary. No slip, isothermal boundary conditions are applied along the test section walls, the film manifold walls, and the core converging-diverging section walls. The wall temperatures are set to 340K in the test section and manifold and 300K in the core converging-diverging section. A reflecting boundary condition is specified along the side walls. The cells in the core and test section are initialized to the core inlet conditions while the louver cells are initialized to the film inlet conditions. The boundary conditions applied in this case can be summarized as follows:

$$\begin{aligned}
 \text{core inlet} : & \begin{cases} P_0 = 1\text{atm} \\ T_0 = 300\text{K} \end{cases} \\
 \text{coolant inlet} : & \begin{cases} P_0 = 0.2\text{atm} \\ T_0 = 340\text{K} \end{cases} \\
 \text{outlet} : & \partial U / \partial x = 0, \partial P / \partial x = 0, \partial T / \partial x = 0 \\
 \text{lower \& upper test section \& film manifold walls} : & \text{no slip, } T_{\text{wall}} = 340\text{K} \\
 \text{side walls} : & \text{reflecting} \\
 \text{core converging - diverging section walls} : & \text{no slip, } T_{\text{wall}} = 300\text{K}
 \end{aligned} \tag{5.11}$$

5.5.3 Turbulence Model

All of the supersonic film cooling simulations were performed using Menter's Shear Stress Transport (SST) two-equation turbulence model [225], which was described in §4.2.2.

5.5.4 Convergence/Steady State

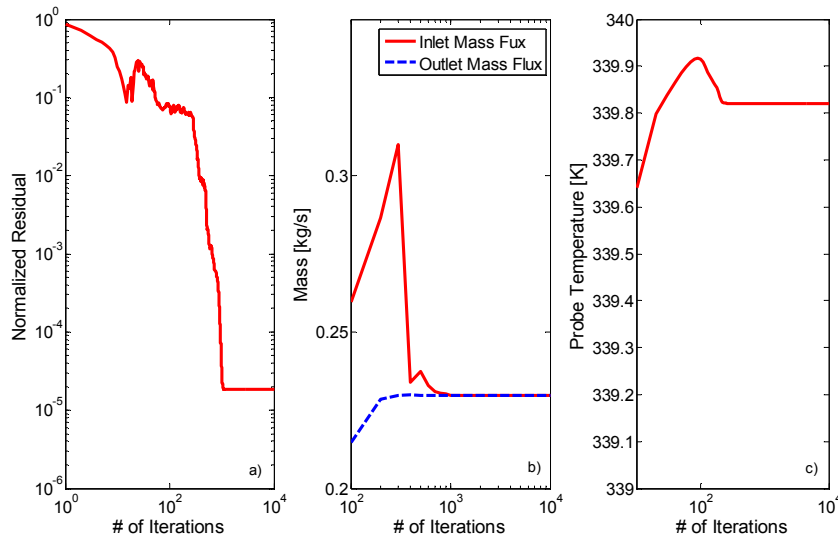


Figure 5-11 a) Residual drop, b) Mass conservation, c) Temperature probe output, as a function of the number of iterations performed for the Off-Baseline #2 case with film heating.

Convergence of the solutions is established by observing the decrease in the overall normalized residual, by comparing the total mass flow at the inlet to the outlet, and by examining the behavior of the static temperature as a function of solution iteration at four probe points located throughout the flow-field (see Figure 5-8). Figure 5-11 is a representative plot for the Off-Baseline #2 film heating case that illustrates this approach. Figure 5-11 a) shows the variation of the overall normalized residuals with iteration number. Figure 5-11 b) shows inlet and outlet mass flows as a function of iteration number. Figure 5-11 c) shows how the temperature at the first probe point, located in the reservoir of the core inlet, varies with increasing iteration number. Figures 5-11 a) shows that 1300 iterations are needed in order to achieve a normalized residual drop of at least 4 orders of magnitude while Figure 5-11 b) shows that mass conservation is satisfied to within 0.1 percent of the total mass flow after 1200 iterations. Figure 5-11 c) also shows that roughly 350 iterations are required to

approach steady state in temperature at the selected probe location. Therefore, running to at least 2000 iterations was considered adequate for ensuring convergence.

5.6 Results

5.6.1 Thermal mixing

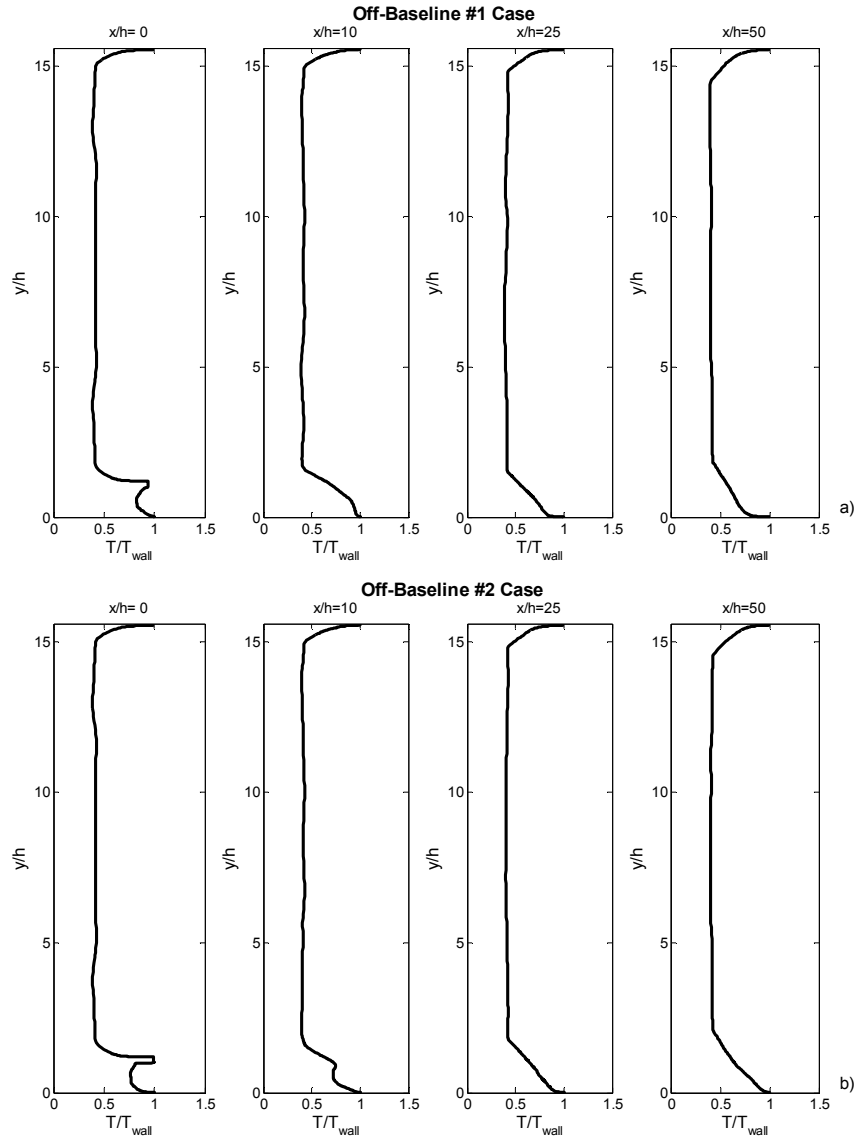


Figure 5-12 Profiles of normalized temperature, T/T_{wall} , at four discrete locations downstream of the point of film injection, associated with film heating of an isothermal wall under the conditions given in: a) the Off-Baseline #1 Case and b) the Off-Baseline #2 Case.

In order to gain insight into the thermal mixing occurring in the near-wall regions of the test section and in the shear layer formed at the film-core stream interface the evolution of normalized temperature (T/T_{wall}) can be plotted as a function of wall normal distance (y/h) at four discrete locations downstream of the point of film injection ($x/h = 0, 10, 25$ and 50). This has been done above in Figure 5-12 a) and b) for the Off-Baseline #1 (subsonic injection) and Off-Baseline #2 (supersonic injection) cases respectively. Considering the lower wall in the Off-Baseline #1 case first, at the injection point ($x/h = 0$) it is evident that the walls are hotter than the core flow and the film. As x/h increases from 0 to 50, the penetration of the core stream into the film stream increases steadily as indicated by the gradual steepening of the slope of the temperature profile near the lower wall boundary. This indicates a decrease in film heating effectiveness with downstream distance. Along the upper wall, which has no film injection, a much different trend is observed. The slope of the temperature profile near the wall is initially quite steep, and only increases very gradually from $x/h = 0$ to $x/h = 50$. This indicates that the heat flux at the upper wall surface remains roughly constant along its entire length and is greater than on the lower wall. It also suggests that turbulent transport is relatively slower in this region. Similar qualitative trends are observed in Figure 12 b) for the upper and lower walls in the Off-Baseline #2 case. The key difference between the two cases occurs above the lower wall at $x/h = 10$. The figure shows that the film in the Off-Baseline #2 case takes longer to mix with the core stream than it does in the Off-Baseline #1 case. This is likely due to the fact that the film is injected supersonically

in the Off-Baseline #2 case enabling it to persist for a longer distance before breaking down.

5.6.2 Momentum mixing

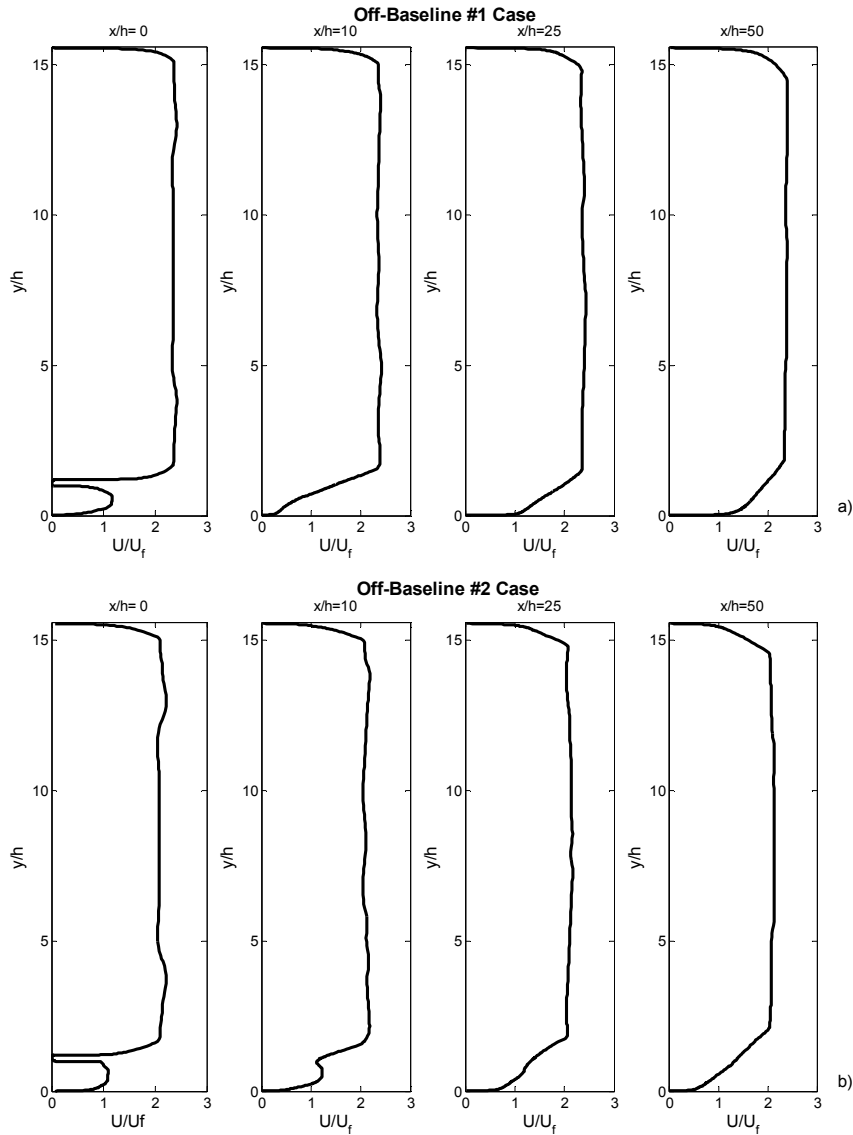


Figure 5-13 Profiles of normalized velocity, U/U_f , at four discrete locations downstream of the point of film injection, associated with the film heating of an isothermal wall under conditions specified in: a) the Off-Baseline #1 Case and b) the Off-Baseline #2 Case.

It is also useful to examine the momentum mixing occurring in the test section under both subsonic and supersonic film injection conditions. To do this the normalized velocity (U/U_f) can be plotted as a function of wall normal distance (y/h)

at four discrete locations downstream of the point of film injection ($x/h = 0, 10, 25$ and 50) in Figure 5-13. The figure shows that in the Off-Baseline #1 and Off-Baseline #2 cases similar qualitative trends are observed for both the upper and lower wall surfaces. Along the lower wall, the injection of the film initially causes a steep velocity gradient near the wall ($y/h = 0$) and at the film-mainstream interface ($y/h \approx 1$). As x/h increases, this velocity gradient become shallower as momentum diffuses from the higher speed core stream towards the lower speed film stream. By $x/h = 25$, the velocity profile has evolved sufficiently to resemble a boundary layer velocity profile and maintains this shape at $x/h = 50$. In sharp contrast, the velocity profile along the upper wall looks like a conventional boundary layer at $x/h = 0$ and remains almost unchanged as x/h is increased from 0 to 50. As in the thermal mixing results, the main differences between the Off-baseline #1 and Off-Baseline #2 cases arise from the differing rates at which the films mix with the core flow. These results suggest that the film persists longer in the supersonic injection (off-baseline) case than it does in the subsonic (baseline) case and that that film heating effectiveness should be higher in the former case.

5.6.3 Heat Flux and Film Heating Effectiveness

Off-Baseline #1 Case

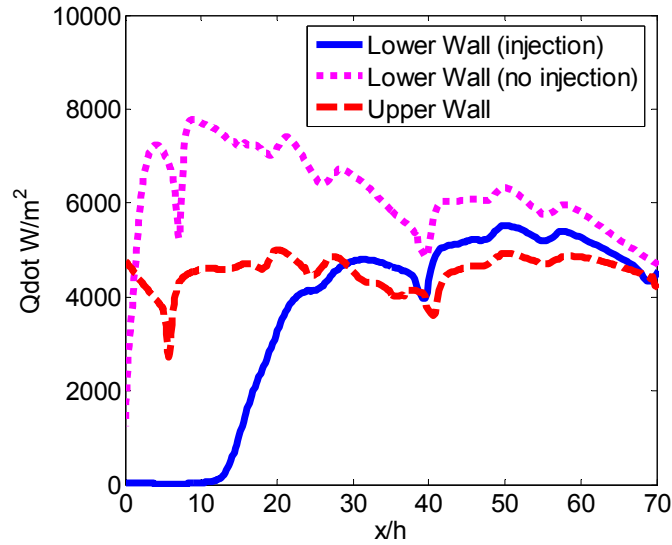


Figure 5-14 Heat flux (\dot{Q}) as a function of non-dimensional streamwise distance (x/h) along the lower and upper test section walls predicted by CHEM for the Off-Baseline #1 case with and without film injection.

Figure 5-14 shows a plot of heat flux (\dot{Q}) as a function of non-dimensional streamwise distance (x/h) along the lower and upper test section walls for the Off-Baseline #1 (subsonic film injection) case with and without film heating. \dot{Q} is computed by the solver using Fourier's Law which relates heat conduction and temperature gradients using the following expression [222]:

$$\dot{Q} = \left(k + \frac{\mu_t C_p}{Pr_t} \right) \nabla T \quad (5.11)$$

where k is the thermal conductivity, C_p is the specific heat capacity, Pr_t is the turbulent Prandtl number and μ_t is the turbulent eddy viscosity.

The solid line in Figure 5-14 corresponds to the heat flux along the lower test section wall with film injection, the dotted line corresponds to the heat flux along the lower test section wall without film injection and the dashed line corresponds to the heat flux along the upper test section wall. It is important to note here that upper and lower wall heat fluxes will be measured simultaneously in the experiment to facilitate comparison to the numerical simulations. The figure shows that initially (when $x/h < 20$) the heat flux along the film heated wall is initially much less than in the other cases. However, for $x/h > 20$ the heat flux rises rapidly with downstream distance until it exceeds the heat flux along the upper wall. By $x/h \sim 40$ the heat flux stabilizes and tracks the heat flux along the upper wall. The sharp dips in the heat flux observed near $x/h = 6$ and $x/h = 40$ are due to shockwave interactions with the boundary layers growing along the walls which significantly complicate the flowfield as illustrated schematically in Figure 5-15.

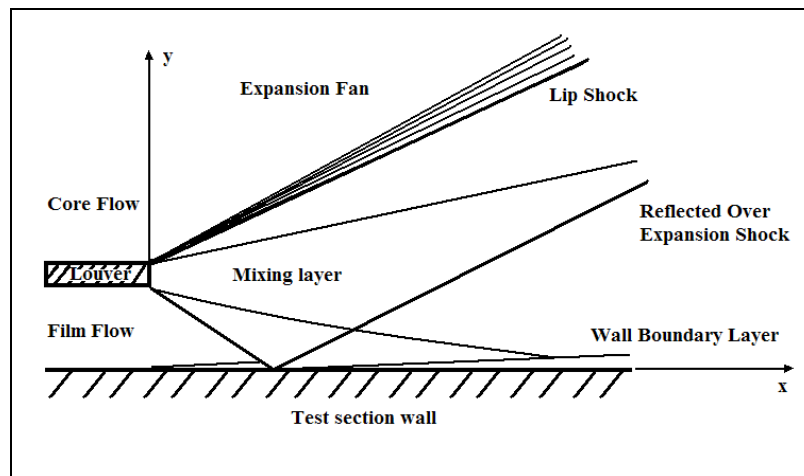


Figure 5-15 Schematic illustration of the supersonic film heating flowfield highlighting the shockwave boundary layer interaction. {Adapted from Bowersox et al. [209] (1994)}

The trends observed in Figure 5-14 can be explained by the fact that the film acts to thicken the wall boundary layer as shown below in Figure 5-16. Thicker

boundary layers provide better insulation from the cooler core flow because they reduce the thermal gradient near the wall by keeping cooler core flow farther away from the wall. In contrast, the heat flux is higher for the test section walls without film heating since the wall boundary layers are thinner as can be seen in Figure 5-15 and the cooler core flow is closer to the wall. Interestingly, a slightly higher heat flux is obtained over the lower wall when there is no film injection through the louver. This is because the small separation region immediately downstream of the louver ‘resets’ the boundary layer making it thinner than the boundary layer on the upper wall which has had a longer streamwise distance over which to grow.

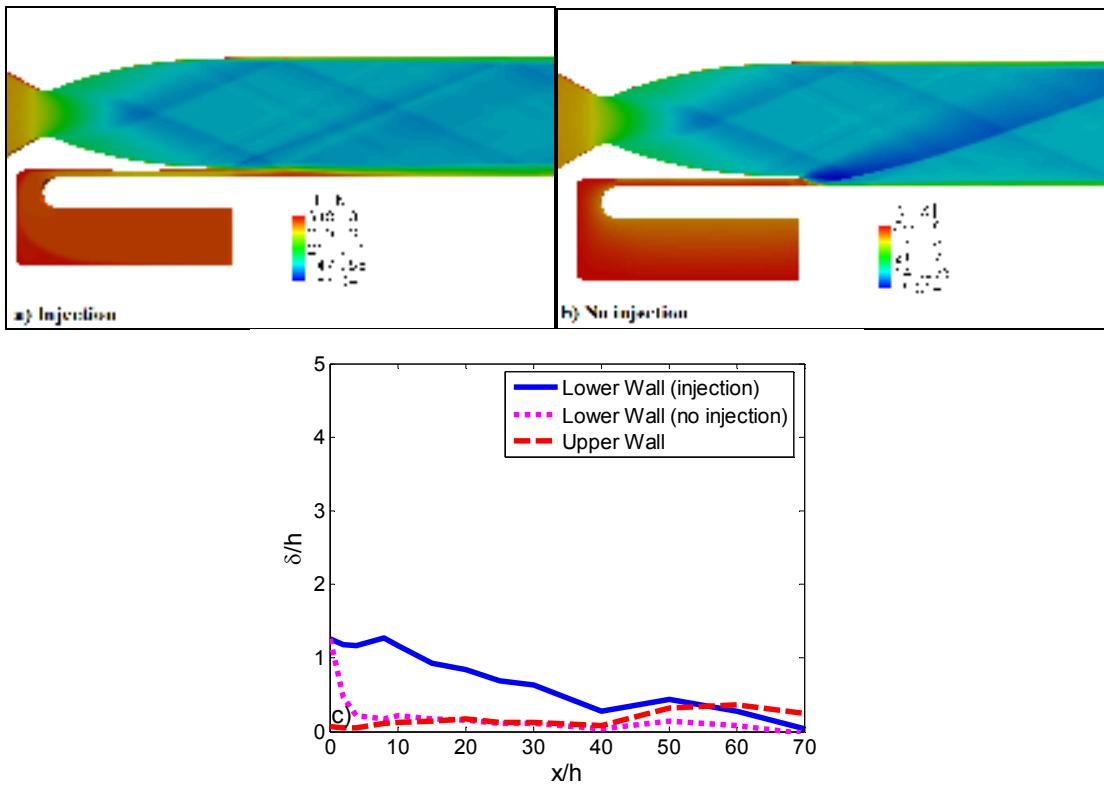


Figure 5-16 Contours of constant temperature associated with the Off-Baseline #1 Case: a) with film injection and b) without film injection. c) Non-dimensional thermal boundary layer thickness⁶ (δ) associated with the upper and lower walls for the Off-Baseline #1 Case.

⁶ The thermal boundary layer thickness (δ) is estimated by finding wall-normal location where the temperature is 2/3 of the wall temperature.

Figure 5-17 shows the film cooling effectiveness as a function of non-dimensional streamwise distance (x/h) for the Off-Baseline #1 case. The dashed line corresponds to effectiveness computed based on \dot{Q}_0 for lower test section wall without film injection while the solid line indicates the effectiveness when \dot{Q}_0 for the upper test section wall is used. The figure shows similar qualitative trends in both cases. The effectiveness is initially very close to unity before it sharply decline towards zero near $x/h \approx 15$. These results can be explained by the fact that the coolant–core stream velocity ratio (r) is 0.30 which means that there is strong shearing (i.e., mixing) occurring at the film–core stream interface. This leads to a relatively large shear layer growth rate that causes the film to break down within a short distance of the point of injection despite the moderately high convective Mach number ($M_c = 0.69$).

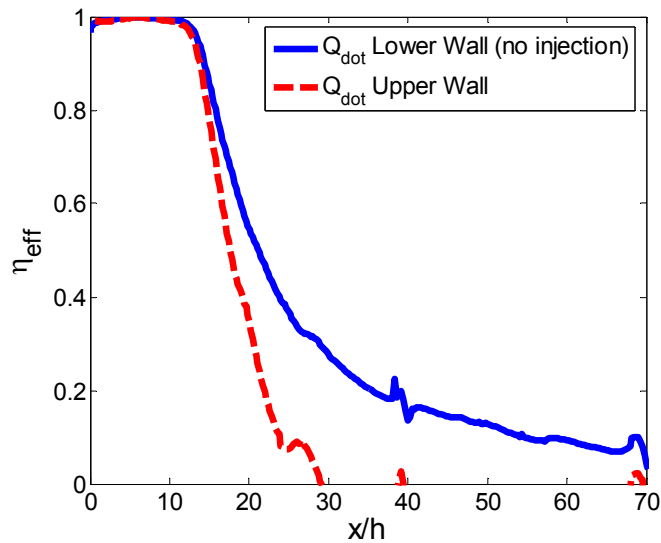


Figure 5-17 Adiabatic film cooling effectiveness (η_{eff}) as a function of non-dimensional streamwise distance (x/h) along the test section wall predicted by CHEM for the Off-Baseline #1 configuration with and without film heating.

These results indicate that the proposed Off-Baseline #1 configuration for the supersonic film heating experiments will be able to produce a measurable change in effectiveness within the length of the test section. Figure 5-17 indicates that the

experiment should have high sensor density between $15 < x/h < 40$ so that the transition point between the initial and developed regions of the film can be resolved. In addition, comparison of the results from the two definitions of effectiveness shows that there is a negligible difference in the predicted effectiveness in the near injection region ($x/h < 20$), with no impact on the transition point. In the far-field ($x/h > 20$) there is a significant impact on the predicted effectiveness observed, however, this occurs in a region of the film that is not physically significant as the effectiveness has by that point decayed to a level which is insufficient to provide thermal protection of the wall.

Off-Baseline #2 Case

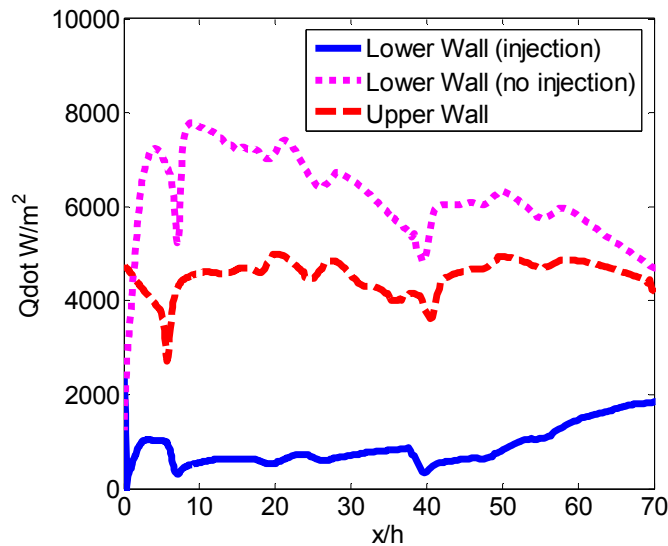


Figure 5-18 Heat flux (\dot{Q}) as a function of non-dimensional streamwise distance (x/h) along the lower and upper test section walls predicted by CHEM for the Off-Baseline #2 case with and without film injection.

Figure 5-18 shows a plot of heat flux (\dot{Q}) as a function of non-dimensional streamwise distance (x/h) along the lower and upper test section walls predicted by CHEM for the Off-Baseline #2 case with and without film heating. The solid line

corresponds to the heat flux along the lower test section wall with film injection, the dotted line corresponds to the heat flux along the lower test section wall without film injection and the dashed line corresponds to the heat flux along the upper test section wall. The figure shows that the lower wall heat flux is much smaller when a film is injected. This occurs because the film thickens the boundary layer as shown in Figure 5-19 a) - c). A thicker boundary layer insulates the wall better than a thinner one, since it keeps the cooler core flow away from the wall thereby reducing the thermal gradient and the corresponding heat flux. As before, if a film is not injected, the boundary layer is much smaller and the heat flux is much higher.

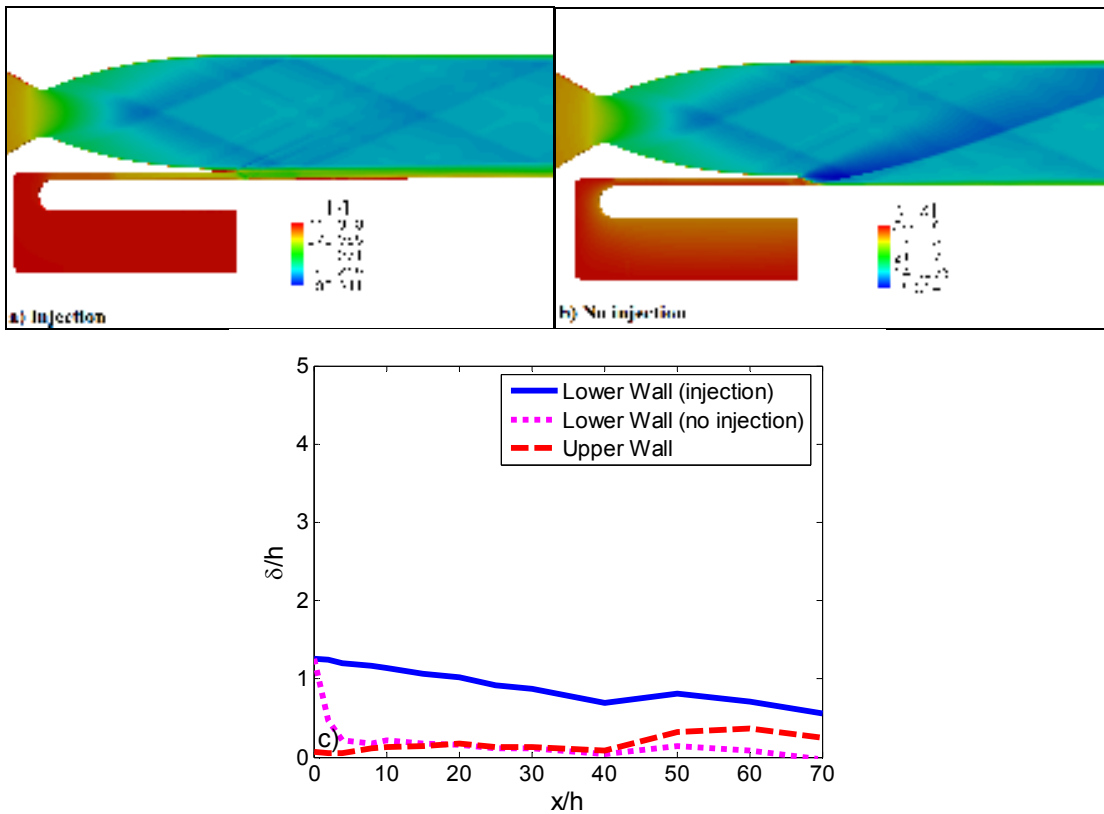


Figure 5-19 Contours of constant temperature associated with the Off-Baseline #2 Case: a) with film injection and b) without film injection. c) Thermal boundary layer thickness associated with the upper and lower walls for the Off-Baseline #2 Case.

Figure 5-20 shows the film cooling effectiveness (η_{eff}) as a function of non-dimensional streamwise distance (x/h) for the Off-Baseline #2 (supersonic film injection) case. The dashed line corresponds to effectiveness computed based on for the lower test section wall without film injection while the solid line indicates the effectiveness when for the upper test section wall is used. As was observed previously in the Off-Baseline #1 case, the figure shows similar qualitative and quantitative trends for both definitions of effectiveness. Initially, the effectiveness is very close to unity but it drops off sharply due to shock impingement near $3 < x/h < 10$. The drop in effectiveness is likely due to shock induced mixing which causes enhancement of mixing in the vicinity of the shock resulting in a local a decrease in effectiveness. Thereafter effectiveness rises and remains almost constant in magnitude between roughly 0.85-0.90 in the range $10 < x/h < 50$. The effectiveness decays rapidly after $x/h = 50$ until it reaches approximately 0.6. These trends can be explained by the fact that the coolant-core stream velocity ratio (r) in this case is 0.75 which is very close to unity. As a result the shearing between the two streams is relatively weak and therefore the film takes a long distance to break down. The low convective Mach number in this case ($M_c = 0.27$), suggests that compressibility effects are relatively unimportant and that the mixing layer formed at the coolant-core stream interface is essentially incompressible.

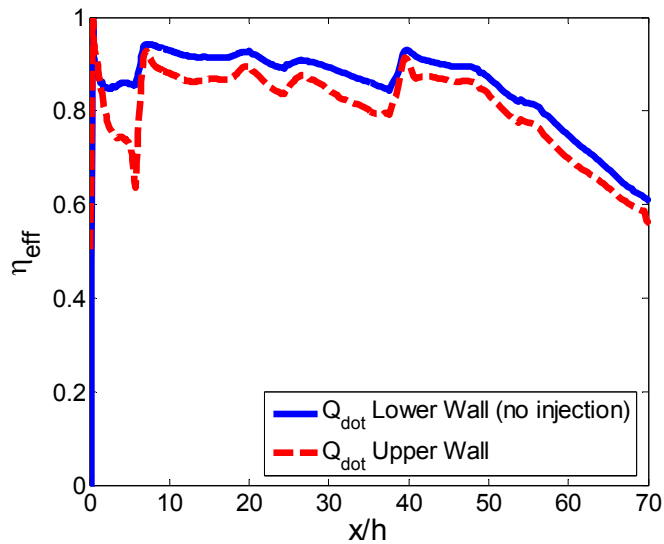


Figure 5-20 Adiabatic film cooling effectiveness (η_{eff}) as a function of non-dimensional streamwise distance (x/h) along the test section wall predicted by CHEM for the Off-Baseline #2 configuration with and without film heating.

Based on these results it can be concluded that the proposed Off-Baseline #2 experimental configuration will be able to produce a change in effectiveness within the length of the test section which is measurable within the length of the test section. Figure 5-20 indicates that the experiment should have high sensor density between $40 < x/h < 60$ so that the transition point between the initial and developed regions of the film can be resolved. In addition, comparison of the results of the two definitions of effectiveness shows that film injection does not seem to make a difference until $x/h > 15$.

5.7 Conclusions

The computationally inexpensive RANS methodology developed in Chapter 4 for the numerical simulation of turbulent, subsonic film cooling flow was adapted to supersonic conditions in order to aid in the design of a supersonic film heating experiment. Two test cases, a subsonic film injection (Off-Baseline #1) case and a

supersonic film injection (Off-Baseline #2) case, were explored. Since the experiment is still being built, the numerical results were used to qualitatively assess the viability of the experiment under design conditions and to guide the layout of instrumentation. Examination of the wall heat flux results showed that the presence of the film significantly reduces the heat flux when compared to a situation without film heating. The simulations show that the film thickens the wall boundary layer thereby reducing the thermal gradient into the wall and increasing effectiveness. A comparison of the effectiveness results for two test cases revealed that a higher effectiveness is expected in the Off-Baseline #2 case because the velocity ratio is close to unity ($R = 1.30$) and the shearing between the film and core streams is low. The added momentum of the supersonic injection also enables it to persist for longer along the wall before breaking down. Comparison of results for two different definitions of the film heating effectiveness revealed that the effectiveness in the near-injection region seems to be controlled by something other than the injection, since the predicted effectiveness was identical in both cases for $x/h < 15$.

Overall, these results indicate that the configuration to be used in the supersonic film heating experiments will be able to produce a measurable change in effectiveness within the length of the test section under both subsonic and supersonic film injection conditions. The simulations also indicate that it is desirable to have high sensor density in the region $15 < x/h < 60$ in order to be able to resolve the transition point between the initial and developed regions of the film.

Chapter 6: Conclusions

6.1 Research Summary

The main focus of this work was to improve the basic physical understanding and prediction of the effects of pressure gradients, density gradients and compressibility on film cooling effectiveness. This was accomplished using a combined program of analytical modeling and numerical simulation employing a computationally efficient RANS methodology.

The first step was to perform a thorough review of the literature on film cooling that ultimately comprised more than 180 references. One of the highlights of this review was the discovery of a longstanding disagreement in the literature over the beneficial or detrimental effects of pressure gradients and compressibility on film cooling performance. In addition, no clear picture emerged in the literature as to the relative favorability of either RANS or LES approaches, although it was agreed that DNS is not yet practical because it is too computationally intensive.

After establishing the current state of the art in film cooling, the second step was to investigate the influence of mainstream pressure gradients on cooling performance. The goal was to resolve the conflicts in the literature and provide a clearer picture of the effect of pressure gradients on the film cooling process. To do this the semi-empirical, incompressible film cooling analysis developed by Simon [114] was extended to account for the effect of main stream pressure gradients. This was achieved through a modification to the momentum equation following Abramovich [27].

The third step focused on improving the understanding of the influence of compressibility and density gradients on film cooling effectiveness. To do this it was necessary to devise ways to quantify velocity and thermal compressibility effects (i.e., the influence of density gradients that arise due to both large velocity and thermal differences) in film cooling flows. Three compressibility parameters: the convective Mach number (M_c), the total temperature ratio (θ_0) and the high speed stream Mach number (M_{HS}), were proposed and used to identify three compressibility regimes, corresponding to weak, moderate and strong compressibility effects. A new model for the growth rate of a compressible mixing layer was formulated by combining ideas from Abramovich [27] and Channapragada [77]. The new model's growth rate estimates were validated using existing homogenous and heterogeneous mixing layer data. Simon's [114] semi-empirical, incompressible model was also extended to account for the effects of density gradients and compressibility on film cooling performance. This was achieved by modifying the energy equation per Abramovich [27].

Concurrent with the analytical work described above was a numerical effort aimed at developing a computationally inexpensive Reynolds Averaged Navier-Stokes (RANS) approach capable of accurately predicting film cooling effectiveness under subsonic conditions. This approach was implemented in Loci-CHEM, a RANS solver being developed by Edward Luke at Mississippi State University in partnership with NASA. CHEM was validated using a series of canonical flow problems in order to establish the solver's ability to accurately predict laminar and turbulent subsonic flows. CHEM was then applied to subsonic slot-jet film cooling data reported by Cruz

et al. [187]. Other work by Cruz et al. [138] suggested that in order to accurately predict film cooling performance under turbulent conditions it is essential to have a detailed characterization of the turbulence (i.e., turbulent kinetic energy, k and turbulent eddy viscosity, μ_t) at the inflow planes of the coolant and core streams. Since this turbulence information was not available experimentally it was necessary to generate it numerically using a series of RANS precursor simulations based on Menter's Shear Stress Transport (SST) turbulence model. The core flow inlet conditions were determined using a developing boundary layer flow precursor simulation, while the coolant conditions were obtained from a fully developed turbulent channel flow precursor simulation. The grid was extended ten slot heights upstream of the coolant injection point to ensure that the physics (such as vortex shedding and flow recirculation) were accurately captured near the point of injection. The simulation results were used to gain insights into subsonic film cooling physics and into the limitations of the RANS methodology when applied to subsonic conditions.

The final step was to extend the RANS methodology to supersonic conditions. This involved using RANS to model a supersonic film 'heating' experiment which is currently being designed and fabricated. The term film 'heating' refers to the fact that the film in this case is hotter than the core flow which means that the direction of the heat flux will be opposite to that found in conventional film cooling. A film 'heating' approach was chosen for the experiment to avoid the problem of having to heat the high-speed core flow. As in the subsonic case, simple 'canonical' flow problems were simulated first to establish the solver's performance under supersonic conditions.

Next, subsonic and supersonic film injection test cases (Off-Baseline #1 and Off-Baseline #2) were simulated to obtain predictions of the heat flux along the test section walls with and without film ‘heating.’ The film cooling effectiveness was then computed from the heat flux at the upper wall and on the heat flux at the lower wall without film injection. These results established the viability of the proposed test matrix for the experiment and provided guidance for the placement of instrumentation along the test section walls to ensure that the key features (such as the transition point between the initial and developed regions of the film layer and the slope of the decay in film cooling effectiveness in the developed region) will be adequately resolved when the experiment is conducted.

6.2 Fundamental Contributions

The most significant contributions of this dissertation are the following:

1. A comprehensive review of past analytical, experimental and numerical work relevant to film cooling that will serve as a useful starting point for future research in this area.
2. Greatly improved understanding of the effects of pressure gradients, density gradients and compressibility on film cooling performance.
 - a. Pressure gradients, density gradients and compressibility effects influence the film cooling effectiveness through the growth rate of the mixing layer formed at the coolant-core stream interface.
 - b. Increasing the growth rate decreases the impingement distance which decreases the persistence of the film and thereby lowers the cooling effectiveness.

- c. Decreasing the growth rate increases the impingement distance which increases the persistence of the film and increases the cooling effectiveness.
- 3. Identified the velocity ratio as the key parameter governing the influence of pressure gradients on film cooling performance.
- 4. Resolved long-standing conflicts in the literature over the effects of pressure gradients, density gradients and compressibility on film cooling effectiveness.
 - a. Pressure gradients can either enhance or degrade cooling effectiveness depending on the velocity ratio (i.e., $R > 1$ or $R < 1$) and type of pressure gradient applied (i.e., favorable or adverse).
 - b. Compressibility effects can be significant, provided the convective Mach number and higher speed stream Mach number (M_c and M_{HS}) are high enough (i.e., M_c & $M_{HS} > 1$) and the total temperature ratio (θ_0) is low enough (i.e., $\theta_0 < 0.3$).
 - c. Previous experimental work has explored a relatively small part of the design space mostly using velocity ratio/pressure gradient combinations that degrade film cooling effectiveness.
- 5. Identified conditions that can lead to enhancement of film cooling performance in rocket and gas turbine engines.
 - a. $U_s > U_\infty$ ($R < 1$) for rocket nozzles ($K_p > 0$).
 - b. $U_s < U_\infty$ ($R > 1$) for suction side of turbine blades ($K_p < 0$).
 - c. $U_s > U_\infty$ ($R < 1$) for pressure side of turbine blades ($K_p > 0$).

- d. Increasing the velocity difference i.e., increasing M_c
 - e. Increasing the temperature difference between the coolant and core streams i.e., decreasing θ_0
6. Guided future experimental film cooling investigations by identifying different combinations of velocity ratio and pressure gradient that can lead to enhanced or degraded film cooling performance.
 7. Identified parameters that can be used to quantify compressibility in film cooling flows and the identification of three distinct compressibility regimes corresponding to weak, moderate and strong compressibility effects.
 - a. The governing parameters are:
 - i. Convective Mach number, M_c
 - ii. Total temperature ratio, θ_0
 - iii. High Speed Stream flow Mach number, M_{HS}
 - b. The compressibility regimes are:
 - i. Weak regime - (M_c & $M_{HS} \leq 0.3$ and $0.6 \leq \theta_0 \leq 1$)
 - ii. Moderate regime - ($0.3 < M_c$ & $M_{HS} \leq 1$ and $0.30 \leq \theta_0 < 0.60$)
 - iii. Strong regime - (M_c & $M_{HS} > 1$ and $\theta_0 < 0.3$)
 8. Demonstrated that computationally inexpensive RANS methodologies are able to predict momentum mixing, thermal mixing, skin friction and cooling effectiveness to within x% (RMS) under subsonic conditions.

9. Identified the importance of properly characterizing the inflow state of the film and core, and showed that under some conditions precursor simulations may be used to characterize the inflow state when complete experimental data are unavailable.
10. Demonstrated the utility of CFD as a design tool for supersonic film heating experiments.
 - a. Verification of suitability of proposed test configuration
 - b. Guidance for instrumentation layout.
 - c. Higher sensor density needed in the region $15 < x/h < 60$ in order to resolve the transition point between the initial and developed regions of the film.

Chapter 7: Extensions and Future work

The first and most important task will be to complete the supersonic film heating numerical simulation test matrix (Table 5.1) by modeling the (subsonic injection) Baseline and the (subsonic injection with favorable pressure gradient) Off-Baseline #3 cases. This will allow a clearer picture to emerge of the trends in the film cooling effectiveness as velocity ratio, density ratio and convective Mach number are varied. The results from the Off-Baseline #3 case will also provide insights into how pressure gradients influence film cooling performance under compressible conditions. These results will also be compared to the predictions of the compressible pressure gradient model (CPGM) to evaluate its predictive performance and gain a deeper understanding of the coupled effects of pressure gradients and compressibility of film cooling effectiveness. Once the supersonic film heating experiment is completed and the test cases are run, the heat flux and film cooling measurements can be compared to the numerical results. This will not only provide more rigorous validation of the numerical simulation results but also allow the accuracy of the RANS methodology to be assessed under compressible conditions. In addition, once new subsonic film cooling velocity and temperature data are obtained with the leak 'fixed,' it will be important to re-evaluate the performance of Loci-CHEM in predicting subsonic film cooling effectiveness, skin friction, momentum mixing and thermal mixing. This will allow the impact of the leak to be assessed and provide a deeper understanding of the impact of pressure gradients on film cooling performance.

In terms of analytical model, future work will involve the development of a Radiative Film Cooling Model (RFM) capable of predicting the effects of radiation

on film cooling performance. By combining the RFM with the Pressure gradient Film Cooling Model (PGFM) and the Compressible Film Cooling Model (CFM) it will be possible to analytically predict film cooling performance in a ‘real’ rocket in which pressure gradients, compressibility and radiation are coupled. This will represent a significant advancement over the current state of the art where computationally intensive CFD simulations are needed to provide such information

Finally, a number of experiments will also be performed to evaluate the conditions identified by the PGFM that lead to enhancement of film cooling performance in rocket and gas turbine engines. Different combinations of velocity ratio and acceleration parameter will be tested spanning the four octants predicted by the PGFM in Figure 2-13. These tests will contribute to the state of the art in film cooling by addressing the deficiencies in the literature that were noted in Figure 2-13, which showed that to date most experimental studies have focused on conditions which degrade film cooling effectiveness.

Appendix

Below is a sample Matlab script illustrating how the two-variable least squares analysis was implemented using the built-in function *lsqcurvefit* and applied to subsonic film cooling data from Cruz et al. [187].

```
% SimonLSQ2CruzY.m

clear;

clc;

% =====

%1. Cruz et al. 2006 Data

% =====

M_Cruz = 2.21838235294118;           % blowing ratio
s_Cruz = 2.705e-3;                   % coolant slot height [m]
x_Cruz1=[1.761,6.456,11.151,15.846,20.541,27.583,36.973,51.058,69.838,88.618,10
7.398,126.178]*s_Cruz;              % streamwise distance [m]
eta_x_Cruz=[0.999,0.994,0.983,0.964,0.943,0.905,0.853,0.765,0.656,0.558,0.4
41];                                 % effectiveness data
omega_Cruz = 0.74835630695809;      % omega constant
x_Ms_Cruz = x_Cruz1./(M_Cruz*s_Cruz); % non-dimensional streamwise distance
x1_est_Cruz = 0.1699;                % impingement length estimate [m]
Ts = 306;                             % slot injection temperature [K]
Tinf = 431;                            % core injection temperature [K]
```

```

Ivs_star = 0.0317; % initial average transverse turbulence
                    intensity of the coolant stream

x1 = x1_est_Cruz; % impingement length [m]

M = M_Cruz; % blowing ratio

s = s_Cruz; % coolant slot height [m]

xdata = x_Cruz1; % x data array

ydata=eta_x_Cruz; % y data array

omega=0.74835630695809; % omega

Iv_s = 0.05; % initial slot turbulence intensity

Iv_inf = 0.016; % initial core flow turbulence intensity

% Starting guesses:

iv=Iv_inf+0.4*abs(Iv_inf-Iv_s); % average turbulence intensity

lb = [0.01;0.01]; % lower bound

ub = [1.5;1.5]; % upper bound

options=optimset('TolFun',eps,'LargeScale','on','MaxIter',500000,'TolX',eps,'MaxFun
Evals', 40000);

for k=1:1:225

    x0 =[abs(randn)/4;abs(randn)/4]; % initial guesses

    [x,resnorm,residual,exitflag,output,lambda,jacob1]=lsqcurvefit(@eta_eff_Cru
z,x0,xdata',ydata,lb,ub,options); % LSQ results

    a0_guess(k) = x0(1); % array of a0 guesses

    N_guess(k) = x0(2); % array of N guesses

    a0_conv(k) = x(1); % array of a0 converged values

```

```

        N_conv(k) = x(2);                % array of N converged values
        residN(k)=resnorm;              % array of residual norms
end

a0_Simon = [0.177];                    % Simon's value for a0
N_Simon = [0.65];                      % Simon's value for N
a0_Cruz = 0.35853;                     % Chosen value for a0 for Cruz's data
N_Cruz =0.81059;                       % Simon's value for N for Cruz's data

% Plotting Results:
figure(2)
hold on;
h=plot(a0_Simon,N_Simon,'rS',a0_guess,N_guess,'bo',a0_conv,N_conv,'gx',a0_Cruz,
N_Cruz,'kd');
set(h,'MarkerSize',12,'LineWidth',3);
h=xlabel('a_0')
set(h,'FontSize',16)
h=ylabel('N')
set(h,'FontSize',16)
set(gca,'FontSize',16);
box on;
axis([0 1 0 1]);
legend('Simon ','Initial Guesses','Converged Vales','Chosen Values Cruz ',1);

```

Bibliography

- [1] Lucas, J. G., and Golladay, R. L., "Gaseous Film Cooling of a Rocket Motor with Injection near the Throat," NASA TN D-3836, February 1967.
- [2] Hines, W. S., McCarthy, J. R., Seader, J. D., Trebes, D. M.; Gerstley, J. G., Hodgdon, D. G., Tobin, R. D., and Wagner, W. R., "Investigation of Cooling Problems at High Chamber Pressures," NASA CR-50773, May 1963.
- [3] Metzger, D., "Cooling Techniques for Gas Turbine Airfoils- A Survey," *AGARD Conference on Heat Transfer and Cooling in Gas Turbines*, CP-390 Paper No. 1, 1985.
- [4] Kestin, J. and Wood, R. T., "The Mechanism which Causes Free-Stream Turbulence to Enhance Stagnation Line Heat and Mass Transfer," *Heat Transfer*, Vol. 2, Elsevier, Amsterdam, 1970.
- [5] Silverstein, A., "Research on Aircraft Propulsion Systems-The Twelfth Wright Brothers Lecture," *Journal of Aeronautical Sciences*, Vol. 16, 1949, pp. 197–226.
- [6] Goldstein, R. J., "Film Cooling," *Advances in Heat Transfer*, Academic Press, New York, 1971, pp. 321–379.
- [7] FS-2008-11-158-MSFC, NASA, George C. Marshall Space Flight Center, Huntsville, AL 35812, http://www.nasa.gov/pdf/187393main_j2x_fs_nov08.pdf [retrieved 20 August 2009].
- [8] Sutton, G. P., *Rocket Propulsion Elements*, 3rd Ed., Wiley, New York, 1963, pp. 236–238.
- [9] Schuchkin, V., Osipov, M., Shyy, W., and Thakur, S., "Mixing and Film Cooling in Supersonic Duct Flows," *International Journal of Heat and Mass Transfer*, Vol. 45, 2002, pp. 4451–4461.
- [10] Bogard, D. G., and Thole, K. A., "Gas Turbine Film Cooling," *Journal of Propulsion and Power*, Vol. 22, No. 2, 2006, pp. 249–270.
- [11] Mayhew, J., Baughn, J., and Byerly, A., "The Effect of Freestream Turbulence on Film Cooling Adiabatic Effectiveness," *International Journal of Heat and Fluid Flow*, Vol. 24, 2003, pp. 669–679.
- [12] Pietryzk, J. R., Bogard, D. G., and Crawford, M. E., "Effects of Density Ratio on the Hydrodynamics of Film Cooling," *Journal of Turbomachinery*, Vol. 112, No. 3, 1990, pp. 437–450.

- [13] Jones, T., V., "Theory for the Use of Foreign Gas in Simulating Film Cooling," *International Journal of Heat and Fluid Flow*, Vol. 20, 1999, pp. 349–354.
- [14] Pedersen, D., Eckert, E. and Goldstein, R., "Film Cooling with Large Density Differences between the Mainstream and the Secondary Fluid Measured by the Heat-Mass Transfer Analogy," *ASME Journal of Heat Transfer*, Vol. 99, 1977, pp. 620–627.
- [15] Lucas, J. G., and Golladay, R. L., "An Experimental Investigation of Gaseous Film Cooling of a Rocket Motor," NASA TN D-1988, October 1963.
- [16] Hansmann, T., Wilhelmi, H. and Bohn, D., "An Experimental Investigation of the Film-Cooling Process at High Temperatures and Velocities," AIAA Paper 93-5062, November 1993.
- [17] Incropera, F. P., and DeWitt, D. P., *Fundamentals of Heat and Mass Transfer*, Wiley, New York, 1985, pp. 546–622.
- [18] Bazarov, V., and Yang V., "Liquid-Propellant Rocket Engine Injector Dynamics," *Journal of Propulsion and Power*, Vol. 14, No. 5, 1998, pp. 797–806.
- [19] Hulka, J., and Hutt, J., "Instability Phenomena in Liquid Oxygen/Hydrogen Propellant Rocket Engines," *Liquid Rocket Engine Combustion Instability*, Vol. 169, Progress in Astronautics and Aeronautics, AIAA, Washington, DC, 1994, pp. 39–72.
- [20] Male, T., Kerslake, W.R., and Tischler, A.O., "Photographic Study of Rotary Screaming and Other Oscillations in a Rocket Engine," NACA RM-E54A29, May 1954.
- [21] Bons, J., Rivir, R., MacArthur, C., and Pestian, D., "The Effect of Unsteadiness on Film Cooling Effectiveness," AIAA Paper 95-0306, January 1995.
- [22] Seo, H. J., Lee, J. S., and Ligrani, P. M., "The Effect Injection Hole Length on Film Cooling with Bulk Flow Pulsations," *International Journal of Heat and Mass Transfer*, Vol. 41, No. 22, 1998, pp. 3515–3528.
- [23] Birch, S., and Eggers, J., "Free Turbulent Shear Flows," NASA SP-321, July 1972.
- [24] Tollmien, W., "Berechnungsturbulenter Ausbreitungsvorgange," *Journal of Applied Mathematics and Mechanics*, Vol. 6, No. 6, 1926, pp. 468–478.
- [25] Liepmann, H. W., and Laufer, J., "Investigations of Free Turbulent Mixing," NACA TN 1257, August 1947.

- [26] Sabin, C. M., "An Analytical and Experimental Study of the Plane, Incompressible, Turbulent Free Shear Layer with Arbitrary Velocity Ratio and Pressure Gradient," AFOSR-TN-5443, October 1963.
- [27] Abramovich, G. N., *The Theory of Turbulent Jets*, MIT Press, Cambridge, 1963.
- [28] Mills, R. D., "Numerical and Experimental Investigations of the Shear Layer Between Two Parallel Streams," *Journal of Fluid Mechanics*, Vol. 33, Part 3, 1968, pp. 591–616.
- [29] Baker, R. L. and Weinstein, H., "Experimental Investigation of the Mixing of Two Parallel Streams of Dissimilar Fluids," NASA CR-957, January 1968.
- [30] Wygnanski, I. and Fiedler, H. E., "The Two-Dimensional Mixing Region," *Journal of Fluid Mechanics*, Vol. 41, Part 2, 1970, pp. 327–361.
- [31] Görtler, H., "Berechnung von Aufgebender freien Turbulenz auf Grund eines neuen Näherungsansatzes," *Journal of Applied Mathematics and Mechanics*, Vol. 22, No. 5, 1942, pp. 244–254.
- [32] Golik, R. J., "On Dissipative Mechanisms Within Separated Flow Regions (With Special Consideration to Energy Transfer Across Turbulent, Compressible, Pr = 1, Mixing Regions)," Ph.D. Thesis, University of Illinois, Champagne, IL, 1962.
- [33] Szablewski, W., "Turbulente Vermischung ebener Heissluftstrahlen," *Ing.-Arch., Bd., XXV, Heft 1*, 1957, pp. 10–25.
- [34] Sabin, C. M., "An Analytical and Experimental Study of the Plane, Incompressible, Turbulent Free-Shear Layer With Arbitrary Velocity Ratio and Pressure Gradient," *Transactions ASME Series D, Journal of Basic Engineering*, Vol. 87, No. 2, 1965, pp. 421–428.
- [35] Miles, J. B.; and Shih, J. S., "Similarity Parameter for Two-Stream Turbulent Jet-Mixing Region," *AIAA Journal*, Vol. 6, No. 7, 1968, pp. 1429–1430.
- [36] Yule, A. J., "Two-Dimensional Self-Preserving Turbulent Mixing Layers at Different Free Stream Velocity Ratios," British Aeronautical Research Council RM-3683, March 1972.
- [37] Brown, G., "The Entrainment and Large Structure in Turbulent Mixing Layers," *Proceedings of the Fifth Australasian Conference on Hydraulics and Fluid Mechanics*, Christchurch, New Zealand, 1974, pp. 352–359.
- [38] Dimotakis, P. E., "Two-dimensional Shear-layer Entrainment," *AIAA Journal*, Vol. 24, 1986, pp. 1791–1796.

- [39] Birch, S. F., "On the Role of Structure in Turbulent Mixing," AIAA Paper 97-2636, July 1997.
- [40] Rodi, W., "The Prediction of Free Turbulent Boundary Layers by the Use of a Two-equation Model of Turbulence," Ph.D. Thesis, Department of Mechanical Engineering, Imperial College, London, England, 1972.
- [41] Pope, S. B., "An Explanation of the Turbulent Round-Jet/Plane-Jet Anomaly," *AIAA Journal*, Vol.16, No. 3, 1978, pp. 279–281.
- [42] Hanjalic, K. and Launder, B. E., "Sensitizing the Dissipation Equation to Irrotational Streams," *Journal of Fluids Engineering*, Vol. 102, 1980, pp. 34–39.
- [43] Menter, F. R., "Influence of freestream Values on κ - ω Turbulence Model Predictions," *AIAA Journal*, Vol. 30, No. 6, 1992, pp. 1657–1659.
- [44] Robinson, D. F., Harris, J. E. and Hassan, H. A., "Unified Turbulence Closure Model for Axisymmetric and Planar Free Shear Flows," *AIAA Journal*, Vol. 33, No. 12, 1995, pp. 2325–2331.
- [45] Zabusky, N. J., and Deem, G. S., "Dynamical Evolution of Two-dimensional Unstable Shear Flows," *Journal of Fluid Mechanics*, Vol. 47, Part 2, 1971, pp. 353–379.
- [46] Riley, J. J., and Metcalfe, R. W., "Direct Numerical Simulation of a Perturbed Turbulent Mixing Layer," AIAA Paper 80-0274, January 1980.
- [47] Metcalfe, R. W., Hussain, A. K., Menon, S., "Coherent Structures in a Turbulent Mixing Layer: A Comparison between Direct Numerical Simulations and Experiments," *Proceedings of the Fifth Symposium on Turbulent Shear Flows Part 4*, Ithaca, NY, 1985, pp. 13-4–13-19.
- [48] Yokokawa, M., Itakura, K., Uno, A., Ishihara, T. and Kaneda, Y., "16.4-TFlops Direct Numerical Simulation of Turbulence by a Fourier Spectral Method on the Earth Simulator," *Proceedings of the 2002 ACM/IEEE Conference on Supercomputing*, Baltimore MD, 2002.
- [49] Clarksean, R., and McMurtry, P., "Direct Numerical Simulation of a Planar Mixing Layer Using the Spectral-Compact Finite Difference Technique," AIAA Paper 90-1495, June 1990.
- [50] Friedrich, R., and Su, M. D., "Large Eddy Simulation of a Turbulent Wall-bounded Shear Layer with Longitudinal Curvature," *Lecture Notes in Physics*, Vol. 170, 1982, pp. 196–202.

- [51] Maruyama, Y., "Numerical Simulation of Plane Turbulent Shear Layer," *Transactions of the Japan Society for Aeronautical and Space Sciences*, Vol. 31, No. 92, 1988, pp. 79–93.
- [52] Claus, R. W., Huang, P. G., and MacInnes, J. M., "Time-accurate Simulations of a Shear Layer Forced at a Single Frequency," *AIAA Journal*, Vol. 28, No. 2, 1990, pp. 267–275.
- [53] Oster, D., and Wygnanski, I., "The Forced Mixing Layer between Parallel Streams," *Journal of Fluid Mechanics*, Vol. 123, 1982, pp. 91–130.
- [54] Weisbrot, I., and Wygnanski, I., "On Coherent Structures in a Highly Excited Mixing Layer," *Journal of Fluid Mechanics*, Vol. 195, 1988, pp. 137–159.
- [55] Vreman, B., Geurts, B. and Kuerten, H., "Large-eddy Simulation of The Turbulent Mixing Layer," *Journal of Fluid Mechanics*, Vol. 339, 1997, pp. 357–390.
- [56] Smagorinsky, J., "General Circulation Experiments with the Primitive Equations," *Monthly Weather Review*, Vol. 91, 1963, pp. 99–164.
- [57] Bardina, J., Ferziger, J. H. and Reynolds, W. C., "Improved Turbulence Models Based on LES of Homogeneous Incompressible Turbulent Flows," Stanford University, Department of Mechanical Engineering, Rep. TF-19, 1984.
- [58] Liu, S., Meneveau, C. and Katz, J., "On the Properties of Similarity Subgrid-scale Models as Deduced from Measurements in a Turbulent Jet," *Journal of Fluid Mechanics*, Vol. 275, 1994, pp. 83–119.
- [59] Clark, R. A., Ferziger, J. H. and Reynolds, W. C., "Evaluation of Subgrid-scale Models Using an Accurately Simulated Turbulent Flow," *Journal of Fluid Mechanics*, Vol. 91, 1979, pp. 1–16.
- [60] Germano, M., "Turbulence: the Filtering Approach," *Journal of Fluid Mechanics*, Vol. 238, 1992, pp. 325–336.
- [61] Zang, Y., Street, R. L. and Koseff, J. R., "A Dynamic Mixed Subgrid-scale Model and its Application to Turbulent Recirculating Flows," *Physics of Fluids A*, Vol. 5, 1993, pp. 3186–3196.
- [62] Vreman, B., Geurts, B. and Kuerten, H., "On the Formulation of the Dynamic Mixed Subgrid-scale Model," *Physics of Fluids*, Vol. 6, 1994, pp. 4057–4059.
- [63] Vreman, B., Geurts, B. & Kuerten, H., "Large Eddy Simulation of the Temporal Mixing Layer Using the Clark Model," *Theoretical Computational Fluid Dynamics*, Vol. 8, 1996, pp. 309–324.

- [64] Comte, P., Silvestrini, J. H., and Begou, P., "Streamwise Vortices in Large-Eddy Simulations of Mixing Layers," *European Journal of Mechanics B/Fluids*, Vol. 17, No. 4, 1998, pp. 615–637.
- [65] Ducros, F., Comte, P., and Lesieur, M., "Large-eddy Simulation of Transition to Turbulence in a Boundary-layer Developing Spatially over a Flat Plate," *Journal of Fluid Mechanics*, Vol. 326, 1996, pp. 1–36.
- [66] Papamoschou, D., and Roshko, A., "Observations of Supersonic Free Shear Layers," *Sadhana*, Vol. 12, Parts 1 & 2, 1988, pp. 1–14.
- [67] Brown, G. and Roshko, A., "The Effect of Density Difference on the Turbulent Mixing Layer," AGARD CP-93, September 1971.
- [68] Brown, G., and Roshko, A., "On Density Effects and Large Structures in Turbulent Mixing Layers," *Journal of Fluid Mechanics*, Vol. 64, 1974, pp. 775–816.
- [69] Lu, G. and Lele, S., "On the Density Ratio Effect on the Growth of a Compressible Mixing Layer," *Physics of Fluids*, Vol. 6, 1994, pp. 1073–1075.
- [70] Papamoschou, D. and Roshko, A., "The Compressible Turbulent Shear Layer: an Experimental Study," *Journal of Fluid Mechanics*, Vol. 197, 1988, pp. 453–477.
- [71] Chen, J., "The Effects of Compressibility on Conserved Scalar Entrainment in a Plane Free Shear Layer," *Proceedings of the Eighth Symposium on Turbulent Shear Flows*, Munich, Germany, Vol. 2, 1991, pp. 23-2-1.
- [72] Sandham, N. and Reynolds, W., "Three Dimensional Simulation of Large Eddies in the Compressible Mixing Layer," *Journal of Fluid Mechanics*, Vol. 224, 1991, pp. 133–158.
- [73] Papamoschou, D. and Bunyajitradulya, A., "Evolution of Large Eddies in Compressible Shear Layers," *Physics of Fluids*, Vol. 9, 1990, pp. 756–765.
- [74] Samimy, M., Elliot, G., and Reeder, M., "Compressibility Effects on Large Structures in Free Shear Flows," *Physics of Fluids A*, Vol. 4, 1992, pp. 1251–1258.
- [75] Sabin, C., "An Analytical and Experimental Investigation of the Plane, Incompressible, Turbulent Free-Shear Layer with Arbitrary Velocity Ratio and Pressure Gradient," *Transactions of ASME*, Vol. 87, 1965, pp. 421–428.
- [76] Ferri, A., Libby, P. and Zakkay, V., "Theoretical and Experimental Investigation of Supersonic Combustion," ARL 62-467, September 1962.
- [77] Channapragada, R., "Compressible Jet Spread Parameter for Mixing Zone Analysis," *AIAA Journal*, Vol. 1, 1963, pp. 2188–2190.

- [78] Slessor, M., Zhuang, M. and Dimotakis, P., "Turbulent Shear-Layer Mixing: Growth-Rate Compressibility Scaling," *Journal of Fluid Mechanics*, Vol. 414, 2000, pp. 35–45.
- [79] Murakami, E. and Papamoschou, D., "Eddy Convection in Coaxial Supersonic Jets," *AIAA Journal*, Vol. 38, 2000, pp. 628–635.
- [80] Zhuang, M., Kubota, T., and Dimotakis, P., "Instability of Inviscid, Compressible Free Shear Layers," *AIAA Journal*, Vol. 28, 1990, pp. 1728–1733.
- [81] Kline, S., Cantwell, B., and Lilley, G., *Proceedings of the 1980-1981 AFOSR-HTTM-Stanford Conference on Complex Turbulent Flows: Comparison of Computation and Experiment*, Stanford University, Stanford, CA, Vol. 1, 1981.
- [82] Lessen, M., Fox, J. A. and Zien, M., "On the Inviscid Stability of the Laminar Mixing of Two Parallel Streams of a Compressible Fluid," *Journal of Fluid Mechanics*, Vol. 23, Part 2, 1965, pp. 355–367.
- [83] Lessen, M., Fox, J. A. and Zien, M., "The Instability of Inviscid Jets and Wakes in Compressible Fluid," *Journal of Fluid Mechanics*, Vol. 31, Part 1, 1965, pp. 129–143.
- [84] Lessen, M., Fox, J. A. and Zien, M., "Stability of the Laminar Mixing of Two Parallel Streams with Respect to Supersonic Disturbances," *Journal of Fluid Mechanics*, Vol. 25, Part 4, 1966, pp. 737–742.
- [85] Gropengiesser H., "On the Stability of Free Shear Layers in Compressible Flows," NASA TT-F-12786, February 1970.
- [86] Sarkar, S., Erlebacher, G., Hussaini., and Kreiss, H. O., "The Analysis and Modeling of Dilatational Terms in Compressible Turbulence," *Journal of Fluid Mechanics*, Vol. 227, 1991, pp. 473–493.
- [87] Vreman, A. W., Sandham, N. D. and Luo, K. H., "Compressible Mixing Layer Growth Rate and Turbulence Characteristics," *Journal of Fluid Mechanics*, Vol. 320, 1996, pp. 235–258.
- [88] Vreman, A. W., "Direct and Large-Eddy Simulation of the Compressible Turbulent Mixing Layer," Ph.D. Thesis, University of Twente, Twente, Netherlands, 1995.
- [89] Bodi, K. V. R., "Large Eddy Simulations of Compressible Mixing Layers," M.Sc. Thesis, Department of Aerospace Engineering, Indian Institute of Science, Bangalore, India, 2005.

- [90] Sandham, N. D., and Reynolds, S. W., “Three-dimensional Simulations of Large Eddies in the Compressible Mixing Layer,” *Journal of Fluid Mechanics*, Vol. 224, 1991, pp. 133–158.
- [91] Sarkar, S., “The Stabilizing Effect of Compressibility in Turbulent Shear Flows,” *Journal of Fluid Mechanics*, Vol. 282, 1995, pp. 163–186.
- [92] Luo, K. H., and Sandham, N. D., “On the Formation of Small Scales in a Compressible Mixing Layer,” *Direct and Large-Eddy Simulation I*, Kluwer, Berlin, 1994, pp. 335–346.
- [93] Luo, K. H., and Sandham, N. D., “Reynolds Number Effects on Transitional Compressible Free Shear Flows: Direct Numerical Simulation,” *Proceedings of the First Asian Computational Fluid Dynamics Conference*, Hong Kong, 1995, pp. 403–408.
- [94] Vreman, B., Geurts, B., and Kuerten, H., “Shocks in Direct Numerical Simulation of the Confined Three-dimensional Mixing Layer,” *Physics of Fluids*, Vol. 7, 1995, pp. 2105–2107.
- [95] Lele, S. K., “Direct Numerical Simulation of Compressible Free Shear Flows,” AIAA Paper 89-0374, January 1989.
- [96] Ragab, S. A., and Sheen, S., “Large-Eddy Simulation of a Mixing Layer,” AIAA Paper 91-0233, January 1991.
- [97] Vreman, B., Geurts, B., and Kuerten, H., “Subgrid-modelling in LES of Compressible Flow,” *Applied Sciences Research*, Vol. 54, 1995, pp. 191–203.
- [98] Chalot, F., Marquez, B., Ravachol, M., Ducros, F. and Poinso, T., “Large Eddy Simulation of a Compressible Mixing Layer: Study of the Mixing Enhancement,” AIAA Paper 99-3358, June 1999.
- [99] Georgiadis, N. J., Alexander, J. I., and Reshotko, E., “Investigation of a Compressible Turbulent Mixing Layer Using a Hybrid RANS/LES Method,” AIAA Paper 2001-2563, June 2001.
- [100] Simon, F., Deck, S., Guillen, P. and Sagaut, P., “RANS-LES Simulations of Supersonic Base Flow,” AIAA Paper 2006-0898, January 2006.
- [101] “Combustor Liner,” [online image]. *Naval Ships Technical Manual S9086-G9-STM-000, Chapter 231*. Naval Sea Systems Command. http://www.tpub.com/content/fc/14104/img/14104_96_1.jpg [retrieved 23 August 2009].

- [102] Kaszeta, R., and Burd, S. "A Typical Turbine Blade with Film Cooling Holes," [online image]. Heat Transfer Laboratory at the University of Minnesota, <http://www.me.umn.edu/labs/tcht/measurements/what.html> [retrieved 23 August 2009].
- [103] Hale, C., Plesniak, M. and Ramadhyani, S., "Film Cooling Effectiveness for Short Film Cooling Holes Fed by a Narrow Plenum," *Transactions of ASME Journal of Turbomachinery*, Vol. 122, 2000, pp. 553–557.
- [104] Weighardt, K., "Ueber das Ausblasen von Warmluft fur Ensteisen," ZWB Research Report No. 1900 (ARF translation Rest. No. F-TS-919-RE, Wright Field, August 1946).
- [105] Papell, S., and Trout, A., "Experimental Investigation of Air Film Cooling Applied to an Adiabatic Wall by Means of an Axially Discharging Slot," NASA TN-D9, August 1959.
- [106] Papell, S., "Effect on Gaseous Film Cooling of Coolant Injection through Angled Slots and Normal Holes," NASA TN-D299, September 1960.
- [107] Hartnett, J., Birkebak, R. and Eckert, E., "Velocity Distributions, Temperature Distributions, Effectiveness and Heat Transfer for Air Injected Through a Tangential Slot into a Turbulent Boundary Layer," *Transactions of ASME Journal of Heat Transfer*, Vol. 83, 1961, pp. 293–306.
- [108] Juhasz, A., and Marek, C., "Combustor Liner Film Cooling in the Presence of High Free Stream Turbulence," NASA TN D-6360, July 1971.
- [109] Marek, C. J., and Tacina, R. R., "Effect of Free-Stream Turbulence on Film Cooling," NASA TN D-7958, June 1975.
- [110] Ko, S. and Liu, D., "Experimental Investigations on Effectiveness, Heat transfer Coefficient, and Turbulence of Film Cooling," *AIAA Journal*, Vol. 18, No. 8, 1980, pp. 907–913.
- [111] Lebedev, V., Lemanov, V, Misyura, S. and Terekhov, V., "Effects from Turbulence Intensity on Slot Protection Performance," *Journal of Applied Mechanics and Technical Physics*, Vol. 32, 1991, pp. 360–364.
- [112] Stollery, J., and El-Ehwany, A., "A Note on the Use of a Boundary-Layer Model to Correlate Film-Cooling Data," *International Journal of Heat and Mass Transfer*, Vol. 8, No.1, 1965, pp. 55–65.
- [113] Sturgess, G., "Account of Film Turbulence for Prediction of Effectiveness from Film Cooling Injection Geometries of a Practical Nature," *Journal of Combustion and Heat Transfer in Gas Turbine Systems*, Vol. 11, 1971, pp. 229–250.

- [114] Simon, F., “Jet Model for Slot Film Cooling with Effect of Free-stream and Coolant Turbulence,” NASA TP-2655, October 1986.
- [115] Zhou, J. M., Salcudean, M. and Gartshore, I. S., “A Numerical Computation of Film Cooling Effectiveness,” *Near-Wall Turbulent Flows*, Elsevier, New York, 1993, pp. 377–386.
- [116] Jansson, L. S., Davidson, L., and Olsson, E., “Calculation of Steady and Unsteady Flows in a Film-Cooling Arrangement Using a Two-Layer Algebraic Stress Model,” *Numerical Heat Transfer, Part A*, Vol. 25, 1994, pp. 237–258.
- [117] Lakehal, D., “Near-Wall Modeling of Turbulent Convective Heat Transport in Film Cooling of Turbine Blades with the Aid of Direct Numerical Simulation Data,” *Transactions of ASME Journal of Turbomachinery*, Vol. 124, 2002, pp. 485–498.
- [118] Jia, R., Sunden, B., Miron, P. and Leger, B., “A Numerical and Experimental Investigation of the Slot Film-Cooling Jet with Various Angles,” *Transactions of ASME Journal of Turbomachinery*, Vol. 127, 2005, pp. 635–645.
- [119] Muldoon, F., and Acharya, S., “Direct Numerical Simulation of a Film Cooling Jet,” *Proceedings of the ASME Turbo Expo*, Vol. 3, 2004, pp. 461–473.
- [120] Muldoon, F. and Acharya, S., “Analysis of k-e Budgets for Film Cooling Using Direct Numerical Simulation,” *AIAA Journal*, Vol. 44, No. 12, 2006, pp. 3010–3021.
- [121] Wilcox, D., *Turbulence Modeling for CFD*, Birmingham Press, San Diego, 1993.
- [122] Tyagi, M. and Acharya, S., “Large Eddy Simulation of Film Cooling Flow from an Inclined Cylindrical Jet,” *Transactions of ASME Journal of Turbomachinery*, Vol. 125, 2003, pp. 734–742.
- [123] Lavrich, P. and Chiapetta, L., “An Investigation of Jet in a Cross Flow for Turbine Film Cooling Applications,” United Technologies Research Center, Report No. 90-04, 1990.
- [124] Guo, X., Schröder, W. and Meinke, M., “Large-eddy Simulations of Film Cooling Flows,” *Computers and Fluids*, Vol. 35, 2006, No. 6, pp. 587–606.
- [125] Roy, S., Kapadia, S. and Heidmann J. D., “Film Cooling Analysis Using DES Turbulence Model,” *ASME Turbo Expo*, Paper GT 2003-38140, June 2003.
- [126] Kapadia, S., Roy, S., and Heidmann J. D., “First Hybrid Turbulence Modeling for Turbine Blade Cooling,” *Journal of Thermophysics and Heat Transfer*, Vol. 18, No. 4, 2004, pp. 154–156

- [127] Martini, P., Schulz, A., Bauer, H. –J, and Whitney, C. F., “Detached Eddy Simulation of Film Cooling Performance on the Trailing Edge Cutback of Gas Turbine Airfoils,” *Transactions of ASME Journal of Turbomachinery*, Vol. 128, 2006, pp. 292–299.
- [128] Jeng, S. M., and Ippolito, S. A., “Prediction of Fuel Film Wall Cooling,” AIAA Paper 90-2511, July 1990.
- [129] Volkmann, J., Tuegel, L. and McLeod, J., “Gas Side Heat Flux and Film Coolant Investigation for Advanced LOX/Hydrocarbon Thrust Chambers,” AIAA Paper 90-2184, July 1990.
- [130] Boden, R. H., “Heat Transfer in Rocket Motors and the Application of Film and Sweat Cooling,” *Transactions of ASME*, Vol. 73, 1951, pp. 385–390.
- [131] Emmons, D., “Effects of Selectee Gas Stream Parameters and Coolant Physical Properties on Film Cooling of Rocket Motors,” JPL TM-62-5, August 1962.
- [132] Volkmann, J., McLeod, J. and Claflin, S., “Investigation of Throat Film Coolant for Advanced LOX/RP-1 Thrust Chambers,” AIAA Paper 91-1979, June 1991.
- [133] Arrington, L. A., Reed, B. D., and Rivera, A., “Performance Comparison of Two Small Rocket Nozzles,” NASA TM-107285, August 1996.
- [134] Stoll, J. and Straub, J., “Film Cooling and Heat Transfer in Nozzles,” *Transactions of ASME Journal of Turbomachinery*, Vol. 110, No. 1, 1998, pp. 57–65.
- [135] Zhang, H., Tao, W., He, Y. and Zhang, W., “Numerical Study of Liquid Film Cooling in a Rocket Combustion Chamber,” *International Journal of Heat and Mass Transfer*, Vol. 49, 2006, pp. 349–358.
- [136] Cruz, C. A., Marshall, A. and Trouvé, A., “Large-Eddy Simulation of Film Cooling Through a 2D Slot,” AIAA Paper 2006-4710, July 2006.
- [137] Matesanz, A., Velazquez, A., and Rodriguez, M., “Numerical Simulation of Slot Film Cooling in Convergent-Divergent Nozzles,” AIAA Paper 93-1977, April 1993.
- [138] Cruz, C. A., “Experimental and Numerical Characterization of Turbulent Slot Film Cooling,” Ph.D. Thesis, Department of Aerospace Engineering, University of Maryland, College Park, MD, 2008.

- [139] Goldstein, R. and Jin, P., "Film Cooling Downstream of a Row of Discrete Holes With Compound Angle," *Transactions of ASME Journal of Turbomachinery*, Vol. 123, 2001, pp. 222–230.
- [140] Teekaram, A., Forth, C., and Jones, T., "Film Cooling in the Presence of Mainstream Pressure Gradients," *Transactions of ASME Journal of Turbomachinery*, Vol. 113, 1991, pp. 484–492.
- [141] Hartnett, J., Birkebak, R. and Eckert, E., "Velocity Distributions, Temperature Distributions, Effectiveness and Heat Transfer for Air Injected Through a Tangential Slot into a Turbulent Boundary Layer," *Transactions of ASME Journal of Heat Transfer*, Vol. 83, 1961, pp. 293–306.
- [142] Seban, R. A. and Back, L. H., "Effectiveness and Heat Transfer for a Turbulent Boundary Layer with Tangential Injection and Variable Free-stream Velocity," *Transactions of ASME Journal of Heat Transfer Series C.*, Vol. 84, 1962, pp. 235–244.
- [143] Pai, B. and Whitelaw, J., "The Influence of Strong Favorable Pressure Gradients on Film-Cooling Effectiveness," Imperial College Report EHT/TN/A/15, 1969.
- [144] Hay, N., Lampard, D., and Saluja, C., "Effects of the Condition of the Approach Boundary Layer and of Mainstream Pressure Gradient on the Heat Transfer Coefficient on Film-Cooled Surfaces," *ASME Journal of Engineering for Gas Turbines and Power*, Vol. 107, 1985, pp. 99–104.
- [145] Kruse, H., *Effects of Hole Geometry*, "Wall Curvature and Pressure Gradient on Film Cooling Downstream of a Single Row," AGARD CP-391, September 1985.
- [146] Escudier, M., and Whitelaw, J., "The Influence of Strong Adverse Pressure Gradients on the Effectiveness of Film Cooling," *International Journal of Heat and Mass Transfer*, Vol. 11, 1968, pp. 1289–1292.
- [147] Zolotogorov, M., "A Study Concerning the Efficiency of Film Cooling Under Real Conditions in Various Moving Systems," *Journal of Engineering Physics and Thermophysics*, Vol. 22, No. 1, 1972, pp. 31–33.
- [148] Lutum, E., von Wolfersdorf, J., Semmler, K., Dittmar, J., and B. Weigand, "An Experimental Investigation of Film Cooling on a Convex Surface Subjected to Favorable Pressure Gradient Flow," *International Journal of Heat and Mass Transfer*, Vol. 44, 2001, pp. 939–951.
- [149] Maiteh, B., and Jubran, B., "Effects of Pressure Gradient on Film Cooling Effectiveness from Two Rows of Simple and Compound Angle Holes in

Combination,” *Journal of Energy Conversion and Management*, Vol. 45, 2004, pp. 1457–1469.

[150] Mayle, R. E., Kopper, E. C., Blair, M. E., and Bailey, D. A., “Effect of Streamline Curvature on Film Cooling,” *Journal of Engineering for Power*, Vol. 99, 1977, pp. 77–82.

[151] Ito, S., Goldstein, R., and Eckert, E., “Film Cooling of a Gas Turbine Blade,” *Journal of Engineering for Power*, Vol. 100, 1978, pp. 476–481.

[152] Papell, S., Graham, R., and Cageao, R., “Influence of Coolant Tube Curvature on Film Cooling Effectiveness as Detected by Infrared Imagery,” NASA TP-1546, November 1979.

[153] Jung, K. and Hennecke, D., “Curvature Effects on Film Cooling with Injection through Two Rows of Holes,” *Proceedings of the RTO/AVT Symposium on Advanced Flow Management: Part B – Heat Transfer and Cooling in Propulsion and Power Systems*, Leon, Norway, 2001.

[154] Kim, Y., Coon, C. and Moon, H., “Film-cooling Characteristics of Pressure-Side Discharge Slots in an Accelerating Mainstream Flow,” *Proceedings of the ASME Gas Turbine Exposition*, Reno, NV, 2005, pp. 889–897.

[155] Carlson, L. W., and Talmor, E., “Gaseous Film Cooling at Various Degrees of Hot-gas Acceleration and Turbulence Levels,” *International Journal of Heat and Mass Transfer*, Vol. 11, 1968, pp. 1695–1713.

[156] Goradia, S. and Colwell, G., “Parametric Study of a Two-Dimensional Turbulent Wall Jet in a Moving Stream with Arbitrary Pressure Gradient,” *AIAA Journal*, Vol. 9, No. 11, 1971, pp. 2156–2165.

[157] Sivrioglu, M., “An Analysis of the Effects of Pressure Gradient and Streamline Curvature on Film cooling Effectiveness,” *Wärme-und Stoffübertragung*, Vol. 26, 1991, pp. 103–107.

[158] Camci, C., and Arts, T., “Short-Duration Measurements and Numerical Simulation of Heat Transfer Along the Suction Side of a Film-Cooled Gas Turbine Blade,” *Journal of Engineering for Gas Turbines and Power*, Vol. 107, 1985, pp. 991–997.

[159] Crawford, M. E., Kays, W. M., and Moffat, R. J., “Full-Coverage Film Cooling. Part II: Heat Transfer Data and Numerical Simulation,” *ASME Journal of Engineering for Power*, Vol. 102, No. 4, 1980, pp. 1006–1012.

[160] Tai, C. H., Kao, A. F., Miao, J. M., and Kuo, J. W., “Numerical Investigation on Film Cooling of a Turbine Blade with Coolant Plenum,” *Transactions of the*

Aeronautical and Astronautical Society of the Republic of China, Vol. 34, No. 4, 2002, pp. 353–361.

[161] Undapalli, S., and Leylek, J. H., “Ability of a Popular Turbulence Model to Capture Curvature Effects: A Film Cooling Test Case,” *Proceedings of the ASME Turbo Expo*, Vol. 5, Part A, 2003, pp. 527–539.

[162] Li, X., and Ting, W., “Computational Analysis of Surface Curvature Effect on Mist Film Cooling Performance,” *Proceedings of the ASME Turbo Expo*, Vol. 4, Part A, 2007, pp. 433–443.

[163] Tao, Z., Young, P., Ding, S., and Xu, G., “Curvature Effects on the Film Cooling with the Rotation,” *Journal of Beijing University of Aeronautics and Astronautics*, Vol. 33, No. 2, 2007, pp. 132–135.

[164] Yang, B., Xu, G., Meng, H., and Wu, H., “Numerical Simulation of Film Cooling Effectiveness on Rotating Curvature Models,” *Journal of Beijing University of Aeronautics and Astronautics*, Vol. 35, No. 4, 2009, pp. 398–402.

[165] Volchkov, E., Kutateladze, S. and Leontev, A., “Effect of Compressibility and Nonisothermicity on the Efficiency of Film Cooling in a Turbulent Boundary Layer,” *Journal of Applied Mechanics and Technical Physics*, Vol. 7, No. 4, 1966, pp. 93–94.

[166] Durgin, F. H., “An Insulating Boundary Layer Experiment,” Ph.D. Thesis, Massachusetts Institute of Technology, Cambridge, MA, 1957.

[167] Repukhov, V., “Effects of Compressibility and Non-isothermal Conditions on the Performance of Film Cooling,” *Journal of Engineering Physics and Thermophysics*, Vol. 19, No. 5, 1970, 1401–1408.

[168] Pedersen, D., Eckert, E. and Goldstein, R., “Film Cooling with Large Density Differences between the Mainstream and the Secondary Fluid Measured by the Heat-Mass Transfer Analogy,” *Transactions of ASME Journal of Heat Transfer*, Vol. 99, 1977, pp. 620–627.

[169] Stalder, J. and Inouye, M., “A Method of Reducing Heat Transfer to Blunt Bodies by Air Injection,” NACA RM-A56B27a, May 1956.

[170] Danneberg, R., “Helium Film Cooling of a Hemisphere at a Mach Number of 10,” NASA TN-D-1550, November 1962.

[171] Goldstein, R., Eckert, E., Tsou, F. and Haji-Sheikh, A., “Film Cooling with Air and Helium Injection through a Rearward-Facing Slot into a Supersonic Air Flow,” *AIAA Journal*, Vol. 4, No. 6, 1966, pp. 981–985.

- [172] Parthasarathy, K. and Zakkay, V., "An Experimental Investigation of Turbulent Slot Injection at Mach 6," *AIAA Journal*, Vol. 8, No. 7, 1970, pp. 1302–1307.
- [173] Cary, A., and Hefner, J., "Film-Cooling Effectiveness and Skin Friction in Hypersonic Turbulent Flow," *AIAA Journal*, Vol. 10, No. 9, 1972, pp. 1188–1192.
- [174] Ferri, A., Mahrer, A., and Hefner, J., "Investigation of Slot Cooling at High Subsonic Speeds," *AIAA Journal*, Vol. 14, No. 7, 1976, pp. 880–885.
- [175] Kanda, T., Masuya, G., Ono, F., and Wakamatsu, Y., "Effect of Film Cooling/Regenerative Cooling on Scramjet Engine Performances," *Journal of Propulsion and Power*, Vol. 10, No. 5, 1994, pp. 618–624.
- [176] Ferri, A. and Libby, P., "The Use of Helium for Cooling Nozzles Exposed to High Temperature Gas Streams," WADC TN-55-318, March 1956.
- [177] Sinha, A. K., Bogard, D. G., and Crawford, M. E., "Film Cooling Effectiveness Downstream of a Single Row of Holes With Variable Density Ratio," *Transactions of ASME Journal of Turbomachinery*, Vol. 113, 1991, pp. 442–449.
- [178] Ethridge, M. I., Cutbirth, J. M., and Bogard, D. G., "Scaling of Performance for Varying Density Ratio Coolants on an Airfoil with Strong Curvature and Pressure Gradient Effects," *Transactions of ASME Journal of Turbomachinery*, Vol. 123, 2001, pp. 231–237.
- [179] Aupoix, B., Mignosi, A., Viala, S., Bouvier, F., and Gaillard, R., "Experimental and Numerical Study of Supersonic Film Cooling," *AIAA Journal*, Vol. 36, No. 6, 1998, pp. 915–923.
- [180] Lushchik, V. and Yakubenko, A., "Tangential-Slot Film Cooling on a Plate in Supersonic Flow: Comparison of Calculation and Experiment," *Fluid Dynamics*, Vol. 36, No. 6, 2001, pp. 926–933.
- [181] Wang, Y. P., and Jiang, P. X., "Supersonic Film Cooling with the Incidence of Oblique Shock," *Journal of Engineering Thermophysics*, Vol. 28, No. 1, 2007, pp. 137–139.
- [182] Wang, J., Sun, B., and Wei, Y. K., "Numerical Simulation of Supersonic Gaseous Film Cooling," *Journal of Aerospace Power*, Vol. 23, No. 5, 2008, pp. 865–870.
- [183] Sun, X., Zhu, K., Xin, W., and Zhao, Y., "Numerical Study of the Flow Field Inside A Combustion Chamber with Gas Film Cooling," *Journal of Tsinghua University*, Vol. 48, No. 8, 2008, pp. 1347–1350.

- [184] Renze, P., Schröder, W. and Meinke, M., “Large-eddy Simulation of Film Cooling Flows at Density Gradients,” *International Journal of Heat and Fluid Flow*, Vol. 29, No. 1, 2008, pp. 18–34.
- [185] Kays, W., and Crawford, M., *Convective Heat and Mass Transfer*, 2nd Ed., McGraw-Hill, New York, 1980.
- [186] Anderson, J., *Modern Compressible Flow*, 3rd Ed., McGraw-Hill, New York, 2003.
- [187] Cruz, C., Raffan, F., Cadou, C., and Marshall, A., “Characterizing Slot Film Cooling Through Detailed Experiments,” *Proceedings of the International Mechanical Engineering Conference and Exposition*, Chicago, IL, 2006.
- [188] Bates, D. M., and Watts, D. G., *Nonlinear Regression Analysis And Its Applications*, Wiley, New York, 1988.
- [189] MATLAB Function Reference – *lsqcurvefit*, Mathworks, accessed July 2009, <<http://www.mathworks.com/support/tech-notes/1500/1508.html#section2>>.
- [190] Papamoschou, D. and Bunyajitradulya, A., “Evolution of Large Eddies in Compressible Shear Layers,” *Physics of Fluids*, Vol. 9, No. 3, 1997, pp. 756–765.
- [191] Coles, D., “Prospects for Useful Research on Coherent Structure in Turbulent Shear Flow,” *Proceedings of the Indian Academy of Science*, Vol. 4, Part. 2, 1981, pp. 111–127.
- [192] Prandtl, L., “Bemerkung zur Theories der Freien Turbulenz,” *Journal of Applied Mathematics and Mechanics*, Vol. 22, No. 5, 1942, pp. 241–243.
- [193] Yakovlevskiy, O., “The Problem of the Thickness of the Turbulent Mixing Zone Between Two Gas Streams of Different Velocity and Density,” *Izv. Akad. Nauk USSR, Otd. Tekhn. Nauk*, Vol. 10, 1958.
- [194] Schlichting, H., *Boundary Layer Theory*, McGraw-Hill, New York, 1960.
- [195] Elliot, G., and Samimy, S., “Compressibility Effects in Free Shear Layers,” *Physics of Fluids A*, Vol. 2, 1990, pp. 1231–1240.
- [196] Korst, H. and Chow, W., “Non-Isoenergetic Turbulent ($Pr_t=1$) Jet Mixing Between Two Compressible- Streams at Constant Pressure,” NASA CR-419, April 1966.
- [197] Abramowitz, M and Stegun, I., *Handbook of Mathematical Functions*, Dover, New York, 1972.

- [198] Stoer, J. and Bulirsch, R., *Introduction to Numerical Analysis*, Springer, New York, 2002.
- [199] Hall, J., “Mixing and Combustion in Compressible Turbulent Shear Layers,” Ph.D. Thesis, Department of Aerospace Engineering, California Institute of Technology, Pasadena, CA, 1991.
- [200] Rossmann, T., Mungal, M. and Hanson, R., “An Experimental Investigation of High Compressibility Non-Reacting Mixing Layers,” AIAA Paper 2000-0663, January 2000.
- [201] Rossmann, T., “An Experimental Investigation of High Compressibility Mixing Layers,” Ph.D. Thesis, Department of Mechanical Engineering, Stanford University, Palo Alto, CA, 2001.
- [202] Urban, W., and Mungal, M., “Planar Velocity Measurements in Compressible Mixing Layers,” *Journal of Fluid Mechanics*, Vol. 431, 2001, pp. 189–222.
- [203] Clemens, N., and Mungal, M., “Two- and Three-Dimensional Effects in the Supersonic Mixing Layer,” *AIAA Journal*, Vol. 30, 1992, pp. 973–981.
- [204] Sirieix, M. & Solignac, J. L., “Contribution a L'etude Experimentale de La Couche de Mélange Turbulent Isobare d'un Ecoulement Supersonique,” *Separated Flows*, AGARD CP-4, 1966.
- [205] Goebel, S., and Dutton, C., “Velocity Measurements of Compressible, Turbulent Mixing Layers,” AIAA Paper 90-0709, January 1990.
- [206] Chinzei, N., Masuka, G., Komuro, T., Murakami, A. and Kudou, K., “Spreading of Two-Stream Supersonic Turbulent Mixing Layers,” *Physics of Fluids*, Vol. 29, 1986, pp. 1345–1347.
- [207] Island, T., Urban, W. and Mungal, M., “Mixing Enhancement in Compressible Shear Layers via Sub-Boundary Layer Disturbances,” *Physics of Fluids*, Vol. 10, 1998, pp. 1008–1020.
- [208] Bell, J. and Mehta, R., “Development of a Two-Stream Mixing Layer from Tripped and Un-tripped Boundary Layers,” *AIAA Journal*, Vol. 28, 1990, pp. 2034–2042.
- [209] Bowersox, R., and Schetz, J., “Compressible Turbulence Measurements in a High-Speed High-Reynolds-Number Mixing Layer,” *AIAA Journal*, Vol. 32, 1994, pp. 758–764.

- [210] Shau, Y., and Dolling, D., "Experimental Study of Spreading Rate Enhancement of High Mach Number Turbulent Shear Layers," AIAA Paper 89-2458, July 1989.
- [211] Gruber, M., "Three-Dimensional Velocity Measurements in a Turbulent, Compressible Mixing Layer," AIAA Paper 92-3544, July 1992.
- [212] Barone, M., Oberkampf, W. and Blottner, F., "Validation Case Study: Prediction of Compressible Turbulent Mixing Layer Growth Rate," *AIAA Journal*, Vol. 44, 2006, pp. 1488–1497.
- [213] Slessor, M., Bond, C. and Dimotakis, P., "Turbulent Shear-layer Mixing at High Reynolds Numbers: Effects of Inflow Conditions," *Journal of Fluid Mechanics*, Vol. 376, 1998, pp. 115–138.
- [214] Browand, F. and Latigo, B., "Growth of the Two-dimensional Mixing Layer from a Turbulent and Non-turbulent Boundary Layer," *Physics of Fluids*, Vol. 22, 1979, pp. 1011–1019.
- [215] Mungal, M., Hermanson, J. and Dimotakis, P., "Reynolds Number Effects on Mixing and Combustion in a Reacting Shear Layer," *AIAA Journal*, Vol. 23, 1985, pp. 1418–1423.
- [216] Abe, T., Funabiki, K., Ariga, H. and Hiraoka, K., "Effect of Flow Non-Uniformity on the Mixing Layer at the Interface of Parallel Supersonic Flows," JAXA Institute of Space and Aeronautical Science Report No. 646, June 1992.
- [217] Chakraborty, D., Mukunda, H., and Paul, P., "Effect of Confinement in High-Speed Reacting Mixing Layer," *Combustion and Flame*, Vol. 121, 2000, pp. 386–389.
- [218] Sellers, C. and Chandra, S., "Compressibility Effects in Modeling Turbulent High Speed Mixing Layers," *Engineering Computations*, Vol. 14, No. 1, 1997, pp. 5–13.
- [219] Lushchik, V. and Yakubenko, A., "Tangential-Slot Film Cooling on a Plate in Supersonic Flow. Comparison of Calculation and Experiment," *Fluid Dynamics*, Vol. 36, No. 6, 2001, pp. 926–933.
- [220] Zakkay, v., Wang, C. R, and Miyazawa, M., "Effect of Adverse Pressure Gradient on Film Cooling Effectiveness," *AIAA Journal*, Vol. 12, No. 5, 1973, pp. 708–710.
- [221] Volchkov, E., P., Kozmenko, V. K. and Lebedev, V. P., "Effect of the Gradient of the Velocity of the Flow on the Effectiveness of a Gas Curtain in Axisymmetric

Nozzles,” *Journal of Applied Mechanics and Technical Physics*, Vol. 18, No. 2, 1977, pp. 196–201.

[222] Luke, E. A., Tong, X-L., Wu, J. and Cinnella, P. “CHEM 3: A Finite-Rate Viscous Chemistry Solver -The User Guide,” MSSU-COE-ERC-10-07, Mississippi State University, Starkville, MS, October 2007.

[223] Tong, X-L., Luke, E. A., and Tang, L., “Evaluation of the Shear-Stress Transport Turbulence Model for Heat Transfer Applications,” AIAA Paper 2003-0769, January 2003.

[224] Luke, E. A., Tong, X-L., Wu, J., Tang, L. and Cinnella, P., “A Step Towards 'Shape-Shifting' Algorithms: Reacting Flow Simulations Using Generalized Grids,” AIAA Paper 2001-0897, January 2001.

[225] Wendt, J. F., *Computational Fluid Dynamics An Introduction*, 3rd Ed., Springer, Berlin, 2009, pp. 15–43.

[226] Tannehill, J. C., Anderson, D. A., and Pletcher, R. H., *Computational Fluid Mechanics and Heat Transfer*, 2nd Ed., Taylor, Washington, DC, 1997.

[227] Menter, F. R., “Two-Equation Eddy-Viscosity Turbulence Models for Engineering Applications,” *AIAA Journal*, Vol. 32, 1994, pp. 269–289.

[228] Gupta, R. N., Yos, J. M., Thompson, R. A., and Lee, K. P., “A Review of Reaction Rates and Thermodynamic and Transport Properties for an 11-Species Air Model for Chemical and Thermal Non-Equilibrium Calculation to 30,000K,” NASA RP-1232, August 1990.

[229] Freitas, C. J., “The Issue of Numerical Uncertainty,” *Applied Mathematical Modeling*, Vol. 26, 2002, pp. 237–248.

[230] Spalart, P. R. and Allmaras, S. R., “A One-equation Turbulence Model for Aerodynamic Flows,” AIAA Paper 92-0439, January 1992.

[231] Roache, P. J., “A Method for Uniform Reporting of Grid Refinement Studies,” *Symposium on Quantification of Uncertainty in Computational Fluid Dynamics*, ASME Fluids Engineering Division, New York, Vol. 158, 1993.

[232] Roache P. J., “A Method for Uniform Reporting of Grid Refinement Studies,” *Proceedings of the Eleventh AIAA Computational Fluid Dynamics Conference*, Orlando, FL, Vol. 2, 1993, pp. 1057–1058.

[233] Oberkampf, W. L., “A Proposed Framework for Computational Fluid Dynamics Code Calibration Validation,” AIAA Paper 94-2540, June 1994.

- [234] Aeschlin, D. P., Oberkampf, W. L. and Blottner, F. G., "A Proposed Methodology for Computational Fluid Dynamics Code Verification Calibration and Validation," *Proceedings of the Sixteenth International Congress on Instrumentation in Aerospace Simulation Facilities*, Dayton, OH, 1995.
- [235] Celik, I. and Zhang, W. M., "Calculation of Numerical Uncertainty Using Richardson Extrapolation: Application to Some Simple turbulent Flow Calculations," *ASME Journal of Fluids Engineering*, Vol. 117, 1995, pp. 439–445.
- [236] Johnson, R. w., and Hughes, E. D., "Quantification of Uncertainty in Computational Fluid Dynamics-1995," *ASME Fluids Engineering Division*, New York, Vol. 213, 1995.
- [237] Oberkampf, W. L., Blottner, F. G., and Aeschlin, D. P., "Methodology for Computational Fluid Dynamics Code Verification Validation," AIAA Paper 95-2226, June 1995.
- [238] Karniadakis, G. E., "Toward a Numerical Error Bar in CFD," *ASME Journal of Fluids Engineering*, Vol. 117, No. 12, 1995, pp. 7–9.
- [239] Roache, P. J., "Quantification of Uncertainty in Computational Fluid Dynamics," *Annual Review of Fluid Mechanics*, Vol. 29, 1997, pp. 123–160.
- [240] Richardson, L. F., "The Approximate Arithmetical Solution by Finite Differences of Physical Problems Involving Differential Equations with an Application to the Stress in a Masonry Dam," *Transactions of the Royal Society of London Ser. A*, Vol. 210, 1911, pp. 307–357.
- [241] Richardson, L. F. and Gaunt, J. A., "The Deferred Approach to the Limit," *Philosophical Transactions of the Royal Society A*, Vol. 226, 1927, pp. 299–361.
- [242] White, F., M., *Fluid Mechanics*, 2nd Ed., McGraw-Hill, New York, 1991.
- [243] Pope, S. B., *Turbulent Flows*, Cambridge University Press, Cambridge, 2003.
- [244] Haaland, S. E., "Simple and Explicit Formulas for the Friction Factor in Turbulent Pipe Flow," *ASME Journal of Fluids Engineering*, Vol. 103, No. 5, 1983, pp. 89–90.
- [245] Bradshaw, P. and Huang, G. P., "The Law of the Wall in Turbulent Flow," *Proceedings of the Royal Society of London A*, Vol. 451, 1995, pp. 165–188.
- [246] Von Kármán, T., "On Laminar and Turbulent Friction," *Journal of Applied Mathematics and Mechanics*, Vol. 1, 1921, pp. 235–236.

[247] Raffan, F., "Experimental Characterization of Film Cooling Flows With Minimally Intrusive Diagnostics," M.Sc. Thesis, Department of Aerospace Engineering, University of Maryland, College Park, MD, 2008

[248] Kruka, V. and Eskinazi, S., "The Wall-jet in a Moving Stream," *Journal of Fluid Mechanics*, Vol. 20, Part 4, 1964, pp. 555–579.

[249] Liepmann, H. and Roshko, A., *Elements of Gas Dynamics*, Wiley, New York, 1957, pp. 104–106.